The University Of Sheffield.

Image-Based Fracture Mechanics with Digital Image Correlation and Digital Volume Correlation

By:

Ahmet Fatih Cinar

The University of Sheffield

Department of Mechanical Engineering

A thesis submitted in partial fulfilment of the requirements for the degree of

Doctor of Philosophy

July 2019

Publications

Journal publications

[1] A. Cinar, S. Barhli, D. Hollis, M. Flansbjer, R. Tomlinson, T. Marrow, et al., "An autonomous surface discontinuity detection and quantification method by digital image correlation and phase congruency," Optics and Lasers in Engineering, vol. 96, pp. 94-106, 2017.

[2] M. M. Selim Matthias Barhli, Ahmet F Cinar, David Hollis, Thomas James Marrow, "J-integral calculation by finite element processing of measured full-field surface displacements," *Experimental mechanics,* vol. 57.6, pp. 997-1009, 2017.

[4] S. Barhli, L. Saucedo-Mora, M. Jordan, A. Cinar, C. Reinhard, M. Mostafavi, et al., "Synchrotron X-ray characterisation of crack strain fields in polygranular graphite," Carbon, vol. 124, pp. 357-371, 2017.

[5] P. Wilson, A. Cinar, M. Mostafavi, and J. Meredith, "Temperature driven failure of carbon epoxy composites–A quantitative full-field study," Composites Science and Technology, vol. 155, pp. 33-40, 2017.

Conference proceedings

[6] A. F. Cinar, S. M. Barhli, D. Hollis, R. A. Tomlinson, T. J. Marrow, and M. Mostafavi, "Autonomous surface discontinuity detection method with Digital Image Correlation," presented at the 10th BSSM International Conference on Advances in Experimental Mechanics, Heriot-Watt University, Edinburgh, UK, 2015.

[7] A. F. Cinar, S. M. Barhli, D. Hollis, R. A. Tomlinson, T. J. Marrow, and M. Mostafavi, "Application of 3D phase congruency in crack identification within materials," presented at the 11th BSSM International Conference on Advances in Experimental Mechanics, University of Exeter, Exeter, UK, 2016.

[8] “A. F. Cinar. C. Simpson, P. Lopez-Crespo, M. Mostafavi, T. Connolley, P.J. Withers, "The evolution of crack tip stress fields as a function of R-ratio and overload during fatigue crack growth in a bainitic steel," in 12th International Conference on Fatigue Damage of Structural Materials, 2016.

[9] C. W. T. Connolley, F. Wang, M. Mostafavi, A.F. Cinar, D. Eskin and J. Mi, "In-Situ X-Ray Observations of the Effect of Ultrasound on Liquid and Semi-Solid Metal Alloys," in THERMEC 2016 International Conference on Processing & Manufacturing Of Advanced Materials, 2016.

[10] D. H. A.F.Cinar, R.A. Tomlinson, C. Reinhard, T. Connolley, T.J. Marrow, M.Mostafavi, "Crack characterization in a Metal Matrix Composite with 3D Phase Congruency and Digital Volume Correlation," in 12th International Conference on Advances in Experimental Mechanics (BSSM), Sheffield, University of Sheffield, 2017.

There is a crack in everything, that's how the light gets in. - **Leonard Cohen**

Acknowledgements

First and foremost, I would like to express my sincerest appreciation, both equally, to my PhD supervisors, Dr Mahmoud Mostafavi and Dr Rachel Tomlinson.

Mahmoud, for his undivided encouragement, instrumental belief, and absolute trust. Without a shred of doubt, only his guidance and extraordinary moral support encouraged and allowed me to go far and beyond.

Rachel, for her timeless motivation, pivotal advice and, undoubtedly, her endless patience. Thank you for consistently steering me in the right direction.

I would also like to sincerely thank Prof James Marrow for his guidance with his immense knowledge and insightful comments. Additionally, I would also like to thank James once again for inviting me to OxfordMaterials and for making me feel integral part of the team. I have gained immeasurable experience during our collaboration.

I would like to thank Dr Dave Hollis, Dr Thomas Connolley and Dr Christina Reinhard for providing their knowledge and logistical support in my experiments.

There are many people who made a significant impact on this growth journey I took, some four years ago, whom I won't be able to fit into this single page. Strangers who became acquaintances. Acquaintances who became friends. Friends who became my family. Family who became my kindred spirit. I would like to thank each and every one of you with my unlimited heartfelt gratitude.

Firstly, in no particular order, I would like to thank the acquaintances who became more than friends; Dr. Selim Barhli, Dr Chris Simpson, Mr Matthew Molteno, Mr Philip Earp, Dr Luis Saucedo-Mora, Mr Matthew Jordan, Mr Shixiang Zhao, Ms Liye Yan, Mr Anthony Reid, Ms Samantha Abrego and Mr Nithiananthan Kuppusamy. To my friends who became my family, making these past four years become a little more enjoyable and taught me the arts of belly laughing. Thank you. Again, in no particular order; Ane, Milad, Joe, Elene, Nick, Peter, Coffee, Ethan, Claire, Rob & Elena, Adam, Sayeh, Rich & Heledd and lastly Ahmed.

I would like to single out and thank, Dr (soon to be) Laura Vergoz for being the lighthouse in my most desperate need and for having the patience to proof read my thesis. ☺

I would like to dedicate this thesis to my loving mother and father. I would not be where I am today without their tireless guidance and support.

Abstract

Analysis that requires human judgement can add bias which may, as a result, increase uncertainty. Accurate detection of a crack and segmentation of the crack geometry is beneficial to any fracture experiment. Studies of crack behaviour, such as the effect of closure, residual stress in fatigue or elastic-plastic fracture mechanics, require data on crack opening displacement. Furthermore, the crack path can give critical information of how the crack interacts with the microstructure and stress fields. Digital Image Correlation (DIC) and Digital Volume Correlation (DVC) have been widely accepted and routinely used to measure full-field displacements in many areas of solid mechanics, including fracture mechanics. However, current practise for the extraction of crack parameters from displacement fields usually requires manual methods and are quite onerous, particularly for large amounts of data.

This thesis introduces the novel application of Phase Congruency-based Crack Detection (PC-CD) to automatically detect and characterise cracks from displacement fields.

Phase congruency is a powerful mathematical tool that highlights a discontinuity more efficiently than gradient based methods. Phase congruency's invariance to the magnitude of the discontinuity and its state-of-the-art de-noising method, make it ideal for the application to crack tip displacement fields. PC-CD's accuracy is quantified and benchmarked using both theoretical and virtual displacement fields. The accuracy of PC-CD is evaluated and compared with conventional, manual computation methods such as Heaviside function fitting and gradient based methods. It is demonstrated how PC-CD can be coupled with a new method that is based on the conjoint use of displacement fields and finite element analysis to extract the strain energy release rate of cracks automatically. The PC-CD method is extended to volume displacement fields (VPC-CD) and semi-autonomously extracts crack surface, crack front and opening displacement through the thickness. As a proof of concept, PC-CD and VPC-CD are applied to a range of fracture experiments varying in material and fracture behaviour: two ductile and one quasi-brittle for surface displacement measurements; and two quasi-brittle and one ductile for volume measurements. Using the novel PC-CD and VPC-CD analyses, the crack geometry is obtained fully automatically and without any user judgement or intervention. The geometrical parameters extracted by PC-CD and VPC-CD are validated experimentally through other tools such as: optical microscope measurements, high resolution fractography and visual inspection.

Contents

List of Figures

List of Tables

Nomenclature

A_n	Amplitude of the nth Fourier Component
ϕ_n	Local phase of the nth Fourier component
PC	Phase congruency function
$E(x)$	Local energy of a signal at $\boldsymbol{x}$
$\Delta\phi_n$	Measure of Phase congruency
ε	Small number to prevent division by zero
T	Noise compensation
c	Cut-off value for the filter
γ	Gain factor that controls the sharpness of the cut-off
A_{max}	The maximum of the amplitudes of the different orders of the Fourier components
$f_{\mathcal{H}}$	Hilbert transform of a function f
h_1, h_2	Riesz's filters in the image domain
H_1, H_2	Monogenic filters
g	Log-Gabor wavelet function
f_M	2D monogenic signal
$W(x)$	Weighting function
r_g	Radius of the Log-Gabor filter in polar co-ordinate system
ω_0	The central frequency of the Log-Gabor wavelet function
$\frac{k}{\omega}$	Log-Gabor Filter's bandwidth
A_n^L	Local amplitude of the monogenic signal
ϕ^L	Local phase of the monogenic signal
θ^L	Local orientation of the monogenic signal
$\bar{E}$	Total energy
$\bar{\phi}$	Total Phase angle
$\bar{\theta}$	Total orientation angle
σ_R	Standard deviation of the Rayleigh distribution
μ_R	Mean of the Rayleigh distribution
σ_G	Standard deviation of Gaussian distribution
R	Rayleigh distribution
k	Number of standard deviations of the noise energy beyond the mean

N	Number of log-Gabor wavelet scales
λ_{min}	Wavelength of the smallest scale filter
α	Scaling factor between successive filters
d_{PC}	Amplification of the calculated phase deviation
α_s	Weight of the smoothing term in the Chan-Vese
μ_{seg}	Mean value of the 3D Phase Congruency field
α_{seg}	Weighting terms for the Propagation field
β_{seg}	Weighting terms for the Geodesic field
δt_{seg}	Time step for each iteration in 3D Region based active contour algorithm
ODw	Outlier Deletion window size
ODt	Outlier Deletion threshold number
Ux, Uy, Uz	Displacement field in the X, Y or Z direction
$CODUx, CODUy, CODUz$	Crack Opening Displacement in the X, Y or Z direction
$\delta_X^+, \delta_Y^+, \delta_Z^+$	X, Y,Z Displacement values of the upper crack face
$\delta_X^-, \delta_Y^-, \delta_Z^-$	X, Y,Z Displacement values of the lower crack face
a	Crack/notch length
$\hat{a}$	Measured crack/notch length
b	Thickness of specimen
W	Width of specimen
d	Notch radius
δ	Crack opening displacement
$\hat{\delta}$	Measured crack opening displacement
ψ	Crack path
$\hat{\psi}$	Measured crack path
σ	Far field stress
σ_0	Yield strength
σ_t	Tensile strength
α	Yield offset
μ	Shear modulus
υ	Poisson's ratio
κ	Plane strain condition
E	Young's modulus

Γ_N	Percentage additive noise
$H(x)$	Heaviside step function
S_{subset}	Subset size
S_{step}	Step size
σ_{Ux}, σ_{Uy}	Standard deviation of the X,Y displacement field after rigid-body movement
R	R-ratio
K, K_I, K_{II}, K_{III}	Stress intensity factor , Mode I, II and III
K_{min}, K_{max}	Minimum and Maximum stress intensity factor
ΔK	Difference between Min and Max stress intensity factor
ΔK_{app}	Applied stress intensity factor range
P_{min}, P_{max}	Minimum and Maximum applied load
P_{close}, P_{open}	Crack closing and opening applied load
J	J-integral
$\theta_{HoughMin}$	Minimum search orientation of Hough transform
$\theta_{HoughMax}$	Maximum search orientation of Hough transform
$Hough_{MinLength}$	Minimum length of the Hough transform detected line
$Hough_{FillGap}$	Degree of connectivity freedom of Hough transform detected line
$Itern$	Maximum number of iterations

List of Abbreviations

ACPD	Alternating Current Potential Drop
AOS	Additive Operator Splitting
CCD	Charge-Coupled Device
CF	Crack Front
CFRP	Carbon Fibre Reinforced Polymer
CL	Crack Length
CMOD	Crack Mouth Opening Displacement
CMOS	Complementary Metal-Oxide-Semiconductor
COD	Crack Opening Displacement
CP	Crack Path
CS	Crack Surface
CT	Compact Tension
CTE	Coefficient of Thermal Expansion
CTIP	Crack Tip
CTOA	Crack Tip Opening Angle
CTOD	Crack Tip Opening Displacement
DCPD	Direct Current Potential Drop
DENT	Double Edge Notch Tension
DIC	Digital Image Correlation
DVC	Digital Volume Correlation
FCG	Fatigue Crack Growth
FE	Finite Element
FFT	Fast Fourier Transform
GAC	Geodesic Active Contour
ILS	Iterative Least Squares
JEEP	Joint Engineering, Environmental and Processing
LED	Light Emitting Diode
LEFM	Linear Elastic Fracture Mechanics
LSM	Least Squares Method

MMC	Metal Matrix Composite
MRI	Magnetic Resonance Imaging
NaN	Not a Number
NLEP	Non Linear Elastic Plastic
ODt	Outlier Deletion threshold
ODw	Outlier Deletion window
OST	Optical Scanning Tomography
OUR-OMA	Oxford University Reinjection-Optimized Meshing Add-on
PC-CD	Phase Congruency-based Crack Detection
PET	Positron Emission Tomography
PIV	Particle Image Velocimetry
px or pix	pixels
ROI	Region of Interest
RSME	Root Square Mean Error
SIF	Stress Intensity Factor
SNR	Signal to Noise ratio
SSSIG	Sum of Square of Subset Intensity Gradients
TSA	Thermoelastic Stress Analysis
UD	Unidirectional
VPC-CD	Volume Phase Congruency-based Crack Detection
XCT	X-ray Computed Tomography
X-DIC	eXtended - Digital Image Correlation
XI-DIC	eXtended and Integrated - Digital Image Correlation
XRD	X-Ray Diffraction

1 INTRODUCTION

1.1 Background

The current standards for structural integrity only require crack mouth opening displacement (CMOD) [11] and based on the CMOD, the standards give an underestimation of the safety of a cracked component. With the growing advancement of engineering science, technology, and exponentially growing computational power, we can generate large amounts of data from an experiment to analyse the data and obtain crack parameters. Additionally, engineering assessments have been over-conservative to ensure the safety of the components with large error margins. However, as the pressure on natural resources and economy increases, reducing the conservatism in our calculations, albeit without compromising safety, is becoming more desirable. Therefore, it is becoming more critical to understand how cracks behave and interact with their surrounding microstructure with the aid of image-based methods. Image-based methods are critical to the quantification of fracture, because they can capture a still moment of any dynamic fracture experiment. The full field digital image can then be resourceful for the characterisation of a cracked body and can be used to obtain useful information in real time. Imaging methods are not only non-destructive, but also non-contact, meaning an experiment can be fully observed without altering the state of the cracked body. A conventional fracture experiment commonly uses a strain gauge and /or clip gauge which require contact with the test specimen. Although strain and clip gauges are very accurate, the contact between the sensor and test specimen may alter the behaviour of the latter. Image-based methods are relatively easy set up and mostly require a “point and capture” philosophy.

Once a crack is detected in a sample, the next step would be to assess and characterise the structural integrity of the cracked body. Crack propagation is a critical factor that effects the life span of a component and characterisation of the crack can give invaluable information regarding the structural integrity and health. Among the quantitative methods of traditional fracture mechanics, several metrics are used to determine the driving force of fracture and help predict when a crack may propagate; The elastic energy release rate, G; stress intensity factor, K; the J-integral; the crack tip opening displacement (CTOD) and crack tip opening angle (CTOA). To obtain these parameters, the physical geometry of a crack plays a significant role and a poor geometrical calculation will impact the crack propagation metric.

A crack is defined quantitatively using the following geometrical parameters: Crack Opening Displacement (COD); Crack Tip location (CT); Crack Length (CL) / growth, Crack Path (CP)/ location.

For the purpose of the study, the crack path is defined by the geometrical mid-point between the crack faces while crack opening displacement is the distance between the crack faces. The underlying assumption for the model-based approach is that the crack is symmetrical, parallel to the crack propagation axis. Figure 1.1 demonstrates the crack model on an experimental image of a cracked body where the red line depicts the crack path and cyan arrows show the opening displacement. Designing materials to withstand stress and damage tolerance requires a detailed understanding of how a propagating crack interacts with the materials microstructure. These parameters help us quantify the state of the cracked body aiding in a better characterisation of a crack.

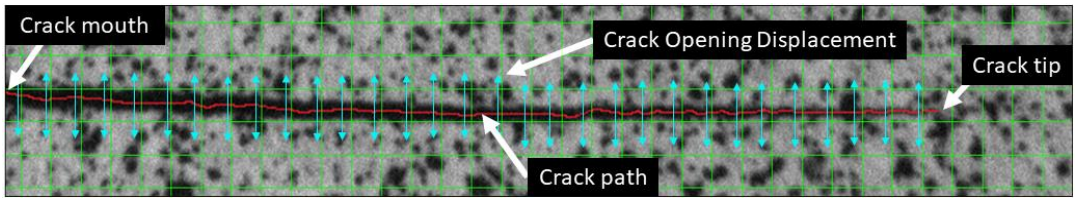

Figure 1.1 The geometrical parameters to describe a crack

There is a power arsenal of apparatus at our disposal when it comes to imaging methods. The use of simple conventional Charged Coupled Device (CCD) camera, where the surface of a cracked body is captured at any given time, can allow for the quantification of the crack parameters. An additional camera can be configured to provide a stereovision arrangement to give information out-of-plane to the captured surface.

High-speed cameras, where the development of laser technology allows us to capture many hundreds and thousands of images per second of the surface, can give invaluable and contemporary understanding of how brittle bodies fracture. High speed imaging can also shed light in the manner of how ductile materials fracture during high strain rates. Multi-million-pound state-of-the-art imaging facilities such as synchrotrons and lab-based X-rays use powerful light sources to capture the volume information of a cracked body. The volume information gives us an extra dimension and depth into the fracture properties which enable the possibility of calculating COD through the thickness of the crack, crack front and crack surface. Using the scientific tools mentioned above can give us a much more precise and deeper understanding of how materials behave when they fail.

Imaging analysis tools such as Digital Image Correlation (DIC) and Digital Volume Correlation (DVC) are based on obtaining displacement fields from digital images and are becoming more and more attractive in experiments. To obtain displacement measurements of the surface, the surface or the volume of the specimen requires uniquely trackable patterns once captured by imaging methods. The trackable pattern could either be the natural microstructure of the material or a speckle pattern paint can be administered on to the surface. Speckle patterns are presented as random clusters of low grey-scale intensity pixels on a high grey-scale intensity background. Visually, it is difficult to differentiate the crack artefact, as the crack artefact often has low grey-scale intensity, very similar to the gray-scale intensity of speckle patterns. Hence, using common image processing approaches are computationally difficult as they will depend on an adaptive way of deciding a threshold to classify the speckle pattern. This issue is usually addressed by creating an interactive algorithm, which includes human judgement. The measurement of surface displacements, deformations, crack opening displacement and the mapping of crack path are key to gain qualitative and quantitative information. The new quantitative information will help to better understand the fracture process for usage of other techniques. In this thesis, commercially available DIC and DVC software algorithm are used as a “black box” and some displacement calculation parameters are uncontrollable by the user.

However, with the growing advancement of data acquisition, scientists using image-based methods are typically faced with rigorous and burdensome task of analysing a high volume of data that constantly requires user judgement and intervention. Therefore, it is becoming a more critical task to detect and quantify cracks from many captured images automatically, so that scientists may spend more time trying to understand what the experimental results mean.

To meet this requirement, this thesis will then present a novel method of automatically determining the location of the crack path from surface and volume displacement fields. The location of the crack path can aid in the use of domain integral or contour integral methods that are used to determine crack parameters such as the J-integral. However, it must be noted that these methods are sensitive to the displacement vectors close to the crack faces (i.e. the geometry of the crack and particularly the crack tip) as their calculation requires the integral path to start and end on the traction-free crack faces [12].

1.2 Aims and Objectives

The aim of this research is to develop a novel method of extracting the maximum information from a fracture experiment using imaging methods with minimal user intervention and judgement.

State-of-the art digital image capture tools, such as CCD and X-ray tomography are shown to be a powerful implementation for any fracture experiment as the technologies can capture the full observable information from a surface or volume of a specimen. However, experimentalists are usually faced with rigorous and cumbersome manual analysis methods of trying to quantify and understand their experimental data. They are also required to use their judgement and opinion in their calculations which may lead to bias in their analysis.

This thesis will show that it is necessary for the research field of image-based fracture mechanics to devise an autonomous tool for deciding and quantifying displacement fields from fracture experiments. The crafted tool should be applicable to all type of materials and material behaviours and can extract fracture parameters from surface and volume displacement fields. Applicability to surface and volume displacement fields will aid into extracting maximum information from experiments. The development of such a tool will ultimately lead to a change in experimental process that is able to calculate fracture parameters of an experiment with ease, in real time with maximal information which can change the standard for material testing. Better assessments allow for a better prediction and understanding of failure in a solid body which will increase the reliability and the lifetime of components.

1.2.1 Aims

The aims are to develop a full-field method that :

- can retrieve the maximum information from a fracture experiment;
- is applicable to all types of material behaviours (brittle, elastic and elastic-plastic);
- is able to extract crack parameters from volume fields;
- requires minimal user interaction to help cut bias and user judgement from calculations.

1.2.2 Objectives

The objective of this thesis is;

- to study the state-of-the-art of fracture mechanics and show that the development of an image-based method is necessary;
- to demonstrate the significance of image-based methods and explore the tools that are available;
- to employ a theoretical study to benchmark the developed method and compare it with ones available in literature;
- to investigate the impact of noise and uncertainty on the accuracy of the developed method;
- to apply a virtual study to benchmark the developed method and compare it with ones available in literature with different crack opening displacement profiles and uncertainty;
- to study the impact of dic parameters that can be tuned by the user, such as step size and subset size, and to study the associated errors on the developed method;
- to present a methodology that uses the developed method to extract j-integral from a measured displacement field;
- to use real experimental dataset, with different material behaviours and different image capturing methods, to demonstrate the suitability and the wealth of information devised by the developed method;
- to validate the crack parameters obtained from the experimental dataset.

1.3 Outline of Thesis

Chapter 2 will first study the state of the art and outline the established scientific tools and methodologies for obtaining information from a fracture assessment experiment. The literature review will first give a brief review of the parameters used to assess a material that exhibits a crack. After, literature review will discuss methods of crack detection, where automation methods (i.e. methods that require minimum user intervention) are explored; and crack characterisation where quantification with the aid of imaging tools are studied. The objective is to explore how we can retrieve the maximum information from a fracture experiment. The literature will also review how failure of brittle, elastic and elastic-plastic materials can be quantified using the studied tools. Discussions are concurred regarding the benefits, error sources and limitations of image-based methods over other established methods in the literature.

A novel Phase Congruency based Crack Detection (PC-CD) and parameter extraction methodology will be outlined in Chapter 3 for two-dimensional, stereo-vision and volume displacement fields. Phase congruency is a powerful tool for highlighting discontinuities and features in images. It is shown that Phase congruency is more noise robust than gradient based tools, which are conventionally usually used in the literature to segment cracks. The 2D and 3D (stereo-vision) methods have been developed to be fully automatic, requiring almost no user interaction while the volume application has been developed to be partially automatic, requiring an easy interaction with the algorithm. The automation of detection and extraction of cracks means the method will require less user judgement than necessary which enables the processing of large quantity of data within a short space of time.

Chapter 3 will also describe a methodology called OUR-OMA (Oxford University Reinjection-Optimized Meshing Add-on) [2] which is a finite element approach to extract the J-integral from surface measured displacement fields. However, the OUR-OMA is not automatic and requires user judgement of the crack location from the displacement field. It is observed that the location of the crack affects the accuracy of J-integral. This thesis will show how OUR-OMA can be utilised for an automatic J-integral calculation by combining the parameters obtained from PC-CD. Later in chapter 5 and 6, the extraction of J-integral coupled with PC-CD will be used on two large experimental datasets: surface displacement fields of a fatigue crack growth overload experiment of Bainitic steel; and volume displacement fields of a crack propagation of aluminium Metal Matrix Composite (MMC) with titanium phase.

In Chapter 4, the novel PC-CD is benchmarked using theoretical and virtual analysis to evaluate its performance with respect to uncertainty. To benchmark the PC-CD method, several virtual datasets have been created using *ODIN* which is a code that allows the user to inject displacement fields and deform images. The created virtual images were used as a controllable simulation of a cracked surface image. The aim was to investigate the impact of crack mouth opening displacement and the effect of uncertainty to determine how accurately PC-CD is able to extract crack parameters. The analysis can act as a guideline to approximate the uncertainty of the crack parameters based on the crack mouth opening of an experiment and uncertainty of the displacement field. The PC-CD tool is also compared with other manual methods in the literature (i.e. Gradient based methods and Heaviside function fitting). The impact of DIC parameters such as subset size and step size on PC-CD extracted crack parameters are studied. Next, PC-CD parameter sensitivity is investigated where the error sources are minimised.

Experimental datasets were used as a proof of concept to give the PC-CD and VPC-CD algorithms real experimental scenarios and to evaluate their performance.

Firstly, the PC-CD algorithm was applied to crack detection and quantification in two different classes of materials in order to examine its accuracy and robustness in real laboratory conditions. The surface studies represented;

- Tensile experiment of a quasi-brittle material with complex microstructure and small- scale displacements. The extracted parameters were validated by superimposing the PC-CD solved crack path to the deformed image;
- Fatigue crack growth of a ductile material with large scale deformation and crack blunting effects. The crack path value obtained by PC-CD algorithm was validated by high resolution optical microscopy of the cracked sample surface;
- Fatigue crack growth overload of a ductile material with crack closure and large plasticity effects. The PC-CD algorithm was validated using a high-resolution image of the fracture surface (i.e. fractography).

The VPC-CD algorithm was then applied to experiments of two different material classes and the effects were studied. The cases represent:

- Two fracture propagation experiments of a ductile material: one large scale yielding; other with small scale deformation. The VPC-CD algorithm is validated by superimposing the VPC-CD solved crack elevation to a few slices of the deformed tomograph;
- Stable fracture propagation experiment of quasi-brittle with non-linear material properties described the effect of microcracking on the elastic modulus in the fracture process zone. Visual inspection of the crack length validated the crack front obtained by VPC-CD analysis;
- Temperature driven fracture of a quasi-brittle material with small scale displacement of a transverse crack. Visual inspection of the tomograph validated the crack geometry calculated by VPC-CD.

2 LITERATURE REVIEW

Fracture mechanics concerns the study of propagation of cracks in materials. Generally, there are two established concepts in predicting crack growth, the energy balance and the stress intensity factor approach.

A cracked material body is within a thermodynamic system and the cracked body's energy balance determines if the crack will propagate or not. A material's energy balance is widely discussed in Griffith's work [13] where he states that "crack growth will occur, when there is enough energy available to generate new crack surface". However, Griffith's work originally dealt with very brittle materials, specifically glass rods. When a material exhibits more ductility, the surface energy alone fails to provide an accurate model for fracture. In 1956, Irwin [14] and Orowan [15] modified Griffith's model of the energy approach, "strain energy release rate" G, to explain ductile fracture behaviour. They suggested that most of the released strain energy is absorbed not by creating new surfaces, but by the energy dissipation due to the plastic flow in the material near the crack tip. G represents material's resistance to crack extension and is also known as the crack driving force. Strain energy release rate is considered as the fracture toughness of the material and is independent to the loading state and geometry of the crack.

While the energy-balance approach provides a great deal of insight to the fracture process, the stress intensity factor approach has proven more useful in engineering practice. The stress state at near a sharp crack tip can be determined analytically using Linear Elastic Fracture Mechanics. Using this knowledge, the stress intensity factor can be solved if the externally applied stress, the geometry factor and crack length are known. Irwin et al. [14] identified three fundamental modes of crack loading modes, mode I, II and III as shown in Figure 2.1. An important property of the stress intensity factors is that they are additive for the same type of loading.

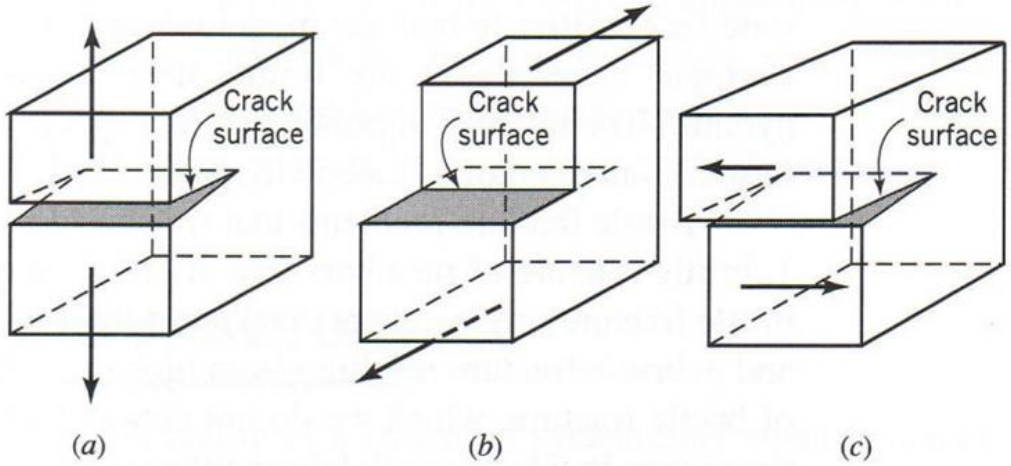

Figure 2.1 Crack loading modes, a) Mode I (opening), b) Mode II (in-plane shear), c) Mode III (out-of-plane shear)

The most general formulation, which has been used to study cracked bodies, is the Muskhelishvili complex variable method[16] . More simpler approaches were also developed by Westergaard [17] and Williams [18], latter being the most commonly used expression for crack tip fields. Williams derived that the crack tip stress and displacement distribution can be expressed by means of a power series. Assuming a plane crack with traction-free faces in a homogeneous linear-elastic isotropic material under mode I loading, the displacement field around the crack tip can be expressed as;

$$U_x = \sum_{n=1}^{\infty} \frac{r^{\frac{n}{2}}}{2\mu} A_n \left\{ \left[\kappa + \frac{n}{2} + (-1)^n \right] \cos\left(\frac{n\theta}{2}\right) - \frac{n}{2} \cos\left(\frac{(n-4)\theta}{2}\right) \right\} \quad (1)$$

$$U_y = \sum_{n=1}^{\infty} \frac{r^{\frac{n}{2}}}{2\mu} A_n \left\{ \left[\kappa - \frac{n}{2} - (-1)^n \right] \sin\left(\frac{n\theta}{2}\right) + \frac{n}{2} \sin\left(\frac{(n-4)\theta}{2}\right) \right\} \quad (2)$$

$U_x$and U_y are horizontal and vertical displacements. In Eq (1) and (2), r and θ are polar coordinates centred at the crack tip. μ is shear modulus defined as $\mu = E/2(1+\nu)$, where E is Young's modulus and ν is the Poisson's ratio. n represents the index of the term of the power expansion and κ is Kolosov's constant depending on plane stress ($\kappa = (3-\nu)/(1+\nu)$) or plane strain ($\kappa = (3-4\nu)$) conditions. Coefficients A_n are functions of relative crack length and are required to be calculated numerically in most cases.

Linear Elastic Fracture Mechanics is only valid if nonlinear material behaviour is confined to a small region surrounding the crack tip. Elastic Plastic Fracture Mechanics (EPFM) is usually used to analyse the large nonlinear material behaviour (i.e. plastic deformation) at the crack tip. There are two parameters that can be used to characterize the nonlinear behaviour at the crack tip, Crack Opening Displacement (COD) and J-integral. The concept of using COD to predict crack propagation was proposed by Wells [19]. He observed that before crack extension, the crack-tip blunts and there is a definite opening at the original crack-tip location. The extent of the opening is dependent on the fracture resistance of the material. ASTM standards [11] use crack length and CMOD to approximate the CTOD.

J-integral is used to calculate the energy release rate in elastic and nonlinear elastic materials, developed by Rice in 1968 [12]. He represented the energy release rate by a path independent line integral. Rice interpreted the J-integral as the difference in potential energy of two cracked bodies submitted to the same boundary conditions but from which the length of cracks differ. The J-integral value is zero over a closed contour and is independent of the path of integration. The J-integral, with units of force per unit thickness, is given by Eq (3),

$$J = \int_{\Gamma} \left(W \mathrm{d}y - T_i \frac{\partial u_i}{\partial x} \mathrm{d}s\right) \qquad (3)$$

Where Γ is an arbitrary curve around the tip of a crack, as seen in Figure 2.2, W is the strain energy density, T_i is the components of the traction vector defined by $T_i = \sigma_{ij} n_j$. u_i is the displacement vector components, $\mathrm{d}s$ is the length increment along the contour, x and y are rectangular coordinates with the y direction taken normal to the crack line and the origin at the crack tip. Rice showed that that for plastic deformation, the J-integral is independent of the path of integration the crack tip. The path independence was later verified by Kobayashi et al. [20] using the finite element analysis.

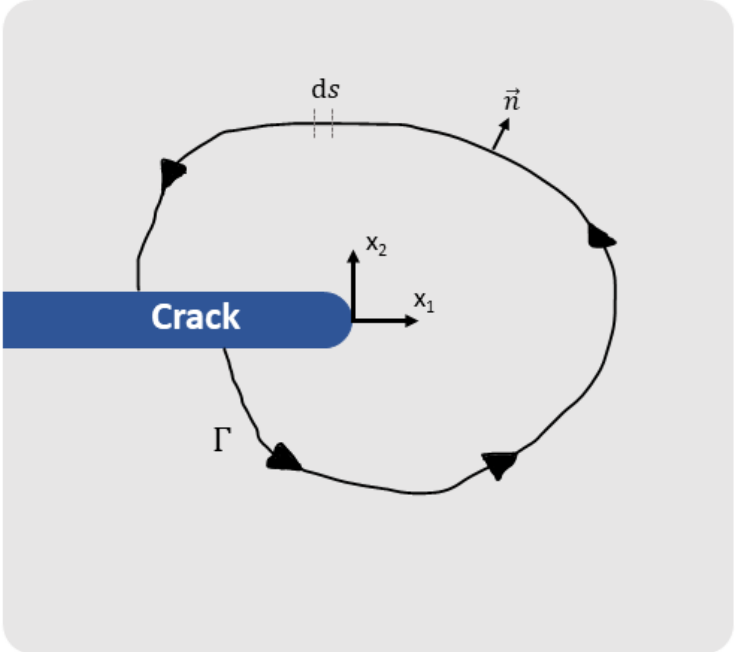

Figure 2.2 Arbitrary contour around the crack tip used in the definition of J-integral.

Shih et al.[21] showed that there is a unique relationship between CTOD and energy release rate for a given material. Although both COD and J are now well-established concepts, EPFM is still very much an evolving field. Currently, the fracture mechanics community are interested in the description of stable ductile crack growth and development of failure assessment methods that combine the effects of plasticity and fracture. This only highlights the importance of gaining maximal information from fracture experiments and to be able to characterize cracks accurately.

2.1 Measurement techniques in fracture mechanics

2.1.1 Single-point measurement

In structural health monitoring, two main approaches exist for damage detection at a local scale; direct measurement and indirect measurement [22, 23]. The direct sensing approach is based on measurements made by a sensor or sensing media that is in direct contact with the damage. One established tool, widely accepted by the scientific community, is the strain gauge [24-28]. A strain gauge (i.e. Figure 2.3) is typically glued onto the surface of a component, and as the surface deforms, the gauge deforms. The electrical resistance of the gauge varies in proportion to the amount of deformation which can be measured. This not only helps getting an accurate and repeatable calculation of strain, but the gauge is also inexpensive, easy to setup, small in size and weight and can be used conveniently for a large variety of environmental conditions. Strain gauges are extremely useful as they can predict how materials behave under loads giving estimations of what strain concentrations should be avoided while maintaining a healthy structural integrity of a component [24]. They are also useful for construction and validation of theoretical and finite element models to help better predict and understand standardised in-situ experiments or specimens of well-defined geometries [29-31].

The calculation of strain is given for a single-point on the surface of a component body, therefore the strain gauge is required to be placed strategically at strain hotspots, where the material is most likely to fail. The criteria make the strain gauge susceptible to error, associated with gauge placement and the likeliness to completely miss strain hotspots and failure. The likeliness to miss failure based on placement is magnified for complex loadings or geometries which is usually a critical process for fracture studies [23].

Indirect measurement techniques take advantage of certain material characteristics that develop once a crack or damage develops, such as material modal frequency [32-34] and Potential drop techniques [35-37]. The changes in the dynamic modal response of the sample can help pinpoint damage location and damage size [32-34]. One of the most commonly used methods for measuring a sample's natural frequency is the impact test using a hammer equipped with an accelerometer [33, 34]. Another application of using modal frequency to detect and estimate the size of cracks is leakage in water pipes [38]. The leak naturally resonates through the whole pipe body so the leak location and leak size can be determined

with two vibro-acoustic emission sensors attached on either side of the pipe, making the application more practical [38].

The potential difference technique relies on the passage of a constant current through a specimen and the measurement of voltage across it. As the crack grows, new surfaces are created at the crack tip, which then increases the electrical resistance in the specimen, hence dropping voltage, due to Ohm's law. Direct Current Potential Drop technique (DCPD) has been used to measure thickness and estimate crack depth on plates and to monitor crack initiation and propagation in crack growth experiments. The Alternating Current Potential Drop technique (ACPD) is like the DCPC, but the current is forced to flow in a thin layer below the surface and therefore overestimates the crack extension as the current path is longer. This allows the crack depth to be estimated. Both methods have been used in fatigue crack growth experiments many times [35-37].

The methods mentioned above generally rely on single point measurement or lack all the desired crack geometrical parameters, which is a conservative method of characterising a crack.

2.1.2 Full-field measurement

Full-field measurement techniques such as Moiré interferometry [39, 40], Photoelastic stress analysis [41], Thermoelastic stress analysis [42, 43] and Image correlation [44] do not suffer the same consequences as single point measurement devices (i.e. strain gauge) and can provide a full field measurement of damage. This ultimately gives a better understanding of localised strain behaviour at any location. These methods have only flourished and become more popular in experimental mechanics over the past three decades thanks to advancements made in cameras, infrared cameras and microcomputers with image processing [45]. The nature of these physical phenomena (Moiré interferometry, Photoelasticity and Thermoelasticity) were all known concepts and were used before, however they heavily suffered from non-automatic processing, meaning the need for tedious and unreliable by-hand manipulations before obtaining any relevant information. Now, these techniques are becoming more established and directly provide displacement, strain or temperature fields of specimens under testing [45].

Moiré interferometry [39, 40, 46] combines the concepts of geometric moiré [47] and optical interferometry [48]. The Moiré effect is the mechanical interference of light by

superimposed network of parallel lines (grating pattern), which are physically attached to the surface of the specimen, and as the specimen is loaded or moved, a fringe pattern is generated since the location of the lines relative to the reference grating changes. The mismatch in pitch between reference and specimen grating (after loading) causes a dark fringe pattern to emerge which describes the type of deformation on the surface [39]. Moiré Interferometry is based on the Moiré effect to calculate displacement measurements by using the superposition of two coherent laser beams of light which creates interference and ultimately fringes, therefore describing the motion [46]. The frequency of the grating patterns is much greater than geometric Moiré (more than 1000 lines / mm) [46], meaning it can calculate displacements up to submicron level [46]. However, Moiré interferometry is very susceptible to environmental disturbances due the high level of sensitivity. The fringe pattern output is optically captured from the experiment and the scale of the displacement is calculated using a mathematical algorithm. The scale of the displacement is coded at the scale of the fringe period. Full-field strain can typically be obtained by numerical differentiation of the displacement measurements via various algorithms [46].

Photoelasticity is a technique for measuring and visualising stresses and strains in a transparent material which utilises a physical phenomenon called birefringence [49]. Birefringence is based on how the wave nature of light interacts with the stress state of material. As white light travels, it emits waves that are omnidirectional and vibrate out at all angles perpendicular to the direction of the light beam. A polarizer only allows one component of the light to pass, dependent on the orientation of the polarizer. Once polarized light hits the material, birefringence causes the light to travel at two different speeds, proportional to the principal strains. Another polarizer is used to combine the two waves to generate an interference pattern which visually shows the stressed state of the material (i.e. Figure 2.3). This then can be captured optically to represent a direct strain measurement of the specimen with high spatial resolution [49]. Photoelasticity presents the advantage to a reliable full-field values of the difference between the principal normal stresses in the plane of the specimen, however the drawback is the method requires the optical property of the cracked body to be birefringent and therefore cannot be applicable to all materials. Photoelasticity has been used many times to describe a fracture experiment [50-53].

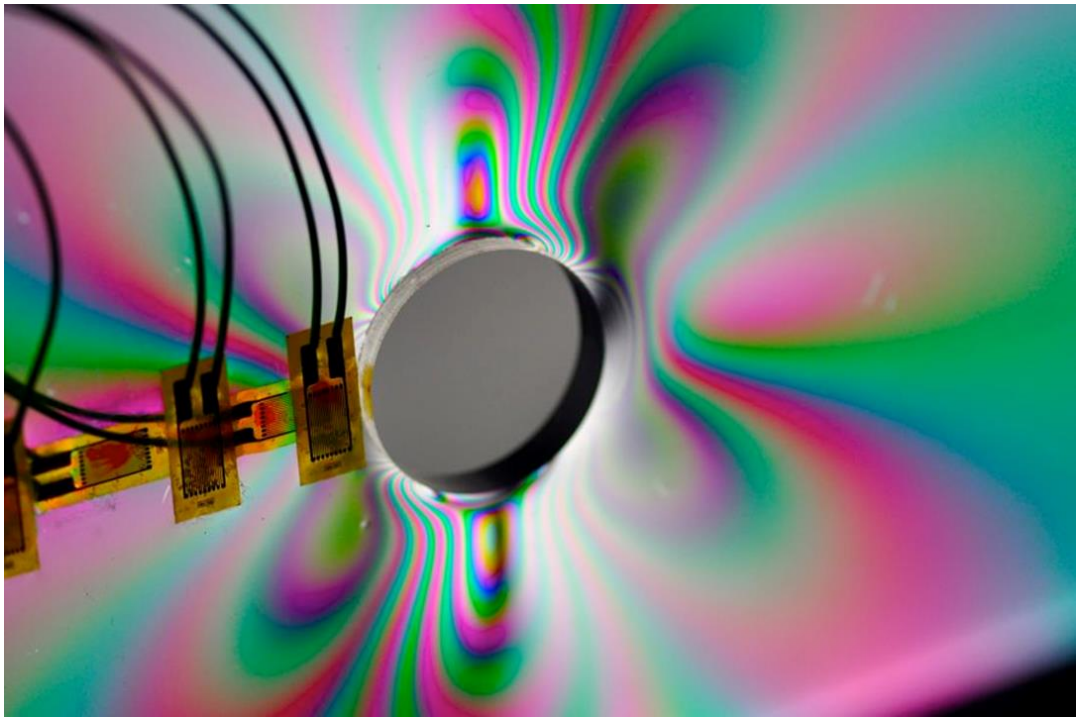

Figure 2.3 Photoelastic stress analysis set up with vertical and horizontal strain gauges (Picture from website alliance.seas.upenn.edu)

Thermoelastic stress analysis (TSA) uses the concept of the thermoelastic effect, where a small temperature change occurs in a material subjected to elastic deformation. The change of temperature has a direct relation to the stresses and strains of the material, allowing to calculate these directly. However, the relation assumes an adiabatic condition (no significant heat loss). As a practical matter, the adiabatic assumption is met by continually and "rapidly" changing the load on the specimen (i.e. fatigue). Heat loss by conduction only becomes an issue in the case of high thermal gradients and therefore the adiabatic assumption needs to be taken under consideration [54]. Using sensitive infra-red sensors these small temperatures can be measured and with some computation and thresholding the full-field stress measurements can be obtained.

2.2 Crack detection using image processing

Crack detection using image processing techniques is advantageous as it provides an accurate quantitative result compared to the conventional manual methods [55]. Most approaches to identify cracks in digital images use edge detection methods such as global and local grey-scale intensity thresholding. These require human interaction to be optimal [56, 57]. For instance, Ikhlas et al. [58] presented a study of different edge detection techniques including the wavelet transform and the Fast Fourier Transform (FFT) to identify cracks in bridges, concluding that the wavelet transform is more reliable than other methods. However, the method is based on a chosen threshold value, which is a parameter crucial to its performance. Tomoyuki et al.[59] proposed a fast crack detection method, applied to concrete surfaces, that was based on percolation-based image processing; quantitative analysis showed this to be computationally more efficient than the wavelet approach but at the cost of precision. Additionally, these methods assume that the crack is sufficiently open to be detectable in the image. This inherently limits these methods' accuracy to a pixel at best. However, a number of image analysis techniques have sub-pixel accuracy. They track the surface displacement of the features near the discontinuity and therefore can detect cracks that are not otherwise visible in the raw image [60]. Avril et al. [61] introduced a method of detecting surface discontinuities and calculation of the crack width with sub-pixel precision, using a grid that is periodically spaced on the surface of the cracked body and with the aid of a windowed discrete Fourier transform to calculate the phase shift between the cracked faces. Not only is the method only applicable to brittle specimens, which limits the material options, but additionally the method requires a user-selected threshold parameter.

2.3 Displacement calculation methods

Full field displacement measurement tools can be put into two categories; interferometric techniques and non-interferometric techniques. Among the interferometric techniques are; holographic interferometry, speckle interferometry and moiré interferometry (mentioned earlier in section 2.1.2). The non-interferometric techniques can be defined as the grid method [62] and Digital Image Correlation (DIC) [63-65] – which will be discussed later in depth in section 2.3.1. The grid method [62] requires a uniformly spaced grid applied to the specimen surface and by calculating the phase shift, accurate surface deformations can be obtained. Interferometric displacement methods require a coherent light source and the measurements are normally conducted on a vibration isolated optical platform in a laboratory, where the displacement is given as a form of the phase difference of the scattered light wave by comparing before and after surface deformation. Digital Image Correlation (DIC) does not require such restrictive preparation and has less strict requirements under experimental conditions. The fundamental setup of a DIC solid mechanics experiment can simply be to point and capture an image of a surface that has random features before and after applied load. Due to its experimental simplicity, the DIC method has been widely accepted and commonly used as a powerful and flexible tool for surface deformation measurement in the field of experimental solid mechanics. The experimental easiness of two-dimensional DIC has been extended and developed such that it is possible to obtain out-of-plane and volume displacement measurements. An additional camera can give a DIC system a stereovision of the sample surface and out-of-plane measurement can be made. Image volume data can be obtained from X-ray tomography which builds image contrast based on the microarchitectural detail of the material. By tracking voxels between reference and deformed configurations, volume displacement measurements can be obtained. Interferometric displacement measurement techniques and the grid method are limited only to surface displacement measurements and cannot be developed in a similar manner to calculate volume displacement measurements. Because of this, this research focussed on displacement measurements obtained from Digital Image Correlation (DIC), Stereo-Digital Image Correlation (3D-DIC) and Digital Volume Correlation (DVC).

2.3.1 Digital Image Correlation

Digital Image Correlation is a tool used to calculate surface displacement measurements and is now the most frequently used optical based method in fracture mechanics. Introduced in the 1980s by Peters and Ranson [63-65], DIC is a full field non-contact method that is relatively easy to set-up and provides high spatial resolution.

The fundamental principle of DIC is to compare grey-scale images of an object surface captured before and after deformation; these are referred to as the reference and deformed image, respectively. The random pattern on the surface (see Figure 2.4) carries information after deformation and is a requirement for surface tracking. Either the natural texture of the material is tracked, or the surface can be administered a randomised speckle pattern that obeys the material surface.

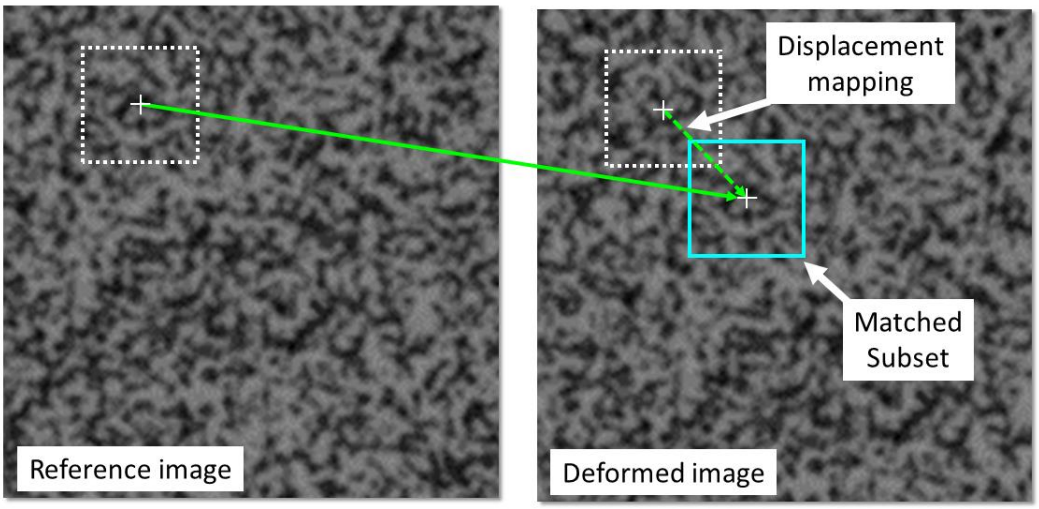

Figure 2.4 Conventional Digital Image Correlation tracking and mapping of a subset (definitions given in Figure 2.5)

Conventionally, the reference image is divided into interrogating windows or subsets that are matched (or tracked) in the deformed image, using a shape function, to obtain the displacement of each interrogation window (see Figure 2.4). Higher order shape functions can be used to obtain improved displacement approximations but usually first or second order provides sufficient accuracy [66]. Different matching procedures can be used to search and evaluate the similarity of the grey-scale pattern [67]. Over time, with the introduction of new and higher accuracy matching procedures, DIC has been successively improved in terms of displacement measurement accuracy and is able to give measurements accurate to 1/100th of a pixel.

Theoretically, the DIC technique allows for full-field displacement measurements, at every data point within a selected region of interest. However, in practice, the displacement data point is not associated to that pixel, but rather to the averaged displacement of the domain around the data point (see Figure 2.5). This results in the loss of spatial resolution at the gain of quantified surface displacement measurement. The change in spatial resolution also has ramifications on the displacement measurement of the surface, especially at locations of high displacement gradient.

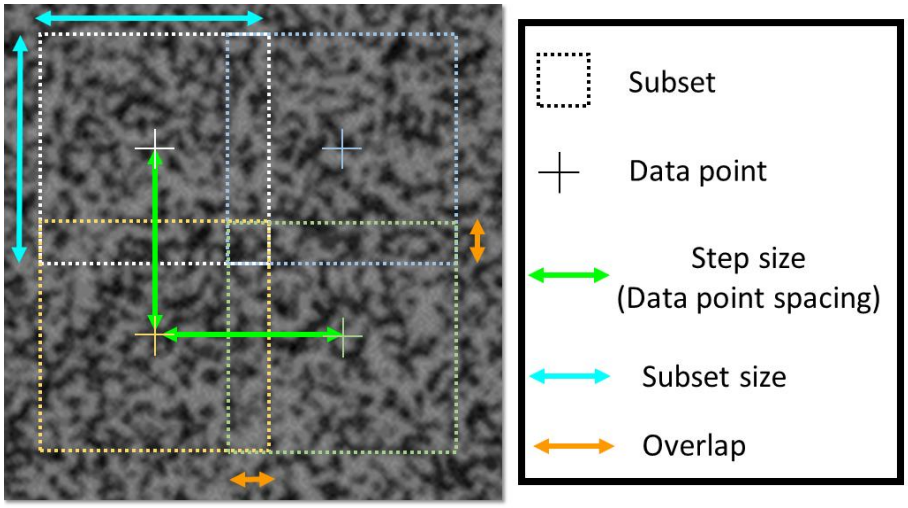

Figure 2.5 Controllable Digital Image Correlation parameters

This research project used the iterative least squares method (ILS) method, proposed by Pan et al. [68] and incorporated in LaVision Davis Strain Master Code [37]. The idea was to use LaVision DaVis Strain Master as a "black box" and attempt to address the user-controlled variables of the code such as subset size and step size or percentage of overlap. (see Figure 2.5). Many studies have been based on the subset size and step size selection; Lecompte et al. [69] showed the influence of mean speckle size on the accuracy of the measured displacement fields using different subset sizes. They report that the larger subsets present better results but highlight the importance for the subset size to be chosen in accordance with the expected deformations; i.e. a large subset will smooth real behaviour of steep gradients in the displacement. Sun et al. [70] introduced a concept of subset entropy that can quantitatively denote the subset image quality for DIC and hence determine an optimal selection of subset size.

Pan et al. [71] presented a guideline for the determination of subset size by quantifying speckle pattern quality using Sum of Square of Subset Intensity Gradients (SSSIG) where they incrementally increased the subset size until SSSIG exceeded the user given threshold. Their method is similar to that of subset entropy [70], but they claim the work presented by Sun et al. [70] lacks mathematical support and that their method, i.e. the use of SSSIG, is more straightforward and agreeable. They emphasised the importance of choice of subset size based on the sharp speckle pattern contrast and the subset size being large enough to contain enough features that can be tracked.

2.3.2 Stereo-Digital Image Correlation

One of the fundamental problems with DIC and other full-field measurements methods is the impact of out-of-plane movement. Out-of-plane displacement is defined as the displacement orientation away or towards the sample surface. The inability to consider out-of-plane displacement in the calculations can result into inaccurate in-plane displacement field measurements [72] which will result in higher uncertainty with the characterisation of a cracked body. Typically, in a stereovision system, two cameras are positioned (i.e. Figure 2.6) so that the same overlapping surface area is captured. Equally distributed white light is compulsory to illuminate the surface and the trackable patterns on the surface

Figure 2.6 Stereovision system. Two cameras and two lights with overlapping RIO (Picture from ARAMIS GOM website – www.gom.com)

The different points of view of the cameras enable an increased perspective and after calibration of the cameras using a pinhole model [73], the images are correlated (using the Stereo-DIC algorithm [73]) to obtain both in-plane and out-of-plane displacement fields. Although an additional camera compliments any fracture mechanics experiment, it tends to increase the cost and complexity of the experiment.

Stereo-DIC has also been successfully applied to fracture mechanics [74, 75]; Sutton et al. [76] used Stereo-DIC to successfully measure the crack mouth opening displacement in Mode I,II, III from a mixed mode experiment (I/III). Similarly, Luo et al. [77] showed via the same method that the out-of-plane displacement at the ductile crack tip of a stainless steel specimen would have impacted in-plane displacement measurements if they used 2D DIC.

The Stereo-DIC technique overcomes many of the disadvantages of previously discussed full-field optical tools (i.e. Photoelasticity, Moire, Interferometry): a simple optical arrangement; low requirement for surface measuring environment; wide applicability to different materials; and automatic data processing. However, the main limitation of Stereo-DIC is that the calculated displacement field is observation of the sample surface only and not representative of the mechanics of the whole body.

Cracks can have a complex geometry within the bulk of the cracked body and cannot be captured by surface measurement techniques. Also, surface measurements are constrained to plane stress conditions where in fact, quite often, the plane strain condition prevails for crack propagation within the material. Therefore, volumetric images can paint a better picture of how a crack behaves and interacts with its surrounding microstructure allowing for less conservatism in our calculations.

2.3.3 Volume imaging and Digital Volume Correlation

Digital imaging of volume techniques such as Computed Tomography [78], Magnetic Resonance Imaging (MRI) [78] or Positron Emission Tomography (PET) [79] have become increasingly important as they allow for a non-destructive method of observation and quantification through the thickness of an optically opaque material. X-ray Computed Tomography (XCT) has been the most popular method in experimental mechanics and its first application to materials dates back as early as the 1990s [80, 81].

The concept of X-ray Computed Tomography is an extension of the classical X-ray radiography and the imaging interior features of a specimen is based on the attenuation of the X-ray beam through a specimen. X-ray radiography provides only a single projection of the sample volume on one single plane. X-ray tomography overcomes this disadvantage by combining the information from a series of many radiographs, each recoded with different known orientations (i.e labelled as θ in Figure 2.7) of the sample in front of the detector. The variation of X-ray attenuation in the volume of the sample can be reconstructed by combining radiographs with an appropriate algorithm. A tomographic scan required an X-ray source, a rotation stage and an X-ray detector as show in Figure 2.7. To reconstruct a sample volume, 180° of 2D projection data is required as the remaining 180° is a mirror data of the first.

The most commonly used algorithm is the Filtered Back-Projection [83] algorithm developed by Feldkamp et al. for cone beam projections. Cone beam projections are first weighted and convolved with a non-local 1-D high-pass filter along a set of lines to create a filtered cone beam data. Subsequently, each sample of the filtered data is transferred into the image domain by a weighted back projection, where it additively contributes to the reconstruction at all points that are located on the ray connecting the sample position with the X-ray source point. Filtered Back – Projection is based on exact or approximate mathematical inversion of the projection that models the data acquisition process. In contrast, Iterative reconstruction methods [84] do not involve explicit inversion, but use an iterative procedure generate a sequence of estimates that eventually converge towards a good solution.

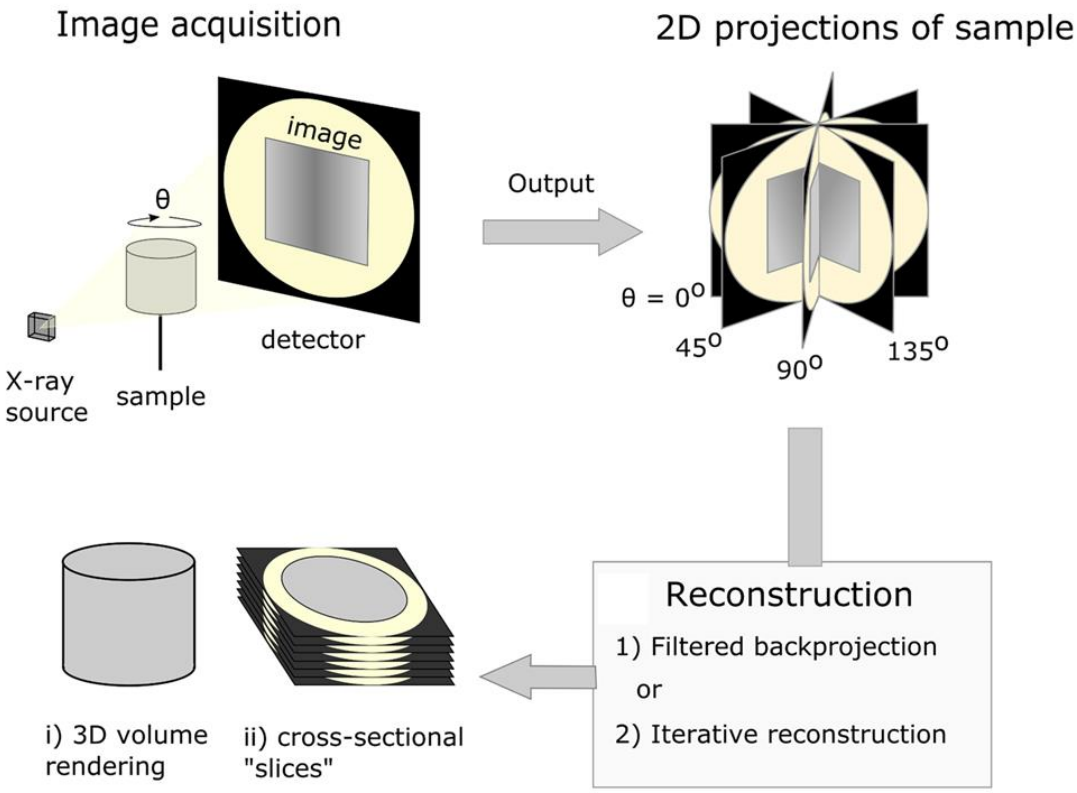

Figure 2.7 Principles of X-ray Computed Tomography workflow [85]

The development of synchrotron sources and detectors has allowed for a dramatical evolution of the spatial resolution of the technique and they have now been applied to all kinds of structural materials. Stock et al. [81] published a review of how XCT was used to investigate different applications in materials while Buffiere et al. [82] demonstrated how in-situ XCT is an attractive tool for studying the mechanical behaviour of materials.

Fracture mechanics also flourished in this developing state of the art method; Marrow et al. [86] used high resolution XCT to study short fatigue crack propagation in cast iron where they utilised direct image measurements to study the crack shape and path. From the same group, Hodgkins et al. [87] used XCT and threshold based image segmentation to observe changes in crack shape with propagation in nuclear graphite (i.e. Figure 2.8). They mentioned that the crack can only be observed when the crack opening displacement approaches that of the dimension of the voxel.

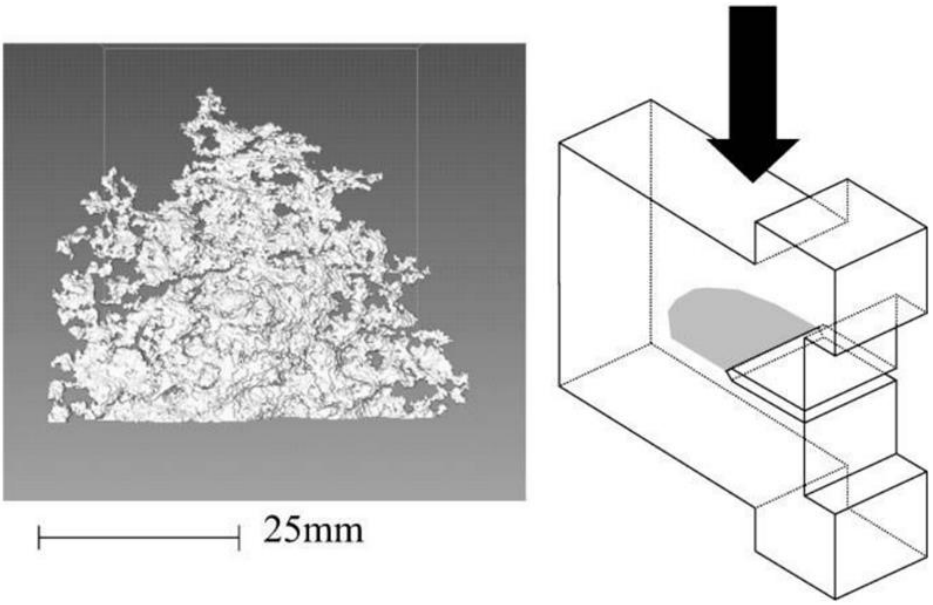

Figure 2.8 X-ray tomography isosurface image of a crack in 50mm thick cracked nuclear graphite CT specimen of graphite, showing significant crack front curvature. Direction of the observation is indicated by arrow[87]

Toda et al. [88] investigated fatigue crack closure in aluminium alloy by calculating COD and crack surface using high resolution synchrotron XCT. With careful assessment of the thresholding criteria, they used grey-level intensity-based centroid spacing to determine the sub-voxel location of the crack faces which aided the calculation of the crack surface and COD through the thickness of their sample.

Digital Volume Correlation (DVC) is a tool used to obtain a volume displacement field between 4D time-resolved volume data which follows the same concepts of DIC. The reference volume data is divided into cubic subsets (see Figure 2.9) and tracked on the deformed volume that follows the reference volume. Hence, the material requires to contain unique trackable features that are naturally occurring (i.e. the impact of the microstructure) for the application of DVC. Similarly, to DIC, the cubic subset size has to be determined as a compromise between spatial resolution and displacement precision and size of the features. This means large cubic subset size allow for a low uncertainty in local mean displacement at the cost of a low spatial resolution. In contrast, small subset size allow for a higher spatial resolution but due to the lower amount of voxels considered, displacement uncertainty is expected to be higher. Correlation between the reference and deformed volumes allows the calculation of 3-dimentional displacement field.

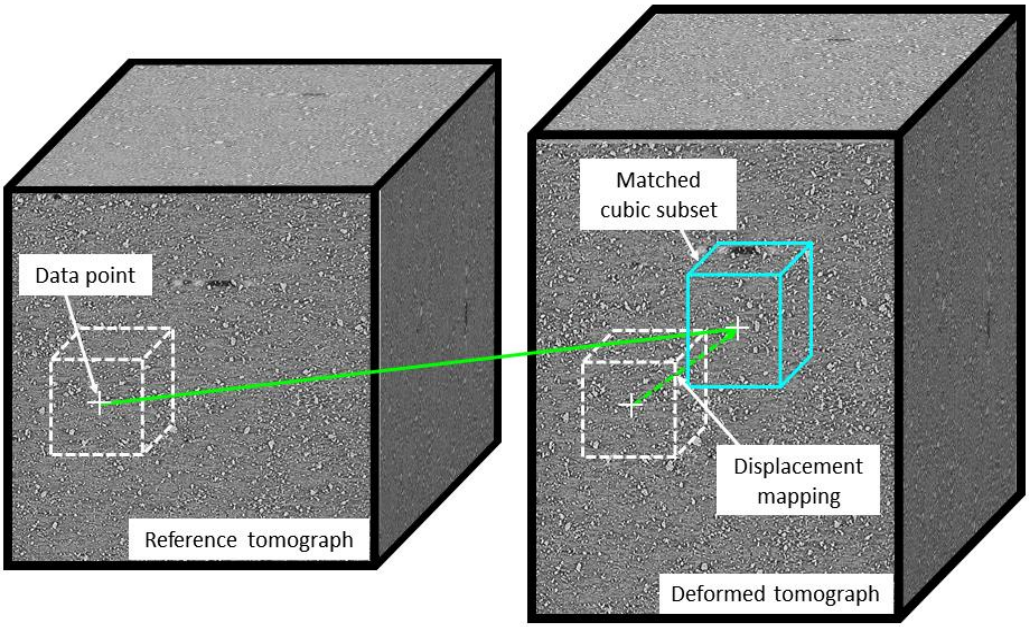

Figure 2.9 Conventional Digital Volume Correlation tracking and mapping of a cubic subset

Introduced in 1999 by Bay et al. [89] to study damage in a trabecular bone, the DVC method has been gathering a lot of momentum. In its initial implementation by Bay et al., DVC was able to provide full continuum-level displacement and strain fields throughout the interior of the sample. Before DVC could fully flourish, the method went through iterations that progressively improved performance and accuracy [90, 91]. It has become evident with each study that number of parameters within the DVC algorithm, as well as the microstructure of the sample can influence its performance. DVC parameters such as correlation function, shape function, changes in image contrast and voxel size can impact the accuracy, precision and of displacement and strain measurements. While numerical and experimental methods can only validate each other, if similar testing arrangements are defined, there is no golden standard to data for the assessment of the accuracy and precision of a DVC strategy. This is due to the unavailability of other accurate techniques that can measure internal strains.

A first attempt compare different DVC techniques was carried out by Madi et al. [92]. He compared the output of a local correlation algorithm based on FFT and another based on a continuous and global code [92, 93]. To calculate the uncertainty of the displacement measurements of the two DVC strategies, he imposed a virtual rigid displacement and studied the distribution reporting uncertainties in displacement ranging from 0.006 to 0.02 voxels. Germaneau et al. [94] attempted to calculate the uncertainty of displacement measurements from DVC by applying rigid body motion to the sample. The data images for the volume were obtained by XCT and Optical Scanning Tomography (OST). In their study, they concluded that the displacement measurement uncertainty is around 0.049 voxels for XCT and slightly lower value of 0.037 voxels for OST.

2.4 Quantification of cracks using displacement fields

In the analysis of cracked bodies, DIC allows for the calculation of fracture parameters such as crack opening displacement (COD) [95, 96], energy release rate [97], stress intensity factor [98] and J-integral [99]. The full field displacement measurement of an experiment can unravel a wealth of valuable information. Crack opening displacement (COD) can be calculated by utilizing the measured displacement vectors closest to the crack, vector values increase as the crack opens giving a full crack opening profile.

One family of techniques [97, 98, 100, 101] used to calculate the stress intensity factor consists in fitting a theoretical linear elastic displacement field devised from Williams [118]. Williams series is fitted to the displacement field determined by DIC and maximising the correlation between the fields by optimising the stress intensity factor.

In theory, this method is forcing experimental data to fit a theoretical linear elastic model hence modifying experimental measurements and ignoring the non-linear elastic measurements close to the crack tip. This will generate imprecise results, increasing the uncertainty of the calculated fracture parameters. It is also critical to add that these methods are also sensitive to inaccurate crack tip location [102] which can be computationally difficult to obtain as the location of the crack tip is lost within the DIC noise and the loss of spatial resolution, hence making it a challenging task to pin point accurately.

An alternative method used to calculate the stress intensity factor is the use of the J- integral. The J-integral is defined as a path independent contour integral that is equivalent to the energy release rate. It's value is zero over a closed contour and is independent of the path integration properties shown in the literature.

The J-integral calculates the energy associated with the changes in the displacement field to obtain the energy release rate. This then can be converted to calculate the stress intensity factor [103].

Becker et al. [99] introduced a method to calculate J-integral as an area integral using DIC displacement field measure and the finite element method. Becker states that there is one limitation with their current version of JMAN, the domain integral.

Their method only considers elastic conditions on the surface whereas most materials exhibit nonlinearity close to the crack tip, where elastic conditions do not apply. Another critical limitation to their technique is that the crack geometry is not imported into their FE model. This means their contour path does not start at a traction free surface although an accurate J-integral calculation requires the contours to start and end at the crack faces. Furthermore, their method requires manual crack feature extraction, which can be tedious to calculate.

However, there are several distinct advantages of using the domain integral method; it does not rely on a presumed field meaning it uses more measured data to reduce its sensitivity to measurement uncertainties; it is insensitive to accurate crack tip location and to inelastic strains close to the crack tip, since domain integral method take a closed area integral.

The most cited research based on characterisation of cracks from displacement fields is the work done by Rethore et al. [104]. In their research, they proposed a routine called eXtended and Integrated DIC (XI-DIC). Not only does this enrich nodes (data points) at vectors close to the crack faces, but it also refers to the fact that the assumed material behaviour and the balance of momentum are directly integrated into the correlation algorithm.

The algorithm uses a standard Heaviside function to fit a linear crack path into the displacement field and to decide the boundaries for the crack faces. A Heaviside function or a unit step function is a discontinuous function $f(x)$ which can be defined as;

$$f(x)\begin{cases}1, & x \geq 0\\ 0, & x < 0\end{cases} \qquad (4)$$

In order to improve the crack path from a linear fit (i.e. Figure 2.10a) to a much more convoluted fit, Rethore presents a procedure called shape optimization. The shape optimization procedure relies on the fact that the crack path is mis-positioned after initial enrichment, therefore producing higher values in the error map at location of the crack path. This error map is scanned along the crack at locations normal to the crack and the optimized crack path is said to be at the location of the maximum error. Figure 2.10b depicts the implementation of their shape optimization.

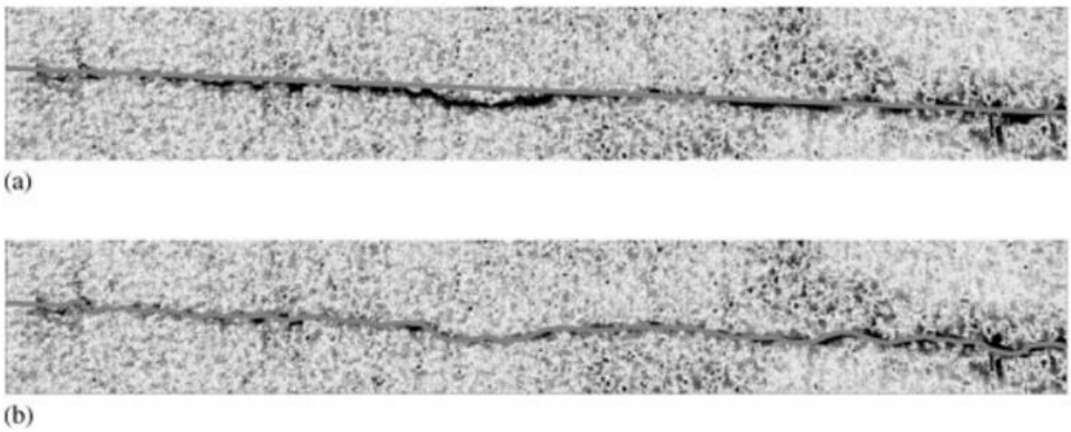

Figure 2.10 Crack shape optimization a) linear fit, b) optimized crack path for a CCT specimen plotted on error maps[104]

Similar methods have been used elsewhere [105, 106]. However, there are a few limitations to their method. Firstly, the procedure assumes the crack face movement of freedom are limited to Linear Elastic Fracture Mechanics (LEFM), so it cannot be applied to Non-Linear Elastic Fracture Mechanics. Secondly, the method can only be applicable for single discontinuities and the application is time consuming, cumbersome requiring constant interaction. Lastly, their method is mostly applicable to cracks with small opening.

Helm et al. [107] used a quasi-regular pattern of dots as a speckle pattern to introduce an effective multiple crack identification process. They combined the use of regularised patterns, cut-off values derived from the correlation error statistics, sanity checks to reduce registration errors and a hybrid spatial/temporal initial guess scheme to handle areas that get segregated from the main analysis. In their research, they compared the quasi-regular pattern to random speckle pattern and showed that quasi-regular pattern produces a much noisier displacement field compared to the random speckle pattern. There are a few limitations to this method. Firstly, the crack detection method relies on the crack artefact corrupting subsets within the deformed images, which creates a difficulty of detecting sub-pixel cracks with the exception of brittle materials. The quasi-regular pattern is a requirement to Helm et al. technique, which returns a more consistent correlation coefficient. The correlation coefficient is then used to apply statistical analysis and threshold for the crack identification process. The second limitation is that the quasi-regular pattern cannot be applied within the volume of a material and is only limited to surface crack identification. Thirdly, the correlation errors can also be subjected to other causes besides registration errors, crack degradation on deformed image or speckle patterns which were all

addressed in Helm et al. paper. The correlation coefficient can also be impacted by poor lighting and dust between the surface specimen and the lens which may increase the likelihood of a false crack detection.

Digital Volume Correlation has also been used both quantitatively and qualitatively to assess the fracture process of cracked bodies. Limodin and Réthoré [108-110] applied DVC analysis to XCT data of a fatigue crack in nodular graphite cast iron. In their work, they adapted their residual error methodology from X-DIC for the analysis of their DVC data. They noticed that the crack surface deviated from the flat surface and the nodules were embedded between the crack faces (i.e. Figure 2.11a). To combat this, they successfully applied a 3D region-based segmentation algorithm to "threshold" the crack surface from the nodules(i.e. Figure 2.11b).

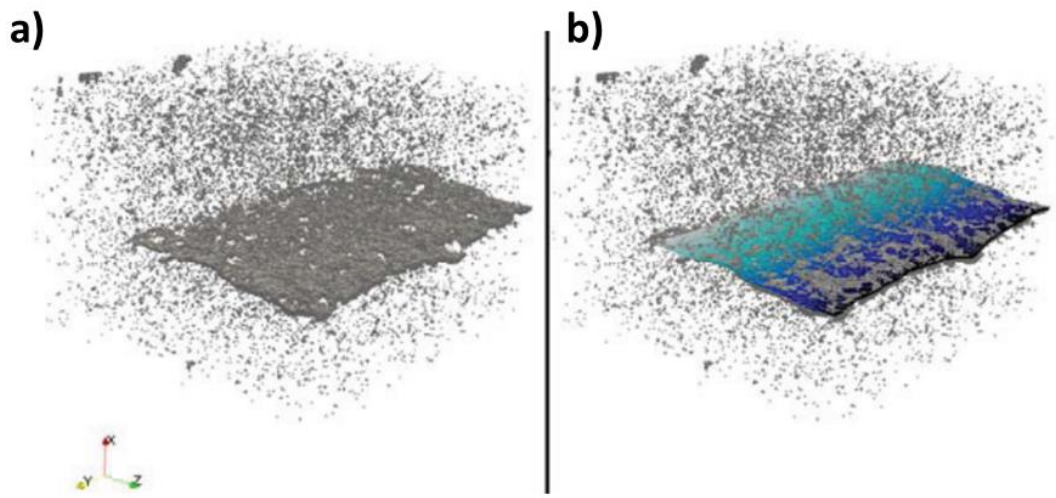

Figure 2.11 XCT of a mode I crack in nodular graphite cast iron; a) thresholded residual error map b) Detected crack surface[109]

Limodin and Réthoré also calculated Mode I COD by taking two slices parallel to the average crack plane on both sides of the crack and subtracting them from each other. Using the crack geometry, such as location of the crack tip and crack path, calculated previously, they extracted SIFs by fitting a theoretical displacement field to the 2D slices from the volume displacement. A similar method was also used elsewhere [111]. They created an FE simulation of the experiment using the DVC and crack geometry as boundary conditions to calculate SIFs and compare those to the field fitting approach which was in strong agreement. Calculating the SIF by field fitting approach of 2D slices of volume displacement was also used in ref [112].

Mostafavi et al. [113, 114] studied crack propagation in polygranular graphite using a stable geometry of the chevron notch using higher resolution (measuring 1.8 µm voxel size) (i.e. Figure 2.12) and standard resolution (measuring 5 µm voxel size) XCT and DVC methods. The difference of resolution enabled them to quantify the uncertainty of the crack measurements based on the captured voxel size. They mention that visual observation of the crack lengths shows no significant difference for different resolutions.

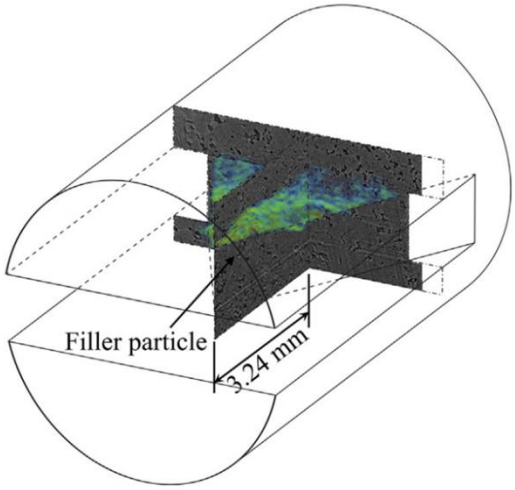

Figure 2.12 Polygranular graphite chevron notch and it's 3D representation of the microstructure (High resolution) with maximum principle strain[114]

By using displacement fields, they were able to successfully map a COD through the thickness of the sample (i.e. Figure 2.13) by observing a discontinuity in 2D slices on the notch plane. They iteratively took a line profile normal to the discontinuity step and subtracted the average between the upper and lower crack faces. The data points separating the crack face causing high synthetic strain were not used in the calculation (Figure 2.12). Fitting methods with discontinuous line profiles on 2D slices to obtain COD was also used in other work [115]. Although fitting methods work well extracting the crack opening displacement profile from displacement fields, the method requires heavy user intervention and judgement which can impact the result.

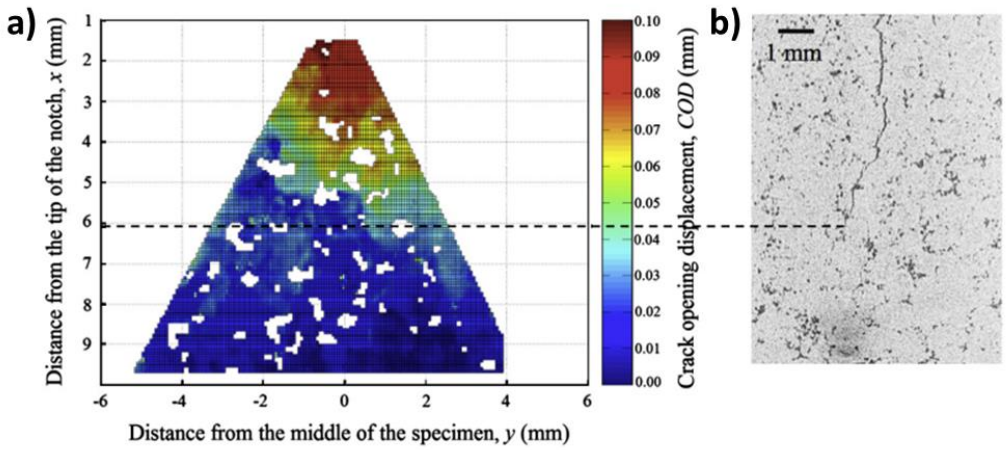

Figure 2.13 Crack opening and length measurement of chevron notch poly-granular graphite a) map of the net crack opening (mm) under load, b) virtual slice at the centre of the specimen (XCT) 101

They mention that the difference between COD measurements calculated from different resolutions differ between 3% and 13%. They note that the crack opening profile suggests that a cohesive model will be a better representative of the mechanical behaviour of graphite compared to the conventional linear elastic approach. Cohesive zone is the nonlinear zone ahead of the crack tip which can be caused by plasticity or microcracking. Usually, Linear Elastic Fracture Mechanics (LEFM) can be a useful tool to solve fracture problems, however the model assumes the nonlinear zone ahead of the crack is minimal and that the stresses at the crack tip is infinite. This is usually not realistic for most materials and therefore the cohesive zone model can be used to predict the fracture behaviour eliminating the crack tip stress singularity.

Mostafavi et al. [116] wanted to highlight the presence of a fracture process zone and obtain the SIFs. They created a library of linear elastic finite element simulations of the experiment using the contour integral method. They incrementally adjusted the crack length in the FE model and extract the normalised COD profile to match with the experimentally measured COD. They conclude that the crack lengths were ~ 1.5 mm longer in the FE simulation compared to the macroscopic observation of the XCT data because the cohesive zone dissipates the energy.

2.5 Conclusion

The literature reviewed the tools available to obtain accurate and maximal information from a fracture experiment. Firstly, the literature discussed that single point measurement tools are well established and can retrieve accurate and precise information from fracture experiments. However, single point measurements (i.e. a strain gauge) are likely to miss strain hot spots, especially for complex loading. Other single point measurement tools that were discussed either depended on the material's conductivity (i.e. ACPD and DCPD) or tried to exploit a material's natural frequency (i.e. vibro-acoustic emission sensors). This requirement limits the materials that can be experimented. Another note contribution from the literature review was that single point measurements can fail to present the full entropy from a fracture experiment.

Full-field measurement techniques such as Moire interferometry, Photoelastic stress analysis and Thermoelastic stress analysis do not suffer the same consequences as single point measurement tools. The tools mentioned above are powerful implementations in an experimental setup, however, they do come with certain limitations. Moire interferometry is very sensitive to environmental disturbances such as vibrations. Photoelastic stress analysis is a powerful technique in visualising stresses and strains, however, the method is only limited to birefringent materials. Thermoelastic stress analysis uses small temperature change on surface to calculate the stresses and strains and is therefore limited to adiabatic materials.

Identifying cracks in digital images using image processing techniques is widely used, simple set up and can be applicable to most materials. The method relies on a crack artefact forming either due to an effect of the microstructure or void between the crack faces. However, image processing techniques require the crack to be sufficiently open so that it can be detectable in the raw image, which limits the accuracy of these methods to a pixel at best. Digital Image Correlation is shown to be more resourceful as it can calculate sub-pixel accurate displacement measurements around the crack. For this reason, Digital Image Correlation is the most frequently used optical method in fracture mechanics which can be applied to stereo-vision and volume images to obtain displacement measurements out-of-plane and in the thickness of a material, respectively. It has been shown that valuable

fracture parameters such as stress intensity factor, J-integral and crack opening displacement can be extracted from displacement information of a fracture experiment. These fracture parameters are critical in predicting crack propagation in elastic and elastic-plastic materials.

To exploit this wealth of information, this research project aimed at using Digital Image Correlation and Digital Volume Correlation as tools. One of the more popular methods discussed in the literature review uses a least square fit to match the measured displacement to linear elastic displacement fields to extract stress intensity factor. Digital Image Correlation measures both elastic and plastic displacement fields, while linear elastic displacement fields, however, do not consider plasticity at the crack tip within the models. The J-integral was also discussed, and it has a few distinct advantages over the field fitting approach. The method does not rely on a presumed field, it is insensitive to accurate crack tip location and to inelastic strains close to the crack tip. Additionally, most of the crack quantification methods stated above require the crack's geometrical parameters (i.e. crack path, crack tip, crack length and crack opening displacement) to be utilized in the calculation. Not only are extracting crack parameters cumbersome but also, they depend on user judgement-based data analysis and thresholding. This can impact the integrity of the crack measurements and hence the outcome of experiments.

The literature showed that there is a need for a tool capable measuring a crack's geometrical parameters automatically without the need for user judgement from experimental displacement fields.

Therefore, this research project will study a discontinuity detection and extraction tool that is automatic, requires minimal user intervention and the accuracy is not dependent on judgement of the user. The automatic application of this tool is required to be versatile and applicable to different fracture experiments and material behaviours.

3 DEVELOPMENT OF A NOVEL PHASE CONGRUENCY-BASED CRACK DETECTION METHOD

This chapter will present a process of extracting a crack's geometrical parameters from displacement fields called Phase Congruency – Based Crack Detection (PC-CD). The flowchart of the PC-CD algorithm is depicted in Figure 3.3. After a short discussion behind the motivation of the method, this chapter will present all the image processing tools that were used for the development of the novel PC-CD. Next, this chapter will present a case study to demonstrate how the PC-CD method can be used to extract crack parameters from a virtually created surface dataset. After, the chapter will show how the PC-CD method can be expanded to extract crack parameters from volume displacement fields. An experimentally obtained X-ray tomography data will be used to as a case study. A methodology will be presented to demonstrate how the PC-CD extracted crack parameters can be used to calculate the J-integral from displacement measurements automatically.

3.1 Background

Cracks have a characteristic signature in their fields of displacement and strain, which can be measured by DIC. The displacement perpendicular to the crack direction (i.e. crack opening displacement) is a discontinuity like a step function, so the opening strain (i.e. the gradient of the opening displacement) has a peak at the crack location. Also, another unique characteristic is due to the opening of the crack in the deformed image which forms a crack artefact. Due to this artefact, in the presence of a crack, conventional DIC algorithms achieve poor correlation for subsets close to the crack faces. This is because the subsets used for correlation can only capture continuous deformations from the reference of the deformed image [105, 119]. While some authors used the intensification of the pixels to detect and highlight cracks (as discussed in the literature review, see section 2.2), a few authors attempted to tackle the erroneous discontinuity measurements by amending DIC algorithms [104, 105, 119-124].

The aim of this project was not to create new DIC algorithms, but to study how the measurement tools can be used effectively to study cracks. Most crack detection algorithms based on displacement measurements apply gradient-based (i.e. strain) methods to highlight the path of the crack [107, 125-131]. Such methods rely on defining a threshold value, which may need to vary between analyses due to change in the quality of the data or the images; for example the levels of strain that define the crack in Figure 3.1(e and f) are an order of different magnitude. Gradient-based methods are sensitive to the gradient magnitude, smoothness and magnification, and do not localise accurately [132]. Other crack detection methods have used least square fitting between discontinuous displacement step into a model such as a Heaviside function [104], which are also dependent on a threshold value.

A simple study was conducted to demonstrate the visualisation of the signature of a crack in a displacement field and to show the impact of a crack artefact pixilation on the displacement field. Figure 3.1(a and b) show virtual images of two cracks, with speckle patterns on the surface. Each image is deformed using a MATLAB-coded tool called *ODIN* [117] (see section 4.6.1 for more information). *ODIN* uses input displacement field, obtained from a theoretical displacement field around a linear elastic crack, presented by Williams [118] to deform digital images. Each image size is 2048×2048 pixels, and the horizontal edge cracks are 1024 pixels in length with 1-pixel and 5-pixel crack mouth opening displacements (CMOD)

respectively. The reference (closed crack) and deformed (open crack) images were analysed with the LaVision Davis 8.2.6 software [37] using an iterative least squares algorithm [68] with subset size 31 pixels with 75% overlap (step size 8 pixels). The resultant opening displacement fields are shown in Figure 3.1(c and d) and those of opening strain in Figure 3.1(e and f). For the CMOD of 5 pixels the image artefact that represents the crack is visible. It introduces displacement errors close to the crack faces due to the discontinuity in the deformed image that was not present in the reference image.

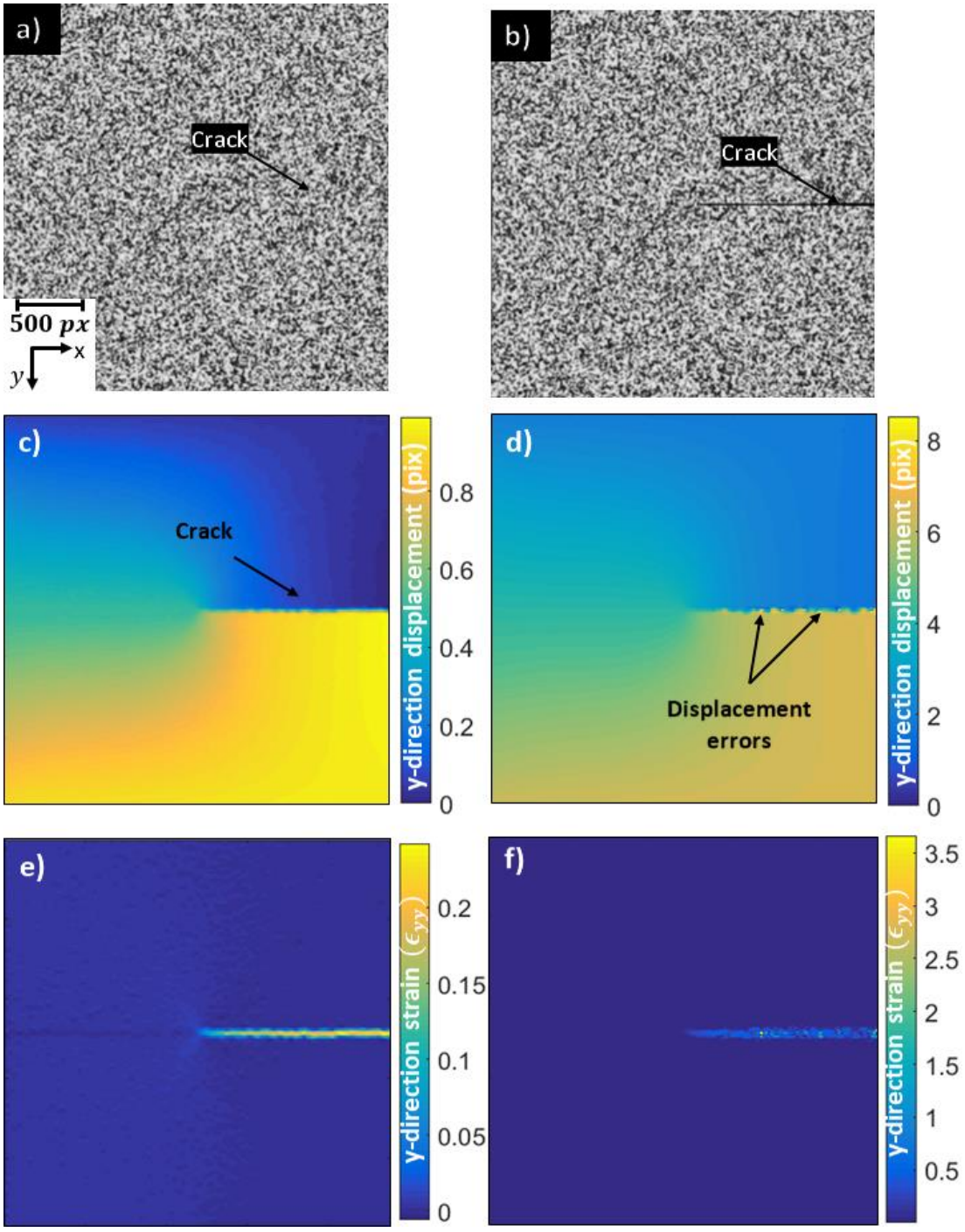

Figure 3.1 a) a 2024x2048 pixel virtual image containing a crack with mouth opening displacement of 1 pixel; b) An image similar to (a) with crack mouth opening displacement of 5 pixels; c) Opening (i.e., Y-direction) displacement of associated with image (a); d) Opening (i.e., Y-direction) displacement associated with image (b); e) Opening strain of (c); f) Opening strain of (d).

A novel Phase-Congruency based Crack Detection tool (PC-CD) was developed in this thesis and successfully used to extract crack parameters from displacement fields. Phase congruency (PC) is a relatively new technique in image analysis that uses Phase information to detect and identify edges and corners [133] in digital images. Phase is a component of a signal in the Fourier representation. It has been reported that human perception presents invariance against illumination changes. There have been studies [134] that suggest that Phase information is a psychological representation of how human visual systems perceive edge like features. Rather than defining features directly at points with sharp changes in value, the Phase congruency (PC) model dictates that features are perceived at points, where the Fourier components are maximal in phase with each another [135-138].

PC returns a dimensionless quantity that is invariant to contrast and scale and therefore does not suffer from the threshold selection problems of other crack segmentation methods [132]. Unlike gradient-based feature detection algorithms, which can only detect step features, PC detects features at all phase angles, and not just step features that have a phase angle of $0°$ or $180°$. Together with the invariance illumination and accurate localisation of PC [132, 133], these characteristics make it an ideal tool for detecting local discontinuities in the displacement fields that are usually the signature of cracks.

The PC outcome is compared with those of opening strain and displacement, applied to a theoretical dataset like those presented in Figure 3.1 with a crack mouth opening displacement of 1 pixel. The variation of Phase congruency, opening displacement, and opening strain is presented along two-line profiles vertical to the crack path: at the crack mouth and at the crack tip; the opening strain is normalised with respect to maximum strain. The normalised strain and displacement maps deteriorated close to the crack tip, while the Phase congruency map remained consistent. The value of the Phase congruency at location (x, y), $\mathrm{PC}\ (\mathrm{x}, \mathrm{y})$, varied from a maximum of 1 (indicating a very significant feature) to 0 (i.e. no significance), and localised to a sub-displacement data point level. This will further aid segmentation of the crack compared to other displacement and strain methods, as there was a loss of spatial resolution in DIC data compared to the original image due the step size between subsets. PC-CD method was directly applied to surface and volume displacement field measurements and can automatically output the crack geometrical representation. Due to the applicability of PC-CD to displacement fields– the application could be extended to other experimentally obtained displacement fields (see section 2.3) such as moiré Interferometry.

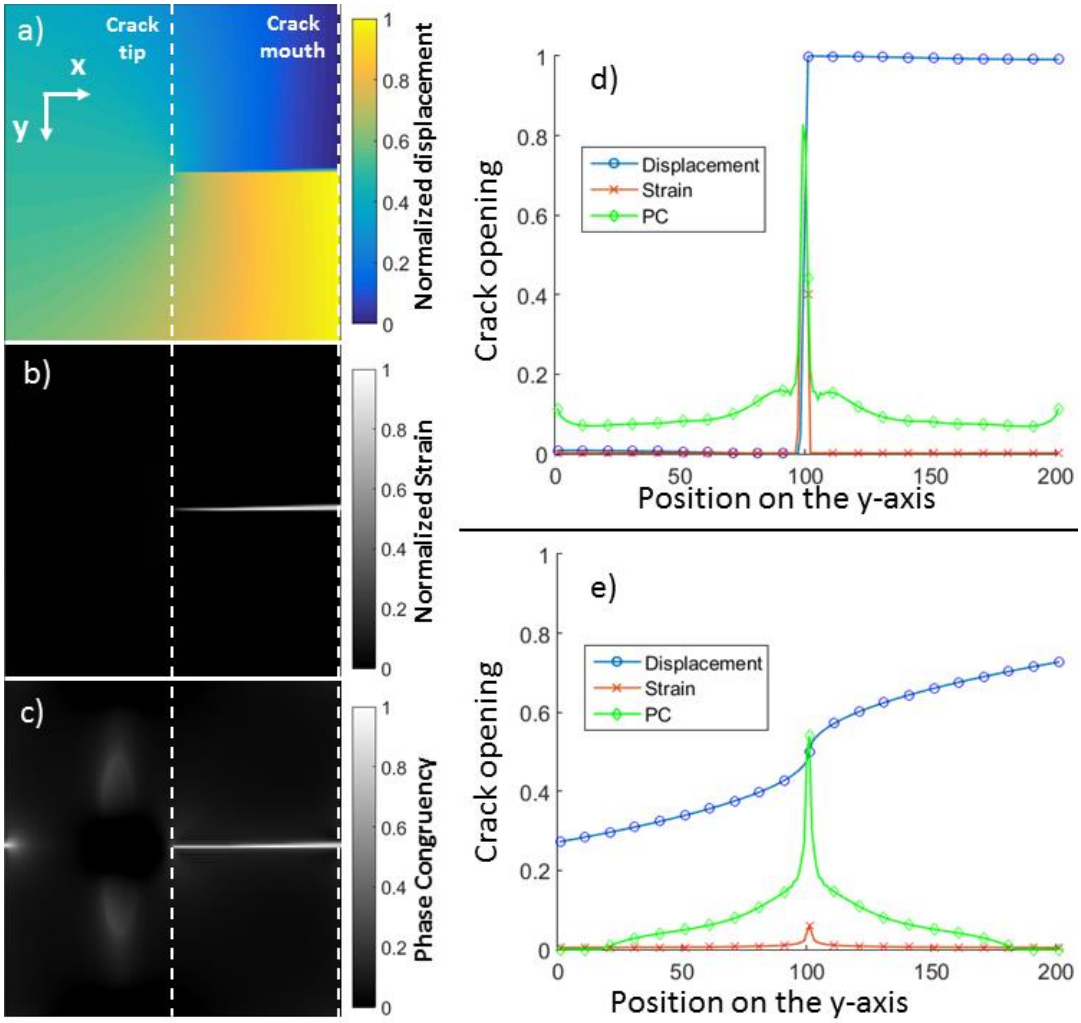

Figure 3.2 a) Theoretical normalised displacement field b) Normalised strain map c) Phase congruency d) Vertical line profile of Crack mouth, one in every ten data points are shown e) Vertical line profile of Crack tip, one in every ten data points are shown

The outline of the PC-CD algorithm is as follows. First, the displacement fields are applied a pre-processing procedure which prepares the displacement fields for the main algorithmic application. The user selects a region of interest and orientation of the crack. The missing displacement vectors, caused by low correlation during the DIC analysis, are filled with extrapolation (see section 3.6). Next, the displacement fields are applied an outlier filter (see section 3.5) to remove spurious vector values and resultant displacement fields are filled using extrapolation (see section 3.6).

The automatic crack detection procedure (see section 3.7) selects a subset of the discontinuity to prepare an initial mask for the active contour segmentation (see section 3.8). To create an automatic initial mask, the displacement field orientation containing a discontinuity is used. First, a Bilateral filter (see section 3.7.1) is applied to smooth the displacement field while preserving edges. Next, a sobel edge detection (see section 3.7.2) is used to create a skeleton binary image of the crack. Hough transform (see section 3.7.3) is used to find the longest line in the skeleton image. Select connected components (see section 3.7.4) is used to select the longest line and create an initial mask image of the selection.

The Phase congruency (see section 3.2) procedure is applied to the displacement field that contains the discontinuity, which returns the location of the crack. The resultant phase congruency maps and the initial map is used in conjunction with the region-based active contour segmentation algorithm which outputs the boundaries of the crack and location of the crack faces. Lastly, the boundary of the crack is used to extract the crack parameters such as crack opening displacement, crack path and crack length. The following chapter will explain how each individual tool has been utilised and give additional information with regards to usage.

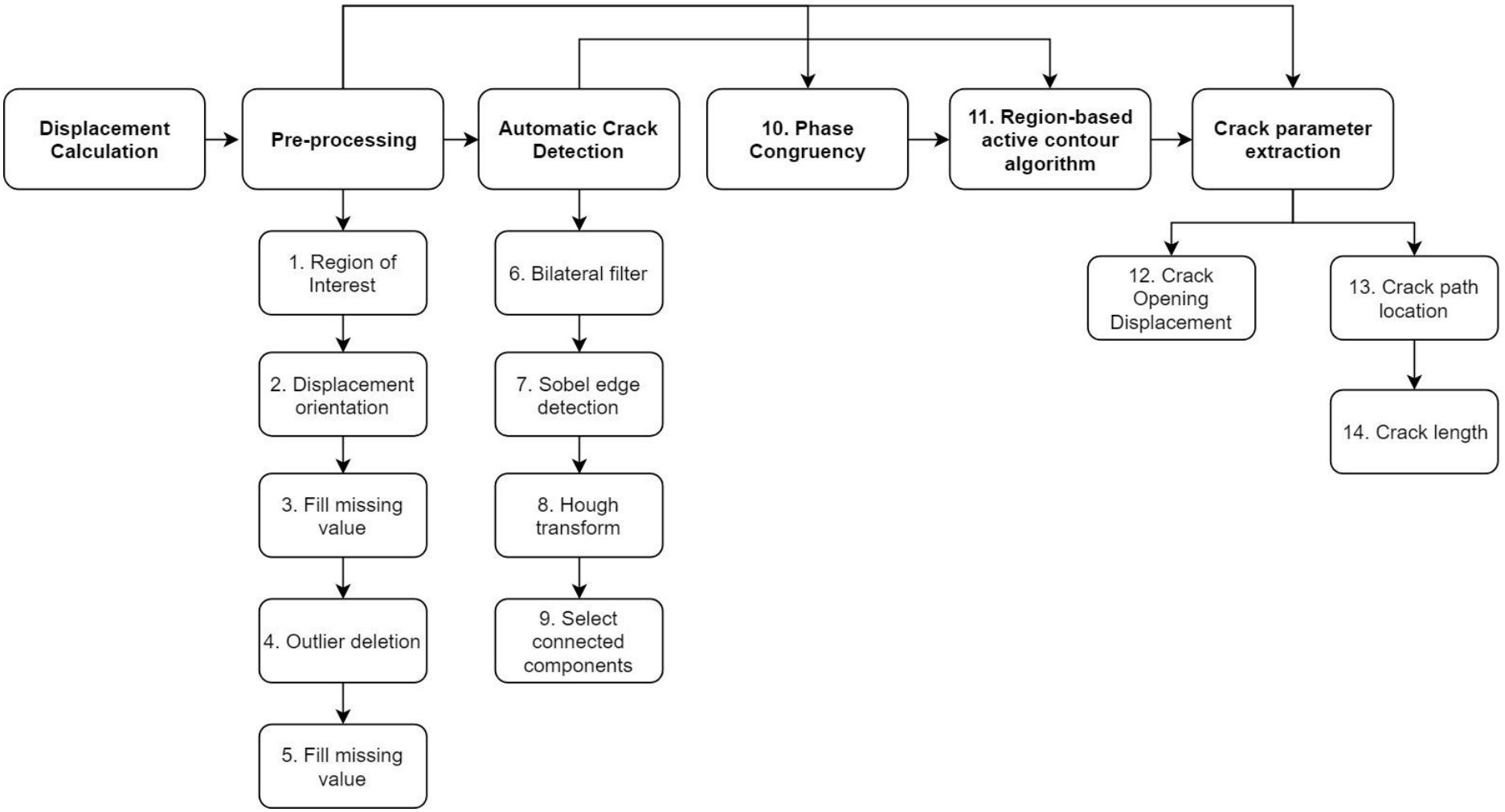

Figure 3.3 Automatic Surface Discontinuity measurement with PC-CD algorithm

3.2 Phase congruency

The phase congruency model is mathematically an advanced formulation and the information can be difficult to comprehend even with the appropriate background. This thesis will not attempt to explain the mathematical description or deviation of the formulation thoroughly – but rather briefly explain and attempt to present a clearer understanding of how each element benefits the formulation. The Phase congruency model proposed in this study is a method based on the one presented by Kovesi [139] which is designed to provide good feature localisation and noise compensation based on log-Gabor wavelet transfer function. Upon further study, it is seen that the formulation was better equipped with the Monogenic scale-space signal proposed by Felsberg et al. [140]. Lijuan et al. [132] showed that not only do monogenic filters require less computational time and less computational memory compared to creating log-Gabor filter bank, but it also improves the accuracy of feature localisation and better sensitivity to noise.

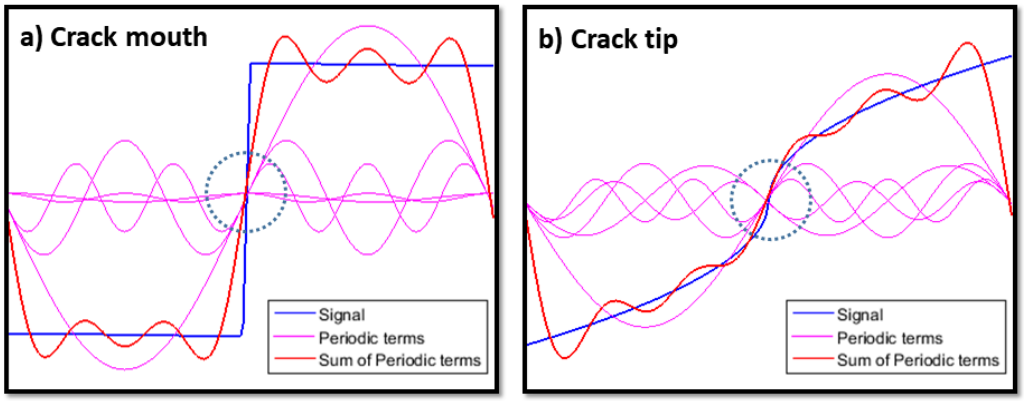

Figure 3.4 Fourier series of a step signal and the sum of the first five terms a) Crack mouth profile b) Crack tip profile

Phase congruency is a frequency-based model. Morrone et al. [134] found that there is a high Phase congruency where features can be perceived in an image. Any signal can be expressed as the sum of the periodic terms of the Fourier transform. Let $f(x)$ denote our $1\mathrm{D}$ step signal. Then using the Fourier series expansion:

$$f(x) = \sum_{n}^{\infty} A_n \cos(xn\omega + \phi_n(x)) \qquad (5)$$

where A_n represents the amplitude of the *n*th Fourier component, and ϕ_n represents the local phase of the Fourier component at position $x \times \omega$ is a constant (usually $\omega = 2\pi$).

Figure 3.4 is a one-dimensional signal of a step; a) crack mouth profile and b) crack tip profile, the very same displacement line profiles used in Figure 3.2. The first five periodic terms of the signal and the sum of the five periodic terms were calculated for both a) and b) using the Fourier series expansion. As the periodic terms increased (towards infinity), the summation of the periodic terms tended closer to the original signal. At the point of the step, all the periodic terms were aligned (shown by the dotted circle) and were the only place in the signal where a congruency was present in the phase.

Morrone et al. [136] developed a 1D Local Energy Model for feature detection via Phase congruency. This model assumed that the compressed image format should be high in information and low in redundancy. Their model searches for patterns in order in the phase component of the Fourier transform. A Phase congruency function, $PC(x)$, at each point x in the signal can be expanded in Fourier component series;

$$PC(x) = \max_{\phi \in [0,2\pi)} \frac{\sum_n A_n \cos(\phi(x) - \bar{\phi}(x))}{\sum_n A_n(x)} = \frac{|E(x)|}{\sum_n A_n(x)} \qquad (6)$$

where $E(x)$ is the local energy of the signal at x, which will be properly defined later.

Under this definition, Phase congruency is the ratio of $|E(x)|$ to the overall path length taken by the local Fourier components in reaching the end point. If all the Fourier components are in phase (aligned with each other) all the complex vectors would be aligned and the ratio of$|E(x)|/\sum_n A_n(x)$ would be 1. If there is no coherence of phase, the ratio falls to a minimum of 0 [133].

However, the constructed formulation does not offer good localisation and is sensitive to noise. Kovesi solved this problem by multiplying a weight function in the formula and supplemented a state of the art noise compensation method based on the Rayleigh distribution [139].

$$PC_2(x) = \frac{\sum_n W(x)[A_n(x)\Delta\phi_n(x) - T]}{\sum_n A_n + \varepsilon} \quad (7)$$

where $\Delta\phi_n(x)$ is the measure of Phase congruency,

$$\Delta\phi_n(\mathrm{x}) = \cos\left(\phi_\mathrm{n}(\mathrm{x}) - \bar{\phi}(\mathrm{x})\right) - \left|\sin\left(\phi_\mathrm{n}(\mathrm{x}) - \bar{\phi}(\mathrm{x})\right)\right| \quad (8)$$

T is the noise compensation and ε is a small number ($\varepsilon = 0.0001$) to prevent division by zero in the numerical calculation. T noise compensation is discussed in section 3.2.1 and formulated in Eq. (29)(30)(31)(32). On a given orientation, weighting function, $W(x)$, is calculated as following:

$$W(x) = \frac{1}{1 + e^{\gamma(c - s(x))}} \quad (9)$$

$$s(x) = \frac{1}{N}\left(\frac{\sum_n A_n(x)}{A_{max}(x) + \varepsilon}\right) \quad (10)$$

where "c" is a cut-off value of filter, γ is the gain factor that controls the sharpness of the cut-off. If $s(x)$ is smaller than c, then the value of PC will be bound to be a small number. N is the total number of the filter function scales, and $A_{max}(x)$ is the maximum of the amplitudes of the different orders of the Fourier components.

Assume that our signal is represented in $1\mathrm{D}$ by $f(x)$ and to extract the local properties (amplitude and phase) of the signal, we need to represent it in its analytic form;

$$f_A(x) = f(x) - i\, f_{\mathcal{H}}(x) \quad (11)$$

where $i = \sqrt{-1}$ and $f_{\mathcal{H}}(x)$ is the Hilbert transform of $f(x)$.

The local amplitude (energy) and local phase of $f(x)$ are given by

$$A(x) = \|f_A(x)\| = \sqrt{f^2(x) + f^2{}_{\mathcal{H}}(x)} \quad (12)$$

$$\phi(x) = arctan(f(x), f_{\mathcal{H}}(x)) \quad (13)$$

More recently, Felsberg and Sommer [140] proposed a novel n-dimensional generalisation of the analytic signal based on the Riesz transform, which replaces the Hilbert transform. Also, they proposed a 2D isotropic analytic signal called the monogenic signal.

Unlike the one-dimensional case, no odd isotropic filter can be constructed for two dimensions if we are restricted to scalar valued filters. For vector valued filters, however, this is possible. Without going into theoretic details, we introduce the following filters in frequency domain:

$$H_1(u,v) = i\frac{u}{\sqrt{u^2+v^2}} \qquad (14)$$

$$H_2(u,v) = i\frac{v}{\sqrt{u^2+v^2}} \qquad (15)$$

The vector $\boldsymbol{H} = (H_1, H_2)$ has unit length in any direction (i.e. it is isotropic) because $|(H_1, H_2)| = \sqrt{|H_1|^2 + |H_2|^2} = 1$ and it is odd function because reflection through the origin yields $(-x, -y) = -\boldsymbol{H}(x, y)$.

The spatial representation of the earlier filters is given by (h_1, h_2 are the Riesz's filters in the image domain):

$$h_1(x,y) = \frac{-x}{2\pi(x^2+y^2)^{\frac{3}{2}}} \qquad (16)$$

$$h_2(x,y) = \frac{-y}{2\pi(x^2+y^2)^{\frac{3}{2}}} \qquad (17)$$

The two monogenic filters H_1 and H_2 are not selective in terms of the magnitudes of the frequencies. Therefore, a log-Gabor wavelet function, g, is chosen as a bandpass filter and is applied to the image in the frequency domain which yields a 2D monogenic signal f_M and "$*$" is the convolution in the frequency domain.

$$f_M(x,y) = \begin{bmatrix} f(x,y) * g(x,y) \\ f(x,y) * g(x,y) * h_1(x,y) \\ f(x,y) * g(x,y) * h_2(x,y) \end{bmatrix} \begin{bmatrix} f(x,y) * g(x,y) \\ f(x,y) * g(x,y) * h_1(x,y) \\ f(x,y) * g(x,y) * h_2(x,y) \end{bmatrix} \qquad (18)$$

where g is defined in the Fourier domain as:

$$G(u,v) = e^{-\frac{log\left(\frac{r_g}{\omega_0}\right)}{2log\left(\frac{k}{\omega}\right)}} \quad , r_g = \sqrt{u^2+v^2} \qquad (19)$$

where r_g is the radius filter given pixel is in polar system, ω_0 is the central frequency of the Log-Gabor wavelet function, $\frac{\mathrm{k}}{\omega}$ controls the filter's bandwidth. $\omega_0 = \frac{1}{\lambda_{max}}$ where $\lambda_{max} = \lambda_{min}.\alpha^{n-1}$. α is the scaling between the centre frequencies of successive filters and n is the number of wavelet scales.

Due to the singularity in the log function at the origin, the corresponding functions in the spatial domain can be obtained by a numerical inverse Fourier transform, which are a pair of filters in quadrature. The appearance is similar to Gabor wavelet functions, although their shape becomes much sharper as the bandwidth is increased. Therefore, Log-Gabor wavelets can be constructed with arbitrary bandwidth and the bandwidth can be optimized to produce a filter with minimal spatial extent. Eq. (18) is called the monogenic signal, under a spherical co-ordinate system, $\phi \in [0,2\pi)$ and $\theta \in [0,\pi)$

$$f_{M,1}(x,y) = A\cos\phi \qquad (20)$$

$$f_{M,2}(x,y) = A\sin\phi\cos\theta \qquad (21)$$

$$f_{M,3}(x,y) = A\sin\phi\sin\theta \qquad (22)$$

The Phase congruency is determined by using a multiscale approach. At each scale n, the log-Gabor wavelet filter captures a particular feature of the spectrum frequency from the image.

Therefore, the local amplitude of the monogenic signal is:

$$A_n^L(x,y) = \sqrt{f_{M,1}^2(x,y) + f_{M,2}^2(x,y) + f_{M,3}^2(x,y)} \qquad (23)$$

The local phase of the monogenic signal is;

$$\phi^L(x,y) = \arctan\frac{f_{M,1}(x,y)}{\sqrt{f_{M,2}^2(x,y) + f_{M,3}^2(x,y)}} \qquad (24)$$

The local orientation of the monogenic signal is:

$$\theta^L = \arctan\frac{f_{M,2}(x,y)}{f_{M,3}(x,y)} \qquad (25)$$

To calculate 2D Phase congruency, Eq. (6) and Eq. (7), the total energy is needed which is then given by the summation of the amplitude at each wavelet scale n.

$$\bar{E}(x,y) = \sqrt{\left|\sum_n f_{M,1}\right|^2 + \left|\sum_n f_{M,2}\right|^2 + \left|\sum_n f_{M,3}\right|^2} \qquad (26)$$

Total phase angle, $\bar{\phi}$, and orientation angle, $\bar{\theta}$, are given respectively:

$$\bar{\phi}(x,y) = \arctan\left(\frac{\sum_n f_{M,1}}{\sqrt{\left|\sum_n f_{M,2}\right|^2 + \left|\sum_n f_{M,3}\right|^2}}\right) \qquad (27)$$

$$\bar{\theta}(x,y) = \arctan\left(\frac{\sum_n f_{M,2}}{\sum_n f_{M,3}}\right) \qquad (28)$$

3.2.1 T noise circle and Rayleigh distribution

A value for the noise circle radius is estimated by

$$T = \mu_R + k\sigma_R \qquad (29)$$

where μ_R is the mean and σ_R is the standard deviation of noise which has Rayleigh distribution.

$$R(x) = \frac{x}{{\sigma_G}^2} e^{\frac{-x^2}{2{\sigma_G}^2}} \qquad (30)$$

${\sigma_G}^2$ is the variance of the 2D Gaussian distribution describing the position of the filter response vectors. The mean of the Rayleigh distribution is given by,

$$\mu_R = \sigma_G\sqrt{\frac{\pi}{2}} \qquad (31)$$

and the variance is

$${\sigma_R}^2 = \frac{4-\pi}{2}{\sigma_G}^2 \qquad (32)$$

k is the number of standard deviations of the noise energy beyond the mean. The code can automatically calculate T noise by the mean or median noise response of the smallest scale 2D filter pair over the image. However, T noise can also be a user specified input determined by simple uncertainty models of the displacement fields. Uncertainty models can be approximated by applying a rigid-body motion to the specimen and calculating the standard deviation (σ_G). Standard deviation can then be converted into T noise parameter by using Eq. (29), (30), (31) and (32). The parameter estimates the expected noise levels in displacement fields and compensates for the noise in phase space, enhancing the discontinuity signal appropriately.

The Phase congruency via monogenic filter algorithm which will be used for this research is an open source MATLAB code developed by Peter Kovesi available at this ref. [141], named "*phasecongmono.m*". Whenever a filter bank is constructed, it requires many parameters depending on the type of features that is required to be highlighted. It has been recommended by Kovesi to use the following filter bank parameters; $\mathrm{N} = 6, \lambda_{\min} = 4, \alpha = 2.1, \frac{\mathrm{k}}{\omega} = 0.55, \mathrm{k} = 3, \mathrm{c} = 0.5, \gamma = 10, \mathrm{d}_{PC} = 1.2$. Median of smallest scale filter was used to determine noise statistics for the calculation of T noise.

The algorithm itself requires ten arguments for the calculation of PC, but seven of which will remain unchanged from their stated default values and do not require any adjustment or fine tuning. However, the parameters that may require adjustment are: input image (i.e. discontinuity signal field); *minWaveLength* ($\lambda_{\min} = 4$); and *deviationGain* ($\mathrm{d}_{PC} = 1.2$). Both parameters could be altered for fine tuning depending on the feature size and spatial resolution of the displacement field. However, both parameters are observed to be dependent on the selection of subset size and step size. Later, a spatial resolution and phase congruency parametric study (see section 4.7) was conducted to evaluate how the parameters $\lambda_{\min}$ and d_{PC} impact the accuracy of the measured crack geometrical values. The latter study showed that PC parameters $\lambda_{\min} = 4$ and $\mathrm{d}_{PC} = 1.2$ are at their optimum default values. and hence will be constant, unless stated otherwise.

3.3 Volume Phase congruency

A Volume Phase Congruency (VPC) map was computed using a pseudo method. Two-dimensional Phase congruency (PC) is calculated iteratively on displacement slices throughout the volume field. The 2D PC slices are then combined to generate a pseudo-Volume Phase congruency map (VPC). One possible cause of a systematic problem is needed to be addressed; each slice is independent of its neighbourhood slices. Slice independency means the features are highlighted in individual slices but are not localised between the slices. However, upon many observations, the slice-independency does not impact the discontinuity detection, as shall be seen in section 3.10.

For a volume displacement field, there are three possible slice plane options; XY plane, XZ plane and YZ plane. The slice plane for the 2D PC calculation is determined based on the discontinuity surface orientation and fracture mode of the crack. The slice plane indexing can be in two orientations as the determination is such that the slice plane is normal to the discontinuity surface.

For mode I cracks:

- If the discontinuity surface is parallel to YZ – plane: the slice orientation XY or XZ – plane can be selected using Ux displacement field;
- If the discontinuity surface is parallel to XZ – plane: the slice orientation XY or YZ – plane can be selected using Uy displacement field;
- If the discontinuity surface is parallel to XY – plane: the slice orientation XZ or YZ – plane can be selected using the Uz displacement field.

Consider the following volume displacement depicted in Figure 3.5 as an example.

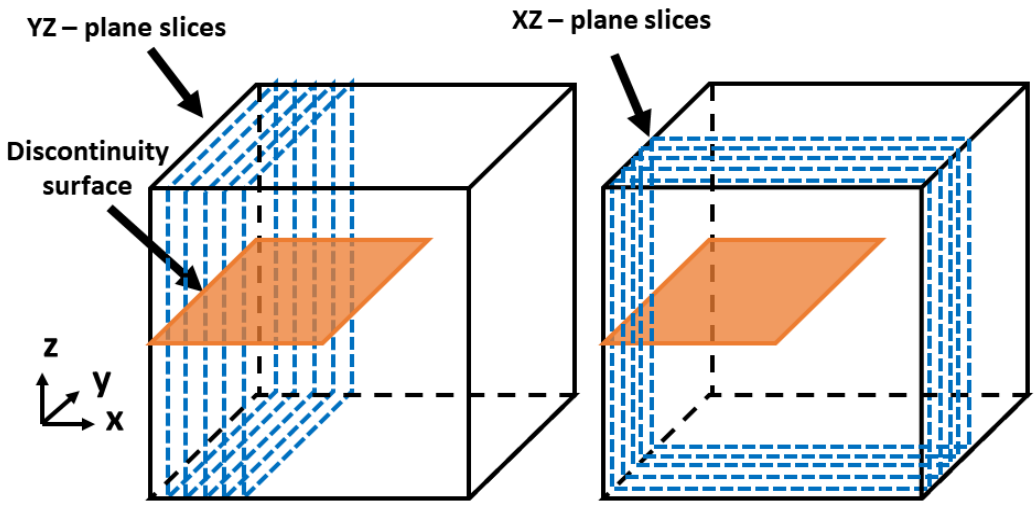

Figure 3.5 Volume Phase congruency slice plane indexing

The discontinuity surface orientation is shown to be in XY plane represented by the orange plane. Normal to the discontinuity surface is the Z-direction which means, the Uz displacement field will yield the highest discontinuity signal (Mode I opening). The Uz displacement field is then coupled with the slice indexing of the YZ – plane or XZ – plane, both depicted respectively in Figure 3.5.

For a mode I opening, if the discontinuity surface is not parallel to any of the planes, the discontinuity signal is distributed into two or three displacement orientations that all yield the same noise. The goal is to channel the discontinuity signal into one orientation to achieve a better signal to noise ratio.

In the case of the discontinuity surface not being completely parallel to any of the planes, the positioning of the voxels on the reference image will need to be changed. By rotating both the initial and deformed tomograph, the positioning of the voxels can be changed.

3.4 Median filter (2D and 3D)

The Median filter is a nonlinear method used to remove noise from images and is widely used in image processing. The main effective ability of the Median filter is with smoothing noise while preserving important edges or features while other linear smoothing filters (i.e. Gaussian filter) moves the location of a feature.

This can be a useful tool to post-process displacement fields as DIC and DVC are very susceptible to noise in digital images. For identifying the crack, it is a requirement to supress noise while preserving the discontinuity location. The algorithm is relatively simple to follow;

Each data point is iteratively highlighted, at each iteration a user selected neighbourhood (window/ subset) is placed around the selected data point. All the data point values in the selected window are converted into an array and the median is calculated by sorting all the values into numerical order. The highlighted data point is then replaced with the median value of its window. The window slides point by point over the entire field. The volume implementation of the Median filter is like the 2D case – instead, a volume neighbourhood is selected.

3.5 Remove outliers (2D and 3D)

An outlier is an observation point that is distant from other observations and in most cases, the analysis is better conducted if the outlier is identified and removed. To be able to identify and remove outliers is an important process in both image analysis and data analysis. Typically, once displacement field is extracted from a fracture experiment with the use of DIC/DVC analysis, the data will inherently contain the error sources produced by the crack (see Figure 3.1) and typical noise. The sources of these errors are difficult to control with the conventional DIC/DVC algorithms. Therefore, a tool is introduced where displacement values with high localised gradients can be removed from the data to be replaced with a better representation of the whole field.

The intention of the outlier deletion is to remove isolated noise spots from the displacement field data. We take advantage of the median filter introduced in the previous chapter and use it as a tool to identify and highlight noise spots. The outlier deletion procedure is depicted in Figure 3.6.

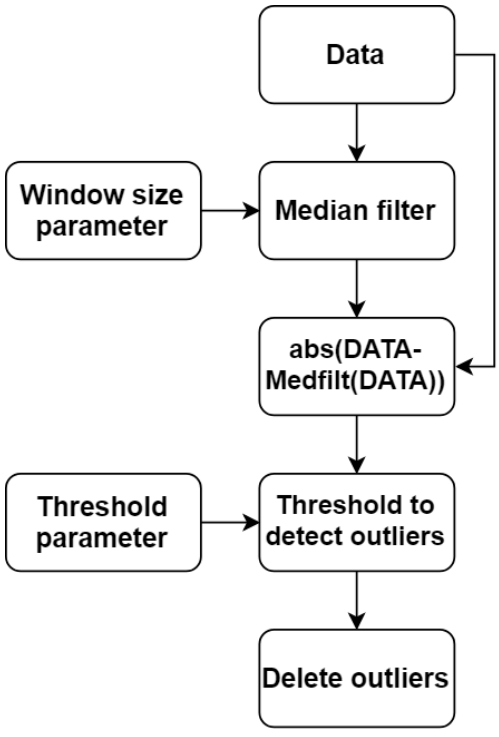

Figure 3.6 Outlier deletion procedure

The Outlier deletion algorithm only requires three inputs; two of the parameters are specified by the user. "DATA" (see Figure 3.6) is representative of the displacement field data, the window size for the median filter and a threshold parameter. The threshold parameter can be a default setting based on the baseline noise which can be determined by calculating the standard deviation of the displacement field. Initially, a median filter is applied to the data which is then subtracted from the input data giving median filter residual.

The median filter residual provided from this process gives a numerical interpretation of locations where significant changes occurred from the Median filter. By a logical step procedure, the absolute difference between data and median filtered data is checked. If above the threshold parameter, the data point is deleted from the displacement field.

3D Outlier deletion has been developed that uses the same algorithm but assesses the validity of each data point in volume displacement by user selected volume neighbourhood distance. Open source MATLAB algorithm, Medfilt3.m computes the median filter in volume data but requires a numerically odd number value for window size. As an example, the outlier deletion procedure is applied to an extremely noisy and erroneous displacement field (see Figure 3.7). The data in Figure 3.7a is of a Uy displacement field created virtually with a CMOD of 0.1 pix and applied high additive noise (see section 4.7) where the conventional crack detection methods have failed to detect the discontinuity. The dimension of the data points is 235×235. As seen in Figure 3.7a, the discontinuity is almost hidden by the additive noise. A median filter is applied to the displacement data, window size of 15 with the output is produced in Figure 3.7b. Data obtained from the median filter is then subtracted from the raw data as depicted in Figure 3.7c. Data values where the difference exceeds the threshold are deleted and replaced with NaN (Not a Number) values as shown in Figure 3.7d. It is observed that 92.3% of the data point values were deleted. The missing data points are then extrapolated (method will be discussed in the next section) and the discontinuity is extracted. The same outlier filter has been implemented to displacement fields obtained from PIV (Particle Image Velocimetry) [142]. Westerweel et al. [143] proposed an outlier deletion filter, also very similar to the one proposed in this chapter. Their method is based on a threshold value of the normalized residual fluctuation of the velocity of one data point relative to its nearest eight neighbours. This residual also takes into account the minimum possible residual by incorporation a tolerance, which corresponds to the precision of the data. Outlier filter and optimization of displacement fields were not researched here and could be added to future work.

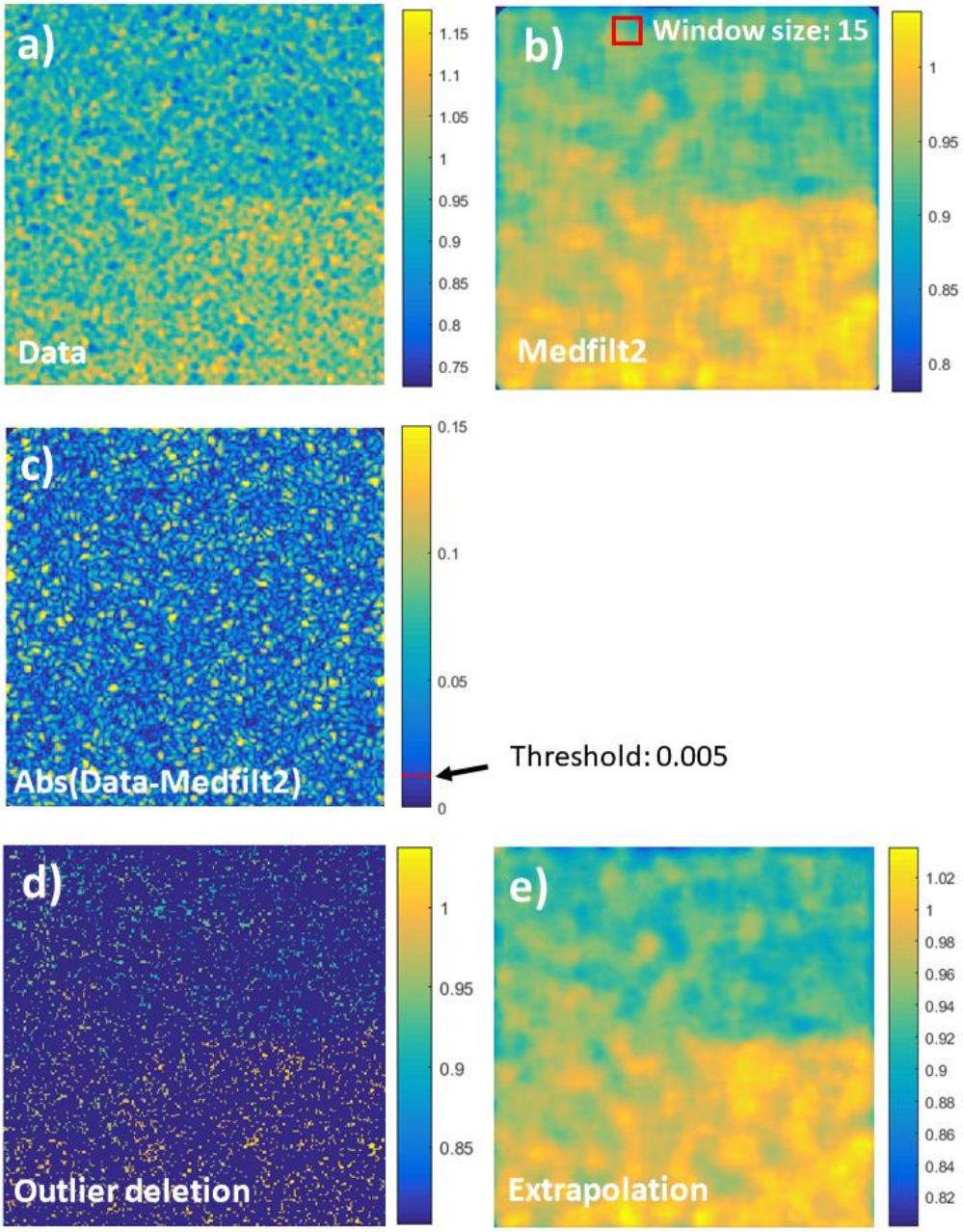

Figure 3.7 Outlier deletion example a) Uy displacement of a virtually created crack with CMOD of 0.1 pix b) Median filter applied to a) with window size 15 c) absolute difference of a) and b) d) Deleted data points of Uy displacement that are above the threshold of 0.005 e) Extrapolation of d)

3.6 Recovery of missing data (2D and 3D)

Missing data points[1] within a displacement field are very common and are usually caused by unmatched subsets or if the correlation coefficient is low during the process of the DIC / DVC algorithm. This can occur for many reasons such as: high deformation leads the matching algorithm to fail; small subsets therefore not enough definition within each subset; and experimental variation between the time series subsets which could be due to; vibrations, blur, change in light intensity, crack artefact corruption of the surface and out – of – plane motion. A crack artefact is the dark pixilation caused by void of the crack. Similar issues also exist in the analysis of DVC.

Another cause could also be due to the outlier deletion procedure. One of the main pitfalls of the phase congruency algorithm is that the image input needs to be a complete field (i.e. no missing data points) for the calculation of Fourier transform and phase information. There have been a few studies related to extrapolation of missing data within displacement field [145-147]. In this research, an open source code *inpaint_nans* [148] is used to fill in the missing data points within our displacement field for surface measurements. The algorithm uses non-NaN (Not a Number) data points to interpolate using a linear least squares approach to obtain a fully filled displacement field. An example of its application is shown in Figure 3.7, where 92.3% of the missing data is recovered adequately and the calculation is depicted in Figure 3.7e. The key component of *inpaint_nans* is that the algorithm fills all the NaN data points without modifying the known data points. The *inpaint_nans* was used before to obtain an approximation of missing data points [149].

Inpaint_nans is only applicable for a two-dimensional data point field. Another MATLAB open source code, *inpaintn* [150], is introduced to extrapolate the missing data points of a volume displacement field. Unlike *inpaint_nans*, this algorithm uses an iterative least squares regression based on a three-dimensional discrete cosine transform to approximate the unknown data points. *Inpaintn* algorithm was used in the recovery of missing data points from displacement fields [151]. The objective of these methods (*inpaint_nans* & *inpaintn*) is to create a quick and easy method with no user interaction to obtain a full field approximation of displacement values. A study of which method is more robust is an open-ended question therefore not investigated in this research and added to future work.

[1] Also known as NaN (Not A Number)

3.7 Automatic initial mask (2D only)

PC-CD algorithm is fully automatic due to the automatic selection of the initial mask for the region-based active contour segmentation procedure. To segment a feature (i.e. crack), region-based active contour segmentation procedure requires two inputs – Image with the feature and an initial mask which is a binarized mask that is a subset or a superset of the feature of interest. Displacement field of the crack represents the image of the feature and therefore can be directly fed into the active contour algorithm. The initial mask acts as an initial guess as to where the location of the feature is. Initial guess location of the feature is labelled as 1 while non-initial guess location is labelled as 0. This section will provide the image processing tools to make the creation of the initial mask automatic based on an unsupervised anomaly detection. Typically, for a successful segmentation of a feature, the user is required to interact with the segmentation algorithm and determine an area localised to the feature that is either a subset or superset of the feature of interest. Automatic initial mask selection removes any user interaction and successfully identifies the feature of interest based on the longest straight line. The straight line is usually the signature of a discontinuity in the binarized edge map of the displacement field and an example shown here [152]. The Hough transform is utilised to find the longest straight line in the binarized edge map. A similar method based on using Hough transform to automatically find damage from displacement fields was used here [153]. The following method is seen to successfully ignore features created by noise or irregularities and construct a single mask if the discontinuity exists and no mask if the discontinuity does not exist.

3.7.1 Bilateral filter

The Bilateral filter is an image-processing tool utilised to smooth images while preserving edges [154, 155]. Similarly, to the Median filter, each location is replaced by an average of its neighbours depending on two parameters that indicate the size and contrast of the features to preserve. This works well with this study as the discontinuity signal is usually hidden in additive (see Figure 3.7a) and the bilateral filter can help enhance the feature in algorithmic noise[154]. Bilateral filter will adjust the magnitude of displacement values, increasing the uncertainty. For this reason, bilateral filter will only be used to identify the location of the crack feature and will not be used to quantify the crack. An open source MATLAB code developed by Douglas Lanman is used [156].

3.7.2 Sobel edge detection

Sobel Edge detection is a gradient-based edge detection operator that simply uses two 3×3 kernels which differentiates an image in two different orientations to construct a gradient magnitude. The main advantage of this image-based tool is that the MATLAB open source code has an in-built automatic threshold method called Otsu method [157]. The Otsu method is very useful as it heuristically and automatically helps skeletonise significant features and edges while being computationally inexpensive.

3.7.3 Hough Transform

The Hough transform is a feature detection technique that can be used to isolate certain features of a particular shape within an image by using a voting procedure. Hough transform was originally developed to detect lines [158] and then later has been generalised to cover arbitrary shapes or features that can be represented by analytic equations [159]. This work utilizes the Hough transform to detect straight lines – or the longest straight line.

Lines can be represented uniquely by two parameters in Cartesian form:

$$y = a\,x + b \tag{33}$$

However, this form cannot represent vertical lines (requires $a = \infty$ or $a = -\infty$), therefore the Hough transform uses the following equation to be able to represent all lines.

$$x\,cos\,\theta + y\;sin\,\theta = r \tag{34}$$

$$y = -\frac{cos\,\theta}{sin\,\theta}\,x + \frac{r}{sin\,\theta} \tag{35}$$

$\theta \in [0, 180[\mathrm{r} \in \mathbb{R})$ or $\theta \in [0, 360[\ \mathrm{r} \geq 0)$

The Hough space for lines has therefore two dimensions, (θ, r) where a line is represented by a single point, corresponding to a unique set of parameters. The idea is, a point in image space is mapped and represented by all lines that can pass through that point yielding a sinusoidal–line in the Hough space for each individual point in image space.

A Hough space accumulator is used to determine the areas where most Hough space lines intersect. For every point that is transformed from image space, the accumulator is incremented for all lines that could pass through that point. The resolution of the accumulator determines the precision which lines can be detected. An in-built MATLAB code *hough.m* takes a binarized map as an input and performs the Hough transform and returns the accumulator. The lines can be found as local maxima in this accumulator. Once in accumulator space, an interpretation is required to interpret the peaks and classification of all lines. All values above the threshold are interpreted as a line, which is given 50% of the maximum value of the accumulator. Simple threshold tends to detect identical lines if peaks in the accumulator are close. Therefore, a suppression neighbourhood algorithm is defined, where two lines must be significantly different before both can be detected. MATLAB code, *houghpeaks.m* was utilised to detect lines and interpret the accumulator where 10 peaks are considered. Each peak is checked to make sure they are not too close to each other using the suppression neighbourhood algorithm. Finding the peaks returns the parameters θ and r with no information of length meaning all detected lines are maximum in length within the boundaries of the image dimension. The MATLAB code, *houghlines.m*, is then used to find the length of the detected lines using the binarized map. The code also connects the same lines (same θ and r parameters) through missing points of up to 10 pixels and merges them into a single line. The algorithm outputs the two end-point co-ordinates of each line, where only the longest connected line is considered.

3.7.4 Select Connected Components

An open source algorithm, *SelectCC.m* [160] is used to select all the connected components from a single identified point. The algorithm input requires a binary map of features and a coordinate-based point. *SelectCC* uses the neighborhood of the identified point to iteratively review all the connected points and add the connected components to the selection. The output information is of a binary map of the selected feature.

3.8 Segmentation algorithm (2D and 3D)

Segmentation is the process of partitioning a digital image into multiple segments or set of pixels. In this research, the interest is to partition the discontinuous data points into an independent set. The “classical” segmentation, i.e. using thresholding or gradient based methods, can struggle to segment the discontinuous data points well and proficiently due to unusual noise of the calculated displacement field. However, Active contour segmentation, can be a powerful and flexible method to segment discontinuous data points. Also known as the Snake algorithm [161, 162], Active contour segmentation is an iterative feature extraction technique which requires initial points/mask defined around a feature that is to be extracted. The benefits of the algorithm can be summarised as: automatically detecting interior contours, robust with respect to noise, ability to detect and represent complex topologies (boundaries, segments) and finally, extraction of geometric measurements such as length, area, volume, intensity of a detected contour, surface or region, respectively. Application of the snake algorithm can be a powerful procedure that can be applied to detect cracks in displacement fields and extract the discontinuous region.

3.8.1 Region based Active contour algorithm 2D

The literature for region based active contour is well developed and established. The most well-known active contour is the Chan-Vese model which is based on the Mumford-Shah functional [163] for region based segmentation. The mathematical depiction of the Chan-Vese model can be found in the paper “Active Contours without edges” [164] which is employed for this research. Mumford and Shah [163] proposed a general optimization framework using an energy functional based on regional geometric properties of a segment. The properties include the length of curves and variation of the individual pixel intensities inside and outside the curve. While most active contours rely heavily on edge detection, the benefit of the Chan-Vese model is that the method ignores edges completely and instead fits a two-phase piecewise constant model to the given input image.

The principle of the algorithm is an energy-minimising spline guided by external constraint forces and influenced by image forces that pull it toward features such as lines and edges, hence locking onto nearby edges, localising them accurately [161]. Also, segmentation boundary is represented implicitly with a level set function, which allows the segmentation to handle topological changes more easily than explicit snake methods.

An open source MATLAB code developed by Lankton [165] based on the very same Chan-Vese model, was used in this work. The Chan-Vese algorithm, requires four input parameters: Input image; Initial mask; Maximum number of iterations and α_s - weight of the smoothing term. Input image is given to be the Phase congruency map, where the discontinuity is likely to be highlighted as a ridge like pattern. Initial mask helps regionalise the desired segmentation feature – in this case the discontinuity, using a skeleton binary map and is selected by an automatic process. The initial mask may be in form of an overshot[2] or an undershot[3]; the active contour algorithm decreases or increases the mask until a convergence or Maximum number of iterations is reached. To reduce dependency on the initialisation, it is observed that undershot initial mask performance is much more reliable for automation. From observation, different undershot masks do not modify the outputted segmentation boundary itself. However, a better skeleton mask will mean the active contour will converge much faster requiring less computational time. While Chan-Vese has a few fine-tuning parameters, the most important is α_s – the weight of the smoothing term. The parameter α_s adjusts the length penalty, which balances between fitting the input image more accurately (i.e. smaller α_s) vs producing a smoother boundary segmentation (i.e. larger α_s). Although cracks can be quite convoluted depending on their microstructure, inherently, DIC is not able to capture a crack's true convolution due a loss of spatial resolution. Therefore, ideally a larger α_s parameter fits better to the scope of it's application. It is observed that for displacement fields with small noise, good crack parameter results are produced where $\alpha_s = 0.8$ and is kept as a default value for all datasets.

[2] Initial mask is a superset of the crack
[3] Initial mask is a subset of the crack

3.8.2 Region based Active contour algorithm 3D

An open source MATLAB code developed by Yan Zhang [166] entails a set of Active contour image segmentation tools such as geodesic active contour (GAC) [167], Chan-Vese [164] and a hybrid region model [168] level-set methods and have the ability to segment 3D surfaces iteratively and semi-automatically. The toolbox uses the semi-implicit solver based on the additive operator splitting (AOS) which is shown to have a better stability [169] of the numerical methods even with very large time steps, thus enabling better convergence for level-set based segmentation. Upon visual trial– the hybrid region model presented the most promising results for the 3D segmentation of cracks. The hybrid region model is designed to segment features that has intensity inhomogeneity [168] using a combination of boundary and regional terms. The mathematical depiction and theory of the region-based hybrid algorithm can be found here [168]. The main idea of using the hybrid region model is how volume phase congruency features are represented. Due to the slice independency, the feature voxel in the data are identified the corresponding 8 out of 26 neighboring voxels that have potentially homogenous intensity while the remaining 18 neighboring voxels can potentially have inhomogeneous intensity.

Using the "*ac_hybrid_model.m*" developed by Zhang et al. [166] requires 6 inputs and outputs the volume segmentation and surface of the crack. First variable takes the 3D phase congruency data, however first the phase congruency data needs to be converted into the propagation field. The propagation field indicates the magnitudes and the direction for the evolving curved line. A negative value in the propagation field data means contraction and positive value means expansion. To obtain the propagation field data, a value of $\mu_{\mathrm{seg}} = 0.2$ is subtracted from the 3D Phase congruency data. Phase congruency is a normalised data where the discontinuity will have high congruence at the location which makes the propagation field easily obtainable. If the high congruence is above μ_{seg} , then propagation data will have a positive value, if below μ_{seg}, naturally the propagation data will be negative. It is seen that μ_{seg} can also be obtained by calculating the mean value of the 3D Phase congruency data. The propagation field is used to calculate the Chan-Vese part of the Hybrid algorithm.

The second parameter is the initial level set, also referred as the seeding point during the first iteration of the "*ac_hybrid_model*" function. The function "*ac_hybrid_model*" is iterated instead of using the function's in-built iterative option. To achieve this, the function's 7th input that controls the maximum number of iterations is given a value of one. This is so that

the response after each iteration feedback can be graphically represented and the segmentation growth visually assessed by the user. The initial level set is updated with the previous iteration output from the function. However, for faster computational time, it is recommended to use the function's iterative process. The seeding point selection completely replaces the initial mask as shown in the 2D region-based segmentation. The seeding point is a binary field, where a $3 \times 3 \times 3$ mask, subset of the discontinuity is visually and manually selected by the user.

The third and fourth parameters, α_{seg} and β_{seg}, are predefined weighting terms balancing the propagation active contour method and geodesic active contour method respectively. They control how much each method takes over the segmentation process, overall weighting in the hybrid model. For simplicity, the parameters are kept constant at $\alpha_{seg} = 0.015$ and $\beta_{seg} = 0.02$ for each dataset.

The fifth parameter is the Gradient field of the 3D Phase congruency map which is used to calculate the Geodesic active contour (GAC) term. The in-built function "*ac_gradient_map*" is used to construct this gradient field.

The sixth term is δt_{seg}, representing the time step for each iteration and controls the convergence of the function. δt_{seg} is kept at the default value of one. Typically, the segmentation iteration is terminated once the active contour converges towards an optimum segmentation. Therefore, the segmentation is either terminated by the user when segmentation growth is observed to be stagnant or the iteration number is selected high enough to cater a stagnant segmentation growth. The segmentation algorithm can be better optimized requiring lower iteration count to reach a convergence with a more precise mask.

3.9 Phase congruency-based Crack Detection (PC-CD)

3.9.1 Introduction

The application of the PC-CD algorithm and its ability to extract discontinuity parameters accurately is depended on the displacement field used to proces. Calculation of the displacement field requires careful attention and optimization for parameters such as subset size, step size and correlation coefficient and outlier filter. There are many guidelines for this in the literature and the impacts are carefully studied [170-172].

The crack detection algorithm can detect surface discontinuities in all orientations (Mode I, II, III) for both Stereo-DIC and 2D-DIC configurations. However, this thesis investigated only Mode I cracks. Displacement field error sources can relate to calculation of surface discontinuities, due to a heterogeneous motion within subsets that contain the crack. More accurate discontinuous displacement measurements are calculated if the discontinuity (crack orientation) is parallel to the axis of the subsets [76, 119, 173]. Therefore, most researchers have ensured that the camera orientation (X or Y camera axis) is parallel to the expected orientation of the discontinuity [76, 125, 174, 175]. Figure 3.8 demonstrates the schematic of camera X-axis setup parallel to the orientation of the crack.

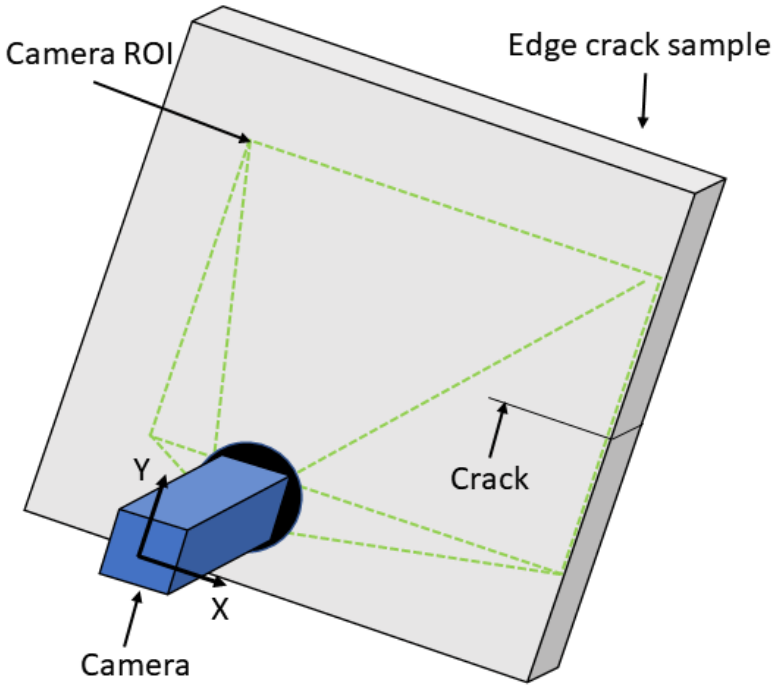

Figure 3.8 Depiction of Camera X-axis parallel to the orientation of the crack.

Parallel orientation not only controls how the discontinuity interacts with the positioning of the subsets but also shifts the magnitude of the displacement jump into a single orientation increasing the signal to noise ratio of the step [119] and also allowing the separation of mixed mode displacement of the crack. A good detection of discontinuity location is mostly based on good signal-to-noise ratio between displacement jump and displacement noise and therefore the orientation can be beneficial to calculating the discontinuity parameters. Coupling two displacement field orientations (or three orientations in the case of stereo-DIC) to locate the crack can lower the signal-to-noise ratio of the signal as all fields contain the same degree of uncertainty. If the discontinuity is at a significant angle with the one of the axes, both displacement field components will yield the displacement jump with its relative noise, which means naturally increasing the magnitude in one orientation will lead to higher signal-to-noise ratio.

If the orientation cannot be determined, the raw images can be rotated post-experiment using accurate interpolation methods [176] before displacement field calculations are exercised. It is important to note that PC-CD can detect cracks at all angles, however for accurate displacement measurement which results to accurate crack parameter extraction, image rotation is recommended. PC-CD is also able to obtain an angle measurement for the longest line segment, which can determine the mode of the crack and can be useful for an automatic two-step algorithmic designed for rotation-based optimization. This has not been further studied in this research and will be added to future work.

The displacement field of a cracked body is calculated using DIC and is exported from LaVision Davis Strain Master Code[37] as a text file and imported into the MATLAB platform. The text file typically contains 4 columns for 2D DIC and 5 columns for Stereo-DIC. Each row is representative of a single data point plotted over the entire reference image either in calibrated coordinate (mm) or uncalibrated coordinate (pixels) system; X-coordinate, Y-coordinate, X displacement (Ux), Y displacement (Uy) and Z displacement (Uz)[4]. The data points outside of the determined masked region, censored data points due to corrupted subsets and subsets lower than the correlation coefficient are also included in the text file. These data points that have no displacement information are prescribed "0" to each displacement column (Ux, Uy and Uz) and will be labelled as NaN (Not A Number). A script is used that meshed the X and Y data point grid to construct Ux, Uy and Uz displacement field maps.

[4] Z displacement /5th column exists For Stereo-DIC

An example dataset is considered to help visualise each algorithmic step (see Figure 3.9 for a better understanding). The example image dataset is 2024×2048 pix of a horizontal single edge crack is stimulated that matches the fracture parameters identical of steel specimen and created virtually with CMOD of 1 pix. Displacement calculations are obtained using pixel-based co-ordinate system where subset and step size are chosen to be 16 and 4 pixels respectively. Pixel based co-ordinate system is recommended as errors associated to the calibration can provide uncertainty in the calculation and obtaining a reference point if the images needs to be re-calibrated is a beneficial foresight. Figure 3.9a depicts the full-field raw vector magnitude of Ux and Uy obtained from LaVision Davis Strain Master Code. The dimensions of the data points are 507×513

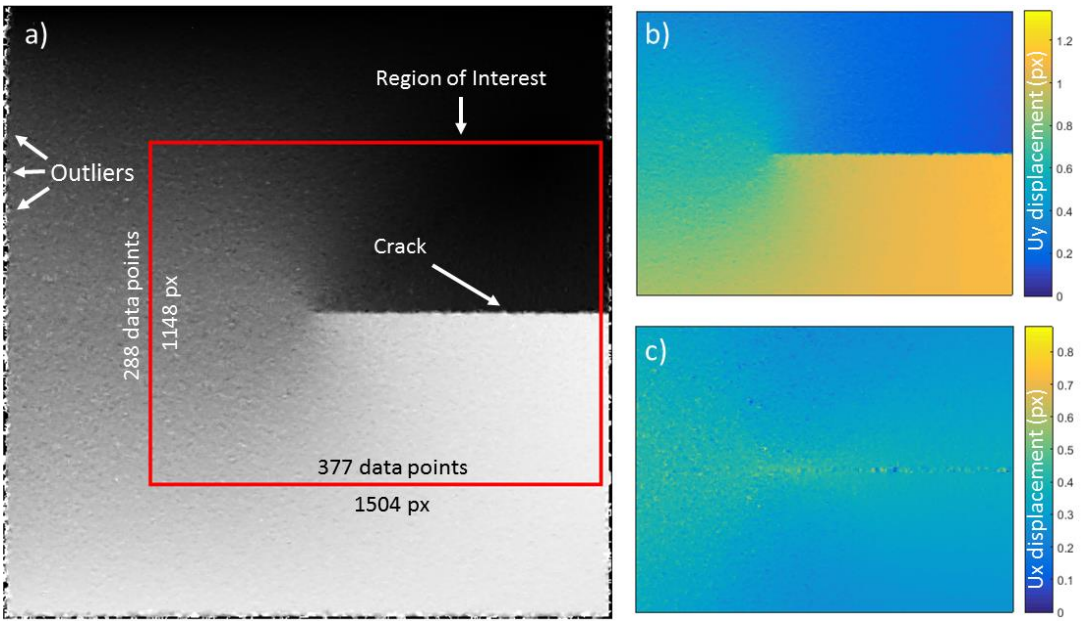

Figure 3.9 Selection of ROI: a) Displacement Vector Magnitude; b) Cropped Uy displacement field; c) Cropped Ux displacement field

3.9.2 Step 1 – Region of Interest

A region of interest is specified by the user to reduce the computational time and crop-out the DIC "masked" data points. (i.e. vectors labelled outliers Figure 3.9a) which can increase the success rate of the crack detection. The displacement fields; Ux, Uy and Uz and the co-ordinate space of the data points are cropped based on the selected rectangular region of interest and are the only fields considered for crack detection and crack parameter extraction. The co-ordinate space carries valuable information as to the placement of data point location on the reference image.

Figure 3.9a shows full-field raw vector magnitude field of Ux and Uy where the red area identifies a user determined Region of Interest (ROI). Considering that the raw image data was not masked before displacement calculation, it is seen in Figure 3.9a, the data points located at the very edge of the field contain spurious values labelled "Outliers". The ROI is selected so that these values are not considered for the PC-CD algorithm (see Figure 3.8a). The dimension of the ROI is given to be 377×288 data points, which translates to 1504×1148 pix. Figure 3.9b and Figure 3.9c depict the cropped Uy and Ux fields respectively which are the output from this step.

INPUT	OUTPUT
Raw displacement field $(\boldsymbol{Ux}, \boldsymbol{Uy}, \boldsymbol{Uz})$	Cropped displacement field (C_Ux, C_Uy, C_Uz)
Co-ordinate space $(\boldsymbol{X}, \boldsymbol{Y})$	Cropped Co-ordinate space (C_X, C_Y)
Region Of Interest	

Table 1 Input and Output table for PC-CD Step 1 – Region of Interest

3.9.3 Step 2 – Displacement orientation

Displacement field orientation with the highest discontinuity magnitude is selected for crack detection and segmentation as the field bears the highest signal of the discontinuity.

- For mode I cracks, the selected displacement orientation is normal to the crack.
- For mode II cracks, the selected displacement orientation is the parallel to the crack.
- For mode III cracks, the selected displacement orientation is out-of-plane to the crack.

Figure 3.9 shows a mode I edge crack along the horizontal direction on the x-plane, highest discontinuity signal will be in the Y – displacement (Uy) orientation as seen by Figure 3.9b.

In this step, the user will have to determine which displacement orientation bears the highest discontinuity and hence will be used for crack detection and segmentation. The determination of displacement orientations can be made automatic using statistical analyses but the automation of this procedure was not investigated in this research.

INPUT	OUTPUT
Cropped displacement fields ***(C_Ux, C_Uy, C_Uz)***	Selection of discontinuity orientation (i.e. Y-direction)

Table 2 Input and Output table for PC-CD Step 2 – Displacement Orientation

3.9.4 Step 3 – Fill missing value

All cropped displacement field orientations (C_Uy and C_Ux) are applied the *inpaint_nans* with linear interpolation (section 3.6). The extrapolation code attempts in the recovery of censored displacement data points which can be caused by the crack artefact, image blurring large speckles and more are discussed in section 3.1.

Figure 3.9b and Figure 3.9c do not contain censored data, therefore change between the displacement fields, before and after, are not implicated from this step.

INPUT	OUTPUT
Cropped displacement fields $(\boldsymbol{C\_Ux}, \boldsymbol{C\_Uy}, \boldsymbol{C\_Uz})$	Filled displacement fields (FC_Ux, FC_Uy, FC_Uz)

Table 3 Input and Output table for PC-CD Step 3– Fill missing value

3.9.5 Step 4 – Outlier deletion

The following two steps (step 4 and 5) considers an optional Outlier replacement procedure, discussed in section 3.5 and 3.6. The user has the option to use this procedure in order to enhance the discontinuity and remove the erroneous displacement values localised at the crack. The user has the option to skip and proceed to Automatic Crack Detection (Step 6 +).

Outlier deletion is utilised with all the displacement field orientations (FC_Ux, FC_Uy, FC_Uz). The displacement information can contain outliers caused by the). Outlier deletion allows the user to control the deletion of imprecise displacement data points by observing a user inputted neighbour (ODw) around each data point. The outlier deletion can improve the crack detection as shown in Figure 3.7, previous chapter.

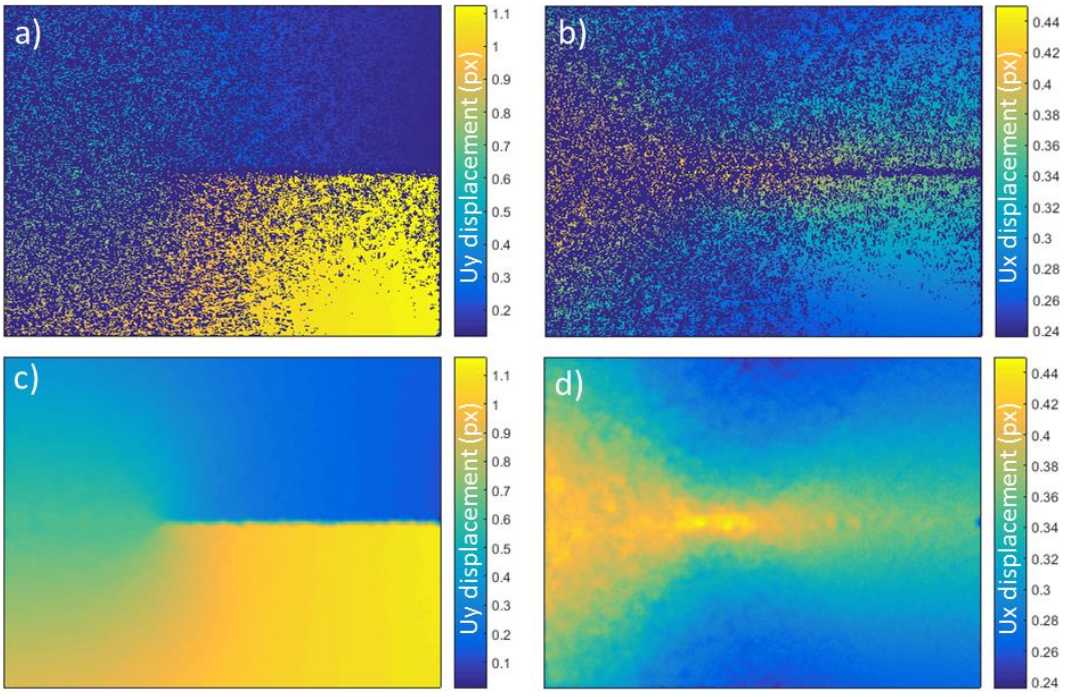

Figure 3.10 Outlier deletion and extrapolation procedure a) Outlier deletion of Uy b) Outlier deletion of Ux c) Extrapolation of a) d) Extrapolation of b)

Outlier deletion parameters for Figure 3.10(a and b) is 5 and 0.01, respectively of window size (ODw) and threshold parameter (ODt). Figure 3.10(a and b) show the locations of the removed data points from Uy and Ux displacement fields, respectively. The application of the outlier deletion has decreased the range for Uy and Ux fields from 1.3 pix (Figure 3.9b) to 1 pix (Figure 3.10a) and 0.9 pix (Figure 3.9c) to 0.2 pix (Figure 3.10b), respectively. The Outlier replacement procedure visually enriches the global features and creates a much sharper field; as observed by comparing before and after displacement fields. (Figure 3.9b vs Figure 3.10c) (Figure 3.9c vs Figure 3.10d)

INPUT	OUTPUT
Displacement fields $(\boldsymbol{FC\_Ux}, \boldsymbol{FC\_Uy}, \boldsymbol{FC\_Uz})$	Filtered displacement field (OFC_Ux, OFC_Uy, OFC_Uz)
Outlier window size $(\boldsymbol{ODw})$	
Outlier threshold parameter $(\boldsymbol{ODt})$	

Table 4 Input and Output table for PC-CD Step 4 – Outlier deletion

3.9.6 Step 5 – Fill missing value

In this step, the outlier deleted displacement values are filled using *inpaint_nans* with linear interpolation (see section 3.6). The output of this step can be seen in Figure 3.10(c and d).

INPUT	OUTPUT
Displacement fields ***(OFC_Ux, OFC_Uy, OFC_Uz)***	Filled Displacement fields ***(FOFC_Ux, FOFC_Uy, FOFC_Uz)***

Table 5 Input and Output table for PC-CD Step 5– Fill missing value

AUTOMATIC CRACK DETECTION

The selected displacement orientation from (section 3.9.3) is used to dictate the displacement field for crack detection. The crack detection procedure does not require precise displacement values, but rather requires the detection and approximate location of the discontinuity. The aim of the automatic crack detection is to detect and create an initial mask of the discontinuity. To produce an undershot initial mask of the crack, the displacement map is smoothed using a bilateral filter (section 3.7.1), which is an image-processing tool that removes noise from images while preserving edges. The usage of a bilateral filter will only be considered for the approximation of the discontinuity location as it is shown to be a powerful tool to suppress noise while preserving edges rather than crack parameter extraction. The next step is the Sobel operator (see section 3.7.2), which is a gradient-based edge detection filter, that produces a map of all the edges in the smoothed image; this includes edges produced by noise and the discontinuity. Next, the Hough transform (see section 3.7.3) is used to find the co-ordinates of the longest line in the binary edge map. The Hough transform is a feature detection technique that can isolate features of a particular shape within an image by using a voting procedure. The detected longest line is the highest likelihood of the discontinuity in the displacement map. This is because the edge-preserving filter applied previously removes most of the displacement noise, leaving only sporadic noise that appears as short edges [126]. The detected longest line is an undershot of the discontinuity highlighted by PC and therefore is used as an initial mask.

In this example, FOFC_Uy (see Figure 3.10c) is labelled as the DetectionField and will be the only input for the Automatic crack detection procedure to output an InitialMask to be used for the segmentation algorithm. The accurateness of the initial mask will only help the region-based active contour algorithm to reach an optimum result much quicker – requiring less iterations hence less computational time. However, if the correct region of discontinuity is selected, the initial mask does not alter the segmentation process and hence the extracted crack parameters.

INPUT	OUTPUT
Selected displacement field orientation ***DetectionField*** ***(i.e. FOFC_Uy)***	Initial discontinuity mask ($InitialMask$)
	Longest line angle ($LineAngle$)

Table 6 Input and Output table for PC-CD –Automatic crack detection procedure

3.9.7 Step 6 – Bilateral filter

The Bilateral filter (see section 3.7.1) is applied to the selected displacement field orientation (FOFC_Uy) to suppress noise while preserving edges or discontinuity-like signals at a default scale-space, increasing the likelihood of a positive crack detection. A Bilateral filter usually requires three inputs, a normalised displacement field, size and contrast of the features to be preserved. However, two of the inputs will remain unchanged: size of the features; and contrast of the features, are optimally selected to be 20 and 0.1 respectively. These parameters are not changed and do not require any adjustment.

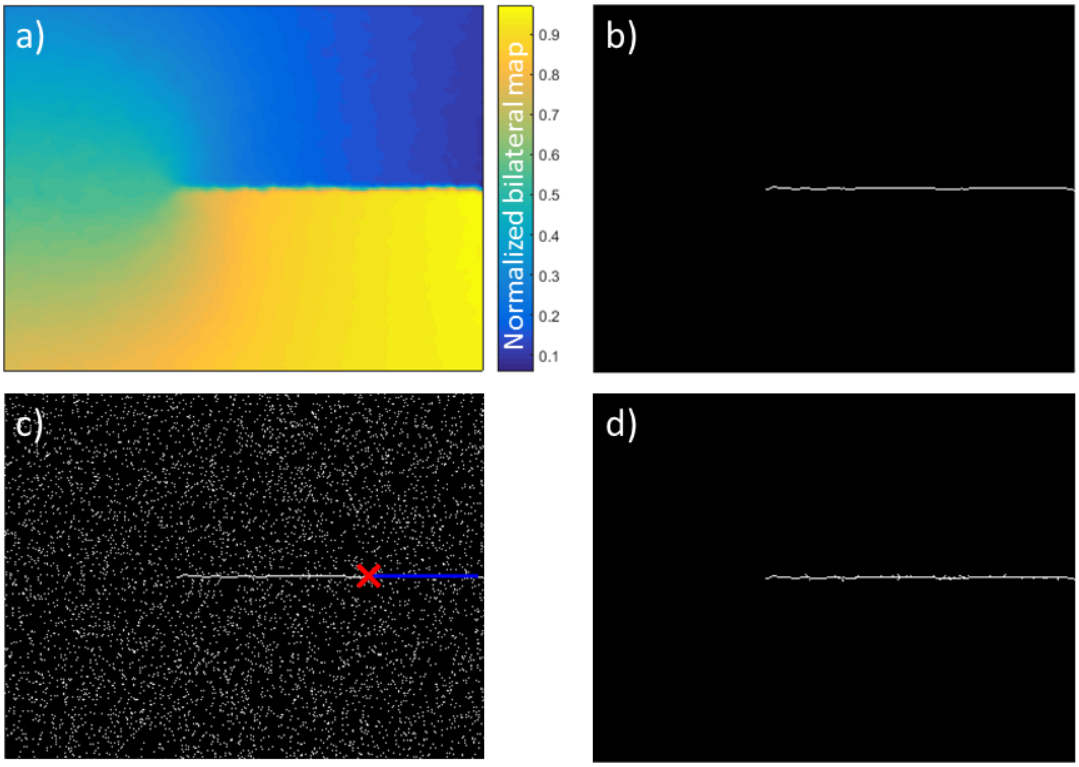

Figure 3.11 Automatic Crack Detection procedure a) Bilateral filter of Figure 3.10c, b) Sobel Edge operator of a), c) Longest line detected using Hough transform from b) and "salt and pepper" noise, d) SelectCC of red cross in c) (Initial mask)

Figure 3.11a depicts the Bilateral filtered displacement field which does not show obvious improvements, as the used displacement field has low amplitude of noise.

INPUT	OUTPUT
Selected displacement field orientation (*DetectionField*)	Bilateral filtered displacement field (*B_DetectionField*)

Table 7 Input and Output table for PC-CD Step 6– Bilateral filter

3.9.8 Step 7 – Sobel edge detection

In this step, the Sobel edge detection (section 3.7.2) is applied to the noise suppressed Bilateral filtered displacement field as the Hough transform requires inputs to be in binary feature space. Edge detection creates a binary map of the discontinuity, approximating to the nearest data point. The edge map may contain other features that were not suppressed due to high gradient or noise with Step 6.

The output of this step, depicted in Figure 3.11b, shows a singular horizontal line without other global binary points and naturally this results to a successful initial mask creation. To demonstrate the robustness to noise and evaluate the feasibility of the following steps for automatic initial mask creation, "salt and pepper" [177] noise with noise density of 0.1 is added to the edge map in Figure 3.11b. The edge map with "salt and pepper" (see Figure 3.11c) is used for Step 8 and Step 9 to show the invariance to Step 6.

INPUT	OUTPUT
Bilateral filtered displacement field ($\boldsymbol{B\_DetectionField}$)	Binary edge map of possible crack paths ($EB\_DetectionField$)

Table 8 Input and Output table for PC-CD Step 7– Sobel edge detection

3.9.9 Step 8 – Hough transform

The Hough transform (section 3.7.3) is used to find and elect the longest edge line in the binary edge map of possible crack paths. The algorithm can output the co-ordinates of the longest line in the logical map automatically which can help localise a desired discontinuity. The detected longest line is usually longest step/discontinuity in the displacement map. The edge-preserving filter was applied previously which removes most of the displacement noise or "speckle". Any remaining noise displayed by the logical edge map is usually random points in the image while the discontinuity of interest is a long line.

The Hough transform uses a voting procedure to find lines in binary images therefore certain criteria can be set for the selection of a line. The algorithm can be set so that lines at only expected orientations can be searched (i.e. between $\theta_{\mathrm{HoughMin}} - \theta_{\mathrm{HoughMax}}$), which helps to decrease the computational time and increase the probability of a positive match. However, the default is set so all orientation of lines is searched (i.e. $\theta_{\mathrm{HoughMin}} = -90°$, $\theta_{\mathrm{HoughMax}} = 89°$). Detected lines are also required to be longer than a specified data point length (i.e. $\mathrm{Hough}_{\mathrm{MinLength}}$). This detection criteria helps filter out the spurious small lines or small dots caused by the noise or effects of high gradient. If the longest detected line is smaller than $\mathrm{Hough}_{\mathrm{MinLength}}$ then no discontinuity is detected.

There are instances where the discontinuity location can be corrupted due to noise or crack artefact, meaning the straight line can be unconnected on the binary edge map. The parameter, $\mathrm{Hough}_{\mathrm{FillGap}}$ is used to give the detected lines a degree of connectivity freedom. Principal of continuity means the distance between disconnected data points can be bridged if the length of the gap is less than $\mathrm{Hough}_{\mathrm{FillGap}}$. The input parameters ($\theta_{\mathrm{HoughMin}}$, $\theta_{\mathrm{HoughMax}}$, $\mathrm{Hough}_{\mathrm{MinLength}}$, $\mathrm{Hough}_{\mathrm{FillGap}}$) will remain unchanged and do not impact the parameter extraction. In the case where the user is detecting short cracks, $\mathrm{Hough}_{\mathrm{MinLength}}$ and $\mathrm{Hough}_{\mathrm{FillGap}}$ may require adjustments.

A noisy “salt and paper” edge map is used as an input with the default Hough transform parameters. The longest line is successfully detected indicated by the dark blue line showing noise robustness as seen in Figure 3.11c. The end points of the line are used to calculate the line angle.

INPUT	OUTPUT
Binary edge map of possible crack paths (***EB_DetectionField***)	If crack is detected (*Binary result*)
	End points of longest detected line
	Longest line angle ($LineAngle$)

Table 9 Input and Output table for PC-CD Step 8– Hough transform

3.9.10 Step 9 – Select connected components

This step is used to create an initial mask using the data obtained in Step 7 and Step 8. If the crack path is convoluted in the binary edge map, the detected longest line will be a subset of the discontinuity. One of the end points of the longest detected line in Step 8 is used with the Select Connected Components (section 3.7.4) with the binary edge map calculated in Step 7. This creates an output of all the connected components to the initial detected longest line and is considered as the initial mask for the discontinuity.

The red cross as shown in Figure 3.11c is selected as the end point used as an input with the *SelectCC* code which computes all the connected component to the selected single point. The output of the *SelectCC* algorithm is depicted in Figure 3.11d. It is observed that Step 8 and Step 9 successfully computes an initial mask localised at the location of the discontinuity, irrelevant of the noise that exists in the edge map. Figure 3.11(b and d) are almost identical maps considering the "salt and paper" noise showing again invariance to noise.

INPUT	OUTPUT
End points of longest detected line	Initial discontinuity mask ($InitialMask$)
Binary edge map of possible crack paths ($\boldsymbol{EB\_DetectionField}$)	

Table 10 Input and Output table for PC-CD Step 9 – Select connected components

3.9.11 Step 10 – Phase Congruency

In this step, the Phase congruency map is created to highlight the crack in preparation for segmentation. The selected displacement orientation from (Step 2) is used to determine the displacement field as it bears the highest discontinuity signal. The Phase congruency algorithm has a default set of parameters stated in section 3.2. The Phase congruency algorithm outputs a normalised field indicating which data points have a likelihood to be a significant feature, where $\lambda_{\min}$ (value between $2-20$), controls the scale of the features (i.e. crack) and d_{PC} (value between $0.8-1.8$) controls the frequency cut-off point and the sharpness of the crack. $\lambda_{\min}$ and d_{PC} have a strong affiliation to the DIC parameters and can be tailored to obtain a better sharpness of the crack.

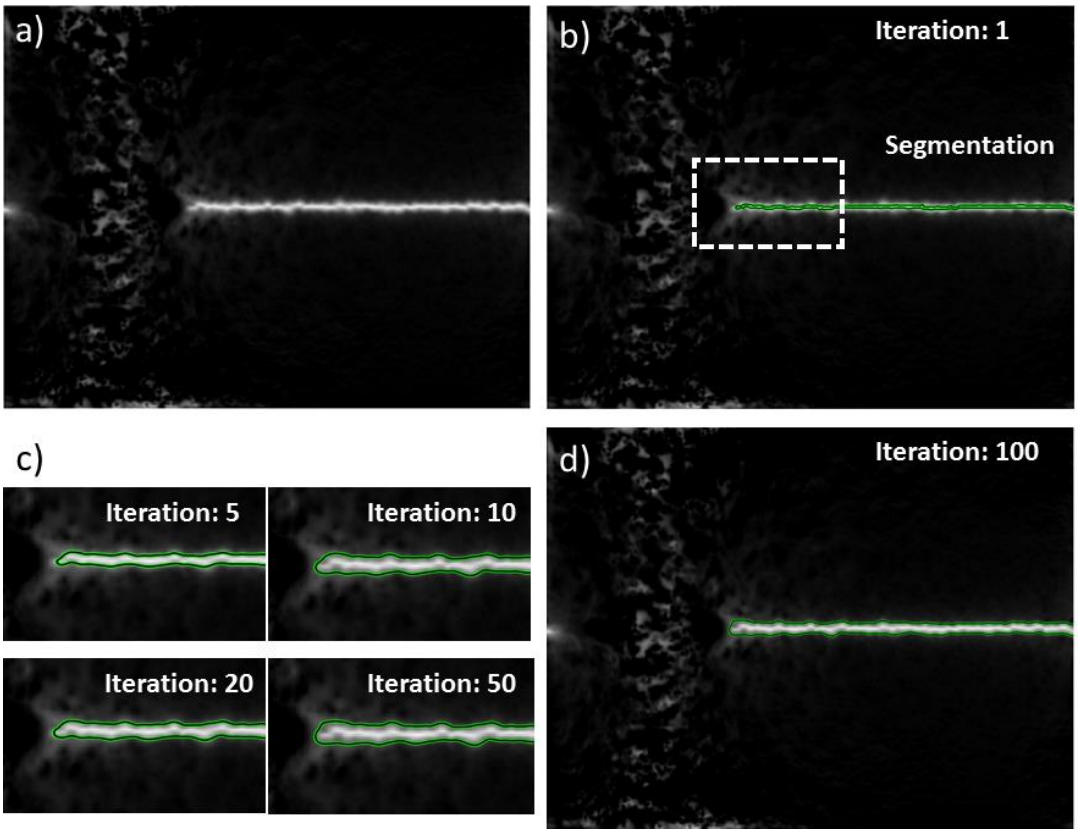

Figure 3.12 Phase congruency map & Discontinuity Segmentation a) Phase congruency map of FOFC_Uy (Figure 3.10c) b) Region based Active contour segmentation first iteration c) segmentation Iterations 5, 10, 20, 50 magnified at the crack tip region d) Region based active contour segmentation last iteration

Figure 3.12a shows a Phase congruency map of the selected displacement orientation, *FOFC_Uy* (see Figure 3.10c), where default the parameters are used. The Phase congruency map produces a normalised map which highlights the location of the discontinuity precisely, irrelevant of contrast.

INPUT	OUTPUT
Selected displacement field orientation (i.e. $\boldsymbol{FOFC\_Uy}$)	Phase congruency map (PC)
λ_{min} (Default: 4) ($\boldsymbol{PC1}$)	
d_{PC} (Default: 1.2) ($\boldsymbol{PC2}$)	

Table 11 Input and Output table for PC-CD Step 10 – Phase Congruency

3.9.12 Step 11 – Region-based active contour algorithm

The Region-based active contour algorithm (see section 3.8.1) is used on the Phase congruency map to mask the location of the data points that contain the discontinuity highlighted by PC. The constructed initial mask in Step 9 is used to help localise and segment the discontinuity iteratively until an optimum segmentation is reached. The active contour algorithm outputs a binary field indicating the crack segmentation and the boundaries of the segmentation is utilised to calculate crack parameters such as COD, crack path and crack tip.

The current representation of the segmentation algorithm requires two additional parameters: maximum number of iterations, (Itern), and the weight of smoothing term, (α_{seg}), which controls how smooth the segmentation contour can be. The Itern parameter must be set high enough for the segmentation algorithm to reach an optimum. The default value for Itern is 200. It is important to note that the better the initial mask, the quicker the optimal segmentation is reached. A code was developed that triggers the end of the iteration process automatically once it detects there is no change in the segmentation, which will negate the requirement of the Itern input parameter. It was observed α_{seg} does not influence the crack parameters, therefore it is not required to be changed, the default value is set to $\alpha_{seg} = 0.8$.

Figure 3.12b shows the first iteration of the segmentation, where Figure 3.12a is used as the map to segment and Figure 3.11d is used as the initial mask. The green line shows the boundary of the segmentation. To see how the segmentation changes over iteration, the crack tip location depicted by the white box in Figure 3.12b is observed closely. Figure 3.12c shows how the segmentation adapts to the Phase congruency ridge at iterations 5; 10; 20; and 50 as the segmentation grows until an optimal segmentation is reached. The segmentation is concluded as it is observed there is no segmentation change between iteration 50 and 100. The default Itern parameter was 200. The output of this step is shown in Figure 3.13a where a segmentation of the discontinuity is constructed.

INPUT	OUTPUT
Phase congruency map (PC)	Segmentation of the discontinuity ($CrackMask$)
Initial discontinuity mask ($InitialMask$)	
Maximum number of iterations $(SEG1)$ $(Default = 200)$	
α_{seg} $(SEG2)(Default = 0.8)$	

Table 12 Input and Output table for PC-CD Step 11 – Region-based active contour algorithm

CRACK PARAMETER EXTRACTION

The segmentation mask gained from the segmentation algorithm identifies the boundaries of the crack faces in the displacement field and can give very valuable information with regards to the crack parameters, Figure 3.13b. Upper and lower boundaries of the crack faces coupled with the displacement field information can give the opening displacement of the crack in Mode I, Mode II and Mode III. The same segmentation mask of the discontinuity of the data point location is combined in co-ordinate space with Phase congruency's sub-data point accuracy and can give the exact location of a feature. However, the crack path and crack tip location are based on the feedback given by the displacement field. The placement of the crack path is an estimated location of actual positions and is very much dependant on data point spacing. The data point spacing is controlled by the DIC parameter, step size.

INPUT	OUTPUT
Segmentation mask of the discontinuity **($CrackMask$)**	Crack opening displacement ($CODUx, CODUy, CODUz$)
Filled Displacement field (FC_Ux, FC_Uy, FC_Uz) **or** ($FOFC\_Ux, FOFC\_Uy, FOFC\_Uz$)	Crack path (CP)
Co-ordinate space (C_X, C_Y)	Crack Length (CL)
Selection of orientation **(i.e. *Y-direction*)**	Crack tip positioning ($CTIP$)
Phase congruency **(PC)**	

Table 13 Input and Output table for the PC-CD – Crack parameter extraction procedure

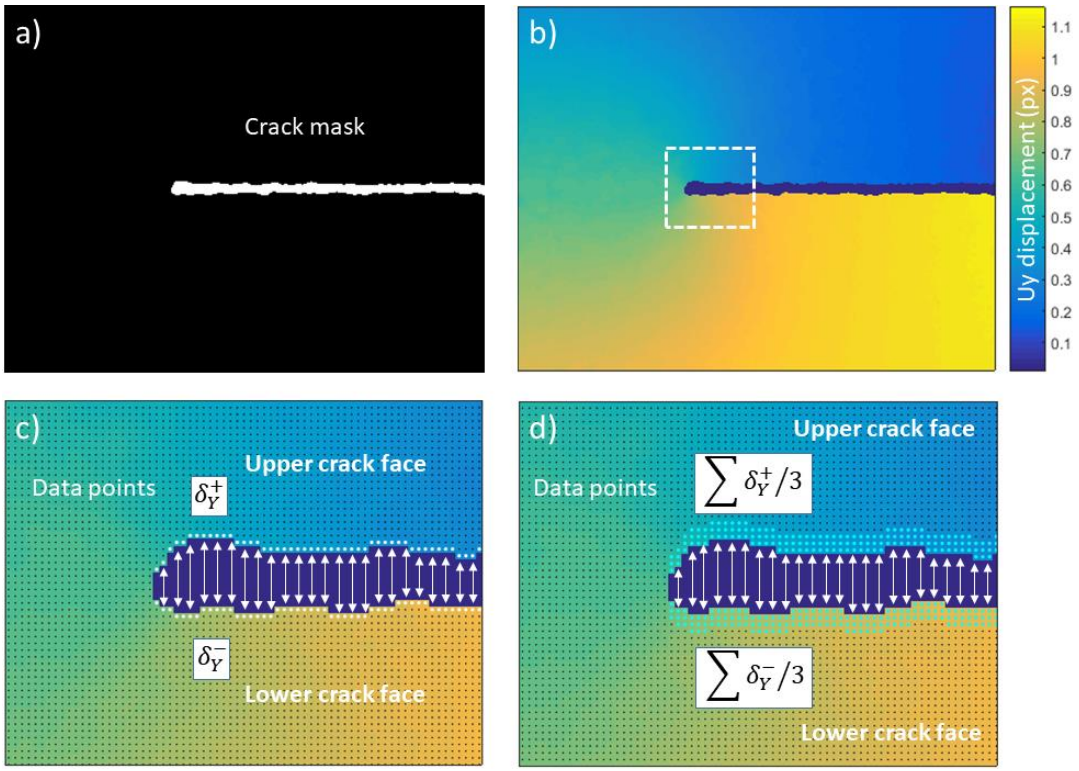

Figure 3.13 Crack segmentation and extraction of COD a) Crack Segmentation b) Crack Segmentation used to mask out FOFC_Uy (Figure 3.10c) c) Crack Opening Displacement configuration d) Three-point Crack Opening displacement configuration

3.9.13 Step 12 – Crack opening displacement

A crack boundary search algorithm is deployed on the given crack mask where the algorithm scans each column or row[5] and finds the boundary of the data points. The boundary data points are classified into upper and lower faces of the crack. Displacement data points at the boundary from opposite faces of the crack are subtracted from each other giving the crack opening displacement for that point.

$$CODUx = |\delta_X^+ - \delta_X^-| \quad (36)$$

$$CODUy = |\delta_Y^+ - \delta_Y^-| \quad (37)$$

$$CODUz = |\delta_Z^+ - \delta_Z^-| \quad (38)$$

Figure 3.13b shows a white rectangular area magnified on the crack tip; this is depicted in Figure 3.13c and d. Each black dot is a representation of a displacement data point that is unused in the calculation. White points show the identified boundary of the crack faces by the crack boundary search algorithm. The white displacement data points are classified as, δ_Y^+ for upper crack face and δ_Y^- for lower crack face. The data points at the boundary act as virtual clip gauges and Eq. (36)(37)(38) are used to calculate COD in the Ux, Uy and Uz displacement fields. If the crack orientation is parallel to an axis, the opening displacements directly represent the opening modes (e.g. Mode I crack opening).

White arrows in Figure 3.13(c and d) show the opposite data points at each side of the crack face that are employed to calculate COD for each $x -$ axis data point. To be able to handle nosier displacement fields, a three data point COD is given as an option to the user. The idea is, the three data points from each crack face are taken and averaged to increase the tracked subset area to obtain a better approximation for smaller subset sizes. Eq. (39)(40)(41) are used to calculate the three point COD.

[5] Row or Column depending on the orientation of the crack (Vertical/ Horizontal)

$$CODUx3P = \left|\sum \delta_X^+/3 - \sum \delta_X^-/3\right| \quad (39)$$

$$CODUy3P = \left|\sum \delta_Y^+/3 - \sum \delta_Y^-/3\right| \quad (40)$$

$$CODUz3P = \left|\sum \delta_Z^+/3 - \sum \delta_Z^-/3\right| \quad (41)$$

Figure 3.13(c and d) show an example; a single data point depicted by white dot versus three data points shown by the cyan data points, respectively.

Mode I Crack opening displacement profile of both methods are shown in Figure 3.14a. It is seen that single point and $3-$ point average COD present a similar COD profile which is confirmed with an RSME (Root Square Mean Error using Eq. (52)) value of 0.007 pixels. The same data points depicted in Figure 3.13(c and d) are used to calculate Mode II and Mode III COD by utilising Ux and Uz displacement fields respectively.

INPUT	OUTPUT
Segmentation mask of the discontinuity ($\boldsymbol{CrackMask}$)	Crack opening displacement ($CODUx, CODUy, CODUz$)
Filled Displacement field ($\boldsymbol{FC\_Ux, FC\_Uy, FC\_Uz}$) **or** ($\boldsymbol{FOFC\_Ux, FOFC\_Uy, FOFC\_Uz}$)	(Optional) 3-point average - Crack opening displacement ($CODUx3P, CODUy3P, CODUz3P$)
Selection of orientation (i.e. *Y-direction)*	

Table 14 Input and Output table for PC-CD Step 12– Crack opening displacement

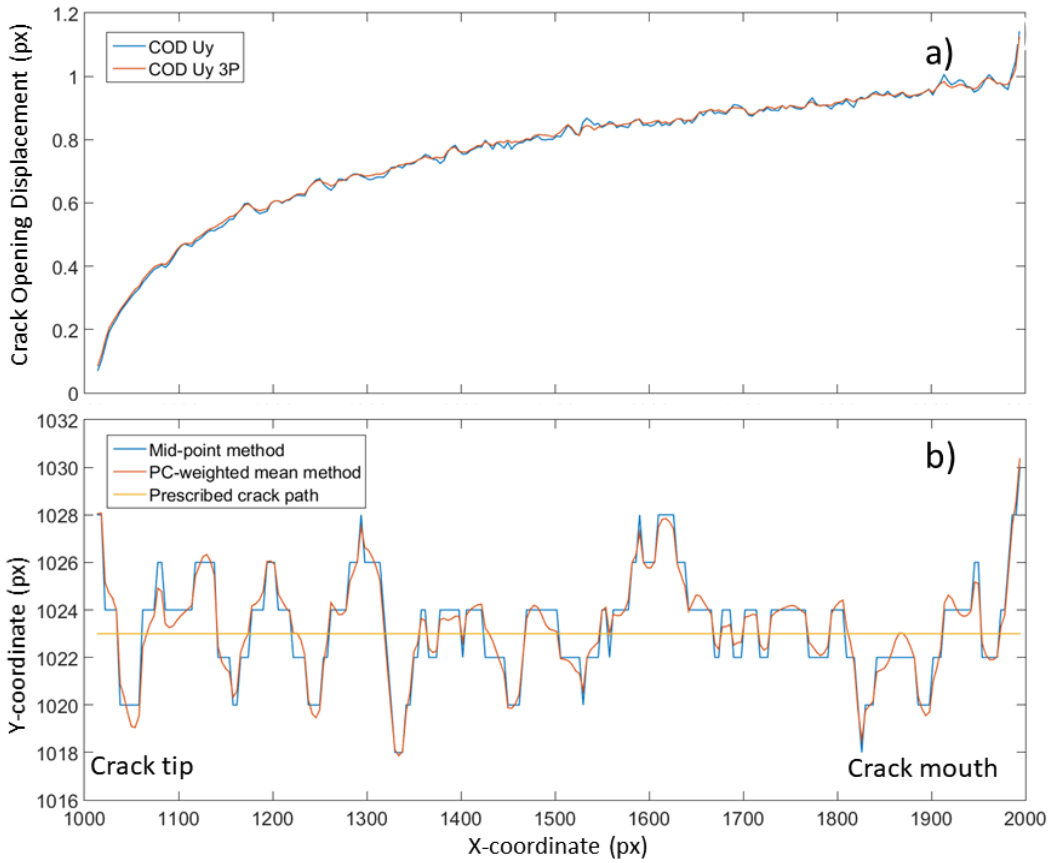

Figure 3.14 Extracted crack parameters a) Mode I Crack opening displacement b) Crack location

3.9.14 Step 13 – Crack path

Two different methods of approximating the crack path location from the crack mask are shown in this step. A mid-point method has been used throughout this work while a PC weighted-mean method is presented as an option, but its performance has not been further studied in this thesis.

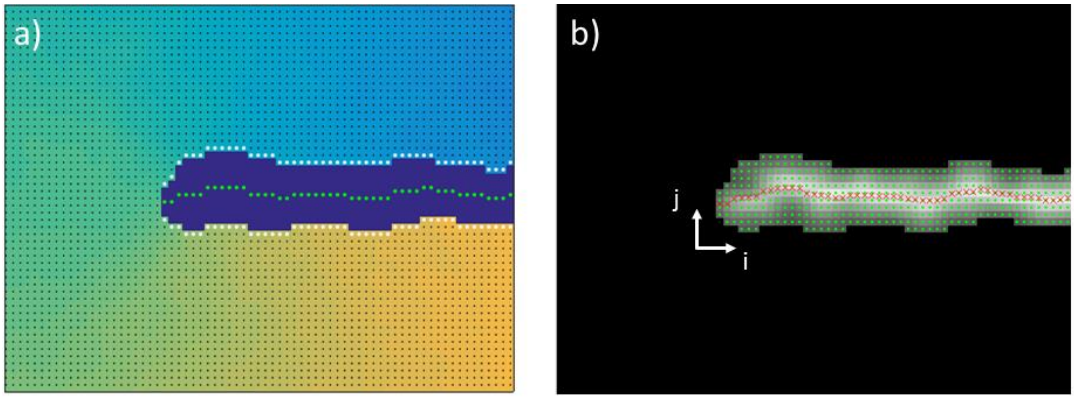

Figure 3.15 Crack path configuration a) Mid-point method b) PC weighted-mean method

MID-POINT METHOD

The following assumption is made regarding the crack path. The approximate location of the crack path is at the mid-point of the upper and lower crack faces. Crack boundary search algorithm is deployed again, and the upper and lower faces of the crack are classified. The data point coordinates[6] at the boundary are used to calculate the virtual mid-point between the crack faces.

The example crack path configuration is shown in Figure 3.15a, where the white dots represent the upper and lower crack face boundary and the computed mid-point of the crack faces is shown by the green points.

Another method that approximates the crack path location is provided in the appendix (see Appendix G), using a weighted mean method and taking advantage of Phase congruency's sub-point edge locator. PC-weighted-mean method has been demonstrated in Figure 3.15b.

INPUT	OUTPUT
Segmentation mask of the discontinuity ($\boldsymbol{CrackMask}$)	Mid-point crack path approximation (CPX, CPY)
Selection of orientation (i.e. $\boldsymbol{Y}$-direction)	(*Optional*) PC-weighted mean crack path approximation (WM_CPX, WM_CPY)
Co-ordinate space $(\boldsymbol{C\_X}, \boldsymbol{C\_Y})$	
(*Optional*) Phase congruency ($\boldsymbol{PC}$)	

Table 15 Input and Output table for PC-CD Step 13 – Crack path

[6] Co-ordinates are in pixels if in image space or mm if calibrated in real world space

3.9.15 Step 14 – Crack length

Both the crack tip location and the crack length calculation use the crack path parameter obtained from Step 13. Crack tip location is simply the end point of the crack path parameter as shown by Eq. (42). The crack length can be determined by simply calculating the Euclidean distance between the two end points from the crack path parameter as shown by Eq. (43).

$$Crack\ tip = (CPX_n,\ CPY_n) \quad (42)$$

$$Crack\ length = \sqrt{(CPX_n - CPX_1)^2 + (CPY_n - CPY_1)^2} \quad (43)$$

$$P2P\ Crack\ length = \sum_{i=1}^{n-1} \sqrt{(CPX_{i+1} - CPX_i)^2 + (CPY_{i+1} - CPY_i)} \quad (44)$$

where n is the last crack path co-ordinate and CPX and CPY are the crack path locations in the X axis and Y axis respectively.

In an ideal situation, the crack length would be the summation of the Euclidean distance between each crack path data point as shown by Eq. (44)(P2P = Point to Point). However, the accuracy of the crack path using the PC-CD is very limited in displacement data point space and the additional convolutions (as observed in Figure 3.14b) can add a degree of uncertainty to the determined crack length by Eq. (44). Eq. (43) can give a better approximation to the crack length as the calculation makes the assumption the crack takes the shortest path between the crack mouth and crack tip.

The prescribed crack tip position on the virtual data was half way across the image, which means the prescribed crack tip location is at $(1012, 1023)$ in pixel coordinate space. The PC-CD has calculated the crack tip location to be $(1012, 1028)$, which is an exact error of 5 pixels while the crack length error is calculated to be $\sqrt{2}$ pixels.

INPUT	OUTPUT
Crack Path approximation ($\boldsymbol{CPX}, \boldsymbol{CPY}$)	Crack length (CL)
	Crack tip location ($CTIP$)

Table 16 Input and Output table for PC-CD Step 14 – Crack length

3.10 Volume Phase Congruency based Crack Detection

The PC-CD algorithm has been developed and refined to detect a single discontinuity in volume displacement fields. The volume crack detection procedure will require Digital Volume Correlation parameters to be selected carefully and optimally. The displacement field fed into the algorithm can segment the discontinuity boundary in three-dimensional space. Careful optimization of DVC parameters such as cubic voxel size, overlap, different passes and uncertainty have been studied previously [178-182]. Using the segmentation boundaries and volume displacement field, the algorithm outputs the crack surface location, crack opening displacement in the thickness and the crack front. Better optimized DVC results are obtained if the user rotates the volume image in two axis orientations so that the expected crack surface is parallel to one of the axis planes. Similar with the surface crack detection application, better displacement measurements are achieved at voxels close to the crack faces. The rotation also allows for the separation of different modes of fracture and may help achieve good discontinuity signal to noise ratio, channelling the discontinuity signal into a single orientation.

The two-dimensional DIC algorithm is established and entails more accurate results than a conventional DVC algorithm. The well-established DIC algorithm uses a second-order shape functions to tailor the shape of the subset to match to the deformed subset. An optimized subset shape is reached using an accurate least square matching procedure method with a conventional accuracy of less than $1/100$th of a pixel [183]. However, the same optimization algorithms are not available with a conventional DVC algorithm mostly due to the computational complexity. Instead a Fast Fourier Transform (FFT) [184] method is utilised to quickly compute the translation and stretch parameters using the convolution theorem of each cubic subset. Considering the “quick and dirty” approach, DVC algorithms have a displacement precision of above $1/20$th of a pixel, considering, the DVC is still computationally, an expensive algorithm.

The idea behind Volume Phase Congruency based Crack Detection (VPC-CD) algorithm is very similar to the surface version, however, there are a few fundamental differences to consider. While the surface algorithm is designed to detect and quantify discontinuity with a two-dimensional data point field, the volume algorithm cannot detect cracks, but can only segment the crack but with three-dimensional data points. Each data point within the three-dimensional space carries displacement information in three special axis orientations; Ux, Uy and Uz. A single displacement orientation that carries the highest discontinuity signal is selected for crack detection and segmentation. Therefore, the key PC-CD algorithm components such as Outlier deletion, recovery of missing data, Phase congruency, Region-based active contour and crack parameter extraction are developed to extract discontinuity from a volumetric displacement field. Due to the nature of the sluggish data acquisition of volume images and high computational time complexity of Digital Volume Correlation, users are rarely tasked to detect cracks from large number datasets. Therefore, a volumetric automatic initial mask selection has not been developed for the proposed algorithm and can be a task in future work.

To act as a replacement for the automatic initial mask procedure, the user is required to interact with the algorithm and select a seeding point which will act as the initial mask instead.

Figure 3.16 depicts the skeleton sketch of the PC-CD algorithm.

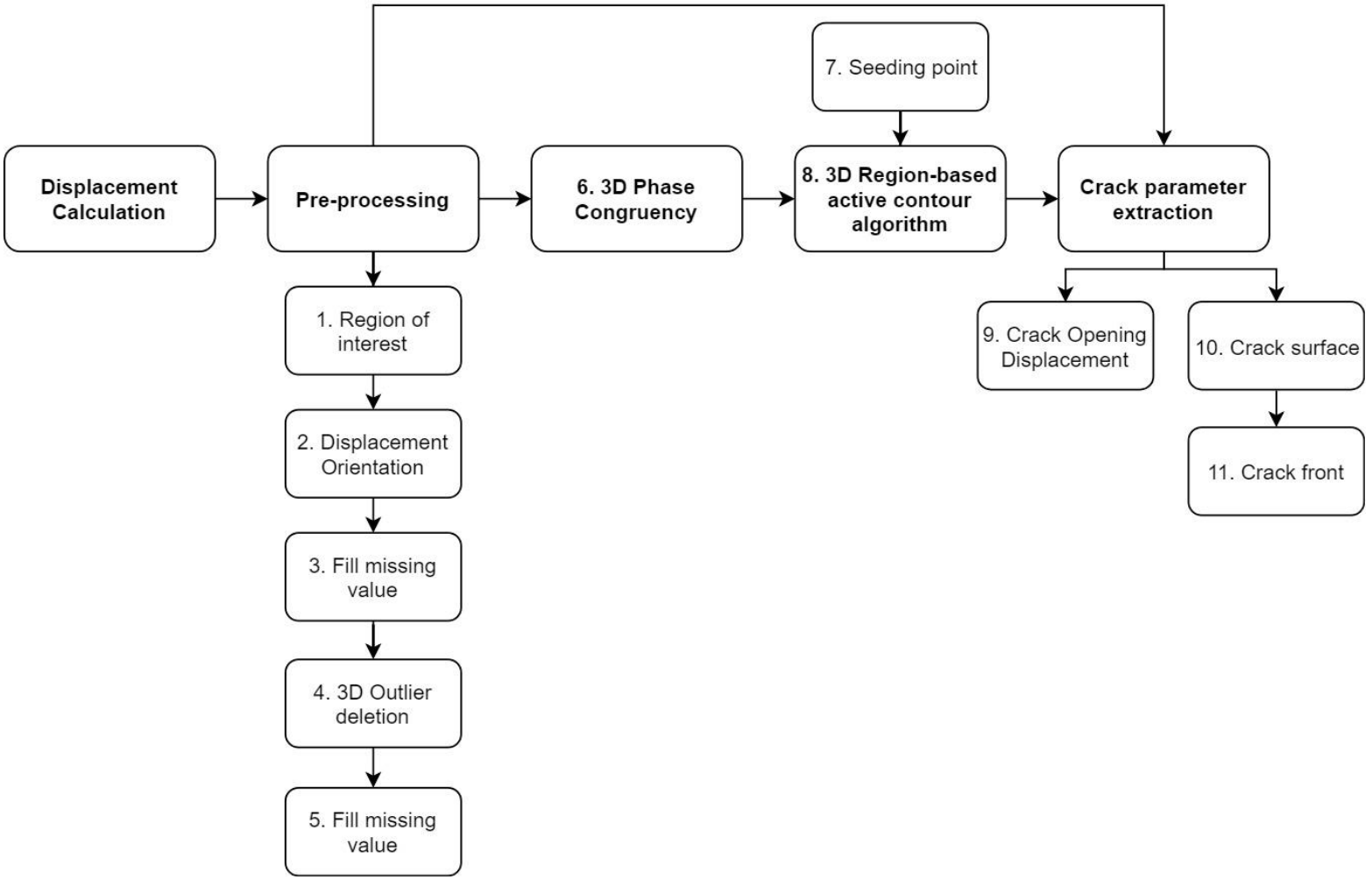

Figure 3.16 Volumetric Phase congruency based Crack Detection Algorithm (VPC-CD)

The dataset presented in section 6.2.2, Ductile Material: Al-Ti Metal matrix composite with short notch (i.e. $a/W = 0.1$) was used as an example dataset to depict how the VPC-CD algorithm flows. Figure 3.17 depicts the deformed tomograph image of the Al-Ti with short notch. The dimension of the tomograph measures $2150 \times 1300 \times 2000$ with a voxel size of $3.25\ \mu m$.

PRE-PROCESSING

The volume displacement field data of the cracked body contains a six-column vector information. The first three columns are representative of the location of a single data point in X, Y and Z axis while the last three are representative of the displacements in Ux, Uy and Uz directions of the same data point. An algorithm is used to construct a volumetric data point space of X, Y and Z co-ordinates and Ux, Uy and Uz displacement data. The procedure shown in the surface crack detection is replicated in the three-dimensional application.

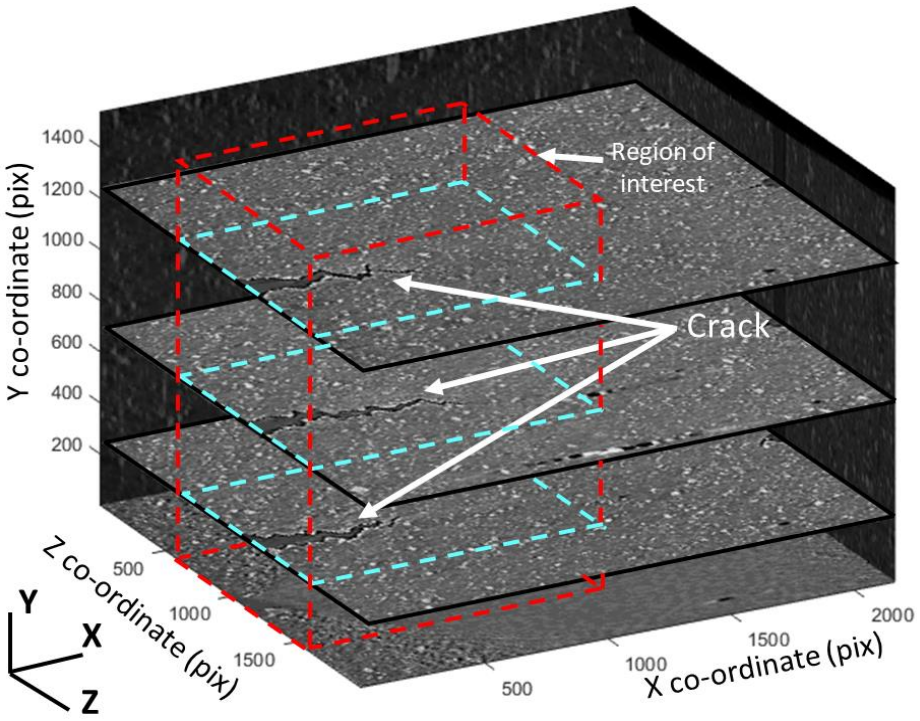

Figure 3.17 Selection of ROI in a volume image

3.10.1 Step 1 – Region of Interest

The user selects a region of interest in three co-ordinate spaces to not only remove outliers caused by the edge effect but also to save computational time. This is important because the dimension size of the data increases the time complexity and data reduction will be necessary to save computational time. Data points localised to the discontinuity are considered to calculate the crack geometry therefore a smaller region of interest can be selected to save computational time.

The imported dimension of the cracked body is $175 \times 213 \times 150$, in the data point scale. The deformed tomograph exhibited two cracks, as seen in Figure 3.17, both propagating behind the notches of the sample. For the following example, the longer crack is centralised for the demonstration of VPC-CD. The region of interest (ROI) can be specified in data point space but in this instance, the ROI was determined in the tomograph, before DVC analysis. The ROI is identified by the red dotted cuboid projected on the deformed tomograph image Figure 3.17. Three XZ – plane slices at locations; $Y = 250, 700$ and 1250 are shown to enable a visualisation through the thickness of the sample, and the progression through the crack analysis through the following steps. The RIO of the displacement slices are the cyan dashed areas.

INPUT	OUTPUT
Volume displacement field $(\boldsymbol{Ux}, \boldsymbol{Uy}, \boldsymbol{Uz})$	Cropped volume displacement field (C_Ux, C_Uy, C_Uz)
Volume co-ordinate space $(\boldsymbol{X}, \boldsymbol{Y}, \boldsymbol{Z})$	Cropped volume co-ordinate space (C_X, C_Y, C_Z)
Region of interest	

Table 17 Input and Output table for VPC-CD Step 1 – Region of Interest

3.10.2 Step 2 – Displacement orientation

The user is required to select the displacement orientation that carries the highest discontinuity signal, which is selected to be the displacement data for crack segmentation. For mode I cracks, the highest discontinuity signal exists in the orientation normal to the crack surface. Selected orientation information also plays a role in constructing the volume Phase congruency map.

The displacement volume is sliced into individual two-dimensional slices where the expected crack surface orientation is required to be known. The crack surface orientation also plays a role in the extraction of the crack parameters. The cropped volume displacement fields can be previewed by the user in this step to help determine the surface orientation of the crack, consequently selection of displacement discontinuity signal field.

The crack surface is parallel to the XY – plane, as seen in Figure 3.17. Therefore, for a mode I crack, the discontinuity signal is in the Uz displacement field.

INPUT	OUTPUT
Masked volume displacement field ($\boldsymbol{C\_Ux}, \boldsymbol{C\_Uy}, \boldsymbol{C\_Uz}$)	Selection of discontinuity orientation (i.e. *Z-direction*)

Table 18 Input and Output table for VPC-CD Step 2– Displacement orientation

3.10.3 Step 3 – Fill missing value

All cropped volume displacement field orientations (i.e. C_Ux, C_Uy, C_Uz) were applied the extrapolation to recover the missing data points that may have been removed from the DVC calculation as discussed in section 3.6. The *inpaintn* algorithm was used as the default configuration. Figure 3.18a shows an extrapolated Uz displacement field using the *inpaintn* algorithm.

INPUT	OUTPUT
Volume displacement fields ($\boldsymbol{C\_Ux}, \boldsymbol{C\_Uy}, \boldsymbol{C\_Uz}$)	Filled volume displacement fields (FC_Ux, FC_Uy, FC_Uz)

Table 19 Input and Output table for VPC-CD Step 3– Fill missing value

3.10.4 Step 4 – 3D Outlier deletion

Outlier deletion (section 3.5), step 4 and 5, is an optional procedure that can be skipped. In the following example shown in Figure 3.18, it was observed that the outlier deletion improves the erroneous displacement values caused by the crack artefact and there it is recommended for dataset that have a significant crack opening.

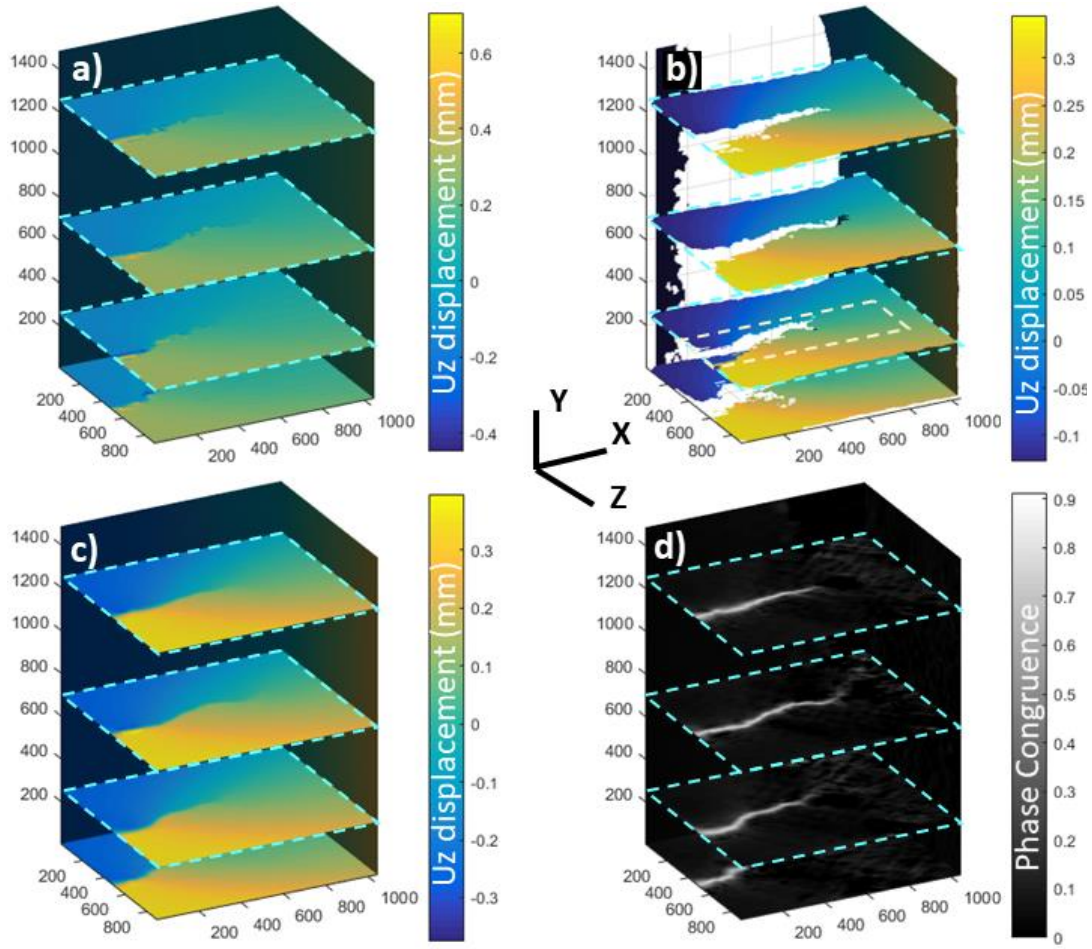

Figure 3.18 Pre-processing & Volume Phase congruency a) Cropped Uz displacement field, b) Outlier deletion applied to a), c) Extrapolation of b), d) Volume Phase congruency of c)

Figure 3.18b depicts where an outlier deletion filter has been applied to the Uz displacement field. The outlier deletion parameters for window size (ODw) and threshold parameter (ODt) were chosen to be to be 20 and 0.001, respectively, after several trials. It can be observed the outlier deletion method has removed the spurious values as described. The outlier deletion was also applied to the Ux and Uy displacement fields.

INPUT	OUTPUT
Volume displacement fields $(\boldsymbol{FC\_Ux}, \boldsymbol{FC\_Uy}, \boldsymbol{FC\_Uz})$	Outlier deleted volume displacement field (OFC_Ux, OFC_Uy, OFC_Uz)
Outlier Deletion Window size $(\boldsymbol{ODw})$	
Outlier Deletion Threshold parameter $(\boldsymbol{ODt})$	

Table 20 Input and Output table for VPC-CD Step 4– 3D Outlier deletion

3.10.5 Step 5 – Fill missing value

In this step, the outlier deleted displacement data point values are recovered using *inpaintn* (see section 3.6).

Figure 3.18c shows the extrapolated Uz displacement field using the *inpaintn* algorithm. The applied outlier filter shows an improvement between the before and after outlier filter was applied. The maximum value has decreased from 0.1 to 0.06 while the minimum value has increased by 0.03. The further evidence of an improvement of the displacement field is the sharpened contrast of the filter, improving the signal to noise ratio of the displacement field while preserving the discontinuity.

INPUT	OUTPUT
Volume displacement fields $(\boldsymbol{OFC\_Ux}, \boldsymbol{OFC\_Uy}, \boldsymbol{OFC\_Uz})$	Filled volume displacement fields $(FOFC\_Ux, FOFC\_Uy, FOFC\_Uz)$

Table 21 Input and Output table for VPC-CD Step 5– Fill missing value

3.10.6 Step 6 – Volume Phase Congruency

The Volume Phase Congruency (VPC) map is constructed using the discontinuity displacement signal field as selected in Step 2. The user will need to select the thickness axis of the specimen to determine the slice indexing as discussed in section 3.3. In the following example, the thickness of the sample is parallel to the crack front (e.g. $Y-$ axis) and therefore the displacement slices are deconstructed to the $XZ-$ plane.

The 2D Phase congruency algorithm is adopted slice by slice where the parameters $\lambda_{\min}$ and $\mathrm{d_{PC}}$ can have values ranging between $2-10$ and $0.8-1.6$ respectively. Both parameters will require to be kept constant for each slice calculation.

Volume Phase congruency was applied to the Uz displacement field (i.e. FOFC_Uz) the slice orientation of the XZ – plane using the default 2D Phase congruency parameters of $\lambda_{\min} = 4$ and $\mathrm{d_{PC}} = 1.2$. The slices are combined to construct the Volume Phase congruency map shown in Figure 3.18d

INPUT	OUTPUT
Selected volume displacement orientation	Volume Phase congruency (VPC)
$\boldsymbol{\lambda_{min}}$ **(Default** $= \mathbf{4}$**)** ($\boldsymbol{PC1}$)	
$\mathbf{d_{PC}}$ **(Default** $= \mathbf{1.2}$**)** ($\boldsymbol{PC2}$)	

Table 22 Input and Output table for VPC-CD Step 6– Volume Phase Congruency

3.10.7 Step 7 – Seeding point

The automatic initial crack mask procedure is replaced with a user interaction based seeding point where the user is given a graphic visualization of the Volume Phase congruency (VPC) map. The user is then required to select a single data point that is the subset of the discontinuity which is highlighted by Phase congruency. The co-ordinates of the selected data point are used to construct an initial mask. A binary matrix is created with the same volume size of VPC map where the seeding point is padded by one voxel creating an initial mask size of $3 \times 3 \times 3$.

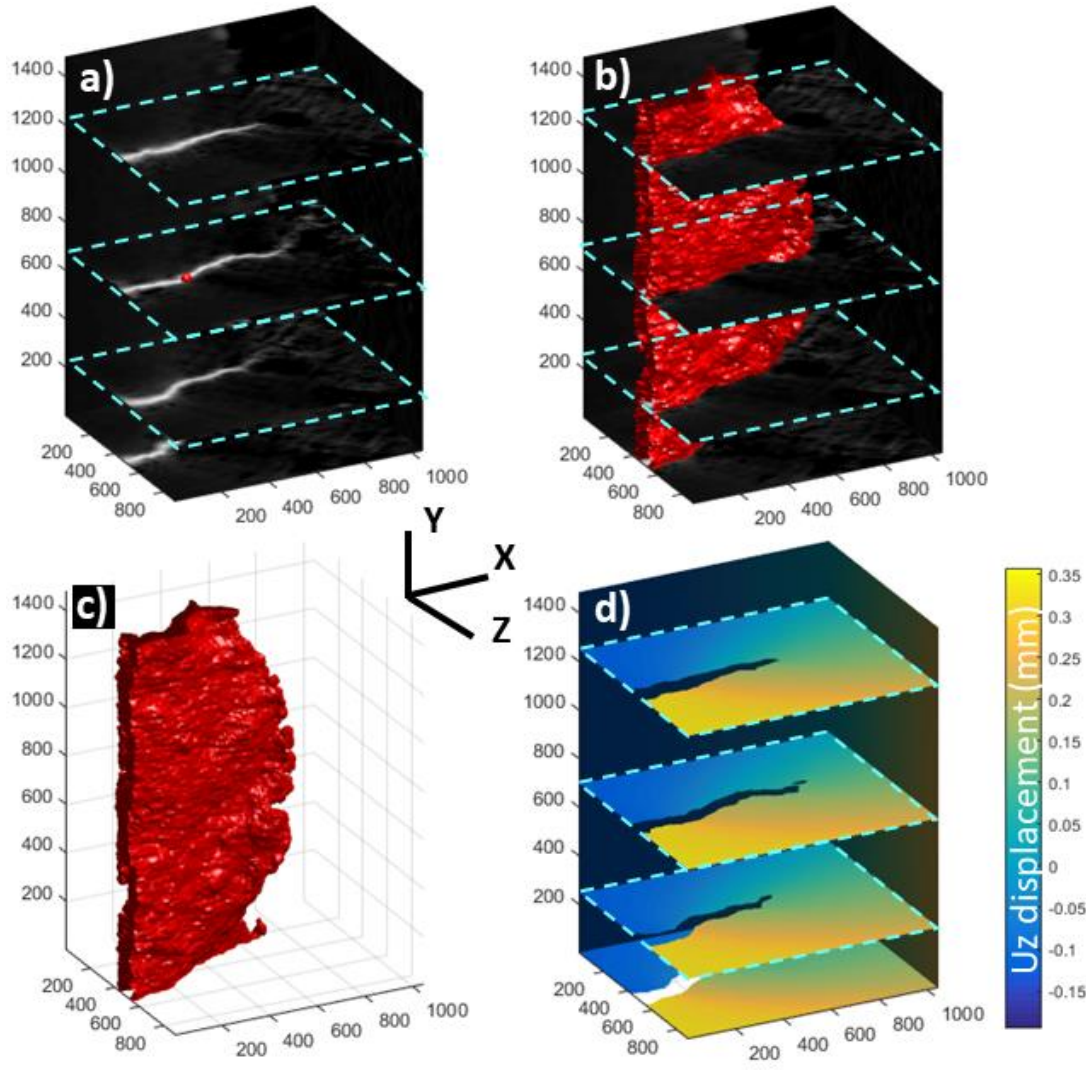

Figure 3.19 Volume crack segmentation procedure a) Selection of seeding point (VInitialMask) on VPC map b) Active contour segmentation overlay on the VPC map c) Segmentation of the discontinuity (VCrackMask) d) Segmentation used to mask out FOFC_Uz (Figure 3.18)

The Volume Phase congruency (see Figure 3.18d) is graphically shown to the user where the seeding point location is identified as $(276, 700, 948)$ in the (x, y, z) pixel axis as shown by the red segment in Figure 3.19a.

INPUT	OUTPUT
User selected seeding point **(*Data point co-ordinate space*)**	Initial mask ($VInitialMask$)

Table 23 Input and Output table for VPC-CD Step 7– Seeding point

3.10.8 Step 8 – 3D Region-based active contour algorithm

The Active contour method described in section 3.8.2 is used to segment the discontinuity in three-dimensional space from the Volume Phase congruency map. While the segmentation algorithm requires seven input parameters, only three are interacting with the algorithm; Volume Phase congruency map, initial mask and maximum number of iterations. The propagation field and the gradient field are calculated using the Volume Phase congruency information and are an input to calculate the Chan-vese and GAC terms respectively to produce the hybrid model. The hybrid model requires the respective weights which are kept at their default values, $\alpha_{\mathrm{seg}} = 0.015$ and $\beta_{\mathrm{seg}} = 0.02$. The user selected mask in Step 7 is used iteratively to grow the segmentation until the segmentation growth becomes stagnant and an optimum segmentation mask is reached. An optimum segmentation mask can be achieved either with a high iteration number to allow a convergence or the user terminates once segmentation growth stagnation is observed, to avoid unnecessary computational iterations.

The VPC map and the seeding point are used as inputs (see Figure 3.19a) for the active contour algorithm and default parameters. After 364 iterations, the segmentation growth becomes stagnant and therefore the loop is terminated to save computational time. Figure 3.19b shows the volume segmentation of the discontinuity ridge superimposed with the volume Phase congruency map. The segmentation is observed to have correctly identified the outer regions of the highlighted discontinuity.

INPUT	OUTPUT
Volume Phase congruency ($\boldsymbol{VPC}$)	Volume segmentation mask of the discontinuity ($VCrackMask$)
Initial mask for segmentation ($\boldsymbol{VInitialMask}$)	
Maximum number of iterations $\boldsymbol{(Itern)\ Default = 200}$	

Table 24 Input and Output table for VPC-CD Step 8 – 3D Region-based active contour algorithm

CRACK PARAMETER EXTRACTION

Volume crack segmentation allows the identification of the virtual crack surface created by the Digital Volume Correlation displacement field. Utilising the boundaries of volume segmentation of the crack in volume space with the displacement components and data point co-ordinates can allow the calculation of very valuable and comprehensive crack geometry. Crack opening displacement in the thickness of the crack can be calculated to paint valuable information as to the plane stress and plane strain conditions of a cracked body. The procedure of extracting the crack geometry from a volume displacement field can be accomplished by treating the volume segment in two dimensional slices and applying the two dimensional crack parameter extraction method described in sections 3.9.13, 3.9.14 and 3.9.15.

INPUT	OUTPUT
Volume segmentation mask of the discontinuity ($\boldsymbol{VCrackMask}$)	Crack opening displacement in the thickness ($CODUx, CODUy, CODUz$)
Filled volume displacement field ($\boldsymbol{FC\_Ux, FC\_Uy, FC\_Uz}$) **or** ($\boldsymbol{FOFC\_Ux, FOFC\_Uy, FOFC\_Uz}$)	Crack surface (CS)
Co-ordinate space ($\boldsymbol{C\_X, C\_Y, C\_Z}$)	Crack length (CL)
Selection of orientation (i.e. $\boldsymbol{Z-direction}$)	Crack front (CF)

Table 25 Input and Output table for VPC-CD–Crack parameter extraction procedure

3.10.9 Step 9 – Crack opening displacement

The volume crack boundary search algorithm is deployed on the crack mask where the algorithm first deconstructs the volume into individual slice segments based on the thickness and the index slicing orientation of the construction of VPC. The Crack boundary search algorithm is applied iteratively where the algorithm classifies the upper and lower face of the crack for each slice. The data points at the boundary for each slice helps with the calculation of the crack opening displacement profile of each slice. The Crack opening displacement profiles are then combined for each slice to obtain an overall volume crack opening displacement in the thickness of the cracked body. The default setting of obtaining COD is using a single data point method from opposite sides of the crack. The same process is applied to all displacement orientations to obtained Mode I, Mode II and Mode III crack opening.

The volume segmentation of the discontinuity ($VCrackMask$) is removed from the $FOFC\_Ux, FOFC\_Uy, FOFC\_Uz$ displacement field where Figure 3.19d shows the latter as an example. All the displacement orientations are deconstructed to XZ – plane slices where $Y-$ axis is the thickness of the specimen and Crack boundary search algorithm is deployed. The COD is calculated for each $XZ-$ plane slice using the methodology from section 3.9.13. Each slice is representative of a single COD measurement of a unit thickness. The COD in the thickness for Ux, Uy and Uz are shown in section 6.2.2, (page number 173), Figure 6.6(b, c and a) in that order. It is seen that the highest crack opening signal is in the Uz orientation which validates the Mode I opening. Also seen in each respective data, the COD profile varies through the thickness of the specimen compared to the specimen surface observation.

INPUT	OUTPUT
Volume Segmentation mask of the discontinuity ($\boldsymbol{VCrackMask}$)	Crack opening displacement ($CODUx, CODUy, CODUz$)
Filled Displacement field ($\boldsymbol{FC\_Ux, FC\_Uy, FC\_Uz}$) **or** ($\boldsymbol{FOFC\_Ux, FOFC\_Uy, FOFC\_Uz}$)	
Selection of orientation (i.e. $\boldsymbol{Z-}$ ***direction*****)**	

Table 26 Input and Output table for VPC-CD Step 9– Crack opening displacement

3.10.10 Step 10 – Crack surface

Once again, the volume crack boundary search algorithm is deployed in the same slice orientation as previously. The crack boundary information is used to find the mid-point crack path location at each slice using the method described in section 3.9.14. The crack path location for each slice is then combined to obtain the crack surface. A PC-weighted crack path method was not developed due to the limitations of the DVC algorithm, discussed in section 2.3.3.

The volume segmentation of the crack (see Figure 3.19c) is used to identify the boundary of the crack in the co-ordinate system and is deconstructed into slices of the XZ – plane. The crack path is found in each individual slice using the mid-point method and is combined to construct a crack path through thickness which enables the approximation of the crack surface as shown in Figure 6.4. The crack surface is presented by $Z -$ axis elevation.

INPUT	OUTPUT
Volume segmentation mask of the discontinuity ($\boldsymbol{VCrackMask}$)	Crack surface approximation (CS) [Mid-point method]
Selection of orientation (i.e. $\boldsymbol{Z-direction}$)	
Co-ordinate space ($\boldsymbol{C\_X, C\_Y, C\_Z}$)	

Table 27 Input and Output table for VPC-CD Step 10 – Crack surface

3.10.11 Step 11 – Crack front

The crack surface parameter obtained in the previous step is used to calculate additional crack geometrical parameters, such as crack tip location through the thickness or crack front and crack length. Depending on the experimental conditions of the fracture (i.e. fatigue crack growth, material parameter) the crack length and crack tip location can vary over the thickness of the cracked body, usually in situations when a material is under plastic deformation.

In the case of defining cracks from volume measurements, the true crack tip location or the true crack length can be defined by the longest crack length over the thickness of the observed cracked body. Therefore, the crack front location is a useful parameter that can be obtained from the previous step for non-linear fracture mechanics. The crack front location is the crack tip of each slice over the thickness of the specimen. The same methodology prescribed in section 3.9.15 is applied to the crack surface parameter, but in individual slices through the defined thickness.

	OUTPUT
Crack surface approximation ($\boldsymbol{CS}$)	Crack length (CL)
	Crack tip location ($CTIP$)
	Crack front (CF)

Table 28 Input and Output table for VPC-CD Step 11 – Crack front

3.11 Crack Characterisation

The ability to characterise and quantify the conditions that will propagate a crack is a critical requirement of fracture mechanics. Although the geometrical parameters of a crack can be used to better understand the structural integrity, additional calculations are required to determine if a cracked component is safe. A novel method has been developed by Dr Selim Barhli [2] where the use of Digital Image Correlation and finite element simulation can be combined to extract the strain energy release rate of a surface measurement of a cracked body. The author of this thesis has been collaborating for the development of the OUR-OMA (Oxford University Reinjection-Optimized Meshing Add-on) and is second author on his paper.

The approach uses a finite element model with imported full-field displacements, measured by DIC and J-integral is calculated, without the knowledge of the specimen geometry and applied loads. However, the algorithm needs the crack geometrical parameters to be fed into the code to calculate the J-integral: the segment of the crack path; low confidence region and free to deform region. The outputs from the PC-CD algorithm can be directly infused with OUR-OMA, removing user judgement and bias from the calculation. The objective is to be able to automatically and accurately extract the J-integral values from displacement measurements of a crack.

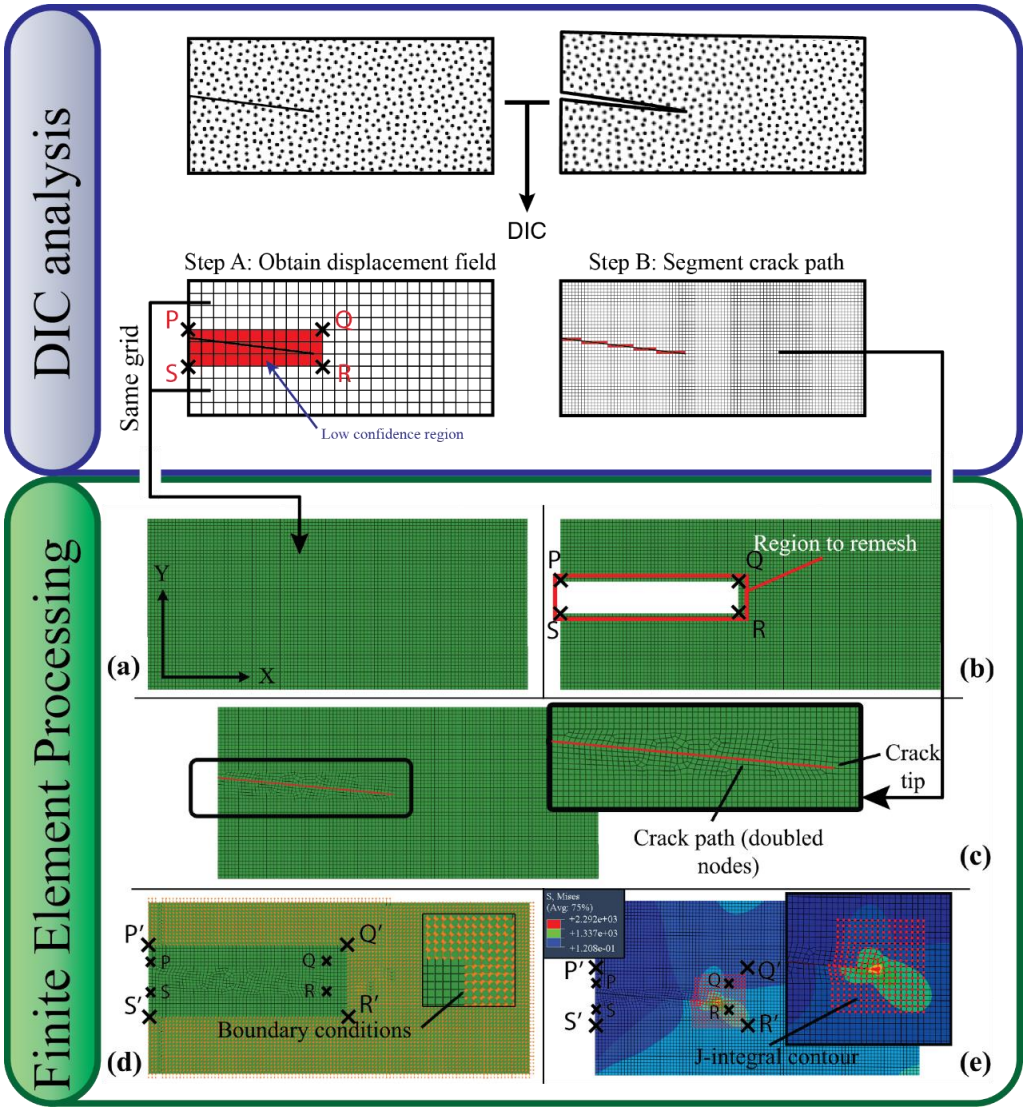

Figure 3.20: Steps of the J-integral calculation process; DIC Analysis – the displacement field is obtained in a two-step analysis with a coarse (step A) and fine (step B) subset size to map the field precisely and identify the crack path; Finite Element Processing - (a) FE mesh registered with the coarse DIC grid (b) The region containing the crack [PQRS] is deleted for re-meshing (c) The crack is inserted in the re-meshed region, nodes are doubled on the crack path (d) Boundary conditions are enforced on the FE nodes, except in the free region P'Q'R'S', which always includes the region PQRS, (e) The J-integral is calculated.[2]

OUR-OMA method requires a two-step DIC analysis: Step A, DIC analysis where a large subset size is used and accurate displacement information is calculated to obtain a better resolved FE model, and Step B, DIC analysis where small subset size is used to obtain high spatial resolution to find the crack location.

For the Step A analysis, the crack and its surroundings are masked (see box PQRS, Figure 3.20), so its discontinuity does not perturb the accuracy of the description of the displacement field that surrounds it. The mask is obtained by excluding those displacement vectors with low correlation coefficient (typically, for a good quality image, a correlation coefficient threshold of 0.8 is used). The crack mask can also be obtained by applying PC-CD to the crack tip field.

The Step B analysis is performed using a small subset size convenient to determine an accurate crack path and crack tip position on the reference grid.

After completing both steps, the vectors of the displacements in the plane of the surface of the sample have been determined with optimal precision (Step A). The data lie on a regular grid, which is not fully populated due to censoring (i.e. masking) of low quality DIC results in the vicinity of the crack. Other regions, remote from the crack, may also have missing values where the correlation quality is low, this may be due to loss of camera focus or parasitic light reflections in optical observations. The crack path has also been determined (Step B), and is described using a finer grid within the masked region.

A finite element approach is used to extract the J-integral from the DIC-measured displacement fields. This is done by importing the displacement field as a set of full field boundary conditions into a finite element model of the crack. A software tool (OUR-OMA) has been written to facilitate this; coded in Python, it runs inside the Abaqus software via its scripting capability[7]. A FE model is created that is registered with the DIC analysis results (see Figure 3.20a) so that the Step A DIC dataset and the FE model share the same coordinate system. Typically, as in the Davis software, the DIC coordinate system for a 2D-DIC analysis is that of the reference image, whilst for a 3D-DIC analysis, the coordinate system is that of the calibrated specimen surface. The spacing of the nodes of the FE mesh is chosen to be coincident with the Step A DIC result grid, using square elements.

[7] OUR-OMA (Oxford University Reinjection-Optimized Meshing Add-on): The software is available from the authors as a GUI or Command Line version, compatible with Abaqus version 6.10 to 6.1314. The GUI version, distributable as an Abaqus plugin, can deal with common experimental cases (e.g. straight cracks). The command line version is more versatile (e.g. kinked and curved cracks).

This registration and grid matching avoid the requirement for interpolation when subsequently applying the DIC displacement field to the FE mesh. The FE mesh is locally refined to insert the crack within the region where the Step A displacement vectors have been censored. A rectangular bounding box is defined that contains the crack and matches the masked region. This region is re-meshed separately using the Step B description of the crack path, with nodes doubled along the crack path to allow the crack to open. The mesh within the bounding box is attached to the nodes of the surrounding coarse mesh in the FE model (see Figure 3.20b and c). The mesh density at the crack tip is aimed to be 3 times finer than the Step A mesh, as a good mesh quality cannot be achieved if the mesh density difference is too large between the two regions. This is done using a constraint established in the FE pre-processer that allows the mesh density to change during meshing to converge towards the finest achievable mesh density with good quality elements[8].

The results from Step A are injected onto the model by enforcing node displacements to the measured displacement vectors. These local boundary conditions are applied everywhere except in a 'free' region that is free to deform in accordance with its surrounding boundary conditions and material properties. (see box P'Q'R'S', Figure 3.20d). This free region includes the re-meshed region (PQRS) that surrounds the crack and can be extended to further censor the Step A DIC dataset. After 'injecting' the displacement field data into the FE simulation using OUR-OMA, the FE software can be used to assign a material law to the model. Plane stress or plane strain elements may be used. In this thesis we have used the Abaqus FE software package and have examined both linear elastic and inelastic (Ramberg-Osgood) material laws, which are both compatible with the J-integral calculation.

[8] In Abaqus, this is done by selecting the "Allow the number of elements to increase only" constraint when defining the local mesh seeds. The minimum aimed mesh side, set to 1/3 of the Step A mesh density by default, can be modified at will.

The Abaqus software implements the domain integral method to calculate the J-Integral. It uses the Virtual Crack Extension method, which applies a virtual displacement field (Q-field) to increase the crack length by a small amount and so evaluate the change in strain energy. To define the Q-field properly, the software requires the definition of a Q-vector; this is normal to the crack front, and, if a 3D geometry is considered, also lies in the local plane of the crack. In the 2D model considered here, the Q-vector is chosen to be collinear with the linear segment of the crack path that is closest to the crack tip. The J-integral calculation is performed over several contours to check for contour independency, and thus retrieves the potential elastic strain energy release rate of crack propagation that is due to the measured displacement field (Figure 3.20e).

The current version of the OUR-OMA code has been implemented in this thesis to show how PC-CD can be used to make OUR-OMA fully automatic. The most recent version of OUR-OMA uses only two crack path points: the crack mouth; and the crack tip location. PC-CD is used in step B analysis to find the crack and feeding the crack mouth and the crack tip location directly into the OUR-OMA code. The OUR-OMA code uses step A analysis with high displacement accuracy with the identified crack location to calculate the J-integral. The crack mask calculated by PC-CD (output from section 3.9.12) can also be used to determine the low confidence region that can be deleted from the imported displacement field. The ability to use PC-CD for crack mask and higher density of crack path points has been added to future work.

3.12 Conclusion

This section presented a methodology of an automatic application to detect and quantify cracks from displacement measurements. The PC-CD methodology is based on automatically determining which data points have a discontinuous movement within its domain subset. Consider Figure 3.21 as a surface example for this explanation. The data point grid is equally spaced on the reference image, spacing and subset determined by the DIC analysis. As a crack propagates through the surface, each data point tracks the surface movement and provides a quantity of the movement in each orientation. However, at locations where the actual crack path splits the domain (subset) of the data point, the DIC algorithm gives an average value of the discontinuous movement. The green data points highlighted in Figure 3.21 show the subsets the crack interacts with. The PC-CD methodology is based on the segmentation (i.e. identification) of the discontinuous data points.

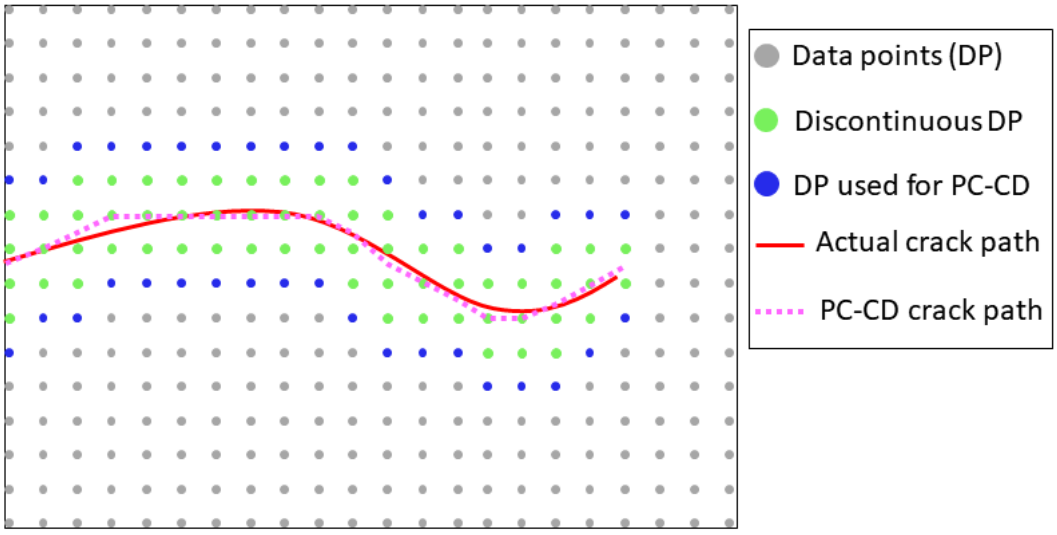

Figure 3.21 Idea behind PC-CD model of discontinuity

Once the discontinuous data points are determined, the methodology uses the boundary data points (blue data points) in order to geometrically model the crack. The blue dots are assumed to be the nearest valid displacement data points to the faces of the actual crack and assumed that the crack does not interact within the domain (subset) of the data points. The blue dots are used as virtual clip gauges to obtain the crack opening displacement by subtracting their displacement values. The mid-point between the blue dots give a virtual approximation of the crack path placement (pink dashed line) on the reference image grid.

However, it is important to note that the DIC analysis plays a large role in the geometrical modelling of the crack. Lower step size adds better placement of subsets on the crack faces which gives a more refined crack path placement. Larger subset size gives higher certainty of displacement values at the loss of spatial resolution. Optimization of the subset and step size were discussed in the literature review (section 2.3.1) and it was concluded that the subset and step size parameters can be fine-tuned with respect to the speckle pattern and camera noise.

The application of PC-CD is fully automatic, and the default parameters are considered for most of the datasets, unless stated otherwise. There are a few parameters that can be fine-tuned based on the imported displacement measurement.

Phase congruency (see section 3.9.7 and 3.10.6) is an automatic step, however λ_{min} and d_{PC} are parameters that control the scale-space of a feature which essentially is the sharpness of the discontinuity signal. The sharpness of the discontinuity is directly related to the choice of subset and step size (data point spacing). For example, considering the data point spacing is constant and larger subset size were used in Figure 3.21, this will mean more data points will have interacted with the crack, giving a blunter discontinuity signal and a larger discontinuous data point region. Smaller subset size means will mean less subsets will interact with the crack giving a much sharper discontinuity signal. A relationship between subset and step size versus λ_{min} and d_{PC} was observed, the relationship was further investigated in section 4.7.

VPC-CD algorithm is virtually the same as the PC-CD application, however, instead of being automatic, the procedure requires easy user interaction where a seed point must be specified. The location of the seed point is invariant to the outcome; therefore, user judgement does not impact geometrical representation of the crack. OUR-OMA algorithm is presented to show how the geometry of the crack, automatically obtained from PC-CD, can be used to calculate the J-integral, which is a critical process towards the characterisation of a crack.

4 THEORETICAL AND VIRTUAL BENCHMARKING OF THE NOVEL PC-CD

4.1 Introduction

The novel PC-CD algorithm extracts the crack geometry purely operating on measured displacement fields. In-order to quantify and benchmark the uncertainty associated with the crack geometry extraction using the PC-CD method, two controlled approaches of obtaining cracked displacement fields were studied.

The ability to create virtual datasets is of prime importance for the development and benchmarking of image analysis-based methods. In the case of crack study through Digital Image Correlation, developing an analysis technique proves difficult and inefficient when working with experimental datasets, for several reasons. Firstly, the dataset parameters are not perfectly controlled or known, it is therefore impossible to determine where the final error comes from. Moreover, the number of available experimental configurations is limited by practical constraints, preventing thorough testing of the method capabilities in different situations. On the other hand, the use of virtual images allows separate control of all fracture parameters and is not limited in term of number of different datasets to produce.

First, a theoretical simulation of a horizontal edge crack was constructed using Williams' series (see Figure 3.2a for an example). The geometrical parameters of the crack were known for the displacement field, therefore could be compared to crack parameters extracted using the PC-CD algorithm. Furthermore, to test the Phase congruency's state of the art de-noising method, zero-mean additive white Gaussian noise for different σ values was added to the theoretical displacement field. The comparisons gave the errors associated with this novel approach and PC-CD method's performance can be benchmarked with respect to the influence of uncertainty in displacement fields. PC-CD was able to accurately detect a crack with a mouth opening of 0.1 pixels with typical experimental noise (i.e. medium noise).

Next, a virtual simulation of a horizontal edge crack was used where a computer-generated virtual speckle pattern was deformed using a computer code (*ODIN*, see later in section 4.6.1). The speckle pattern was deformed using five different cracked displacement fields, which varied in crack mouth opening displacement. The aim of the study was to investigate how the discontinuity signal, steeper crack tip gradient and controlled noise levels impact the uncertainty of crack geometry obtained by PC-CD method. Furthermore, the PC-CD method was compared with the Heaviside function fitting to displacement field with characterised uncertainties.

4.2 Methodology of the theoretical experiment

In this section, a theoretical displacement field of a crack in an infinite linear elastic plate (i.e. Williams' series [186]) was used to quantify the accuracy of the algorithm. Crack parameters such as crack opening displacement profile $\delta(x)$, crack path $\psi(x)$, and crack length are known parameters in the theoretical crack tip fields and can readily be compared with those calculated by the PC-CD method. To evaluate the algorithm's robustness to noise and investigate the influence of uncertainty, zero-mean additive white Gaussian noise [187] was added to the theoretical displacement field with an incremental standard deviation of Gaussian noise.

The continuum mechanics solution of the displacement field ahead of a crack in an elastic medium is an asymptotic function [101]. Assuming only the first term of the asymptotic function for a crack along the horizontal direction i.e. $X-$ axis shown in Figure 3.2a, the opening displacement, Uy, around the crack as a function of the far field applied stress, σ, can be presented by:

$$Uy\,(r,\theta) = \frac{\sigma\sqrt{\pi a}}{2\mu}\sqrt{\frac{r}{2\pi}\left[sin(\frac{1}{2}\theta)\left\{\kappa+1-2cos^2(\frac{1}{2}\theta)\right\}\right]} \qquad (45)$$

where μ is the shear modulus and r and θ are radial and phase distance from the crack tip and a is the crack length. The origin of this $XY-$ coordinate system is at the crack tip. The crack opening displacement $\delta(x)$ is calculated by [188]:

Displacement in crack plane $\theta = \pi$; $r = a - x$

$$Uy = \frac{(1+\nu)(\kappa+1)}{E}\frac{\sigma}{2}\sqrt{2a(a-x)} \qquad (46)$$

$$\delta(x) = 2Uy(x) = \frac{(1+\nu)(\kappa+1)}{E}\sigma\sqrt{2a(a-x)} \qquad (47)$$

Where υ is Poisson's ratio and $\kappa = 3-4\upsilon$ for the plane strain condition.

The Uy displacement field and COD was constructed with an arbitrary Young's modulus of $8\,GPa$ and Poisson's ratio of 0.3. It should be noted that only the singular term of displacement field was used in this study.

As the distance from the crack tip increases the contribution of non-singular terms increases [189] and the crack opening displacement calculated by Eq.(47) is no longer valid. However, the aim of this theoretical study was to compare a known crack opening displacement with that calculated by the PC-CD method to estimate its accuracy and therefore the unrepresentativeness of the selected field has no impact on the estimated accuracy.

Accurately modelling the typical experimental DIC noise was challenging as there are many different factors that contribute to the uncertainty in the displacement field. Hence, to simulate the effects of uncertainty in displacement field, additive Gaussian noise with mean value of 0, and different increments of standard deviation were added to the theoretical displacement field. The standard deviation σ_G, percent additive noise, Γ_N, was introduced with the following form:

$$\Gamma_N = \frac{\sigma_G}{(\Delta Uy)} \times 100 \qquad (48)$$

ΔUy is the range of the displacement field, and has value 1 as Uy is normalised. The simulated Γ_N ranges from 0% (no noise) to 10% with increments of 0.01%. For a predefined value of Γ_N, σ_G is the standard deviation of a normal distribution from which a random value is extracted, $N(i,j)$, and added to the displacement field as shown in:(49)

$$Uy_{noise}(i,j) = Uy(i,j) + N(i,j) \qquad (49)$$

$$N(i,j) \sim N(0, {\sigma_G}^2) \qquad (50)$$

4.2.1 Heaviside step function

The Heaviside step function can be used to fit a discontinuous function to the displacement field line profile normal to the crack for every profile along the crack. This was usually used to obtain the crack opening displacement. The Heaviside step function is defined as;

$$H(x) = \begin{cases} 0 & x < 0 \\ 1/2 & x = 0 \\ 1 & x > 0 \end{cases} \qquad (51)$$

However, the discontinuity location or crack path is needed before fitting the Heaviside function to the line profile. Three different methods were looked at to find the crack location:

- Global maximum gradient of the line profile across the discontinuity;
- Maximum of difference between windowed moving average with a set smoothing threshold;
- 1D canny edge detector - Convolution with a Gaussian derivative kernel with a selected noise suppression.

A threshold was chosen to determine when the crack location is not detected. This threshold also determines the crack length that is found. The Heaviside function was then fitted using least square method coupled optimum threshold parameters and COD was subsequently calculated.

4.2.2 Error estimation of the geometrical parameter of a crack

To evaluate the errors, the square root of the mean square error (RSME) was used. For the crack opening displacement:

$$RSME(\hat{\delta}) = \sqrt{\frac{\sum(\hat{\delta} - \delta)^2}{\hat{a}}} \quad (52)$$

where $\hat{\delta}$ is the calculated crack opening displacement profile extracted from Uy_{noise} , δ is the theoretical COD profile given by Eq. (47) and $\hat{a}$ is the observed crack length.

For crack path analysis, the error is defined by:

$$RSME(\hat{\psi}) = \sqrt{\frac{\sum(\hat{\psi} - \psi)^2}{\hat{a}}} \quad (53)$$

where $\hat{\psi}$ is the calculated crack path and, ψ is the prescribed crack path; in this case it is constant as the crack path is a straight line.

For crack length, the error defined by:

$$\text{Relative Error } (\hat{a}) = \frac{|a-\hat{a}|}{a} \times 100\% \quad (54)$$

Where, $\hat{a}$ is the observed crack length and a is the prescribed theoretical crack length.

4.3 Theoretical analysis and discussion

The COD profile $\hat{\delta}$, crack path position $\hat{\psi}$ and crack length $\hat{a}$ were extracted from the noisy displacement discontinuity models using the PC-CD method with default parameters, and compared with the one extracted by fitting Heaviside function (see section 4.2.1).

The theoretical data was also assessed by three types of Heaviside analysis: Gradient-based, Gaussian derivative-based [25], and windowed-smoothing based. Out of these, the Gradient-based method (Figure 4.1b) yielded the most accurate and least scattered results for the crack path, with an almost consistent RMSE of less than 0.5. While Gaussian and Windowed Heaviside methods higher range scatter with a range of 0.2 and 0.35, both above 1 RMSE. However, the crack length measurement for Gradient Heaviside (Figure 4.1c) was strongly impacted by the additive noise giving a maximum error of 25%, at near 10% additive noise. Windowed smoothing-based and Gaussian derivative-based methods were more noise robust for extracting crack length, but the additive noise impacted the precision of the crack path (see Figure 4.1b) and gave a less precise COD profile (Figure 4.1a). Among the Heaviside techniques, the Gaussian derivative-based method performed relatively better in finding the crack length and crack path with the additive noise.

Although the Heaviside method of calculation of COD was noise robust, it was also imprecise due to non-linear variation of displacement across the crack near the crack tip (see Figure 3.2e). Furthermore, it was also sensitive and strongly dependent on the location of the crack path and length, suggesting the crack path error impacted the COD measurement. The Heaviside performance was sensitive to thresholding parameters; therefore its accuracy can be restricted to the adopted threshold parameter, causing a level of uncertainty in the final result. It should be noted that the Heaviside results presented in Figure 4.1 selected the best manual threshold as its automation would be difficult.

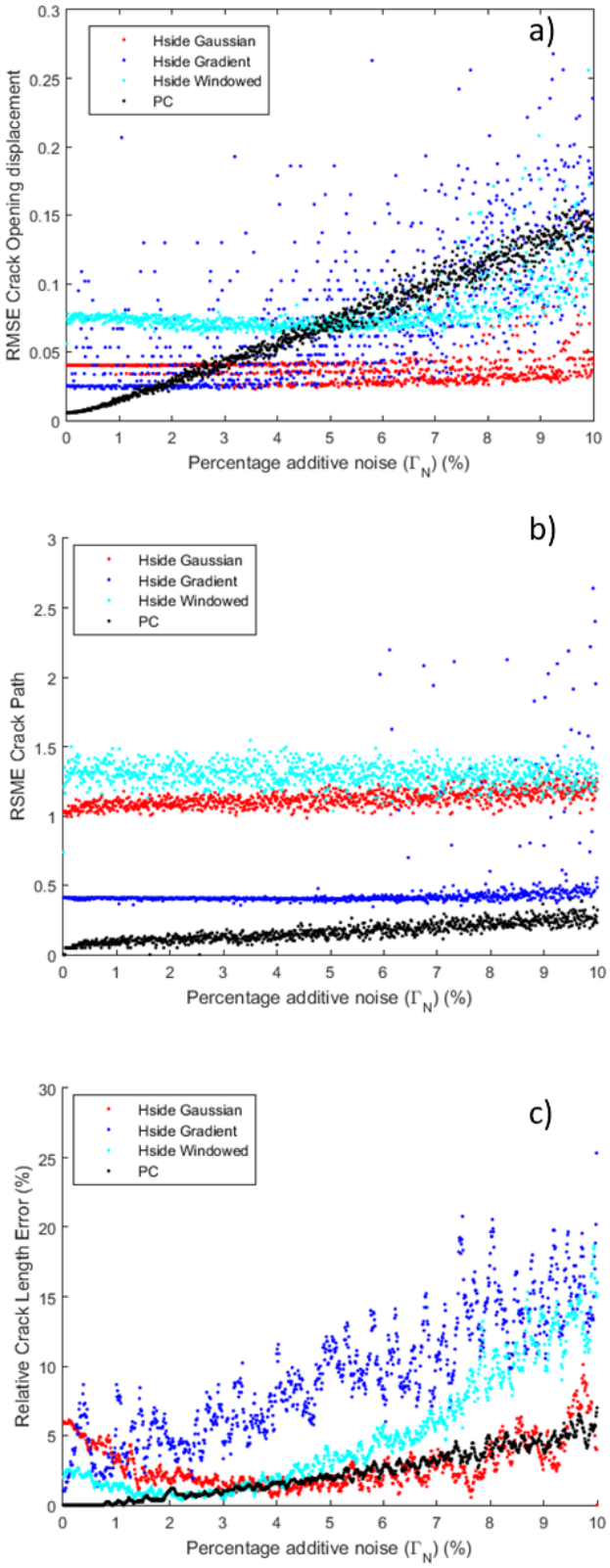

Figure 4.1 Theoretical Uy noise analysis a) Error analysis for Crack opening displacement b) Error analysis for Crack path c) Relative crack length error with different additive noise

4.4 Spatial resolution and overlap analysis and discussion

The DIC technique allows for full-field displacement measurements, theoretically, at every data point within a selected region of interest. However, in practice, the displacement data point is not associated for that pixel, but rather the averaged displacement of the domain around the data point. This results in the loss of spatial resolution at the gain of quantified surface displacement measurement. The change of spatial resolution has ramifications on the crack parameter extraction. The impact of overlap and spatial resolution will be studied in this section.

Computing the displacement measurement of a surface using the least squares method (LSM) algorithm requires the step size and subset size to be characterised by the user. Subset size illustrates the area over which each displacement data point position and displacement measurement is averaged. Step size represents the pixel-based distance between each displacement data point on the reference image which can also determine the amount of overlap between the subsets. If the spacing size is equal to the subset size, this results in each subset being an independent measurement, meaning there is no overlap between subsets. Overlapping subsets usually represent the smoothing of the surface displacement measurement.

The calculation of the overlap is given by:

$$\text{Overlap } \% = \frac{S_{\text{subset}} - S_{\text{step}}}{S_{\text{subset}}} \qquad (55)$$

An overlap study was conducted to determine the best analysis parameter to study the spatial resolution. Subset size (S_{subset}) was kept at a constant of 31 while varying step sizes from 1 to 31 (S_{step} = 1,2,3 … 30, 31) which provided a homogeneous overlap spacing between 0% to 96.8%. The displacement calculations were made using the “accurate” mode with no smoothing and no outlier filter on the DaVis 8.2.3 software package. The displacement calculations for the spatial resolution study were all made on a single dataset; CMOD with 1 pix and no virtual image noise. The reason for choosing this crack profile was the crack artefact is not visible on the deformed image and therefore the analysis would be independent of the error sources posed by the crack artefact. It is difficult to isolate all error sources within displacement calculations, however using this profile removes one source of error for this study.

PC-CD algorithm was used iteratively and automatically to successfully calculate the crack parameters. Crack parameters such as COD, crack length and crack path were obtained from the displacement field and then compared to virtual crack parameters used to deform the initial image, once again using Eq.(52)(53)(54). The overlap study is depicted in Figure 4.2.

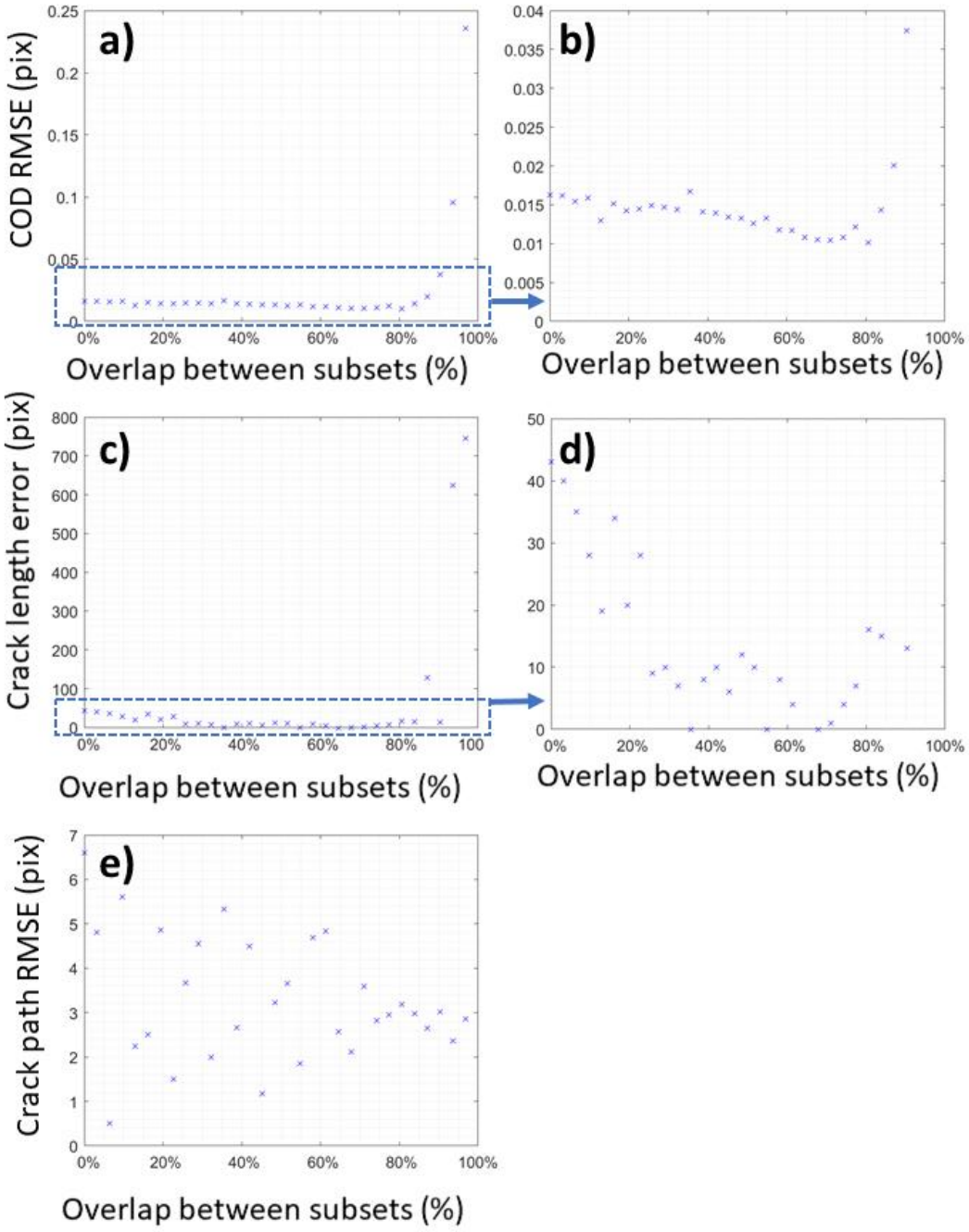

Figure 4.2 DIC subset overlap error study with subset size 31 a) COD RMSE, b) COD RMSE of the blue dashed region in a), c) Crack length error d) Crack length error of the blue dashed region in c), e) Crack path RMSE

It is seen that the DIC overlap plays a somewhat significant role in the accuracy of the extracted crack parameters. Figure 4.2(a and b) show that the RMSE for Crack Opening Displacement gradually decreases from 0% to 70-80% overlap where the error hits a minimum of ~0.01 pix. After ~80% overlap, the error is seen to increase drastically, hitting a maximum error at 96.8% overlap with an error of 0.23 pix. Figure 4.2(c and d) show the crack length error with respect to different overlap and it is observed to follow a similar trend to RMSE COD with a larger spread. Figure 4.2d shows that the crack length error hits 0 three times, overlaps at 36%, 54% and 68% which appear to be random arbitrary values. Figure 4.2d also shows that between overlap values of 25% to 80%, the crack length error is consistently below 10 pixels, and doesn't seem to show an obvious improvement between this range (25% to 80% overlap). However, after 80% overlap, the crack length error is seen to increase to more than 10 pixels. After 85% overlap, the error exceeds 100 pixels suggesting that the PC-CD algorithm fails to extract the full discontinuity successfully. The crack path RSME, depicted in Figure 4.2b, however, shows that there are no obvious trends between crack path RSME and overlap as and the error appears to be random. The minimum crack path RSME is observed to be at 10% overlap with a step size of 29 while the maximum error is at 0% overlap. However, there seems to be a trend with the range of the crack path RSME. The range appears to decrease as the overlap is increased and the error appears to be tending towards ~3 pix RMSE, with no obvious improvement for the crack path parameter between 75 -96.8% overlap. This study shows that the most optimum overlap parameters are between 70% to 80% between interrogating subsets.

Now, a spatial resolution will be conducted using the optimum overlap parameters found above. The overlap for the following study will be kept relatively constant between $74\% - 78\%$, this time, modifying both subset size ($\mathrm{S_{subset}}$) and step size ($\mathrm{S_{step}}$). The overlap parameter cannot be kept at an absolute constant as subset and step size, both require to be an integer. The displacement calculations were made using the "accurate" mode with no smoothing and no outlier filter on the DaVis 8.2.3 software package. The displacement calculations were made on the same dataset as the overlap study; CMOD with 1 pix and no virtual image noise. The twelve-displacement field with varying subset and step sizes (see Table 29) were then exported and MATLAB version of PC-CD algorithm was used iteratively and automatically to successfully calculate the crack parameters. Crack parameters were once again obtained from the displacement field and then compared to the virtual crack parameters used to deform the initial image, using Eq. (52)(53)(54).

Table 29 depicts the DIC parameters that were used for the spatial resolution analysis to achieve a relatively constant overlap.

SUBSET SIZE (PIX)	STEP SIZE (PIX)	OVERLAP (%)
9	2	77.8
13	3	76.9
17	4	76.5
21	5	76.2
25	6	76.0
29	7	75.9
31	8	74.2
39	9	76.9
43	10	76.7
65	15	76.9
85	20	76.5
105	25	76.2

Table 29 Iterative least square DIC parameters used for spatial resolution study

The spatial resolution study is depicted in Figure 4.3. It was seen that by increasing the subset size, the displacement field was smoothed out and therefore COD values provided a higher level of certainty in Figure 4.3a. This did result in a loss in spatial resolution and crack definition. Decreasing the subset size increased the spatial resolution, making the crack well defined within the displacement field hence enabling PC-CD method to extract the crack path and crack length with a lower error as seen in Figure 4.3(b and c).

It was observed that there are outliers in Figure 4.3(b and c) as the relation between subset size and error is expected to be a linear relation. This is due to the inconsistent data point positioning for each spatial resolution analysis, which cannot be controlled. It was apparent that the data point positioning played a pivotal role in the accurate calculation of the crack path. It is shown that displacement data point positioning is an under-looked parameter with in the displacement calculation that impacts the calculated displacement field hence effecting the crack parameters. However, if the crack artefact is visible, the error posed by the crack artefact is dependent on the percentage of corrupted pixels within each subset [60]. This suggests that subset size plays a pivotal role with the uncertainty of the displacement data close to the crack faces which are important for when crack parameters need to be extracted.

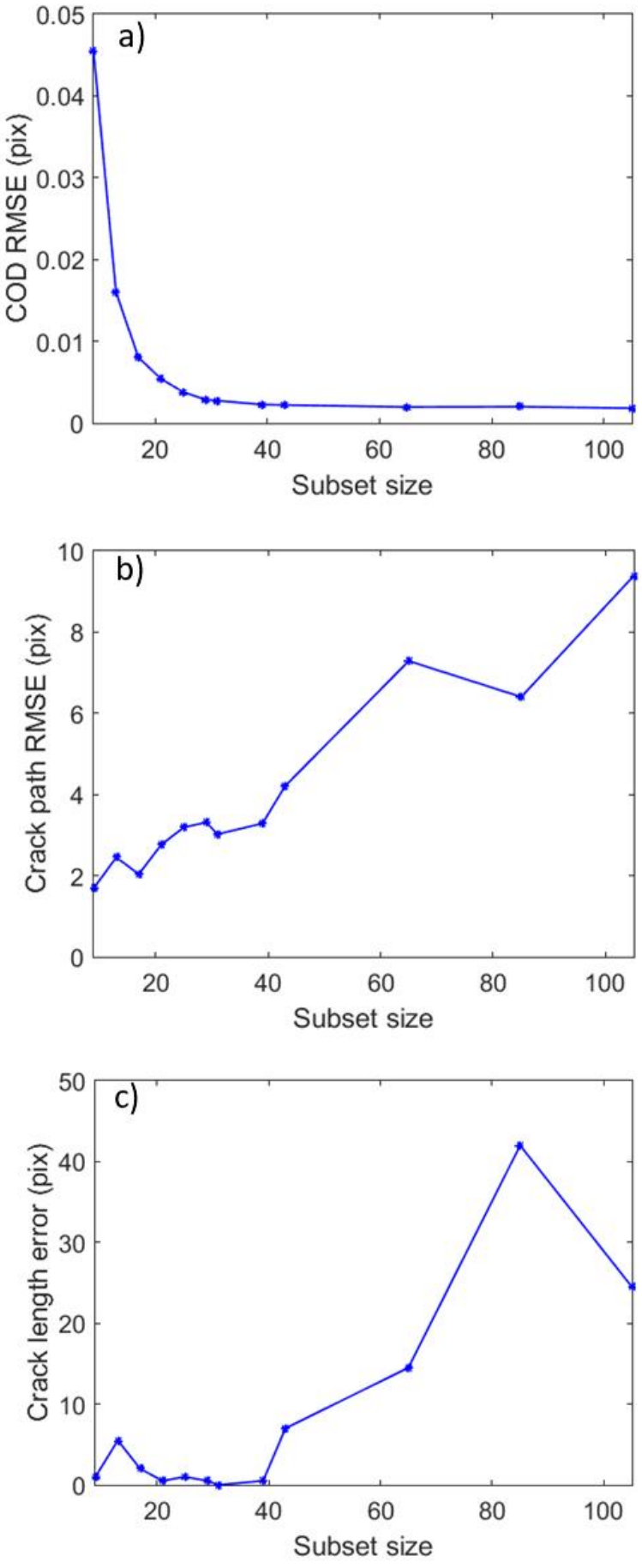

Figure 4.3 Spatial resolution study a) COD RMSE b) Crack path RMSE c) Crack length RMSE

For accurate COD measurements, large subset size and for accurate crack definition (crack path and crack length), lower subset size is essential. It is interesting that this observation is similar to the one stated in section 3.11, regarding crack characterisation. A good compromise for subset size selection is between 25-31 which minimises the error for all extracted crack parameters. Increasing subset size beyond 31 shows little improvement in COD accuracy while decreasing subset size below 25 shows little improvement in crack length and 1.1 pix (compared to 9 px subset size) improvement in crack path. However, if the user desired to optimise both crack path and crack length at a cost of further analysis and time complexity, the developed method should be used twice. Firstly, small subset size for optimised crack length and crack path positions and secondly, large subset size for optimised COD measurements.

4.5 Selecting Phase Congruency parameter values

This section will investigate the sensitivity of the Phase congruency parameters on the accuracy of the extracted crack parameters. A simulation study was carried out to find optimal values for the phase congruency parameters λ_{min} and d_{PC} using a single virtual dataset. The virtual dataset used in this study was used previously, CMOD with 1 pix with no virtual image noise. The displacement calculations were made using the "accurate" mode with no smoothing and no outlier filter on the DaVis 8.2.3 software package with subset size of 31 and a step size of 8. Crack parameters were extracted from the displacement field automatically, while incrementally adjusting PC parameters, λ_{min} and d_{PC}.PC parameter, λ_{min} is adjusted between 2 to 20, incrementally by 1 while d_{PC} is adjusted between 0.6 to 1.8, incrementally by 0.1. The extracted crack parameters are then, compared to virtual crack parameters used to deform the initial image, once again using Eq.(52)(53)(54).

Figure 4.4 depicts the outcome of the study.

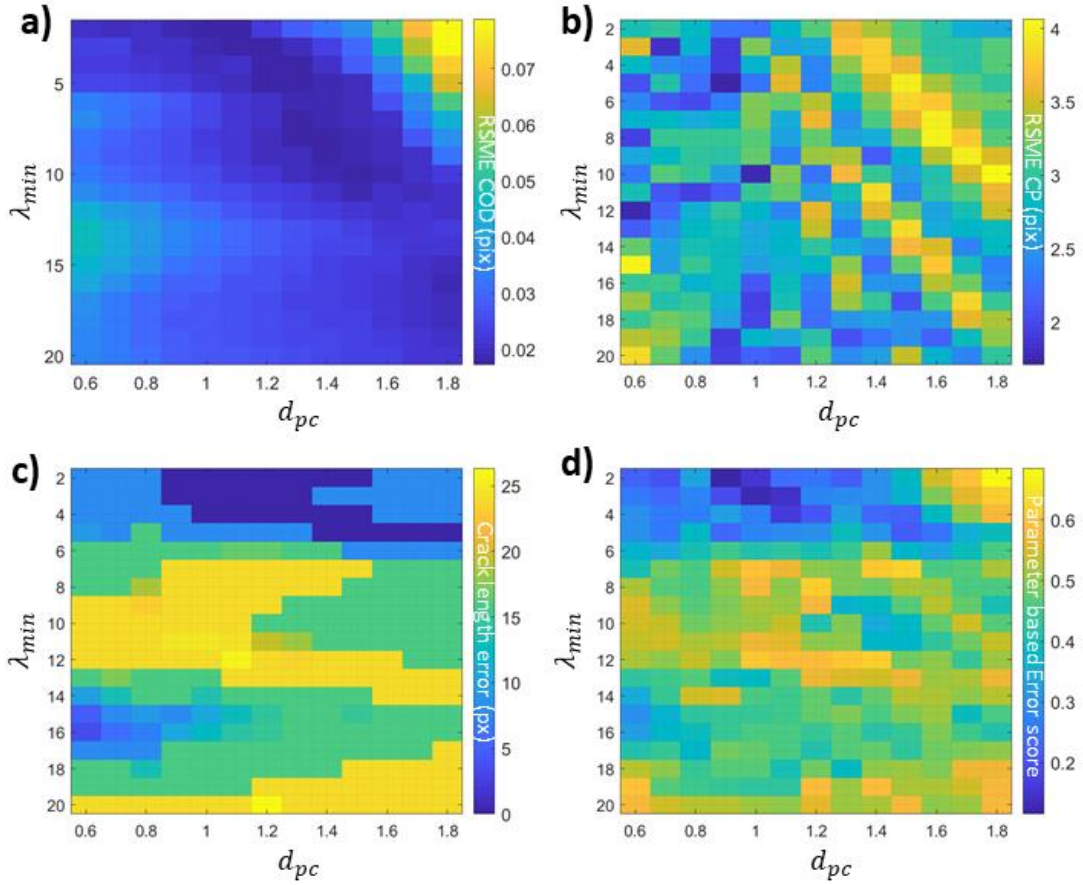

Figure 4.4 Phase congruency parametric study of λ_{min} and d_{PC}, a) Impact of PC parameters on the RSME COD b) Impact of PC parameters on the RSME crack path (CP), c) a) Impact of PC parameters on the error in crack length, d) PC parameter error score – summation of normalized a), b) and c).

To find the most optimum PC parameters, RMSE COD, RMSE CP and crack length error values (i.e. Figure 4.4(a, b and c) will need to be minimized. A universal error matrix is created by combining all the error matrices Figure 4.4(i.e. a, b and c). First, the error matrices are normalized so that each PC parameter (i.e. λ_{min} and d_{PC}.) is given a score between 0 and 1, 1 representative of maximum error, based on how well it performed for each error matrix. Next, all the normalized error matrices are summed together to create a parametric based error score matrix (i.e. Figure 4.4d). The lowest scores on the parametric based error score matrix indicate the best crack extraction PC parameters. Observation of Figure 4.4d show that the best PC parameters live in $\lambda_{min} = 2 - 5$ and $d_{PC} = 0.9 - 1.2$ giving an average error score of ~0.2 and a maximum error score of 0.3. The default PC parameters ($\text{i. e.}\, \lambda_{min} = 4$ and $d_{PC} = 1.2$) selected for all the studies (see section 3.2) lie within this optimized parameter boundary.

4.6 Methodology of the virtual experiment

In order to benchmark the PC-CD method, several virtual datasets were created using *ODIN*. The aim was to investigate the impact of crack mouth opening displacement and noise to determine how accurately the method can extract crack parameters from cracked bodies. The analysis can act as a guideline to approximate the uncertainty of the crack parameters based on the crack mouth opening of an experiment and uncertainty of the displacement field. Additionally, in this analysis the PC-CD method was compared to Heaviside function fitting where PC-CD yielded better results.

4.6.1 Generated Datasets with ODIN

In the present work, a MATLAB code named *ODIN* [190] was developed by Dr. Selim Barhli, University of Oxford. *ODIN* allows one to create a set of virtual images from a finite element model. The input consists of the nodal and elemental structures of the finite element model as well as the displacement vector at each node. The code has been tailored to accept various element shapes (triangle and quadrilaterals). The user also defines the pixel size of the virtual camera and a multiplier to apply to the displacement values if needed. Finally, a picture of the surface speckle pattern was also to be provided.

Using the William's series to displace a virtual speckle pattern is limited to an idealised crack in an infinite elastic plate. To study the performance of the developed algorithm in more general conditions, *ODIN* code was used to deform virtual images with the displacement field output of a finite element simulation. A virtual camera pixel size of $0.125\ \mathrm{mm/pixel}$ was used to produce the images with a size of 2048×2024 pixels that replicates a typical experiment. The speckle pattern, Figure 4.5, was also computer generated.

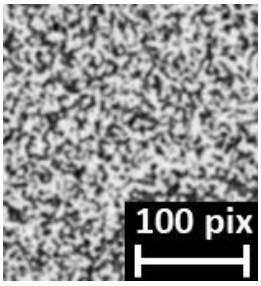

Figure 4.5 Virtual speckle pattern

The virtual specimen was a 253×256 cm plate containing a straight edge crack, of 126.5 mm in length. The FE simulation was used to deform the virtual specimen as a linear elastic material with nominal properties of $E = 207$ GPa and $\nu = 0.3$. Datasets with crack mouth opening displacements of $0.1, 0.5, 1, 5$ and 15 pixels were generated by altering the by the multiplier (i.e. from 12.5 μm to 1.875 mm).

4.6.2 Study of displacement uncertainty and image noise

The aim of the virtual experiment was to evaluate the uncertainty induced in crack path, length, and opening displacement measured by the algorithm. The effects of experimental uncertainties in the displacements calculated by DIC were studied, by adding Gaussian noise to the virtual data both in the un-deformed and in the deformed images. The speckle pattern, subset size and step size were kept constant to simplify the comparison between displacement noise and experimental noise: subset size and step size of $31, 8$ pixels respectively, were used for the following studies.

To include the experimental noise, a similar adaptation of Eq. (48) was used:

$$\Gamma_N = \frac{\sigma_G}{(I_{max} - I_{min})} \times 100 \qquad (56)$$

where Γ_N is percent additive noise, σ_G is the standard deviation of Gaussian noise, I_{max} is maximum grey-scale intensity, and I_{min} is minimum grey-scale intensity of the images. A random but similar magnitude additive noise was added to each of the reference and deformed images for every analysis. The reference and deformed images were analysed by the LaVision Davis' Strain Master software. Percentage additive image noise in terms of grey-scale values ranging from 0% to 4% was studied with increments of 0.01. In the case where no deformation was applied, the DIC analysis returned zero average

displacement in x and y directions. The standard deviation of the displacements in x and y directions from zero quantifies the error that is due to the added noise. The relationships between percentage additive image noise, image signal to noise ratio (SNR) and image displacement uncertainty are shown in Figure 4.6a, which shows that displacement uncertainty increases as the SNR decreases. Figure 4.6a also shows that the uncertainty for both Ux and Uy are similar and increase at the same rate as the SNR decreases. There is a linear relationship between percentage additive image noise and uncertainty in Ux and Uy displacement field, however, the relationship stops being linear once the SNR is below $28\ \mathrm{dB}$. Once the SNR is below $15\ \mathrm{dB}$, the uncertainty in the displacement fields starts the decrease. The reason for this is because synthetic noise corrupts image pixels such that the DIC least squares algorithm cannot match subsets or that the correlation value is below the threshold and hence displacement vectors are not obtained. Figure 4.6b shows that all the subsets are matched until 2% percentage additive noise which is like $28\ \mathrm{dB}$ SNR. After 2% of additive image noise, the percentage of unmatched vectors start to increase reaching $\sim 90\%$ unmatched vectors at 3.8% additive image noise. After 3.8% additive image noise, the DIC algorithm cannot obtain any displacement vectors from the images.

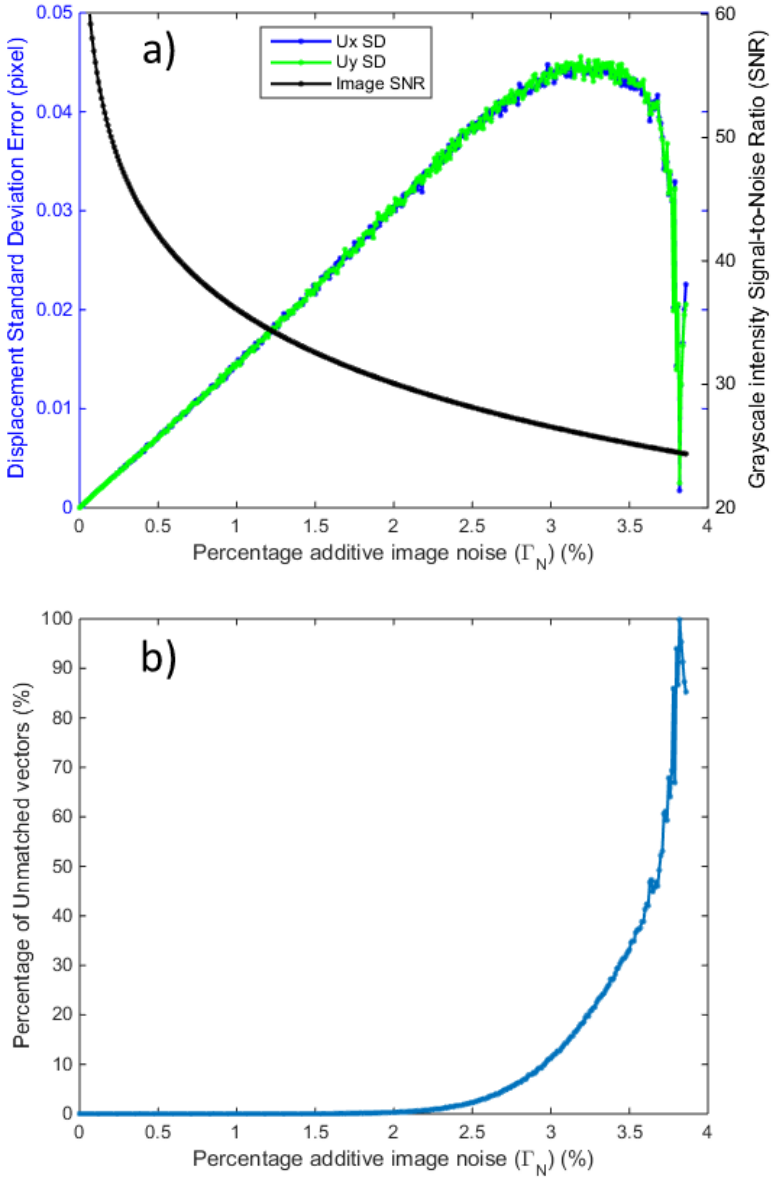

Figure 4.6 Displacement uncertainty analysis a) Image Noise vs SNR and Displacement SD b) Image Noise vs Missing data

The SNR of a digital image varies with parameters such as lighting conditions, exposure time and CCD sensor, and typical CCD cameras present SNR values between $30 - 100$ dB [191]. Three different noise levels were therefore selected for further study: (i) No noise ($\Gamma_N = 0$ and SNR $\rightarrow +\infty$ dB) which is an idealised case; (ii) medium noise which is selected to represent a typical experiment ($\Gamma_N = 0.7$ and SNR $= 39.2$ dB); (iii) High noise ($\Gamma_N = 3$ and SNR $= 26.56$ dB) which is selected at the edge of the boundary where the Digital Image

Correlation software with a least square algorithm fails to carry out the analysis. . The percentage of additive image noise level for case (ii) was chosen after evaluating the quality of the images taken in a number of recent experiments carried out by Stanier et al. [192] and also those available in the literature [193-195]. Stanier et al. [192] calculated the SNR to be ~ 40 dB in one of their deformation experiments and they state that it is likely to be adequate for producing detailed and smooth deformation fields. Baldi et al. [193] calculate ~ 52 dB for their displacement error studies and also note that this noise induced bias is very small compared to typical experimental noise. Tong [194] created synthetic image noise to assess the accuracy of his proposed improved subpixel registration algorithm. He uses 6 synthetic image noise levels, $0\%, 0.25\%, 0.5\%, 1\%, 2\%$ and 4% on an 8-bit image (256 gray colours) which produce SNRs of $+\infty$, $4760, 1204, 311, 74.1$ and 18.6 dB respectively. It can be seen from his work that he displays only four SNR's for his study, which are $1\%, 2\%$ and 4% image noise levels as the results for the 0.25% and 0.5% were too close. In his work, 1% and 2% image noise was used to simulate a normal experimental image noise, which gives an SNR range of 311 dB to 74.1 dB. To accommodate all the SNR values in the references stated below, 39.2 dB was selected conservatively to simulate a normal experimental noise.

4.7 Virtual analysis and discussion

The five different CMOD were considered for each noise level, and the crack path, length, and opening displacement profile were extracted in all cases using the PC-based algorithm. The best performing Heaviside function that was identified from the previous section, i.e. Heaviside Gaussian derivative kernel [25] and was used to extract the crack parameters to compare with the PC-based algorithm. The deformed images were analysed by DIC using LaVision's Strain Master [37] using the least square technique with uniform subset grid size of 31 with step size 8. No smoothing or outlier filter was used. The positioning of the uniform subset grid was constant for all CMOD profiles on all the reference images to preserve positioning independency.

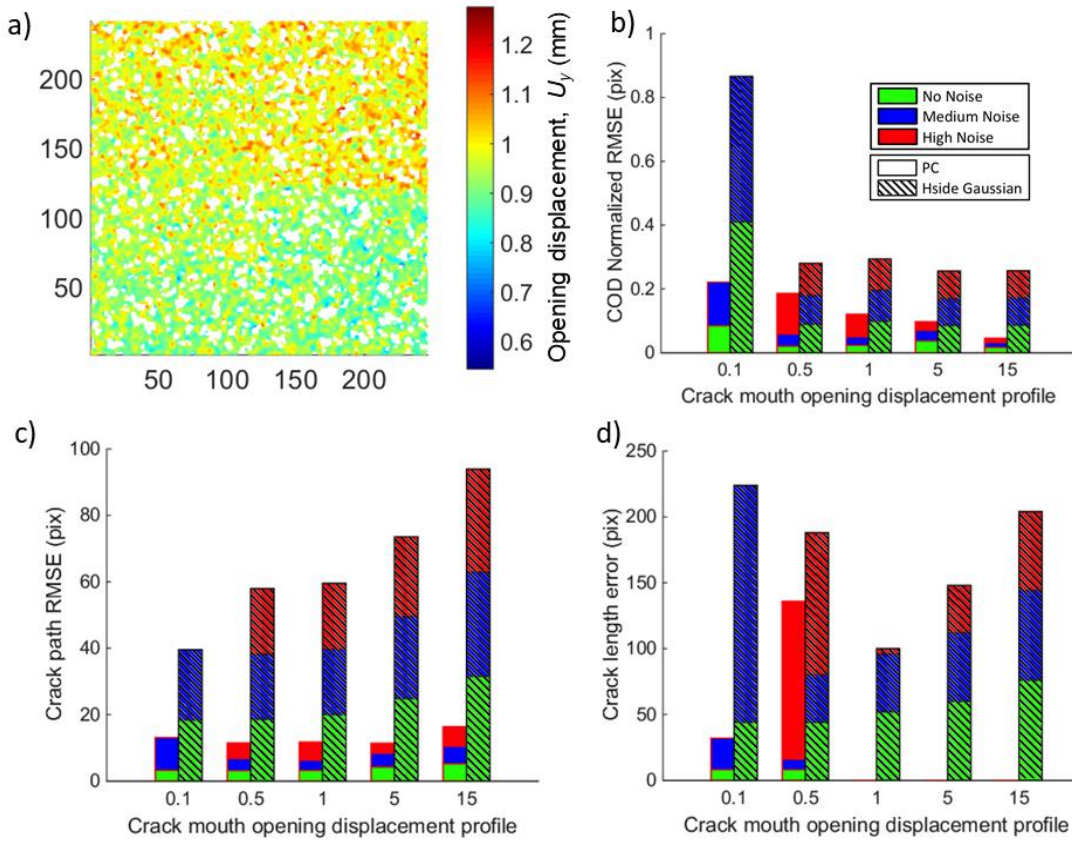

Figure 4.7 Virtual analysis of crack detection methods a) Uy map of CMOD 0.1 pixels with high additive image noise b) Crack opening displacement error c) Crack path error d) Crack length error

The PC-CD algorithm is fully automatic[9] while the Heaviside algorithm required adjustment and thresholding in each case to obtain optimal crack parameters. An example of the map of the displacement in the y direction for the 0.1 pixel CMOD with high additive image noise is shown in Figure 4.7a. The white regions of the displacement map are uncorrelated subsets. Visually, a distinguishable step in the displacement field was observed, but in relatively small manner compared to the noise, while a large fraction of the displacement vectors was lost due to image noise, causing the discontinuity to be less visible in the displacement map. Both crack detection methods (automatic PC-CD) failed to detect the crack in this case. It was not possible to obtain fracture parameters from this displacement field without the aid of smoothing or fitting techniques, however this will amplify the uncertainty of the parameters and was not pursued. However, by outlier deletion, an attempt to remove the additive noise and to amplify the discontinuity can be attempted. Figure 4.7a was used as an extreme example to depict how an outlier deletion and recovery can be used in section 3.5.

In all the other cases, both PC-CD and Gaussian Heaviside successfully computed the crack parameters and the parameters were then compared to their true value using Eq. (52)(53)(54) which are depicted in Figure 4.7(b, c and d), respectively. It is clearly seen that PC-CD performs better than Gaussian Heaviside in all instances of crack path, COD and crack length. Figure 4.7b shows that PC consistently gave precise COD measurements for no noise and medium noise for different CMOD profiles while high noise measurements showed the error was declining as the CMOD profile was increased.

[9] The automatic and default parameters were used with no adjusting. Outlier deletion procedure was not used in the analysis

This was an indication that the discontinuity profile is increasing in signal compared to the noise. However, this was not observed for the Gaussian Heaviside which suggests that there could be systematic errors similar to those associated with COD observed in Figure 4.7a. Sub-pixel data accuracy of the algorithm was observed in Figure 4.7c: given that spatial resolution (step size) is 8 pixels, the algorithms successfully detected the crack path less than 5 pixels of error. Gaussian kernel derivative's limitation to point precision for discontinuity detection was shown in the Figure 4.7c with crack path errors of more than 18 pixels. It was observed for CMOD of 15 pixels, the error has increased to roughly 6 pixels for each noise study.

Figure 4.7d shows the algorithm accurately found the crack tip location for CMOD of $1, 5, 15$ pixels without any error whereas for CMOD of 0.1 and 0.5 pixels, the crack tip discontinuity was lost within the noise. As for Gaussian Heaviside, crack length error increases as the crack mouth is more open as observed for no noise. This was because Heaviside function fails to fit the step function close to the crack tip, hence detecting a smaller crack.

4.8 Conclusion

The novel PC-CD technique was derived to extract the crack's geometrical parameter from predetermined and controlled 2D displacement fields via theoretical and virtual methods. The technique was benchmarked on these controlled linear-elastic displacement fields for the effects of uncertainty and discontinuity signal and have shown to extract the crack's geometrical parameters with good accuracy. A spatial resolution study on a virtual dataset showed that the placement and size of the subsets play a role in the uncertainty of the measured crack parameters. The method was fully automatic which removed the user judgement and bias from the analysis. Although the application can be applied to any surface geometry, the benchmarking has only been administered to long mode I cracks. Detection and benchmarking of mixed mode and short cracks have been added to future work.

Furthermore, it was shown that the accuracy of PC-CD was dependent on the uncertainty of the imported displacement fields. For example, results presented in Figure 4.7 have been a key evidence to show that noise and crack artefact impact the crack measurements, however PC-CD seemed obviously more noise and crack artefact robust ready to tackle these problems. The analysis demonstrated that the PC-CD algorithm is a robust automatic technique for crack detection and parameter extraction.

5 APPLICATION OF PC-CD TO EXPERIMENTAL SURFACE DISPLACEMENT FIELDS

5.1 Introduction

The novel PC-CD method and its application to theoretical linear elastic displacement fields has been presented in the previous chapter. In this chapter, the PC-CD method was applied to crack detection and quantification in two different classes of materials, in order to examine its accuracy and robustness in real laboratory conditions. The cases of quasi-brittle and ductile materials were studied. The PC-CD was applied to an additional ductile experiment where the effects of crack closure and overload were studied. The crack geometry extracted by PC-CD was validated through optical microscopy, high resolution fractography and visual inspection.

5.2 Quasi-Brittle Material: Rock

The cracking process of a rock material is highly influenced by the microstructure of the material. By using the natural texture of the specimen surface as speckle pattern, cracking and crack growth can be monitored in detail in relation to the structure of the rock material. A brief description of a test on a double edge notch tension (DENT) rock specimen is presented. This is not a geometry recommended by the International Society of Rock Mechanics [196] and as such it may not necessarily render a valid fracture toughness value.

Since the aim of the experiment was to verify the applicability of PC-CD algorithm on quasi-brittle material and not produce a valid fracture toughness test, it has no negative impact on the results. The experimental application was designed and realised by Dr Mathias Flansbjer, (SP Technical Research Institute of Sweden). The data was made available to this study after the experiment. The author of this thesis takes no credit for production of the experimental images, however, the analysis of the images was fully conducted by the author of this thesis and was used in his paper [1].

5.2.1 Experimental details

The specimen was a fine-grained granitic rock with a surface area of $60 \times 60\ \mathrm{mm}^2$ and a thickness of $10\ \mathrm{mm}$. An annotated photo of the test set up is shown in Figure 5.1a; the sample width was ($2W$) was $60\ \mathrm{mm}$, each of its notch length (a) was 10, and each of its notch radii (d) was $5\ \mathrm{mm}$. The studied material was a fine-grained granitic rock. To make the texture more prominent in the images, the surface of the specimen was polished in a grinding machine before testing. This allowed the natural pattern of the specimen be used for DIC analysis without need for an artificial speckle pattern (e.g. spray paint) which can obscure the crack tip. However, this method can result in blurriness in the speckle pattern due to the height difference of the surface asperities. Therefore, to evaluate the effectiveness of the natural pattern of the specimen as speckle pattern, a detailed noise analysis was performed which is explained in the next section.

The specimen was glued to the loading platens of the testing machine, ensuring that the loading line and the centre axis of the specimen coincided as close as possible. The tensile load was controlled at a constant crosshead displacement rate of 0.06 mm/min.

A 2D DIC measurement setup comprised a 4 megapixel CCD camera and a Schneider-Kreuznach Componon-S 2.8/50 Macro lens was used for the image acquisition. The observed area ($65 \times 65\ \mathrm{mm}^2$) covered slightly more than the entire specimen surface, corresponding to a pixel size of approximately $32\ \mu\mathrm{m/pixel}$. To obtain high contrast levels, the specimen was illuminated by a white LED light panel.

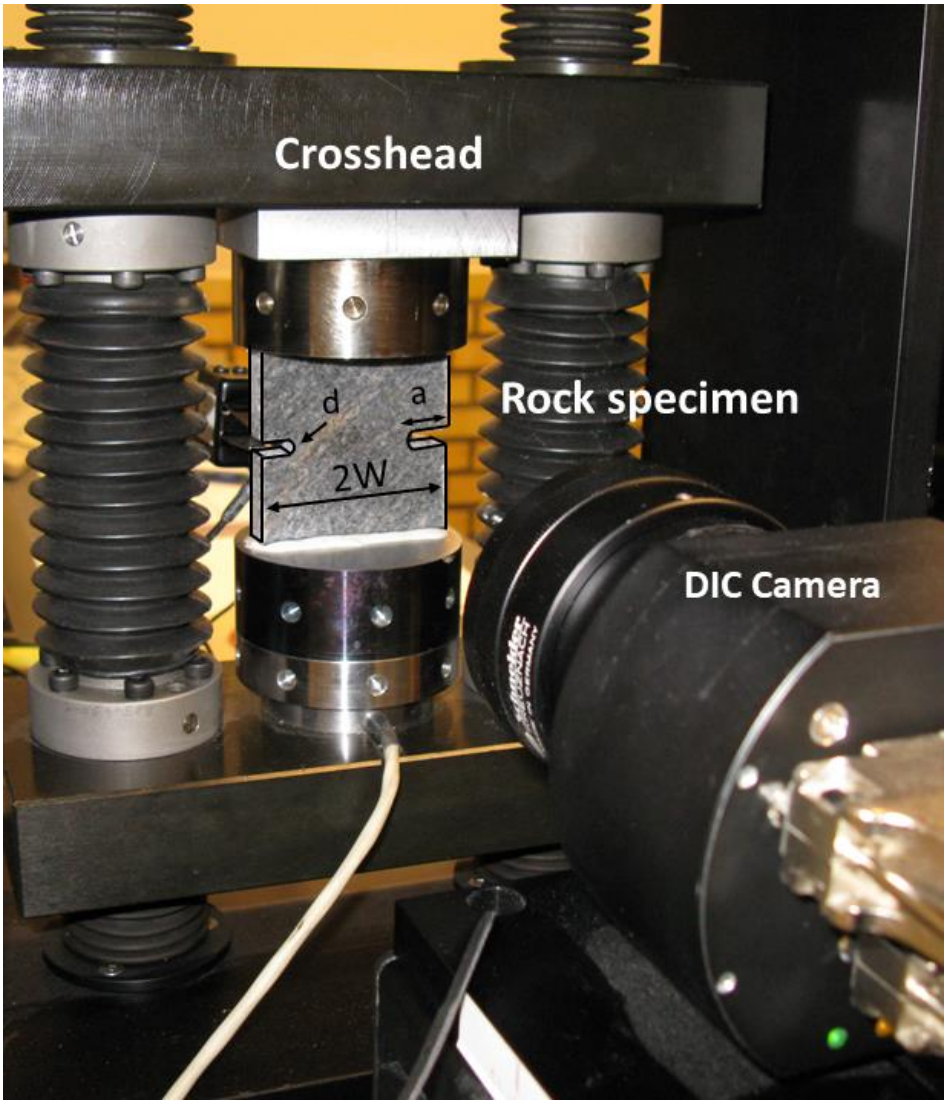

Figure 5.1 Small scale doubled edge notch tensile experiment setup of quasi-brittle material: 2W (width) =60 mm, a (notch length) =10 mm, and d (notch radius) = 5 mm

5.2.2 Analysis and discussion

A sequence of 8-bit 2048×2048 pixel images were obtained (see Figure 5.1), from which a smaller region of 1329×681 pixels was selected (see Figure 5.2a with a white dashed box) to reduce computation time and to mask the round tip of the notch. The region of interest before and after load (i.e. reference and deformed images, Figure 5.2b and c) shows two cracks in the deformed image.

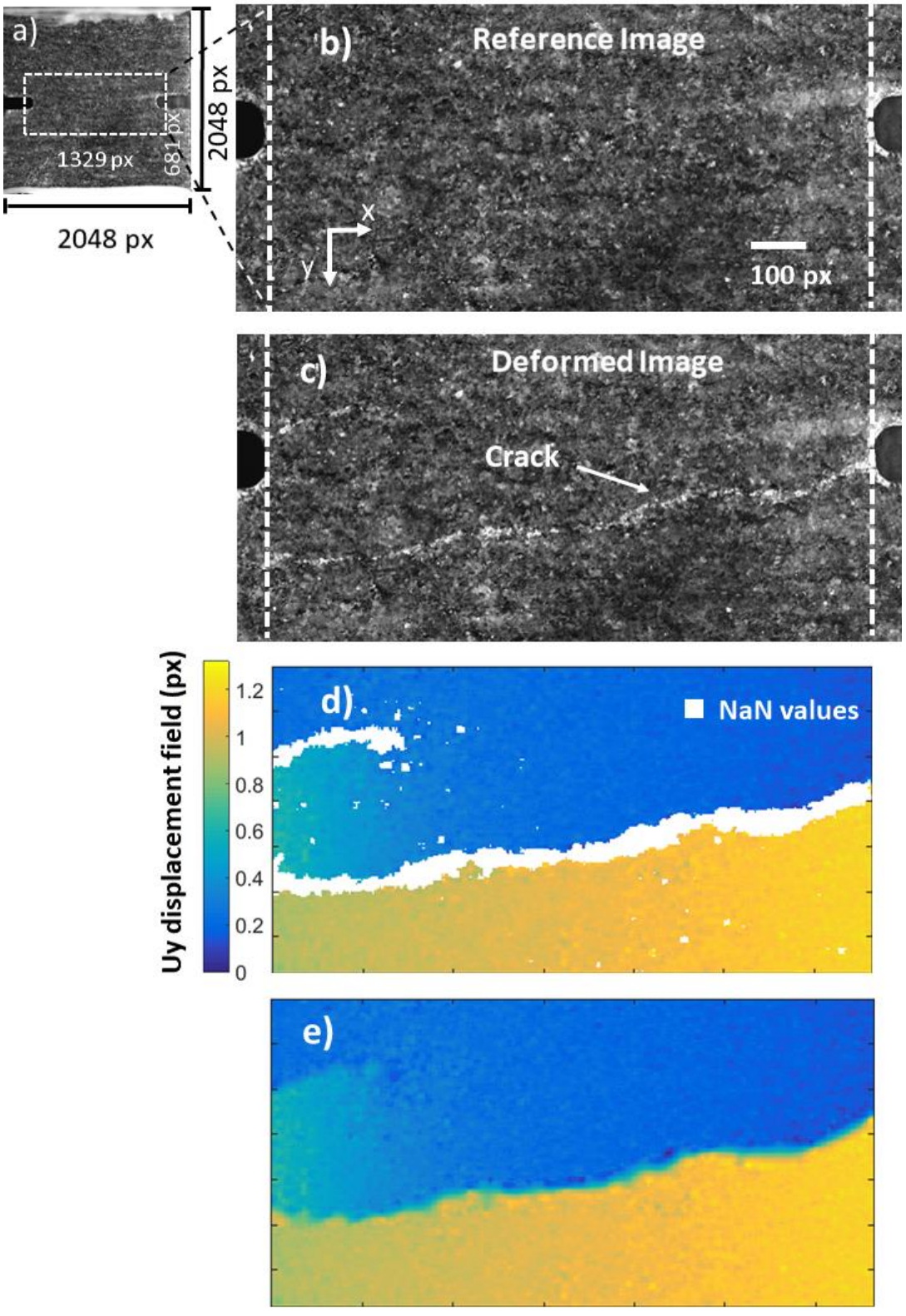

Figure 5.2 Quasi-Brittle test and analysis (a) captured image of the surface, region of interest is indicated between two white dashed lines (b) reference region of interest (c) deformed region of interest d) calculated opening displacement Uy field (e) extrapolated Uy displacement field with no missing data points

The PC-CD algorithm could be used to detect and analyse multiple cracks, but for simplicity, only the larger surface discontinuity labelled in the Figure 5.2b as "Crack" was considered in this study. A DIC analysis was performed on the images using least squares method with subset size 17 pixels and step size of 4 pixels; no smoothing or outlier filter was applied. The calculated opening displacement map, Uy, is shown in Figure 5.2d. To estimate the expected noise within the displacement field, a baseline noise analysis (no deformation / movement) is conducted with the same DIC parameters giving a noise level of $\sigma_{Ux} = 0.009$ and $\sigma_{Uy} = 0.012$ pixels which is similar to the medium noise analysis that was studied previously in section 4.6.2. The mean grey-level intensity within the region of interest changed from 85.3 to 86.5 counts between reference and deformed images. This change of grey-level intensity is visually seen at the location of the discontinuity which resulted to poor correlation for the subsets that include the crack, as shown by the censored displacement data (Figure 5.2d). Subsets with correlation coefficient of less than 60% were censored. The missing data were extrapolated using a linear least square approach (see section 3.6) without modifying known values to obtain the final displacement field (Figure 5.2e).

Automatic PC-CD algorithm was applied to the data with the default parameters and outlier deletion was not applied. The key steps of the application of the crack detection algorithm are depicted in Figure 5.3: this shows the outcome of the phase-congruency analysis (Figure 5.3a), the path segmentation using Hough transform on the phase congruency result (Figure 5.3b); an overlay of the segmented crack on the displacement data (Figure 5.3c) and the crack opening profile (Figure 5.3d) on the deformed image. The algorithm successfully exposes the discontinuity and quantifies its length, opening displacement profile and path. Visual inspection of the data shows that the crack path has been identified with an accuracy better than 2 pixels from the mid-point of the damage. Close to the crack tip, the COD is less than a pixel, and the crack is observable only in the image due to the light reflected by the crack face which changes the grey-scale intensity. At some points, the reflected region measured 20 pixels across, which will typically give an over estimation of the crack opening displacement if the conventional crack segmentation algorithms were used (i.e. thresholding). The damage location (i.e. crack path) is also difficult to map from the deformed image, even with visual observation, due to the inhomogeneous intensity. Since the novel PC-CD method is based on displacement fields, the approach tracks the behaviour of the crack faces. Although, the reflection affects the correlation, but nonetheless the crack is very well detected without user intervention.

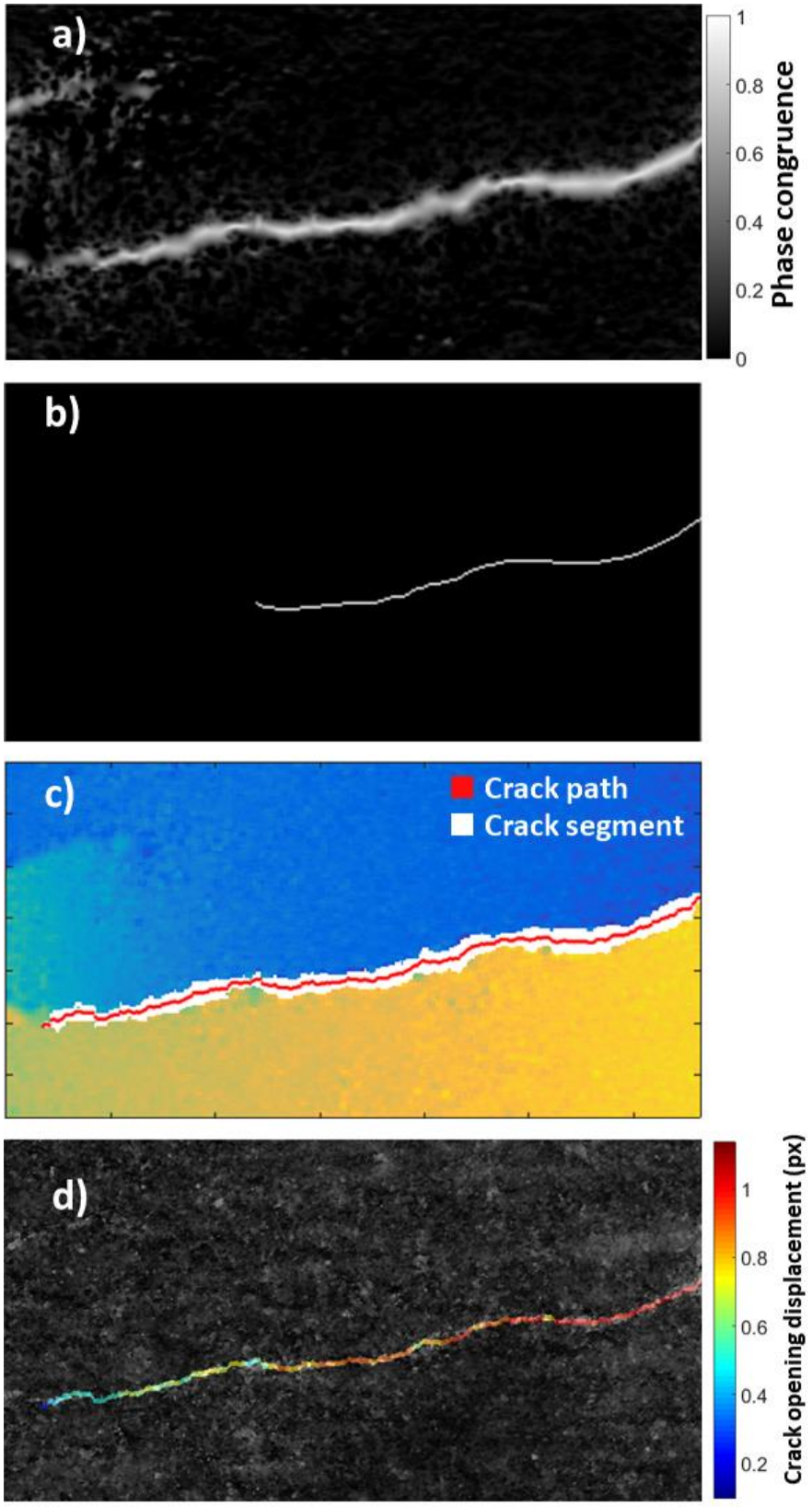

Figure 5.3 PC-based crack detection (a) Phase congruency of Figure 5.2e (b) segmentation using Hugh transformation (c) segmented crack path overlaid on the displacement field (d) Crack path and crack opening displacement profile overlaid on the deformed image

5.3 Ductile Material 1: Aluminium alloy 2024

Ductile materials show high levels of plasticity around the crack and therefore the large strains of the surface can induce errors in the Digital Image Correlation analysis. An experimental dataset was obtained using a fatigue pre-cracked Compact Tension (CT) specimen of an aluminium ($\mathrm{Al}2024$) alloy. The material was provided by Airbus Group as a $20\ \mathrm{mm}$ thickness plate in the $\mathrm{T}351$ condition (i.e. solution heat treated and stress-relieved by stretching). Post-experiment optical microscopy observation of the 3D-DIC analysis surface aided in precise location of the discontinuity. To verify the PC-CD observation, the optical microscopy calculated crack path and crack tip, which was calculated manually, was compared to the crack path and tip calculated by PC-CD algorithm. The experiment was designed by Dr. Selim Barhli to be used for his paper [2]. The author of this thesis participated in the experiment and the calibration of the 3D DIC system and was also fully responsible for the analysis of the 3D DIC image data and the optical microscopy observation of the crack surface. The author of this produced results in his paper [1]. The experimental equipment (3D DIC system, optical microscopy, tensile machine and experimental rig) was made available by Professor James Marrow, University of Oxford and the OxfordMaterials team.

5.3.1 Experiment details

A fracture test of aluminium alloy 2024 was carried according to $\mathrm{ASTM\ E399}$ [11] , details of which is given elsewhere [2]; a brief description of the experiment is given here. A fatigue pre-cracked Compact Tension (CT) specimen, schematic of which is shown in Figure 5.4, with a width of $W = 50\ \mathrm{mm}$ and $a/W = 0.5$ (a is the crack length) was tested; other dimensions of the specimen are related to W according to $\mathrm{ASTM\ E399}$. The specimen was loaded by moving the upper loading pin at a constant displacement rate of $0.2\ \mathrm{mm/min}$ until the crack started growing. The loading of a CT sample is predominantly dominated by bending around a plastic hinge unlike the DENT specimens tested in the previous section which is mainly tensile. This change of loading mode provides an extra degree of dissimilarity between the two experiments in addition to the difference in material behaviour to evaluate the performance of PC algorithm further.

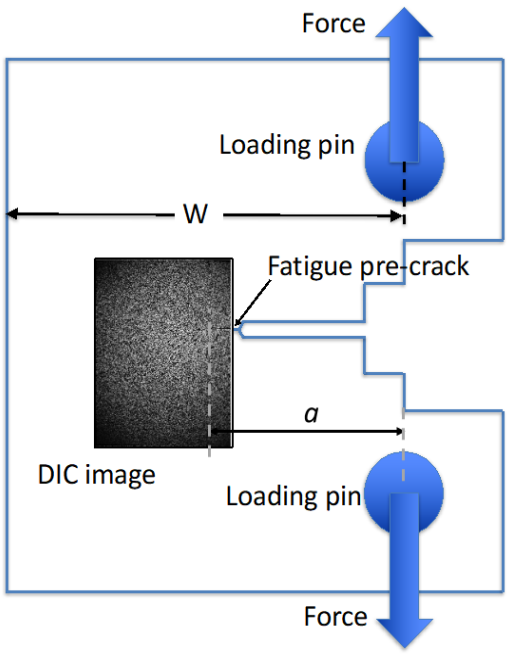

Figure 5.4 Fracture test of ductile material

The images were collected using a stereo-DIC system comprising 2 Toshiba-Teli CSB4000CL-10A cameras; each camera captured 2008×2047 pixel size 10-bit images of the surface of the specimen which had a painted speckle pattern applied to it. The pixel size was $15\ \mu m$, calibrated using a 058-5 LaVision 3D calibration plate.

5.3.2 Micro analysis – Optical Microscopy

After the fracture test, optical microscopy observation of the surface verified the location of the discontinuity. The specimen surface in the vicinity of the crack was cleaned with ethanol to remove the paint that had been applied to create the speckle pattern. A set of 2560×1920 pixel images were obtained from the surface of the crack specimen at low magnification $(1.04\ \mu m/pixel)$, and at high magnification $(0.14\ \mu m/pixel)$. The low magnification images were manually stitched using the overlapped region to construct a larger image with dimension of 6625×4865 pixels (see Figure 5.5a). The high magnification images were similarly stitched to create an image of 39927×6932 pixels (see Figure 5.5b); this was subsequently scaled down by binning to match the low magnification image resolution. Although spatial resolution was lost, the visibility of the crack faces was improved and a more accurate crack tip location was obtained (see Figure 5.5c and d).

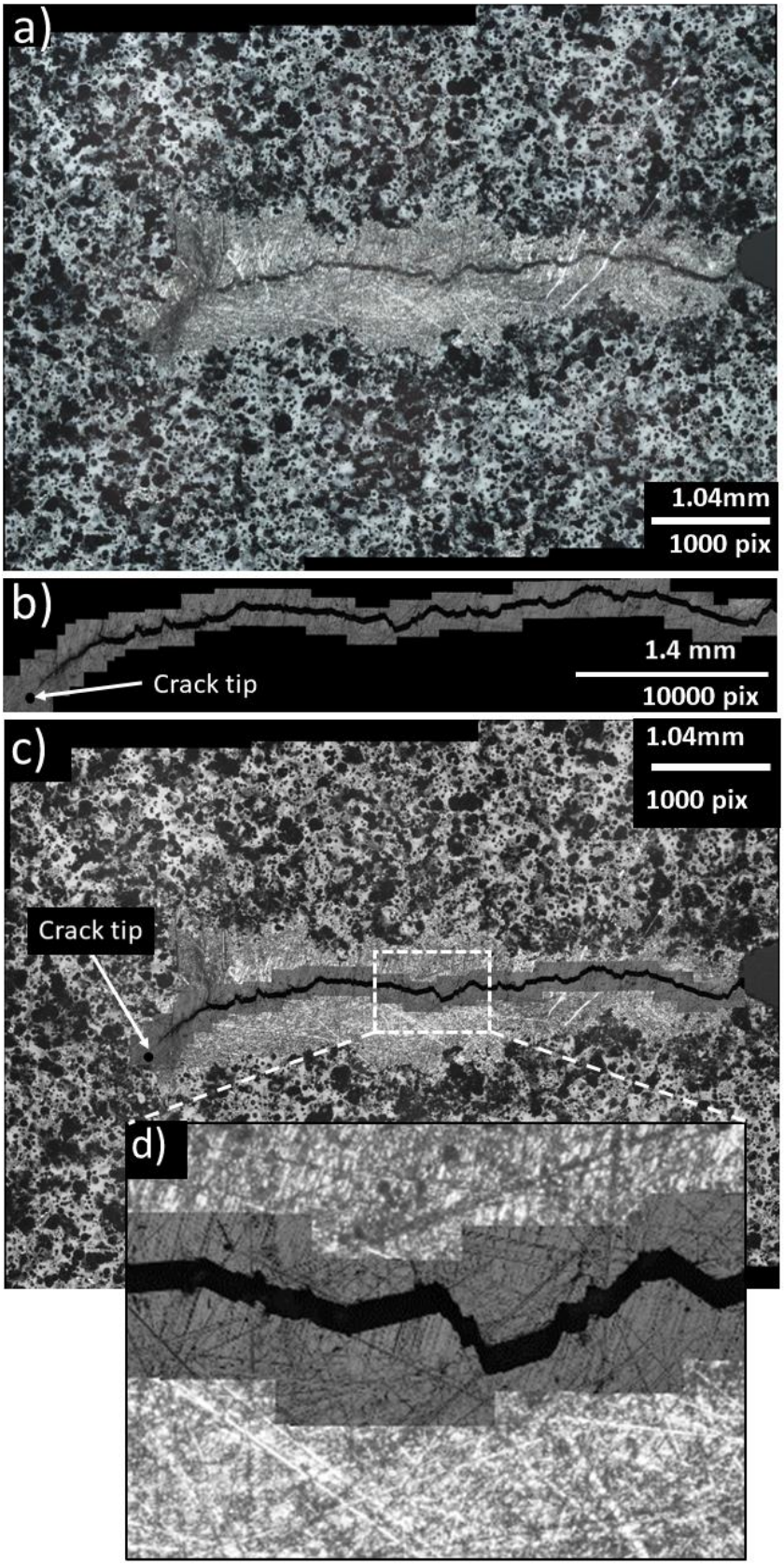

Figure 5.5: Optical microscopy analysis (a) lower magnification image (b) higher magnification image (c) high and Low magnification image stitched (d) zoomed in of (c)

A pair of stereo images, comprising four images, was analysed: two reference images recorded by cameras at different angles to the surface of the non-deformed specimen, and two similarly recorded images of the loaded specimen. An example of an image captured by the left camera, after the distortion correction, is shown in Figure 5.6a. For a faster computational analysis, a region of interest of 400×300 pixels was selected (marked by a dashed white area in Figure 5.6a). This region of interest is compared in Figure 5.6(b and c) for the reference and deformed images. The same region, observed by optical microscopy at low magnification, is shown in Figure 5.6d.

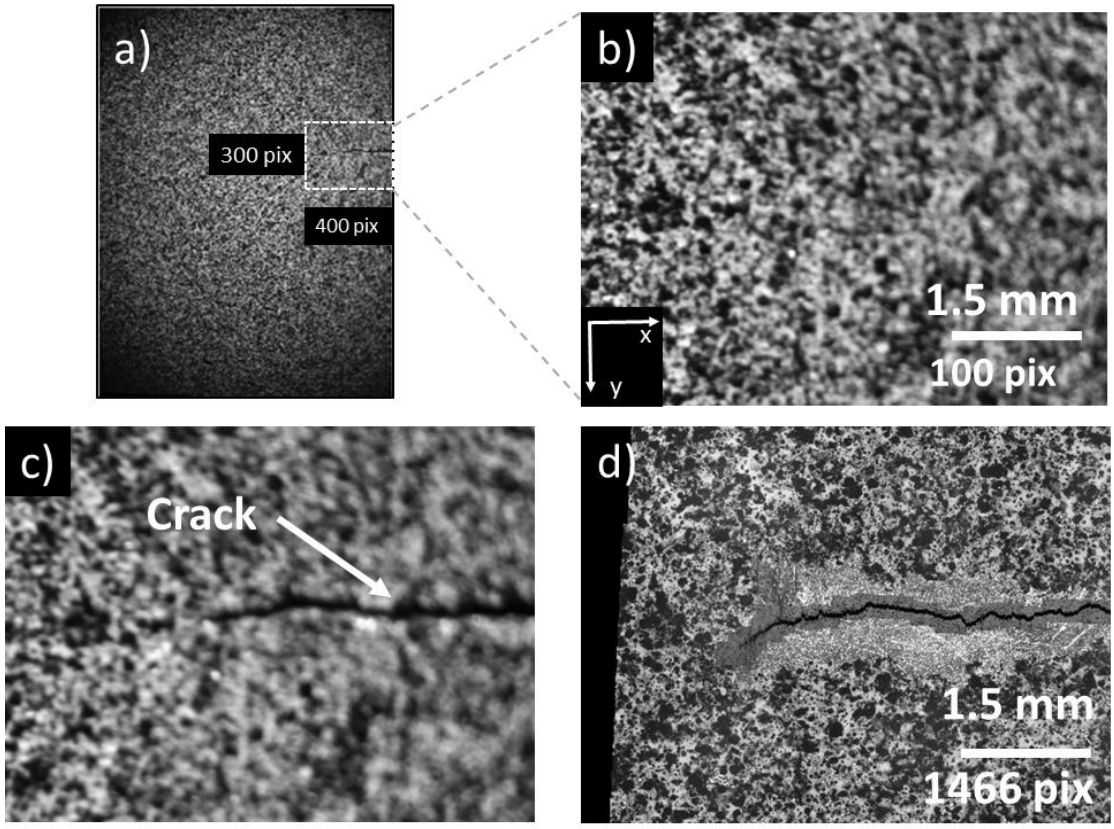

Figure 5.6 Ductile fracture test and analysis (a) full field reference image from left-hand camera (b) region of interest reference image (c) region of interest deformed image (d) stitched image of optical microscopy (see Figure 5.5c) of the same region as shown in (b)

The images were analysed with subset size of 9 pixels and step size of 1 pixel (~88% overlap) to obtain the displacement fields shown in Figure 5.7a. Small subset size were chosen to optimise the crack path and crack length parameters in-order to better compare with the parameters obtained from optical microscopy. A better COD profile can be obtained by using larger subset sizes and lower overlap value.

Increased numbers of missing vectors (shown as white patches to the right side of the displacement map) occurred due a loss of focus during the experiment (see Figure 5.7b and c). However, the non-correlated areas are mostly local, which allowed interpolation to be used results of which is given in Figure 5.7b. Best user judgement was employed to manually segment the crack from Figure 5.5c, shown with a red line with the crack tip identified by a white cross.

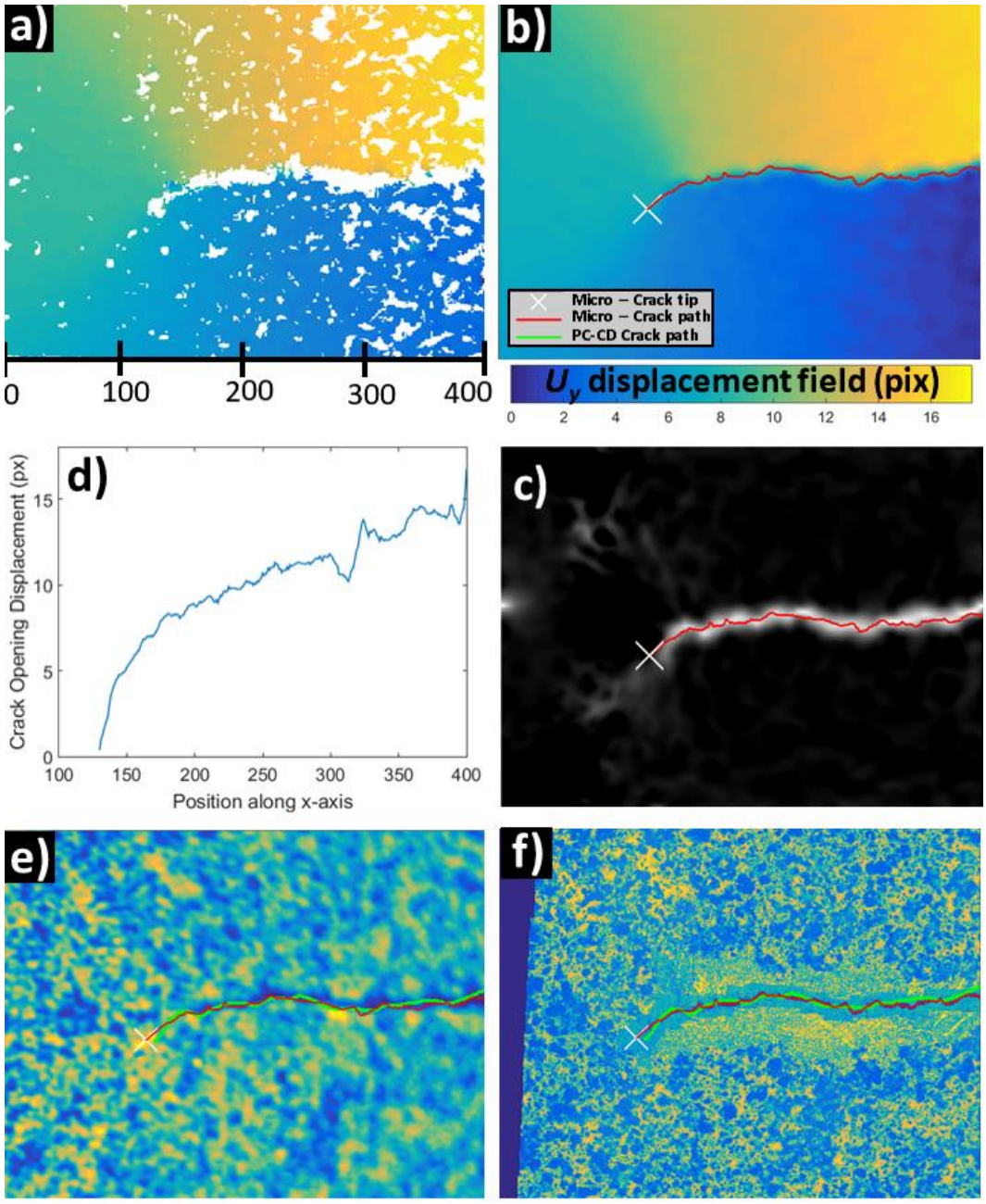

Figure 5.7 Stereo-DIC analysis (a) Uy map (b) missing Uy map extrapolated (c) Phase congruency of Uy map (d) crack opening displacement (e) crack path calculated by the algorithm (f) crack path calculated by the algorithm

5.3.3 Analysis and discussion

The Phase congruency map of the displacement field, shown in Figure 5.7c, highlights the discontinuity quite clearly. The crack opening displacement profile, calculated automatically by the algorithm is given in Figure 5.7d and that of the crack path in Figure 5.7e. They are overlaid on the images taken during Digital Image Correlation experiment.

The crack path was also overlaid on the stitched image taken by the optical microscope with low magnification and is shown in Figure 5.7f. In these figures, the manual segmentation is represented in red while the automatically identified crack path is given by green. It is appropriate to take the manual segmentation of the crack (red line) as true data has higher resolution of the surface was captured and the crack path calculated. Using Eq. (53), RMSE between manual segmentation and crack path proposed by this study was calculated to be 2.53 pixel over the whole length of the crack. Significantly, the time required to obtain the displacement field and the crack parameters using the proposed algorithm was approximately 1 min 22 seconds including the DIC analysis. The time to map the crack manually by optical microscope was approximately 10 hours.

5.4 Ductile Material 2: Bainitic Steel

The experimental work was completed at the Diamond Light Source on the I12:JEEP beamline. A fatigue crack growth overload experiment on Compact Tension (CT) samples, with different R-ratios (i.e. $R = 0.1$ and $R = 0.4$) and same overload was conducted in conjunction with 3D-DIC, which allowed insight into the crack driving force at the surface of the specimen. The surface measurement was acquired at six different stages, before overload, at overload and at four crack length positions relative to the overload. The cracks were detected, and their parameters were extracted from the experimental data and the impact of the crack growth beyond the plastic zone applied by the overload is studied. The fractography information was compared to the crack length calculated by PC-CD to assess PC-CD's performance and a potential impact of crack tip blunting on the calculation. The crack opening displacement profiles, calculated by PC-CD, were compared between each R ratio at each stage and loading. Higher certainty displacement calculation was used to obtain the J-integral values using a code [2] developed by Dr. Selim Barhli, University of Oxford (see section 3.11) and compared to the crack mouth opening displacement values. The experiment was designed by Dr Chris Simpson for the purpose of quantifying overload on fatigue crack growth retardation mechanics with X-ray diffraction and the full experimental details are explained elsewhere [8]. The fractography data was obtained by collaborators. The author of this thesis was fully responsible for the experimental observation via Stereo-DIC setup which included calibration, data acquisition and analysis of the image data, which included the J-integral calculations.

5.4.1 Experimental details

Two in-situ fatigue crack growth (FCG) overload experiments were completed of fine-grained bainitic steel CT-samples under plane strain conditions, one at $R = 0.1$ and the other at $R = 0.4$. Both tests employed the same stress intensity factor range, $\Delta K_{app} = 27\ \mathrm{MPam}^{1/2}$.

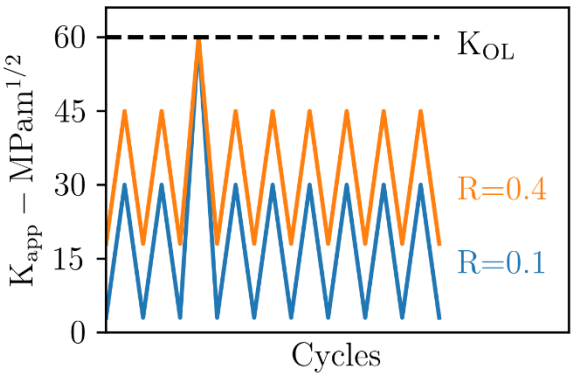

Figure 5.8 Fatigue Crack Growth schematic for testing R=0.1 and R=0.4, from [7]

Table 30 Experimental conditions for both tests, with the values for K and ΔK being given in MPam$^{1/2}$

	R=0.1	**R=0.4**
$\mathbf{K_{max}}$	30	45
$\mathbf{K_{min}}$	3	18
ΔK	27	27

A schematic of the fatigue cycling can be seen in Figure 5.8, with the associated driving force parameters being further detailed in Table 30. $R-$ ratio is the ratio of the minimum stress and maximum stress experienced during a cycle (e.g. $K_{max}/K_{min} = R-$ ratio), while ΔK is the difference between maximum and minimum applied stress during a fatigue cycle (e.g. $\Delta K = K_{max} - K_{min}$).

The experiment was completed under constant or pseudo-constant ΔK, which is to say a load shedding technique was employed to maintain ΔK_{app} close to the noted level of $27\ \mathrm{MPam}^{1/2}$. The crack growth rate was monitored using an Alternating Current Potential Drop (ACPD) system (see Figure 5.9). The ACPD method was mentioned in the literature review (see section 2.1.1). At the end of pre-cracking and at a crack length of $23.5\ \mathrm{mm}$ ($\sim 2.5\ \mathrm{mm}$ after notch tip), both the CT samples were subject to an overload to $K = 60\ \mathrm{MPam}^{1/2}$, which corresponded to an overload factor of 2 and 1.33 at $R = 0.1$ and $R = 0.4$ respectively. The plastic zone was estimated by Irwin approach [197] and the fatigue crack was grown in incremental steps through and ultimately beyond the plastic zone. Throughout the experiment, the surface of both R-ratio CT samples was captured by Stereo-DIC setup as seen Figure 5.9. Although both specimens were observed by X-ray diffraction (XRD), this thesis will not entail the results.

Prior to the experimental time on the I12 beamline, pre-cracks were introduced into the Compact Tension (CT) samples using a load shedding methodology at $R = 0.1$. The final stress intensity factor range used in this initial Pre-Cracking (PrC) was $11\ \mathrm{MPam}^{1/2}$ to ensure limited plasticity. After the initial pre-cracking (PrC), random speckle patterns were induced to both specimen's surface; white background coating and small random black speckles to cover one side. The objective was to achieve high density small black speckles which dictated the size of the displacement subset. The small precise random black speckles were achieved by a few trial and error attempts on a mock surface. The optimum size was achieved by spraying the black canister from approximately two meters away from the sample surface at an angle of $60°$ from the floor. This method forced for the heavier larger black projectiles to fall to the floor before hitting the sample, leaving the much finer and smaller projectiles to hit the sample. It was observed from both the sample specimens, the black speckle size ranged from $0.01 - 0.15\ \mathrm{mm}$.

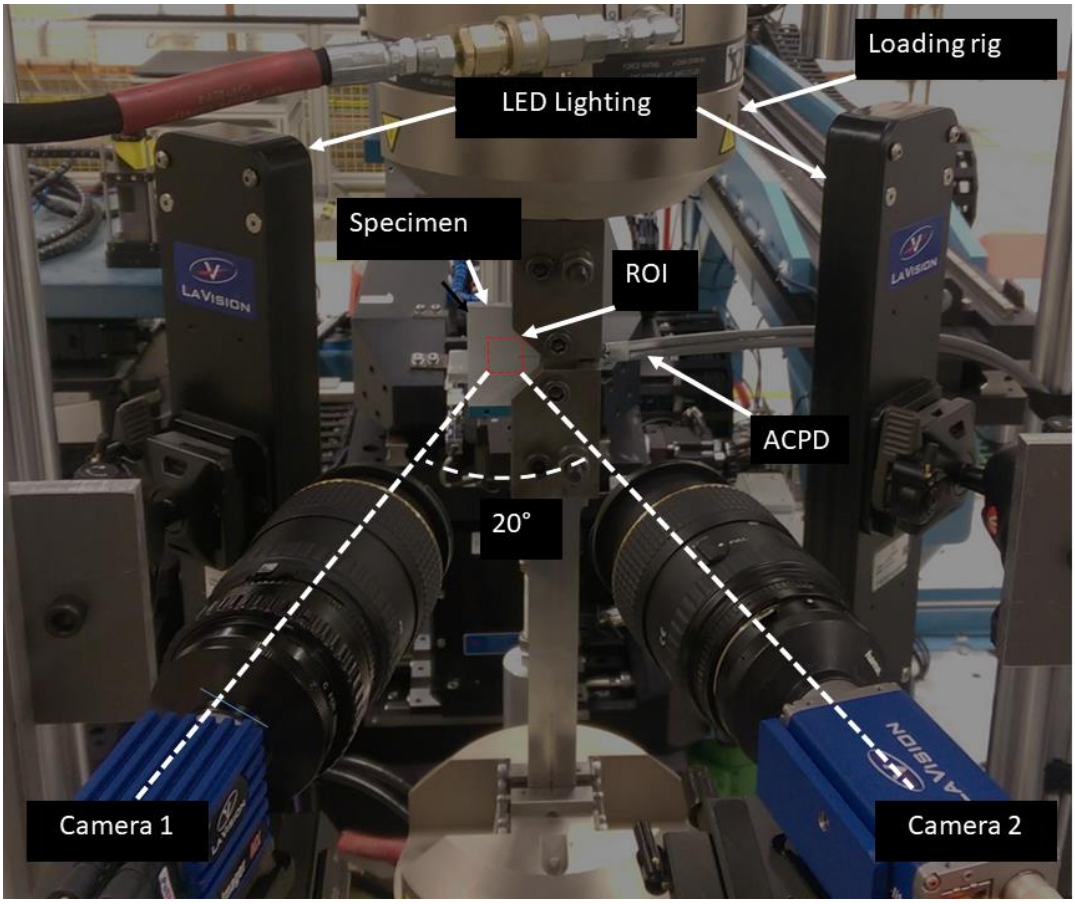

Figure 5.9 Experimental setup of the Stereo-DIC

The LaVision stereo-DIC system (see Figure 5.9) comprised two cameras: a CMOS Imager MX4M capturing an image size of 2048×2048 pixel with a 10-bit depth and a pixel size of $5.5\ \mu m$; and a CCD Imager E-lite 5M which an image size of 2456×2058 pixel with a 12-bit to depth and a pixel size of $3.45\ \mu m$ labelled, Camera 1 and Camera 2 respectively. The cameras were both positioned approximately $340\ mm$ from the sample surface (CCD and CMOS chip to surface), on the same height with a $\sim 20°$ angle between cameras (see Figure 5.9). The aim of this setup was to capture a magnified field of view of the surface, for a higher resolution crack analysis. However, the camera frame and grips did not allow for the cameras to be positioned closer to the surface of the specimen, with a lower working distance. Therefore, extension tubes and an optical lens were used, for both cameras, to increase the magnification of each camera, in effect, increasing the field of view. Each camera was equipped with a macro lens adapter ($15\ mm$ focal length), extension tubes ($36\ mm$ focal length) and a Tokina AF $100\ mm$ F/2.8 macro lens accumulating to a total of $160\ mm$ in focal length. Lighting was achieved by using two 12-LED pulse lights (see Figure 5.9) which were pointed towards the surface of the specimen at an angle, both pulse triggered with the image acquisition power unit.

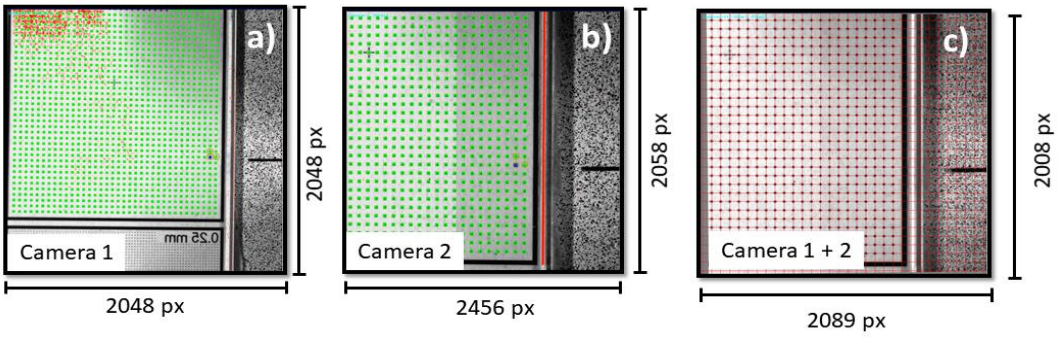

Figure 5.10 Calibration of the Stereo-DIC a) View of the calibration plate from Camera 1 b) View of the calibration plate from Camera 2 c) Summation of the calibrated Camera 1 and Camera 2

Computation of the calibration is accomplished using the in-built LaVision's camera pinhole model. Three calibration image pairs of a LaVision calibration plate, regular dot grid spacing 0.5mm (see Figure 5.10), where different views were captured. The calibration images were imported to the LaVision software where the in-built algorithm detected the regular dot patterns from both Camera 1 and 2 (see Green grid dots in Figure 5.10(a and b)). Three grid dots were selected from both Camera 1 and 2 (Figure 5.10a and b) which are used to map Camera 1 and 2 together while triangulating the images. The thickness of the calibration plate is $z = 1.5\ mm$ and was weighted in the calibration calculation.

Although the two cameras had different pixel sizes, it did not impact the calibration and mapping process which can be seen in Figure 5.10c, where the two cameras calibrated views are summed. It is seen that Camera 1 is de-warped using the triangulation parameters and will be used in the surface displacement calculation. With this set-up, the achieved pixel size was $7.5\,\mu\text{m/pixel}$ on the re-projected images, as determined from the calibration parameters.

The DIC calibration, using LaVision Davis 8.4.0 software, applied the polynomial calibration algorithm and the obtained re-projection error was less than 0.06 pixels and 0.04 pixels for Camera 1 and 2, respectively. The re-projection error is the mean difference between the positions of the calibration marks in the calibration image, after correction, and their known positions.

Stage	Crack length (mm) (ACPD)	Cycles after Overload
PrC	1.50	-
S0	2.37	-
OVL	2.37	-
S1	2.62	2900
S2	2.78	4900
S3	3.49	10200
S4	4.34	16700

Table 32 Evolution of crack lengths for R=0.1

Stage	Crack length (mm) (ACPD)	Cycles after Overload
PrC	1.50	-
S0	2.58	-
OVL	2.58	-
S1	3.05	20000
S2	3.42	32000
S3	4.36	69000
S4	4.86	79000

Table 31 Evolution of crack lengths for R=0.4

Table 32 and Table 31 present the evolution of the internal crack lengths between each stage for $R = 0.1$ and $R = 0.4$ respectively where fatigue cycling was induced to grow the crack. Each stage represents when load shedding methodology was applied. After the experiment, the collected ACPD data, which gives the average crack length through the thickness of the sample, was re-calibrated using the fractography data.

The surface analyses for both samples were recorded once the desired crack length for Stage S0 was acquired. The surface of both the samples was captured using 3D-DIC system: P_{min}; P_{max}; and at each integer load between P_{min} and P_{max}, for stages shown in Figure 5.11. The fatigue cycle was captured for every stage. For $R = 0.1$ and $R = 0.4$, in total, 97 and 110 different load states were captures, respectively.

For every load state or frame number, 50 static images were captured from each camera at 10 Hz. An image averaging technique [198] was applied before the displacement calculation. The procedure is to divide the sum of the multiple images by 50 to obtain one image for each surface load state. The image averaging technique was applied to minimise the inherent displacement errors caused by the CCD/CMOS signal variation.

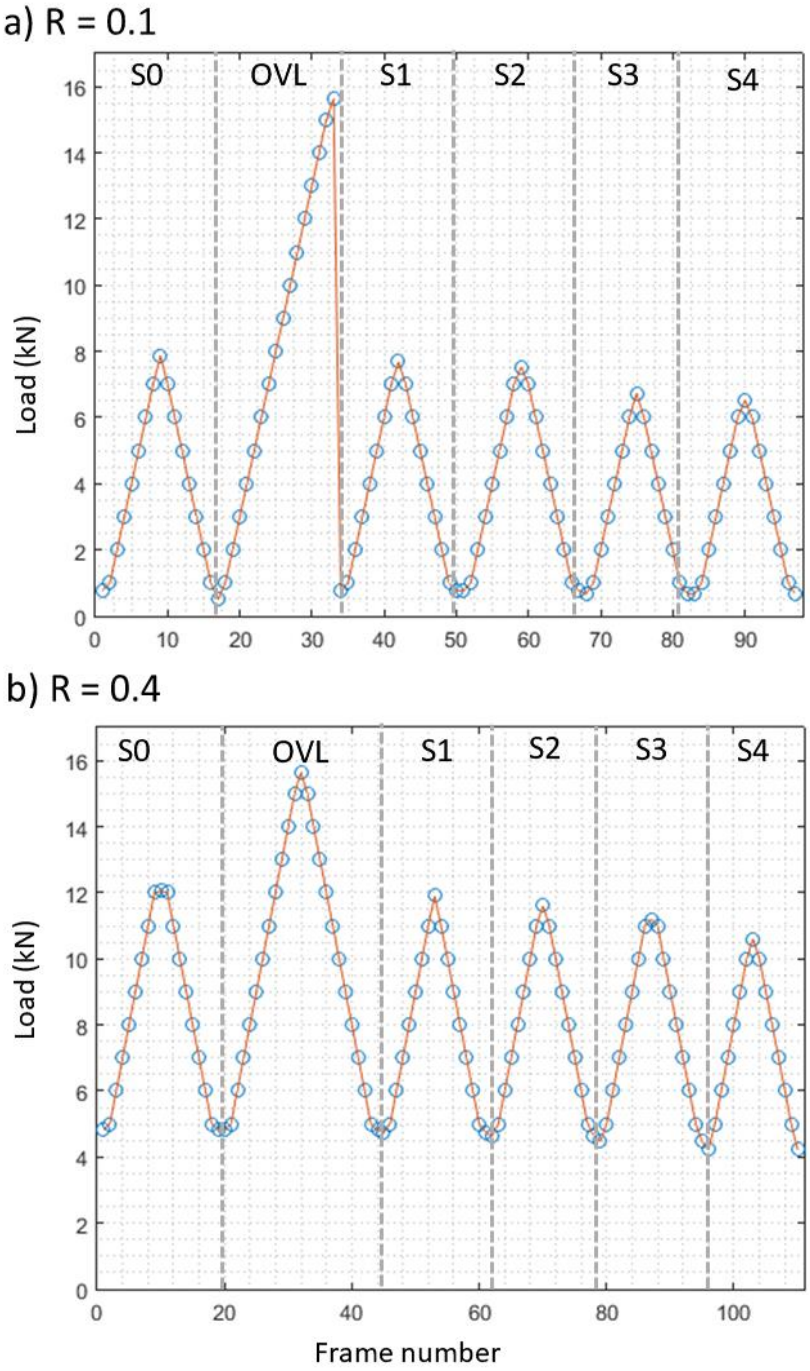

Figure 5.11 Data acquisition of the surface load state a) R=0.1 b) R=0.4

Fractography of the samples were performed by collaborators, where the samples were cooled in liquid nitrogen and were broken open where the fracture surface was observed. The fractography was higher resolution information which was paramount to comparing the crack length on the surface analysis of the sample with crack length calculated by PC-CD and for the re-calibration of ACPD. The re-calibration of the ACPD allowed for the calculation for a more accurate ΔK_{app}.

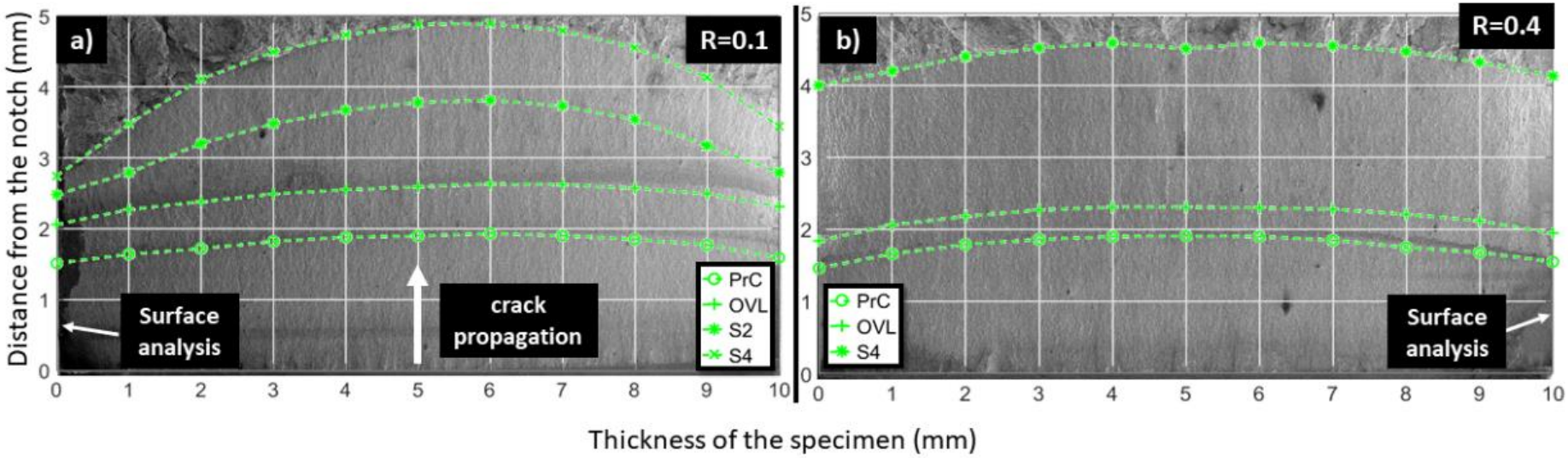

Figure 5.12 Fractography of the fracture surface a) at R=0.1 b) at R=0.4

5.4.2 Analysis and discussion

For both $R = 0.1$ and $R = 0.4$ experimental datasets, the analysis procedure was exactly the same, unless stated otherwise. An image-based region of interest was selected for the displacement calculation measuring approximately $8.5\,\mathrm{mm} \times 9.1\,\mathrm{mm}$, positioned just behind the crack notch tip. This protocol was followed in order to reduce the time complexity and control the data point positioning which in return enables control over the crack length calculation. The reference image for the analysis was the initial image taken ($\mathrm{Frame\ number} = 1$), where the sample was already cracked and under the influence of a small load of P_{min} ($K_{min} = 3$ and $P_{min} = 18$ for $R = 0.1$ and $R = 0.4$, respectively), which was taken under consideration for J-integral calculation. A noise study based on spatial resolution was conducted.

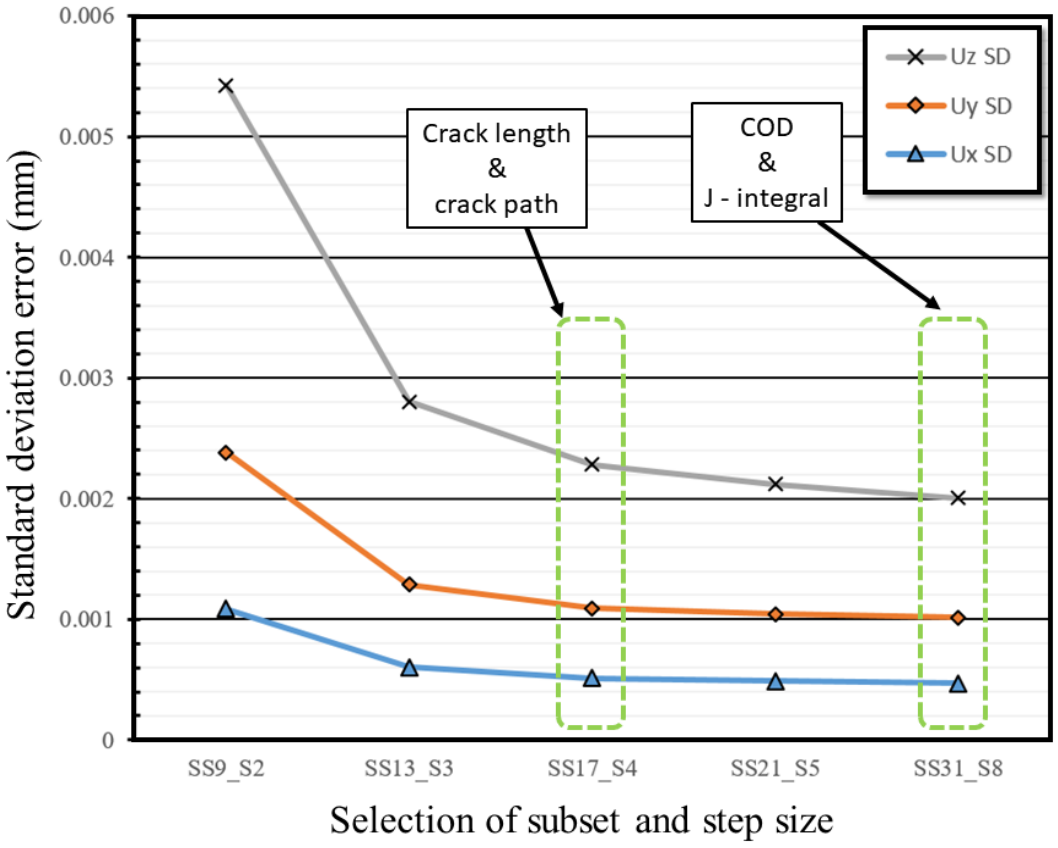

Figure 5.13 Uncertainty analysis with spatial resolution

The objective was to minimise the inherent systematic DIC noise while deviating subset size and step size, keeping overlap constant. The noise study will also be useful for the prediction of expected uncertainty for the crack parameter calculations. A rigid body motion was applied to the specimen, $R = 0.4$, and displacement field of the rigid body motion was calculated using five different parameters; Subset size: $9, 13, 17, 21, 31$ with their respective step size parameters; $2, 3, 4, 5, 8$. (same parameters specified in section 4.7). Standard deviation of each Ux, Uy and Uz displacement field was then calculated and is depicted in Figure 5.13. As expected, it is seen in Figure 5.13, that a larger subset size provides higher displacement certainty, but the study shows where the difference in certainty between subset size is negligible.

Two Stereo - DIC analysis were considered. smaller subset with higher spatial resolution to find the crack length and crack path to compare with the fractography data and also to feed in the crack path for J-integral calculation (see section 3.11). A larger subset with higher displacement certainty was used to obtain COD and also the displacement field imported into an FE model for the calculation of J-integral values. Davis 8.4.0 strain master was used to obtain two stereo-DIC analyses of both $R = 0.1$ and $R = 0.4$ datasets; Subset size 17 with a step size of 4 and Subset size 31 with a step size of 8 as identified in Figure 5.13 . The PC-CD was employed iteratively and automatically to all the displacement fields to detect and extract the crack parameters; Crack path, crack length and COD. The orientation of the crack was specified by the user and outlier deletion was not used in the analysis. The parameters for PC-CD were all kept at their default values, i.e. $\lambda_{\min} = 4$, $\mathrm{d_{PC}} = 1.2$, $Itern = 200$, $\alpha_{\mathrm{seg}} = 0.8$.

The PC-CD calculated crack lengths for $R = 0.1$ and $R = 0.4$ are depicted in Figure 5.14(a and b). It is important to note that the figure is not a direct representation of the physical crack length of the sample, but in fact, observed crack length at the surface by stereo-DIC with respect to load. Normally, the crack length at the surface of the sample can be approximated at P_{max}, when the crack faces are not in contact. However, as the load is decreased, the crack physically closes, and the crack faces are in contact starting at the crack tip, decreasing the observed crack length. This is due to the crack closure effects caused by the fatigue crack growth. Even though the specimen is applied a small load (P_{min}), the crack appears fully closed as the zone has residual compressive stress and is unable to be measured by PC-CD.

As seen for S0, before overload was exerted to the specimen, the crack was peeled open as the load was increased to P_{min}, but then fully closed as the load was decreased to P_{min} (Figure 5.14a and b). The overload was then applied to the samples, however, a change in crack length was not observed at the surface of the sample. The causation is that the overload blunts the crack tip and creates a large plastic field ahead of the crack tip.

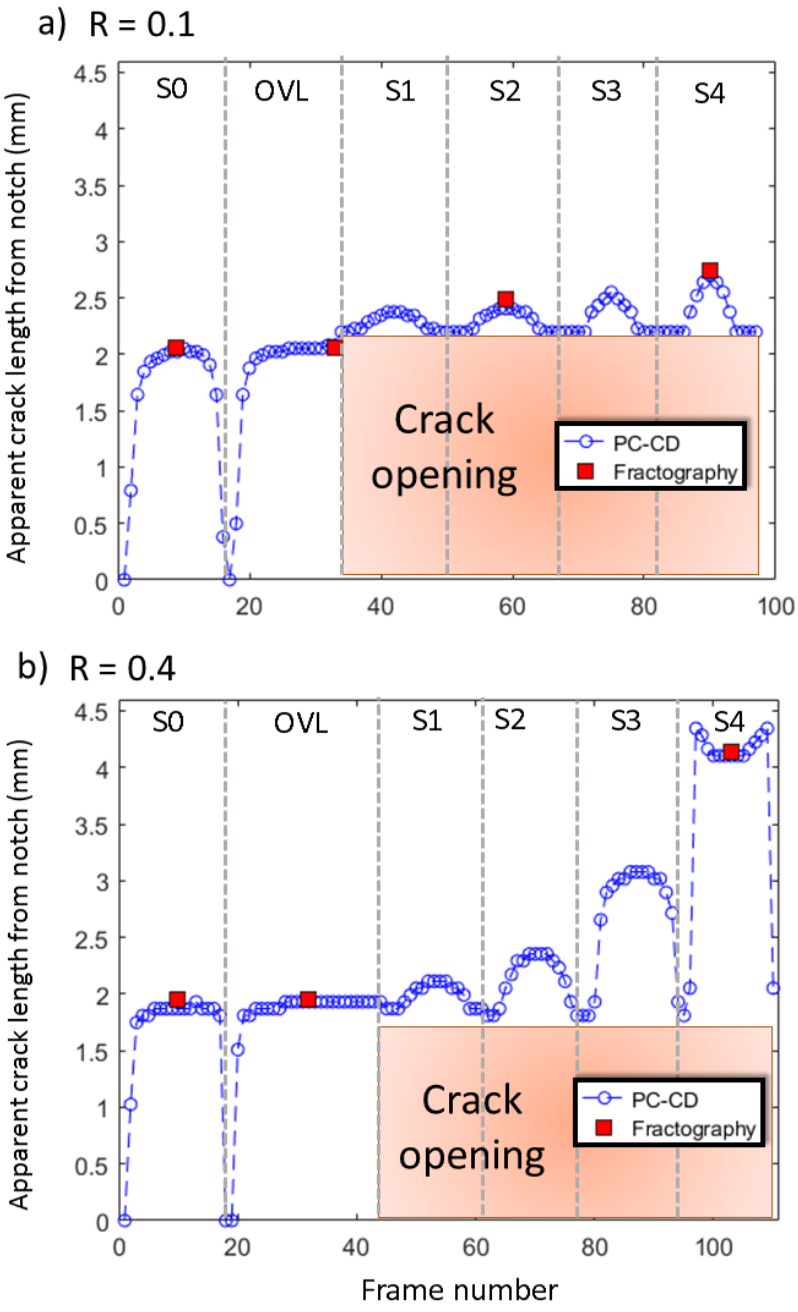

Figure 5.14 Crack length measurement of the surface of different load states a) R=0.1 b) R=0.4

The crack was then grown incrementally past the plastic zone, (i.e. S1, S2, S3, S4), however as seen through the crack length information (see Figure 5.14a and b), the plastic zone was keeping the crack faces apart at P_{min} (from crack notch to approximately the blunting area for both R ratios) as it was detected as a surface discontinuity by PC-CD. Figure 5.14 also shows the change of P_{open} and P_{close} loads, which are at loads where a crack starts to open and close, phenomenon explained in [199, 200] observed to change as the crack is grown past the plastic zone, applied by the overload.

The crack length on the fracture surface (see Figure 5.12) was manually measured (distance from notch to crack tip) in the higher resolution fractography data ($1.5\ \mu\mathrm{m/pixel}$) to compare with the PC-CD analysis. It was seen in the fractography data that the crack tips were in strong agreement with both $R = 0.1$ and $R = 0.4$ giving an average crack length error of $0.0441\ \mathrm{mm}$ and $0.0418\ \mathrm{mm}$, respectively between the two different observations. However, for $R = 0.4$, Stage 4 (see Figure 5.14b), PC-CD crack length data points gave inconsistent results as the load was lowered to P_{min}. This is strongly in relation with the sensitivity of Phase congruency to discontinuities and features. Figure 5.15(a and b) depict the displacement field (calculated with subset size 31 and step size of 8) of P_{min} and P_{max} for stage 4, sample $R = 0.4$, used to highlight the discontinuity via Phase congruency.

In this situation, Phase congruency appeared to have extended the crack segmentation to include the non-linear displacement field ahead of the crack tip as part of the discontinuity (see Figure 5.15a). Based on the PC-CD crack length data, $R = 0.1$ crack growth on the surface of the cracked body was significantly lower compared to the $R = 0.4$ data which was satisfied by the fractography data. The PC-CD crack length is incomparable with the ACPD data as they observe different areas of the crack. ACPD calculates the average crack length through the thickness while PC-CD calculates the crack length on the specimen surface. The fractography data shows that the crack front was elliptical during pre-cracking stage.

Figure 5.16a and Figure 5.17a depict the COD profiles for each frame number and all fatigue stages, respectively of $R = 0.1$ and $R = 0.4$. The calculation was made using the higher certainty displacement field data (Subset size 31, step size 8) and a static PC-CD crack segmentation obtained at P_{max} at last stage was used. The maximum segmentation acts as a selection of data points and as the sample surface is under the influence of deformation, the selected data points act as a virtual clip gauge across the propagating crack. Crack opening displacement profiles are plotted at P_{min} and P_{max} at each stage as shown in Figure 5.16(b and c) and Figure 5.17(b and c) for $R = 0.1$ and $R = 0.4$ respectively. The crack opening displacement profiles, with the exemption of $R = 0.4$ stage 4, agreed with the crack length measurements calculated previously.

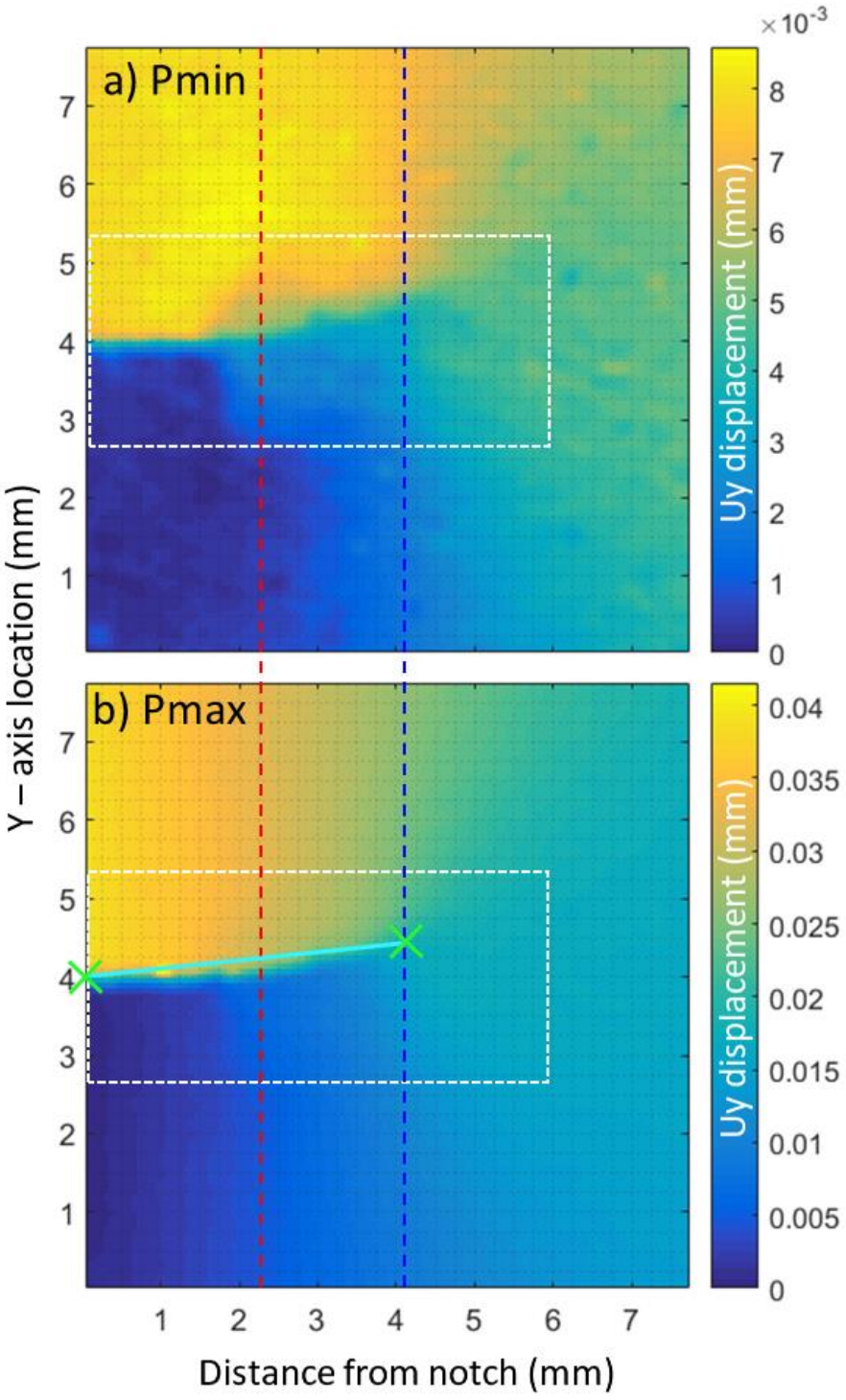

Figure 5.15 Uy displacement field of sample R=0.4 at stage 4 a) Pmin , b) Pmax Red dashed line -location of overload, blue dashed line - location of the crack tip using fractography data, white dashed area - selected region to re-mesh area for the J-integral calculation, Green cross – crack mouth and tip locations calculated by PC-CD, Cyan line – crack path used to calculate the J-integral

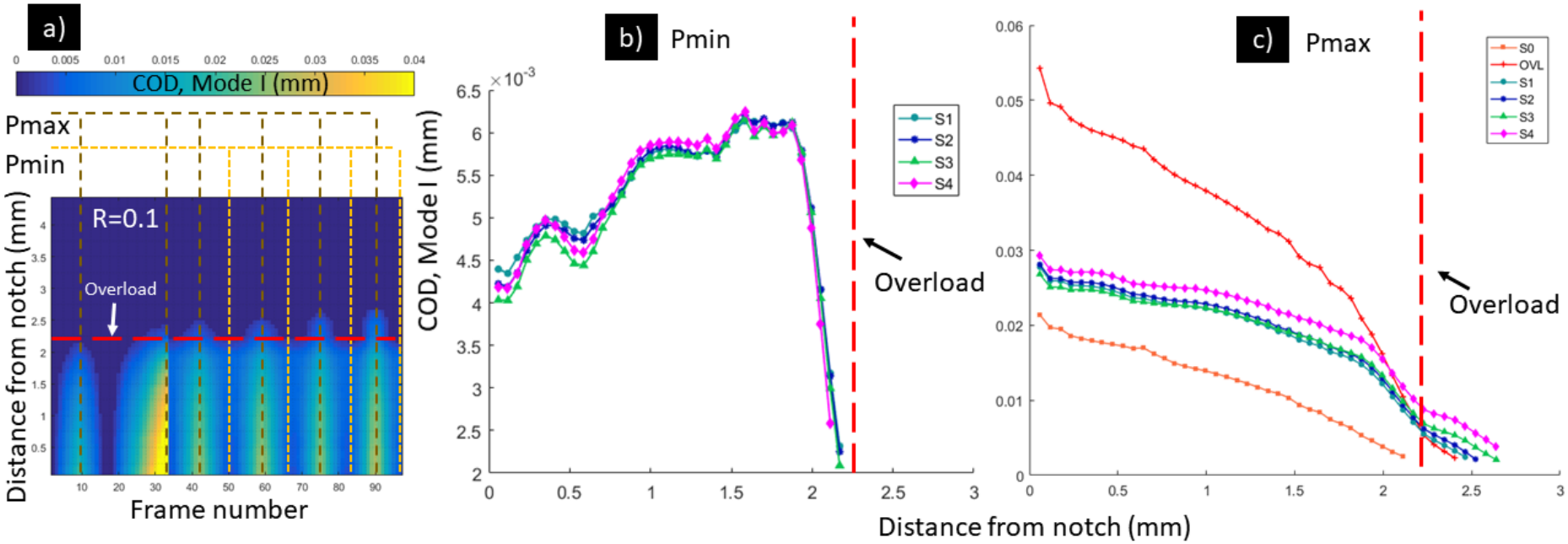

Figure 5.16 Mode I Crack opening displacement for R=0.1 a) COD profile for all the frame numbers , b) COD profile for each stage at Pmin c) COD profile for each stage at Pmax

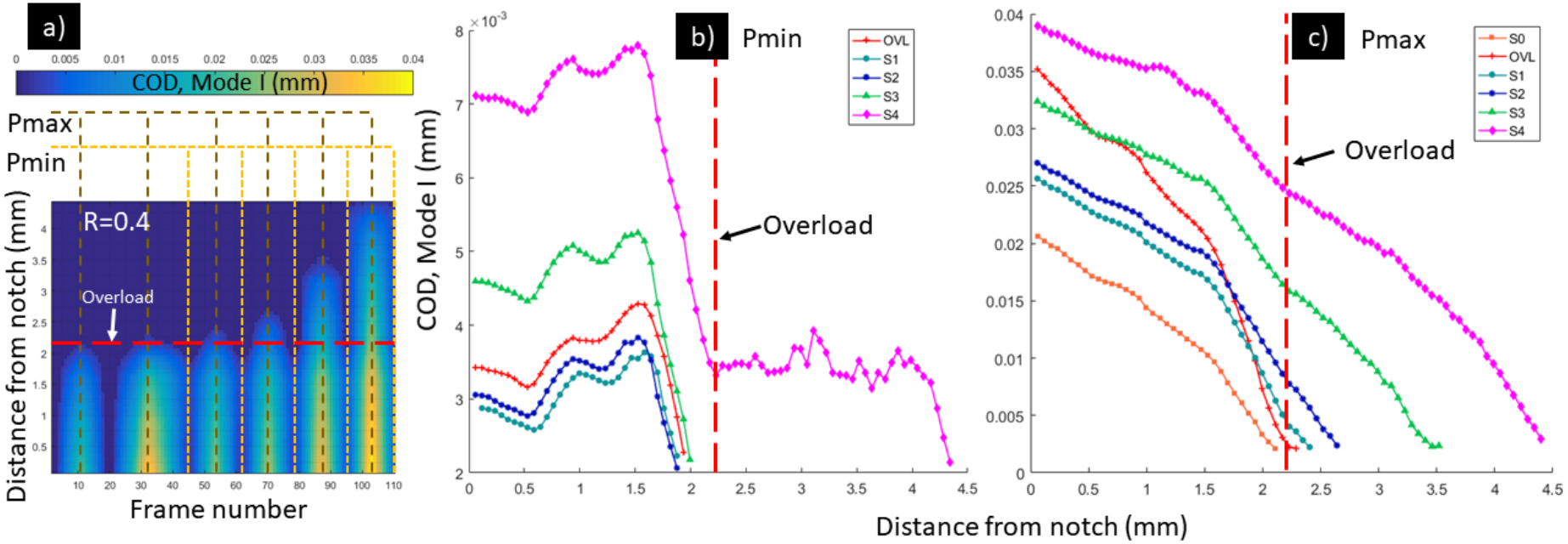

Figure 5.17 Mode I Crack opening displacement for R=0.4 a) COD profile for all the frame numbers , b) COD profile for each stage at Pmin c) COD profile for each stage at Pmax

Observation of P_{min} in Figure 5.16b and Figure 5.17b indicates that the crack opening was higher, closer to the overload location compared to the opening at the crack mouth. While P_{min} opening profiles stayed constant as the crack was grown in each stage for $R = 0.1$, the opening displacement increased in magnitude for $R = 0.4$. It is also observed that once the crack had grown beyond the plastic region, the plasticity kept the newly grown crack faces apart (i.e. $R = 0.4$, S4). The same phenomenon was not observed in the surface analysis for $R = 0.1$ as the majority of the crack growth was proceeding in the middle of the sample as verified by fractography data (see Figure 5.12).

Figure 5.16c and Figure 5.17c show the maximum opening displacements for $R = 0.1$ and $R = 0.4$ respectively. For both R ratios, S0 at P_{max} crack opening displacement profiles are completely identical, which is expected as the 3D-DIC calculation was made of the intra-cycle of stage 0 and for both samples at a constant $\Delta K_{app} = 27\ \mathrm{MPam}^{1/2}$ was applied onto the cracked body. The COD profile of both R ratios at overload were different even though the same K was applied, this is due to difference in K at P_{min}. The COD at overload of $R = 0.1$ was representative of $57\ \mathrm{MPam}^{1/2}$, while $R = 0.4$ was representative of $42\ \mathrm{MPam}^{1/2}$. It was seen for $R = 0.1$ and $R = 0.4$ that some compressive forces acted near the overload location at P_{max}. The COD profiles at P_{max} for $R = 0.4$ showed a larger change of $0.015\ \mathrm{mm}$ in opening displacement as the crack was grown while for $R = 0.1$, the change was as small as $0.0025\ \mathrm{mm}$. This was expected, as the crack was applied a higher load and the crack length was longer at the surface analysis for $R = 0.4$.

The impact of mode II and mode III was investigated on the controlled mode I fatigue crack growth overload for both $R = 0.1$ and $R = 0.4$. To accomplish this, the crack opening displacement profiles were extracted from the Ux (mode II) and Uz (mode III) displacement fields for each frame number and all the fatigue stages.

The crack segmentation used to extract the mode I opening for $R = 0.1$ and $R = 0.4$ (i.e. Figure 5.16a and Figure 5.17a respectively) was utilized by PC-CD. Figure 5.18 shows the extracted mode II and mode III opening displacement for both $R = 0.1$ and $R = 0.4$. It is observed that mode II for both $R = 0.1$ and $R = 0.4$ (Figure 5.18a and c) the maximum crack opening from all the surface composition is almost 15 times smaller than the maximum mode I crack opening (Figure 5.16a and Figure 5.17a). While the maximum opening of mode III for $R = 0.1$ (i.e. Figure 5.18a) is observed to be more than 500 times less than the maximum opening of mode I (i.e. Figure 5.16a). However, it's important to note that the maximum opening of mode III for $R = 0.1$ $(5.9 \times 10^{-5} mm)$ is much lower than the uncertainty analysis forecasted observed at subset size 31 for the Uz displacement field (i.e. Figure 5.13). For $R = 0.4$,the majority of the crack opening in mode II and mode III (Figure 5.18c and d) is observed to be between 2.5mm and 4.1mm away from the crack notch. This effect can be further backed up by observation of the crack path in Figure 5.15.

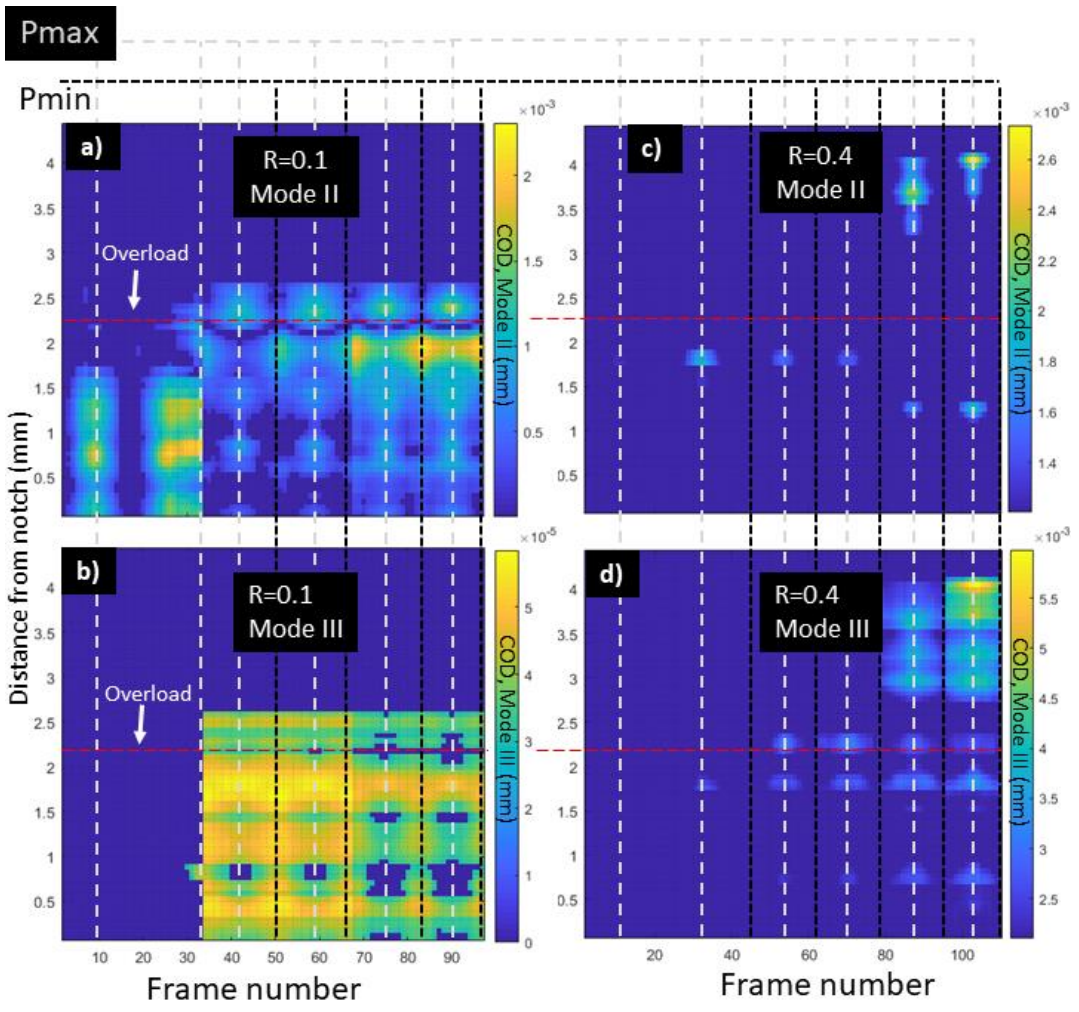

Figure 5.18 Mode II and Mode III Crack Opening Displacement profiles of R=0.1 and R=0.4 a) Mode II COD for all the frame numbers of R=0.1, b) Mode III COD for all the frame numbers of R=0.1, c) Mode II COD for all the frame numbers of R=0.4, d) Mode III COD for all the frame numbers of R=0.4

The crack path appears to have propagated diagonally (0.3mm in the y-direction), between 2.5mm and 4.1mm away from the crack notch. It can be concluded that the impact of mode II mode III was minimal on the experiment.

Higher certainty displacement fields for both $R = 0.1$ and $R = 0.4$ (Subset size 31) was imported into ABAQUS 6.14-2 using OUR-OMA (section 3.11), where the crack mouth and crack tip location (see Figure 5.15b marked as the green cross for P_{max}) for each load was automatically found using default PC-CD parameters. Each J-integral calculation was performed using linear elastic properties (see section 1.1) with plane stress, $E = 210$ GPa, $\nu = 0.3$ where the J-integral contours were only taken from the values inside the "Free to deform region".

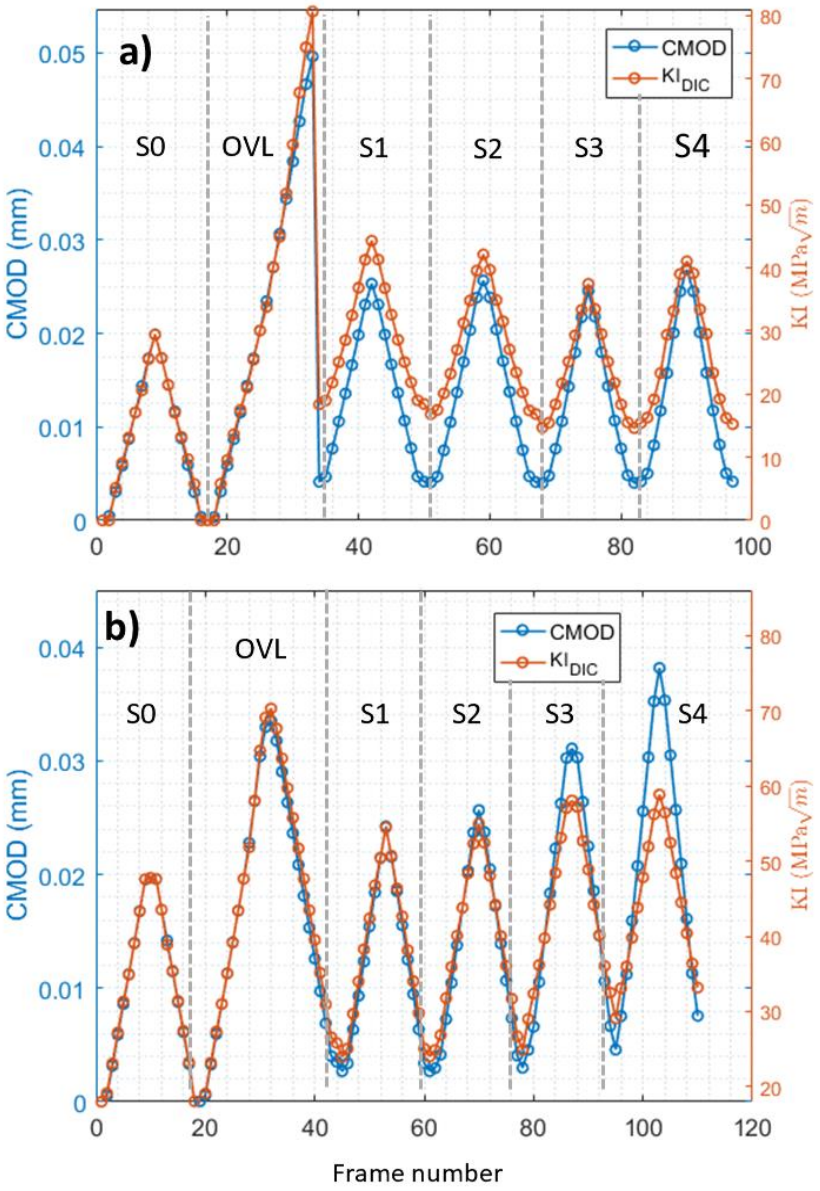

Figure 5.19 Mode I Stress Intensity Factor and CMOD obtained from DIC a) R=0.1 , b) R=0.4

The plastic field (i.e. impact of local crack closure and overload) was fully deleted and therefore the J-integral calculation is representative of the global field measure of the energy release rate. The deleted area is marked by the white dashed area in Figure 5.15(a and b). The deleted area was FE mesh refined locally around the crack path (i.e. Cyan line, Figure 5.15b). The J-integral calculated was performed over several contours to check for contour independency. It was seen for all image frames, that the J integral values converged after 5 contours. The application was fully automatic due to the combination of PC-CD and OUR-OMA to calculate the J-integral values. The percentage of uncertainty of the global measure of the J-integral values was approximated to be $\sim 4\%$ using the benchmarked guideline in Ref. [2]. The uncertainty of crack tip positioning (~ 6 pixel error calculated by the fractography data)) and elastic model uncertainty are considered. To be able to compare the J-integral values with the CMOD, the values were converted to stress intensity factor using the following equation;

$$K = \sqrt{J * E'} \qquad (57)$$

where $E^{'} = E$ for plane stress conditions. Figure 5.19(a and b) depicts the comparison between K_I calculated via OUR-OMA and CMOD using the higher displacement certainty (i.e. Subset size 31). The CMOD measurements were taken from the PC-CD data. The limits of the secondary axis (i.e. K_I) was configured so that for Stage 0, both K_I and CMOD data points were aligned. This allows for the study of the overload.

5.5 Conclusion

The characterisation and quantification of cracks from image-based experiments improve the understanding of their behaviour. This chapter has shown that using a combination of displacement fields and the novel PC-CD method is a powerful tool of extracting the geometrical parameters of a crack but is also versatile. PC-CD method helped with the automatic extraction of the crack parameters and the extraction was shown to not only be limited to linear-elastic or brittle failure mechanisms but also can be applied to elastic-plastic fracture, crack blunting and crack closure. For elastic-plastic fracture mechanics, the application of PC-CD is beneficial as measurements such as crack opening displacement (in mode I, II and III) and the J-integral can be obtained. Due to the automation of the PC-CD method, the application can be administered to fracture experiments in real time, which can be a decisive tool to propagate a crack in a controlled manner.

6 APPLICATION OF VPC-CD TO EXPERIMENTAL VOLUME DISPLACEMENT FIELDS

6.1 Introduction

Previously, the research carried out in this thesis applied the PC-CD method to displacement measurements of surface cracks automatically without user judgement. The idea was to show the applicability and the proof of concept of this method in the analysis of displacement measurements of volume cracks. The following chapter depicts the volume crack study of two different material classes; ductile and quasi-brittle.

6.2 Ductile Material: Al-Ti Metal matrix composite

The experimental work was carried out at the Joint Engineering, Environmental and Processing (JEEP – I12) beam line at the Diamond Light Source in the UK [63]. Two aluminium double edge specimens with Titanium particles, one with a long notch and the other with a short notch, were loaded until fracture. Limited-angle X-ray tomography scans were recorded, before and after fracture to enable the calculation of volume displacement field. VPC-CD was used to demonstrate the calculation of the crack opening displacement in the thickness, the location of the crack surface and the crack front from the measured volume displacement fields of both specimens. The displacement analysis of the short notch was conducted with high spatial resolution (i.e. cubic subset size of 32^3 pixels)., while the analysis for the long notch required higher spatial resolution of cubic subset size of 16^3 due to the small size of the crack before failure.

The crack surface location obtained from the VPC-CD analysis was superimposed to the deformed tomograph of the cracked body. The comparison between the two showed a strong agreement. The semi-autonomous crack analysis from the dataset revealed the complex mechanics of the crack. The displacement field of the small notch was coupled with the crack parameters obtained from VPC-CD and was imported into Abaqus FE software package (version 6.14) slice by slice using the methodology detailed in section 3.11. The inelastic (Ramberg-Osgood) material law was applied to account for the large yielding observed in the displacement field. Domain integral of each slice through the thickness was calculated from the FE model giving a unique comprehension to describe the structural integrity of the fractured body through its thickness.

6.2.1 Experimental details

A newly developed material, Metal Matrix Composite (MMC) of an aluminium with titanium (named Al-Ti) is studied. The combination of different X-ray attenuation of aluminium and titanium evenly distributed throughout the aluminium matrix made the Al-Ti material particularly suitable for DVC analysis. According to ASTM E8 [201], the Al-Ti material parameters and the Ramberg-Osgood relationship were calculated to be: Young's modulus of $E = 100$ GPa; Poisson ratio of $\nu = 0.3$; Yield strength of $\sigma_0 = 103$ MPa; yield offset of $\alpha = 2.75$ and hardening exponent of $n = 6$.

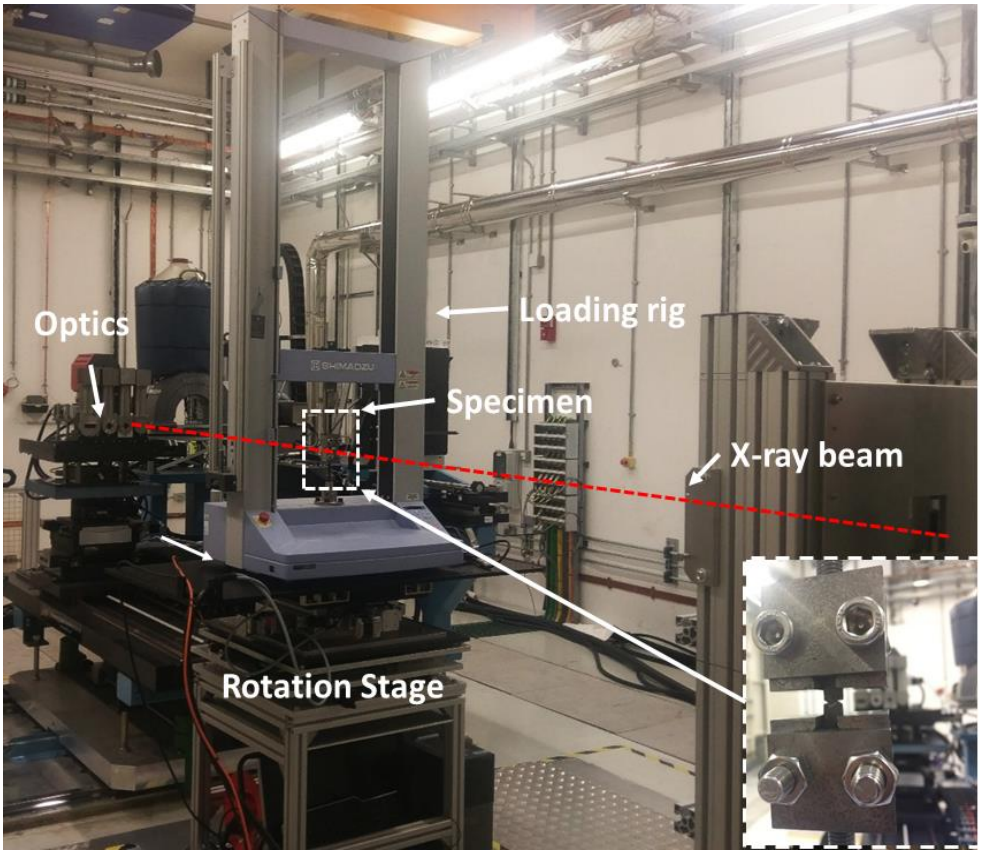

Figure 6.1 Experimental setup in EH2, I12, DLS with a fractured specimen inside the loading jig (b) specimen dimensions, a is the crack length, W the specimen width and b its thickness c) Loading jig

The experiment, setup is shown in Figure 6.1, was designed to compare the fracture behaviour of a metal matrix composite (Aluminium matrix with titanium particles) in four different sample conditions: thick specimen with short and long notch (i.e. standard specimen), thin specimen with short and long notch. Due to the unavailability of the Instron $100\ \mathrm{kN}$ loading frame originally planned for this experiment, a $10\ \mathrm{kN}$ Shimadzu loading frame was installed on the rotation stage. This meant only the thin specimens ($b = 5\ \mathrm{mm}$ – see Figure 6.2) could be tested as the thick specimens ($b = 20\ \mathrm{mm}$) required much higher loads than $10\ \mathrm{kN}$ to initiate the fracture.

The test specimen (see Figure 6.2b) was designed to facilitate tomography observations whilst the load was increased until initiation of the fracture. Two thin specimens ($b = 5\ \mathrm{mm}$) with two different notch lengths (a – see Figure 6.2b) were tested: $a/W = 0.1$ and $a/W = 0.5$ ($2W = 8\ \mathrm{mm}$). A small load of $50\ \mathrm{N}$ was applied to remove any rigidity from the experiment to minimise the rigid body motion between the reference and deformed tomographs.

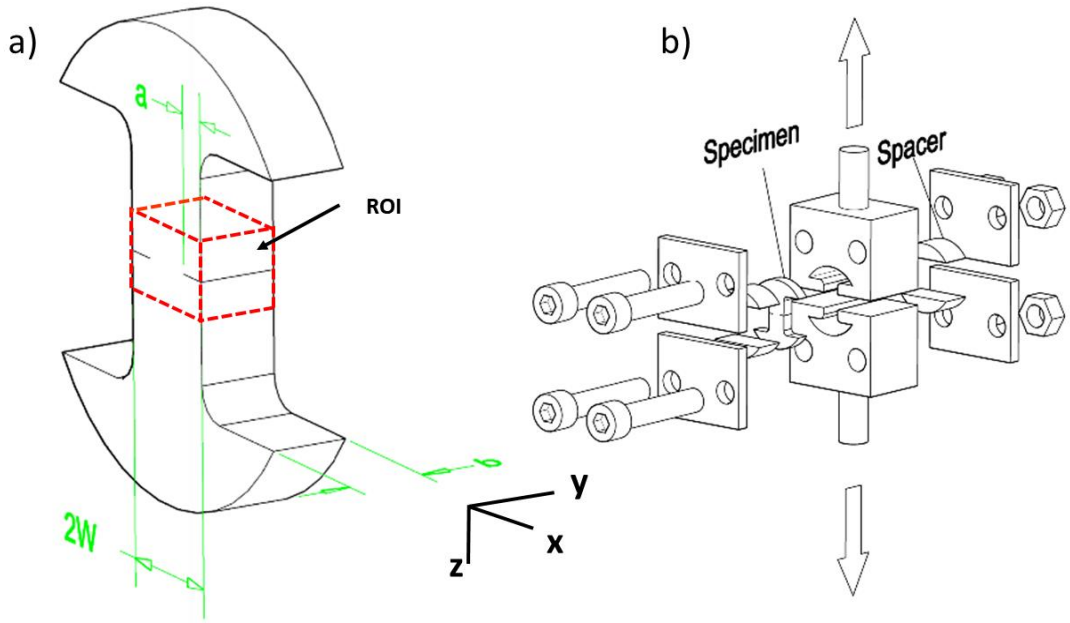

Figure 6.2 Experimental Setup a) Specimen geometry, a is the crack length, W the specimen width and b its thickness , b) Schematic view of the loading details

Radiographs were recorded using a PCO4000 CCD camera (2560×2160 pixels, 16-bit depth), with Module 3 optics selected to image an area of 8.3×7.0 mm (i.e. 3.25 μm per pixel). However, the loading frame obstructed $34.5°$ of the incident beam, resulting in limited angle tomography with $145.5°$ being carried out; 2500 projections were recorded with 0.05 seconds exposure at 61.86 keV. The samples were loaded in tension progressively and observed by radiography to detect the onset of cracking from the notch. Tomographs of the sample with short notch ($a/W = 0.1$) were recorded at loads 50 N and 6200 N while the sample with the long notch ($a/W = 0.5$) was recorded at loads 50 N and 3500 N. The image reconstruction code was modified by Diamond Light Source staff to cater for the limited angle tomography where the obstructed views were interpolated within the sinogram.

6.2.2 Analysis and discussion of Al-Ti - Short notch

Both before and after deformation tomographs for $a/W = 0.1$ was applied a rotation of $15.2°$ anti-clockwise around the $Z -$ axis (co-ordinate system shown in Figure 6.2) in three-dimensional space to ensure the crack surface was at the same orientation as the XZ – plane allowing for the separation of different modes of fracture. The new tomographs, Load 50 N and 6200 N, (see Figure 6.3) each bore the dimension of $2560 \times 1550 \times 2000$ pix (8.32×6.5 mm) covering the full thickness of the sample and the crack was visually observed to be developing behind both notches. Each tomograph was bi-cubically down-sampled from 16-bit to 8-bit data set (i.e. 0 and 255) to speed up the DVC analysis. A 3D median filter with a radius of 2 pixels in all three dimensions was subsequently applied to the down-sampled data. The 3D median filter was used for noise reduction while preserving the titanium particle features, seen as high intensity features in Figure 6.3.

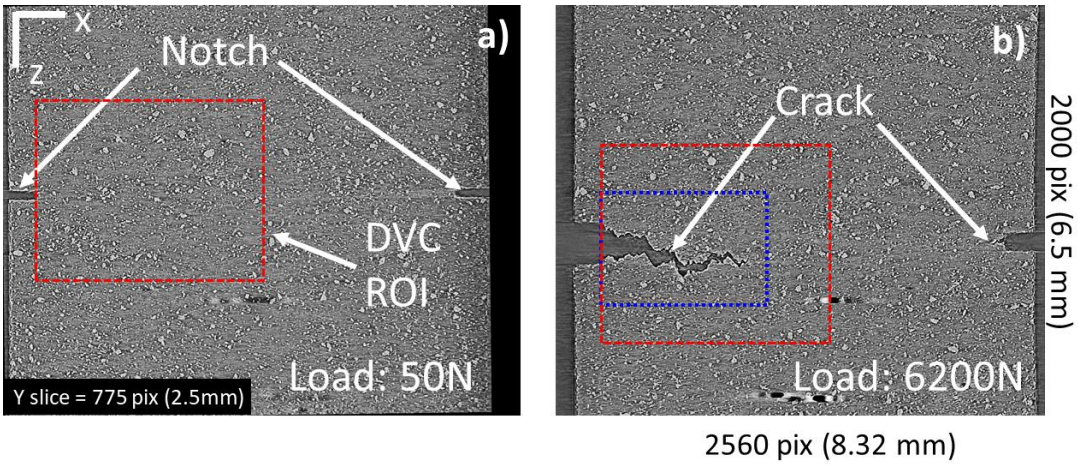

Figure 6.3 X-ray Tomographs of short notch at Y slice = 775 pix (2.5mm) a) Reference tomograph at 50N load , b) Deformed tomograph at 6200N

The longer crack was assessed for the VPC-CD analysis and therefore a region of interest measuring $1050 \times 1550 \times 900$ pix depicted by the red dashed line (see Figure 6.3) was cropped from both reference and deformed tomographs. The further cropped tomography data were used in the DVC analysis to retrieve displacement fields.

The DVC analysis was performed using the LaVision DaVis (Version 8.3.0) software, employing a multipass FFT-based algorithm; the first pass used cubic subset size of 256^3 voxels with an overlap between subsets of 50%, second pass 128^3 voxels with an overlap of 80%, a third pass 64^3 voxels with an overlap of 80% and a final pass of 32^3 with an overlap of 80% which gives 6 voxels spacing between each data point. This displacement dataset will be labelled as V32 for the rest of this section. All points with a correlation coefficient below 0.8 were discarded (i.e. set to NaN values). The displacement field was then corrected for small rigid body displacements and rigid body rotations, measured relative to the reference, based on the algorithm described in [202].

The full thickness ($Y-$ axis slices) of the specimen for the reference tomograph was partially not captured as the specimen partially moved outside of the field of view during tomography. The DVC analysis produced 213 data points instead of 258 data points, missing 45 data points from the full thickness of the specimen. The missing data points equated to approximately 272 pix (0.85 mm) that ranged 1278 pix to 1550 pix from the end of the specimen. The region of missing geometry of the specimen is identified in Figure 6.4. The missing displacement data points did not affect the crack detection or the analysis procedure and therefore was not investigated further in this research. The V32 displacement field was specifically used to employ the VPC-CD algorithm and approximate the crack surface location (i.e. elevation) and crack opening displacements in three fracture modes.

A further DVC analysis was performed with larger subset size (labelled V64) to calculate the stress intensity factor through the thickness of the sample. The larger subset size consisted of much more accurate displacement values and can be imported into an FE model using the methodology outlined in section 3.11. The V64 DVC analysis used the same tomography images as the previous DVC analysis (i.e. V32), however only the first three passes were considered. Therefore, the final pass was cubic subset size of 64 with an overlap of 80% (V64)). Similarly to the V32 DVC analysis, the V64 DVC analysis also presented missing data points caused by the missing geometry. The average uncertainty (standard deviation of Ux, Uy and Uz after rigid body motion) for both DVC measurements was calculated to be 0.0042 mm (i.e. 0.13 voxels) for V32 and 0.0015 mm (i.e. 0.046 voxels) for V64.

The V32 displacement dataset was used previous in section 3.9 as an example to show how the VPC-CD was employed to displacement fields. It was observed that the discontinuity was successfully extracted, and the crack's geometrical parameters are presented in this section for further discussion and analysis. Visual inspection of the cracked tomograph showed that

crack opening behind the notch was observed to be much larger than 100 pix which caused erroneous displacement field values at the location of the discontinuity. The removal of the spurious displacement values intensified at the crack location was accomplished by the outlier deletion and recovery procedure.

The VPC-CD analysis of the crack elevation depicted in Figure 6.4, shows an almost semi-elliptical and symmetric crack front where the line of symmetry is at $Y = \sim 2.05\ \mathrm{mm}$. The crack length varied through the thickness of the sample where the minimum and maximum crack length was $1.57\ \mathrm{mm}$ and $2.51\ \mathrm{mm}$ relative to notch. The crack elevation also indicated that the crack surface was complex and convoluted through the thickness of the sample, where the elevation range was $\sim 1.2\ \mathrm{mm}$.

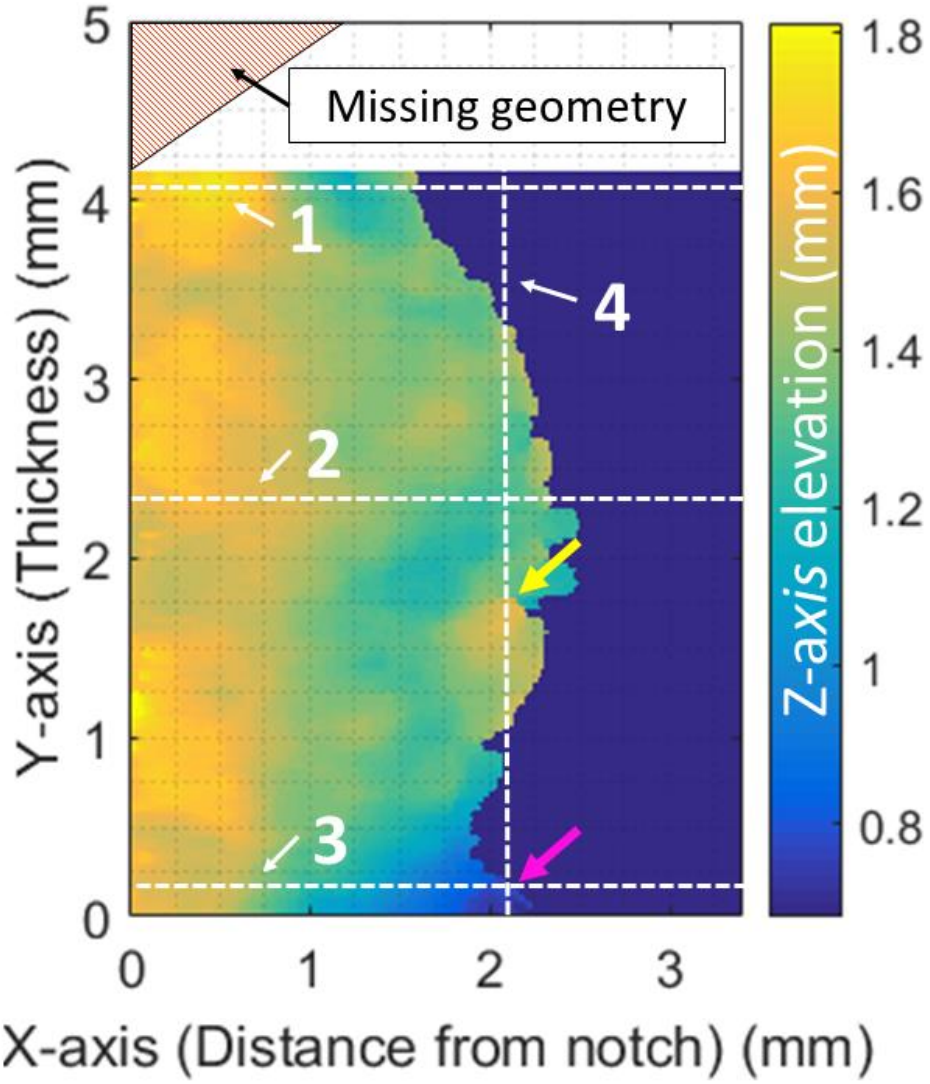

Figure 6.4 Crack surface elevation of short notch crack with labelled slices

Crack surface extracted from the proposed method was validated by superimposing the crack surface location calculated by VPC-CD to the deformed tomograph. Four 2D slices of the deformed tomograph, all slice orientations normal to the crack surface, are taken to help with the visualisation. The location of the four 2D slices are in Figure 6.4 distinguished with a white dashed line, all labelled 1 to 4. The first three slices, shown as horizontal white dashed lines, are in the XZ – plane, the region of interest depicted by the blue dashed area in Figure 6.3. The first three slices are at different locations through the thickness, $y = 4.08$, 2.32 and 0.19 mm respectively. The slices are selected to show the agreement between VPC-CD and visual inspection through the thickness. The superimposition of the crack path on each individual tomograph slice are shown in Figure 6.5(a, b and c), respectively, which shows a good agreement.

A further tomograph slice (i.e. slice 4, Figure 6.4) is chosen perpendicular to the first three slices to evaluate the crack front and observe the discontinuous crack surface. The discontinuous crack surface is identified by the yellow arrow, Figure 6.4, where the VPC-CD showed a sudden change in crack elevation at $X = 2.11$ mm. The purple arrow, in Figure 6.4, highlights the location where a large change in crack elevation was observed through the thickness of the specimen. The tomograph slice of the labelled slice 4 is shown in Figure 6.5d, where once again, a strong agreement was observed between VPC-CD crack path and visual inspection. The yellow arrow points towards the discontinuous crack surface near the middle of the thickness of the sample. The purple arrow points towards the crack near the sample surface where a large change in elevation is observed, almost completely in alignment with the VPC-CD crack path, validating the VPC-CD crack surface analysis. However, the tomograph slice (see Figure 6.5d) also shows a full fracture between the yellow and purple arrows and the same is not observed in the VPC-CD crack surface analysis. The discontinuity signal direction (i.e. $Z-$ axis) was checked and no discontinuity was observed in the same region. A good reason for the absence of the crack surface is due to the change of the crack opening direction from purely $Z-$ axis to the combination of Z and Y axis where the discontinuity signal is lost within displacement noise.

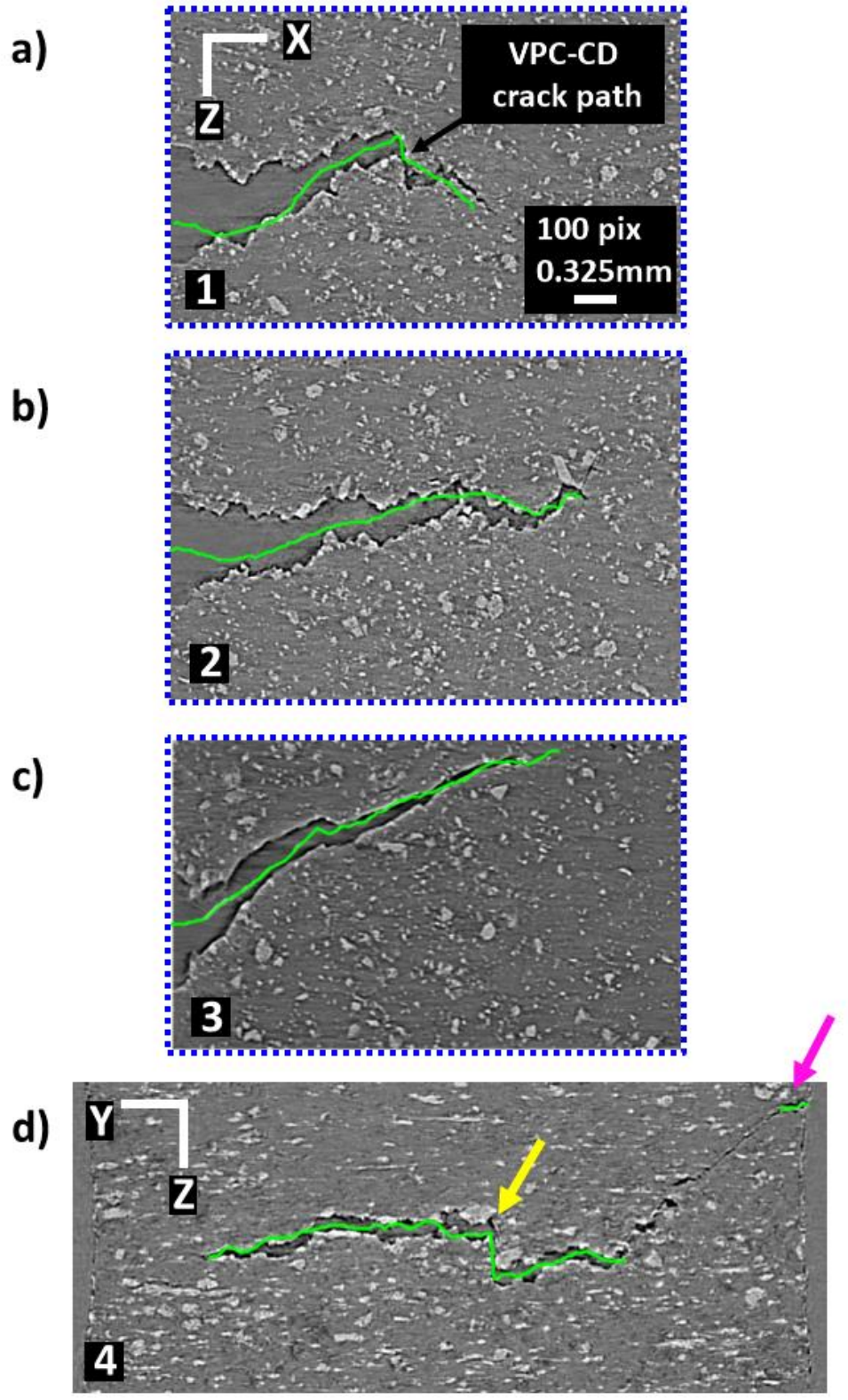

Figure 6.5 Crack surface superimposed on the tomograph slices shown in Figure 6.4, Horizontal white dash line profile (XZ- plane): a) y= 4.08mm , b) y=2.32mm c) 0.19mm, Vertical white dash line profile (YZ – plane): d) X = 2.11mm

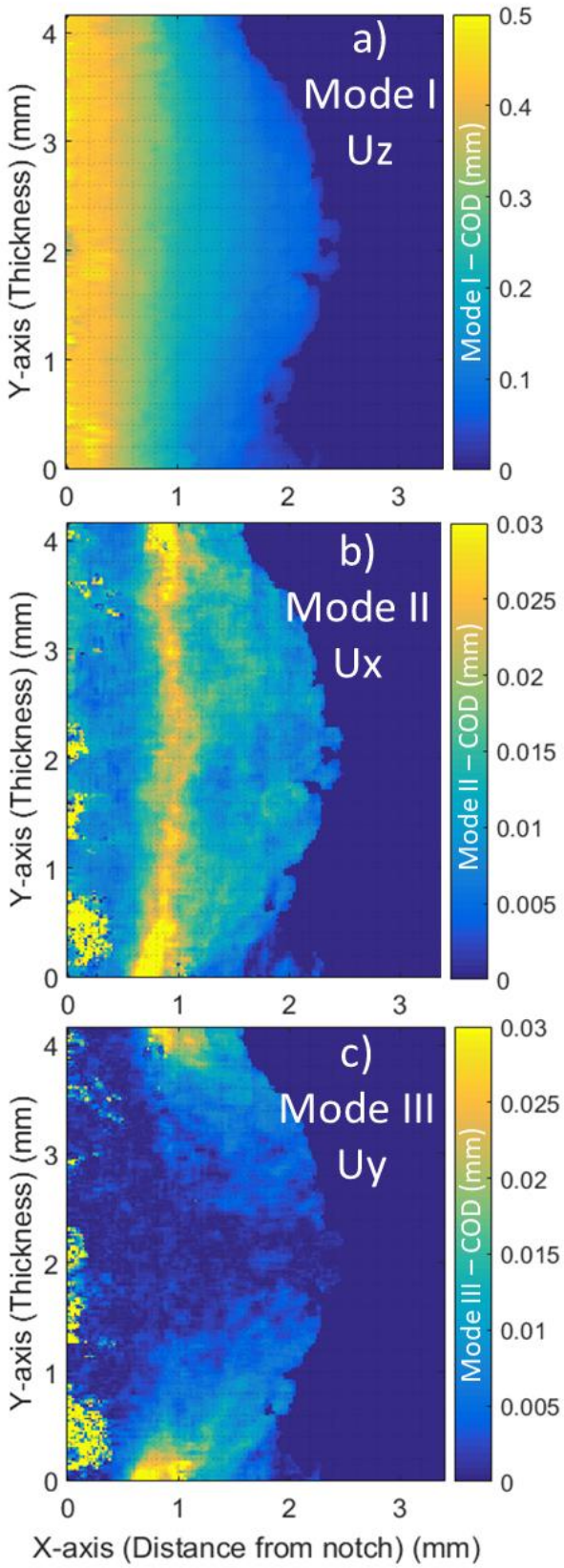

Figure 6.6 Crack opening displacement of different fracture modes through the thickness of Al-Ti with short notch a) Mode I, b) Mode II, c) Mode III

Figure 6.6 depicts the crack opening displacement through the thickness of the sample. Although the experiment was of a pure mode I fracture experiment, due to slight misalignment, the data showed small in-plane (mode II) and out-of-plane (mode III) crack opening. The mode I COD (see Figure 6.6a) showed a constant maximum crack opening at the crack mouth (distance from notch $= 0$ mm) throughout the thickness of the specimen.

At approximately $X = 0.7 - 0.9$ mm distance from notch, a radical change in the crack surface elevation (see Figure 6.4) occurred for the whole thickness of the specimen. The change in elevation contributed the mode II COD at the same exact location (see Figure 6.6b), further agreement of VPC-CD method. The slight misalignment in the experiment also effected the mode III COD (out-of-plane sliding) (see Figure 6.6b) at the sample surface at $Y = 0$ and $Y = 4.15$. However, the crack opening is seen to be close to zero at middle of the thickness ($Y = 1.8 - 2.4$ mm) where the sample is the most secure against tearing.

The fracture toughness through the thickness was calculated automatically using OUR-MA code (Section 3.11) by coupling the larger cubic subset DVC analysis (V64) and VPC-CD analysis. Due to the large yielding and plasticity, the inelastic Ramberg-Osgood model was adopted within the FE treatment. The volume displacement data was deconstructed into 2D XZ-plane displacement slices, each 2D plane represents a slice from the thickness of the sample. Figure 6.7 depicts the FE solution of the von Mises stress directly calculated from the injection of a displacement slice from approximately middle of the fracture (i.e. $Y = 2.32$ mm).

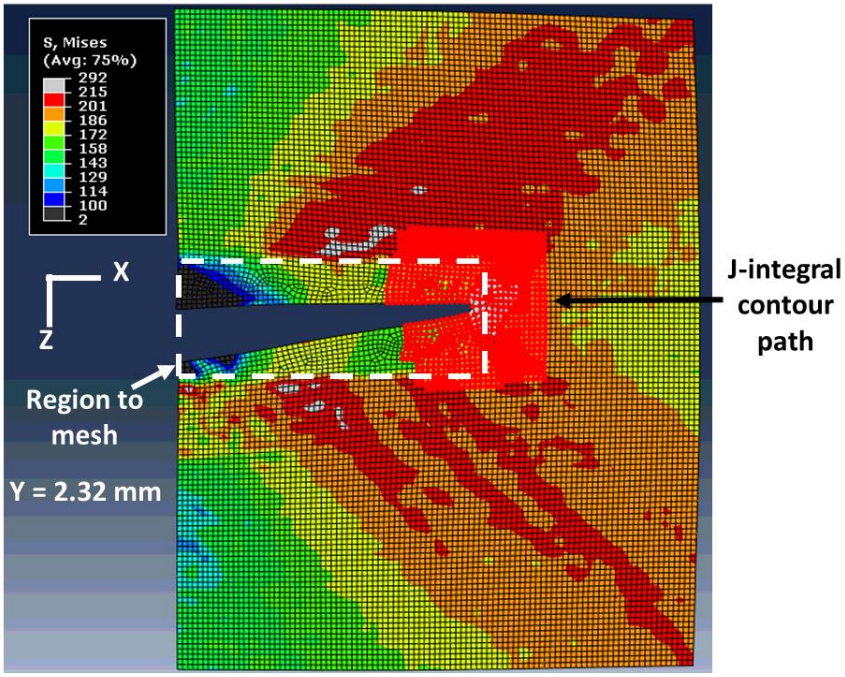

Figure 6.7 FE von Mises stress of a displacement slice at Y =2.32mm

The "region to mesh" highlights the area where displacement data points are deleted, and an FE mesh was refined locally around the crack path. J integral calculation was performed over several contours to check for contour independency. Semi-automatic J-integral calculation was achieved by keeping the region to mesh area and contour number constant for each slice. The J integral calculations were converted to stress intensity factor assuming plane stress conditions using the following equation.

Figure 6.8 shows the strain energy release rate of the crack with respect to the thickness converted to stress intensity factor. The percentage of uncertainty was approximated to be $\sim 7\%$ using the benchmarked guideline in Ref. [2] where uncertainty of crack tip positioning (~ 50 pix error) and inelastic model uncertainty are considered. Red arrow points to the location of a single displacement slice depicted in Figure 6.7. The figure shows clear evidence of lower stress intensity factor at the middle of the sample compared to the sample surface giving a maximum range of $\sim 17 \pm 2.4\ MPam½$ for a thin sample.

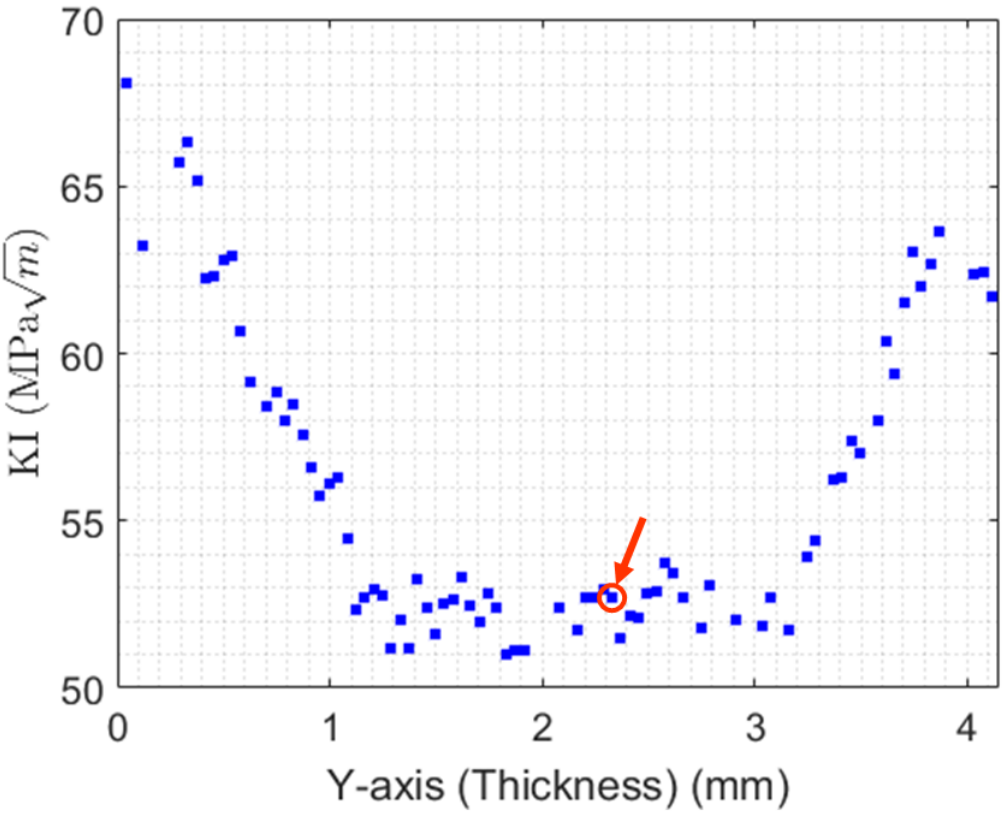

Figure 6.8 Mode I Stress Intensity Factors (K_I) obtained from the J-integral of slice by slice displacement analysis through the thickness of Al-Ti with short notch

6.2.3 Analysis and discussion of Al-Ti – Long notch

Both before and after deformation tomographs for $a/W = 0.5$ were applied a rotation of $16.5°$ anti-clockwise around the $Z-$axis and cropped bearing a new dimension $1200 \times 1550 \times 1000$ (i.e. $3.9 \times 5 \times 3.25$ mm) as seen in Figure 6.9

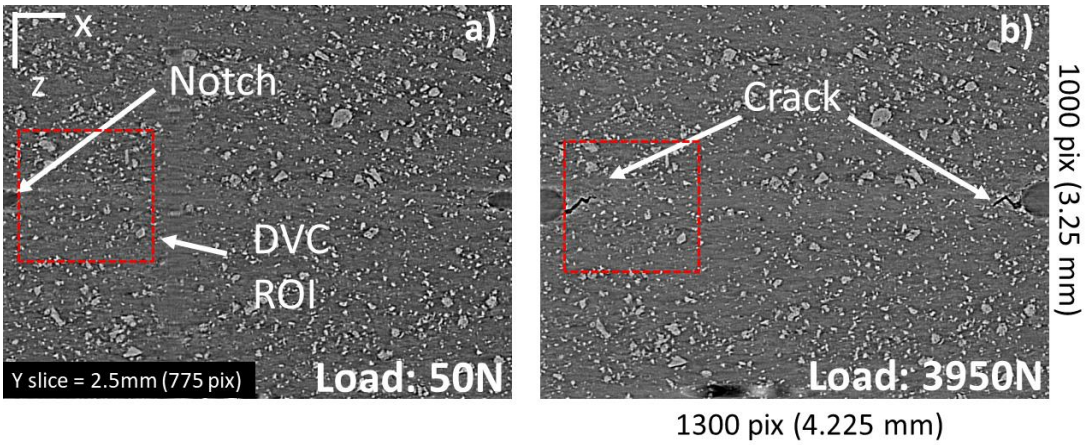

Figure 6.9 X-ray Tomographs of long notch at Y slice = 775 pix (2.5mm) a) Reference tomograph at 50N load , b) Deformed tomograph at 3950N

Two cracks were observed, propagating behind both notches, and were similar in size. A single crack was considered for the VPC-CD analysis and a region of interest measuring $300 \times 1550 \times 300$ pix was established for the DVC analysis (see Figure 6.9). Smaller cubic subset size was performed on the long notch, as the crack is much shorter and therefore more data points are required to be localised around the crack. The DVC analysis was performed using the LaVision DaVis (Version 8.4.0) software, employing a multi-pass FFT-based algorithm; the first pass used cubic subset size of 256^3 voxels with an overlap between subsets of 50%, second pass 64^3voxels with an overlap of 50%, a third pass 32^3 voxels with an overlap of 50% and a final pass of 16^3 with an overlap of 80%. The final pass resulted in a high spatial resolution displacement field and a 3 voxel spacing between each data point. All points with a correlation coefficient below 0.8 were discarded (i.e. set to NaN values). The combined dataset was then corrected for small rigid body displacements and rigid body rotations, measured relative to the reference, based on the algorithm described in [202] . The average uncertainty (standard deviation of Ux, Uy and Uz after rigid body motion) was 0.005 mm (1.54 voxels). VPC-CD was successfully utilised to obtain crack surface /elevation, crack front and crack opening displacement through the thickness as shown in Figure 6.10(c and d) respectively.

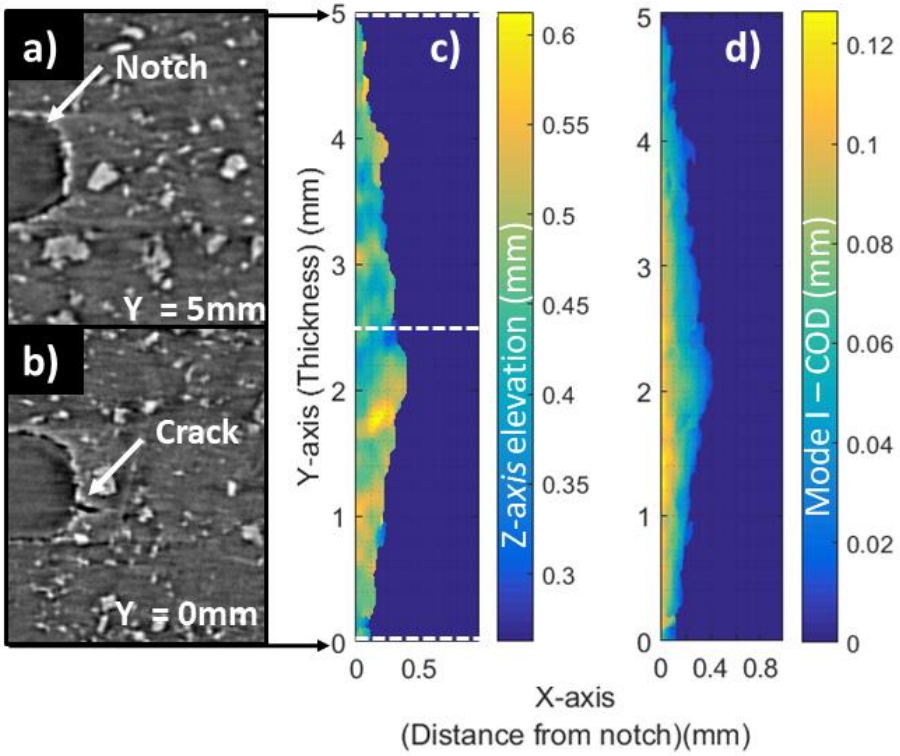

Figure 6.10 VPC-CD analysis of Al-Ti long notch a) Deformed tomograph slice at Y = 5mm, b) Deformed tomograph slice at Y = 0mm, c) Crack surface elevation, d) Mode I crack opening displacement through the thickness

Outlier removal was used to remove the erroneous displacement values caused by the crack artefact where outlier window size and threshold parameters were 15 and 0.0007 respectively. The VPC-CD required some interaction where the PC parameters were fine-tuned to $\lambda_{\min} = 20$ and $\mathrm{d_{PC}} = 1.7$ which is seen to improve the discontinuity signal, making it sharper. The segmentation algorithm was set to the default parameters and took 273 iterations for the segmentation to become stagnant and reach an optimized condition.

The crack elevation of the long notch (see Figure 6.10b) showed a small ~ 0.35 mm range in elevation. The crack front was seen to take the shape of an arrowhead where the line of symmetry and maximum crack length location was at $Y = 2.05$ mm, similar location as the crack front of the short notch (see Figure 6.4). The VPC-CD data shows that the crack has not fully propagated through the whole thickness of the sample, where between the thickness $Y = 4.85 - 5$ mm, no crack values were given. Two tomograph slices (see Figure 6.10a and b) at both sample surfaces depict that while $Y = 0$ mm showed an evidence of crack propagation behind the notch, $Y = 5$ mm did not, hence in line with VPC-CD analysis.

An attempt was made to extract the stress intensity factor using the same methodology applied in the previous section (see section 6.2.2). However, due to the length of the crack (from notch tip), large subsets (Cubic subset size 64 and 80% overlap) lacked the spatial resolution and data point spacing to capture the crack. The crack length (i.e. from notch tip) measured maximum 5 displacement data points, for Cubic subset size 32 and overlap of 80%. Therefore the measured crack length limited only 5 contour paths to be taken, which was not sufficient for convergence. Due to the time limitation of this thesis, SIF extraction from the long notch was not investigated further. However, the problem may be solved by tweaking the DVC parameters so that displacement measurements are made with smaller data point spacing which will solve the lack of data points across the crack surface.

6.3 Quasi –Brittle Material 1: Graphite

The strain field in a polygranular isotropic nuclear graphite, a quasi-brittle material, has been studied during stable fracture propagation and has been published [4]. The experimental work was carried out at the Joint Engineering, Environmental and Processing (JEEP – I12) beam line at the Diamond Light Source in the UK [203]. The specimen was incrementally loaded and unloaded in a total of ten stages whilst the propagation of the crack was analysed with VPC-CD. The crack opening displacement profiles through the thickness, crack surface location and crack front were obtained from the displacement field calculated with large cubic subset size (lower spatial resolution i.e. 128^3 pixels). The crack front calculated by VPC-CD was compared with the manual visual inspection of the crack front. The experimental application was designed and realised by Professor James Marrow, University of Oxford and the data was made available to the author of the thesis for the purpose of the crack analysis from displacement data. The author of this thesis takes no credit for production of the experimental data but was responsible for the crack quantification analysis.

6.3.1 Experimental details

The material is one of the graphite's used in the UK Advanced Gas-cooled Reactor fleet. Manufactured by Graftech (formally UCAR) and supplied by EDF Energy Generation, the moulded IM1-24 Gilsocarbon (GCMB grade) polygranular nuclear graphite has weakly anisotropic properties. Depending on orientation, the reported Young modulus, E, is between 11.6 and $11.9\,\mathrm{GPa}$, with a Poisson ratio, ν, of 0.2 and a tensile strength, σ_t, between 19 to $20\,\mathrm{MPa}$ at a strain of approximately 2.5×10^{-3} [204]. The same grade has been studied in previous works by some of the authors from references [205-208].

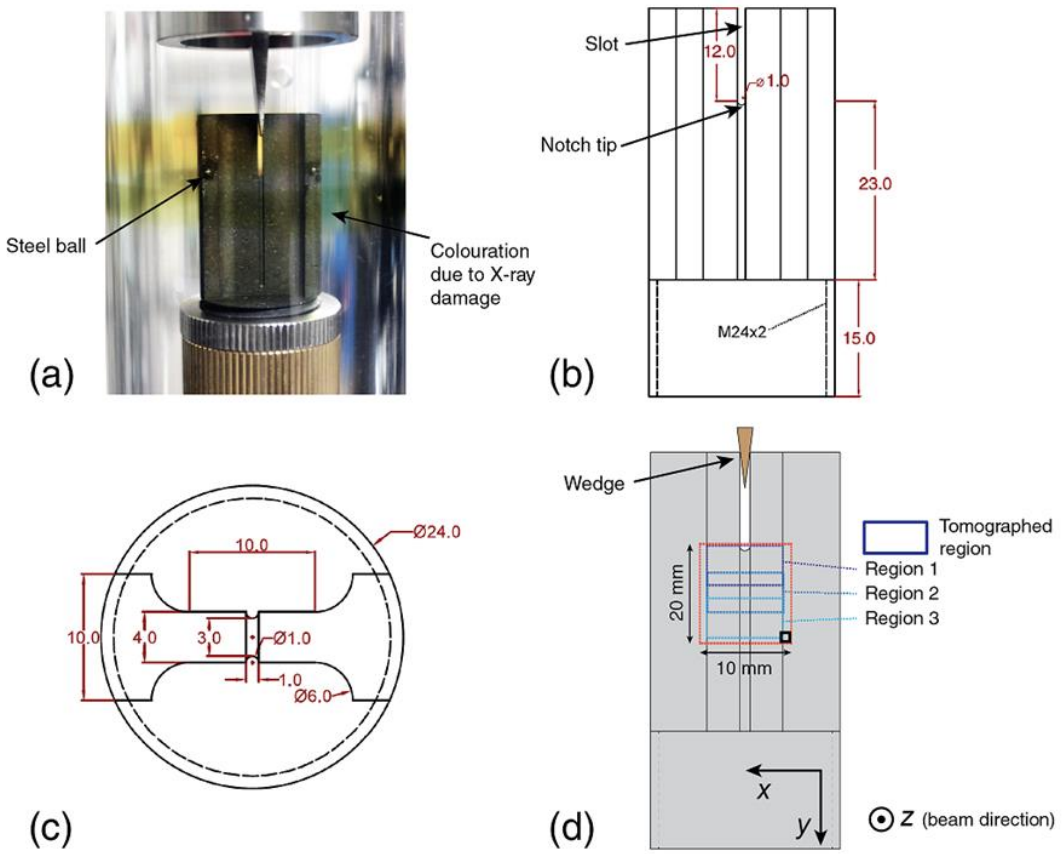

Figure 6.11 (a) The specimen, with wedge inserted, showing a pair of steel balls attached as fiducial points. The specimen is within the polycarbonate tube of the loading rig, which has been discoloured by exposure to high energy X-rays (b) Side-view drawing of the specimen (c) Top view drawing of the specimen (d) Regions of interest for tomography within the specimen. [4]

The test specimen (Figure 6.11) was designed to facilitate tomography observations whilst fracture was propagated quasi-statically from a stress concentrating notch.

Radiographs were recorded using a PCOedge CMOS camera (2560×2160 pixel, 16-bit depth), with optics selected to image an area of 8.3×7.0 mm (i.e. 3.24 μm per pixel). The exposure was 0.3 seconds for radiographs.

Tomographs were recorded with 3000 radiographs over a $180°$ rotation, and a standard back-filtered projection algorithm [209] was used for the image reconstructions. For noise reduction, a slice-by-slice 2D median filter of 1 pixel radius was applied to the horizontal slices of the reconstructed 3D volumes using the software ImageJ [210]. At each observation, three overlapping tomographs were acquired to record a total volume of $17.0 \times 7.0 \times 7.0$ mm, the overlap between tomographs was 2 mm in the vertical axis (Figure 6.11d). The maximum path length of X-rays through the specimen was greater than the dimension of the tomographed volume, but due to the low X-ray attenuation of graphite, no corrections for

the specimen geometry were applied in the reconstruction of these region-of-interest tomographs.

A reference tomograph was obtained with the wedge inserted at a pre-load of $8\ \mathrm{N}$. The wedge was then inserted further in displacement control at a rate of $0.2\ \mathrm{mm/min}$ whilst the load was monitored. Visual inspection of radiographs was used to assess the approximate increment of the crack length, and the wedge insertion was arrested at constant displacement when the crack was judged to have propagated a sufficient distance. A set of tomograph maps were obtained of the loaded specimen, which was then unloaded completely by removal of the wedge, and tomography mapping was repeated. This procedure was cycled to obtain 5 sets of loaded and unloaded data of a progressively propagated crack, although the available beam time did not permit the collection of a final set of tomographs of the unloaded specimen in the 5th cycle.

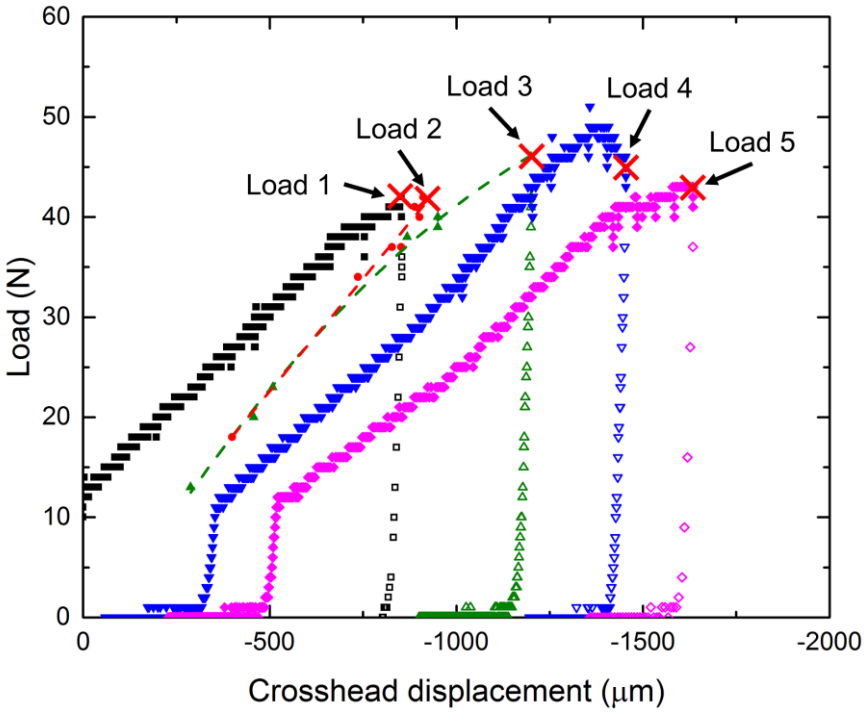

Figure 6.12 Load – crosshead displacement data for all cycles; loading is shown with solid symbols, and unloading with open symbols. For Cycle 2 and Cycle 3, the loading curve is traced through the available data using a quadratic best-fit (both R2 > 0.99). Tomographs maps were collected at the points labelled "Load 1" etc. [4]

The raw data of the load vs. crosshead displacement for the 5 load cycles are presented in Figure 6.12, in which the red crosses identify the recording tomographs whilst the specimen was maintained under load at a fixed wedge displacement. The load at these observations was manually recorded, before and after each imaging sequence, and did not reduce by more than 12% over each period. Contact between the wedge and the test specimen above 10 N was apparent in the initial loading of each cycle – the wedge was removed completely between each cycle. The data were offset in displacement between cycles, which is attributed to damage that occurred at the contact between the wedge and the specimen. The reported displacements did not correctly represent the wedge position in the specimen's notch during unloading. This is due to friction that allowed slack movement in the thrust bearing to be taken up when the crosshead displacement was reversed, before the wedge itself was removed. A software issue affected data logging during cycles 2 and 3 and fewer load/displacement data points were available to show the loading curves, so the trend line has been fitted through the available data.

6.3.2 Analysis and discussion

DVC analysis was applied to all of the tomographs to retrieve the displacement field relative to the reference tomograph. The 16-bit images were first converted to 8-bit; the extreme values of the 8-bit range (i.e. 0 and 255) were assigned to the same minimum and maximum grey level values that were observed in the 16-bit data for all the scans, with the objective of reducing the potential data loss in this process. Each tomograph was cropped to $2560 \times 1536 \times 2112$ voxels to remove the majority of the empty volume outside of the specimen. The DVC analysis was performed using the LaVision DaVis (Version 8.1) software, employing a multi-pass FFT-based algorithm; the first pass used cubic subset sizes of 2563 voxels with an overlap between subsets of 75% and the second pass 1283 voxels with 75% overlap. All points with a correlation coefficient below 0.8 were discarded (i.e. set to NaN values). For each observation, the 3 overlapping tomographs were processed separately and the displacement vector data were stitched by averaging in the overlapped region. On comparison of the average vector representative of each tomograph in the overlap region, the magnitude of the difference between vectors was less than 2.0 μm (i.e. 0.6 voxel). This was regarded as a measure of the uncertainty in the DVC measurement of displacements.

The combined dataset was then corrected for small rigid body displacements and rigid body rotations, measured relative to the reference, based on the algorithm described in The final data have a coordinate system defined such that: the lowest point of the notch tip is at $Y = 0$ and the Y axis is positive towards the bottom of the specimen; the X axis is positive towards the right, with the notch tip at $X = 4.5\ \mathrm{mm}$; and the Z axis is in the X-ray beam propagation direction, with centre of the notch at $Z = 1.5\ \mathrm{mm}$.

The VPC-CD algorithm was used to extract the crack parameters from the displacement fields of all loading sequences iteratively and automatically. Displacement orientation Ux is selected as the highest discontinuity signal orientation. Outlier deletion was not used utilised as the displacement field consisted of accurate values due to the large subset size. The volume Phase congruency was constructed using XZ – plane slices with default PC parameters, $\lambda_{\min} = 4$ and $\mathrm{d_{PC}} = 1.2$. A seed point was selected at a constant location for all loading sequences, just below the notch tip where the segmentation algorithm reached stagnant crack mask between $10 - 96$ iterations for each loading sequence. Figure 6.13 depicts the crack parameters extracted via VPC-CD for the final observation. The experiment was designed to investigate the energy release rate of a mode I propagating crack, however, the final observation showed evidence of mixed mode loading. VPC-CD analysis not only approximates the crack surface location but can also map out a full field mixed mode crack opening of the crack surface as seen in Figure 6.13(a, b and c). The mixed mode crack opening mapping can be a useful tool for the characterisation of any fracture. It can be seen from Figure 6.13b that crack mouth opening displacement in mode II is non-uniform through the thickness where a maximum opening is between $Z = 0.1\ \mathrm{mm}$. The non-uniform opening appears to have caused mode III opening, pivoting from the crack tip and could also be the cause of the convoluted crack front.

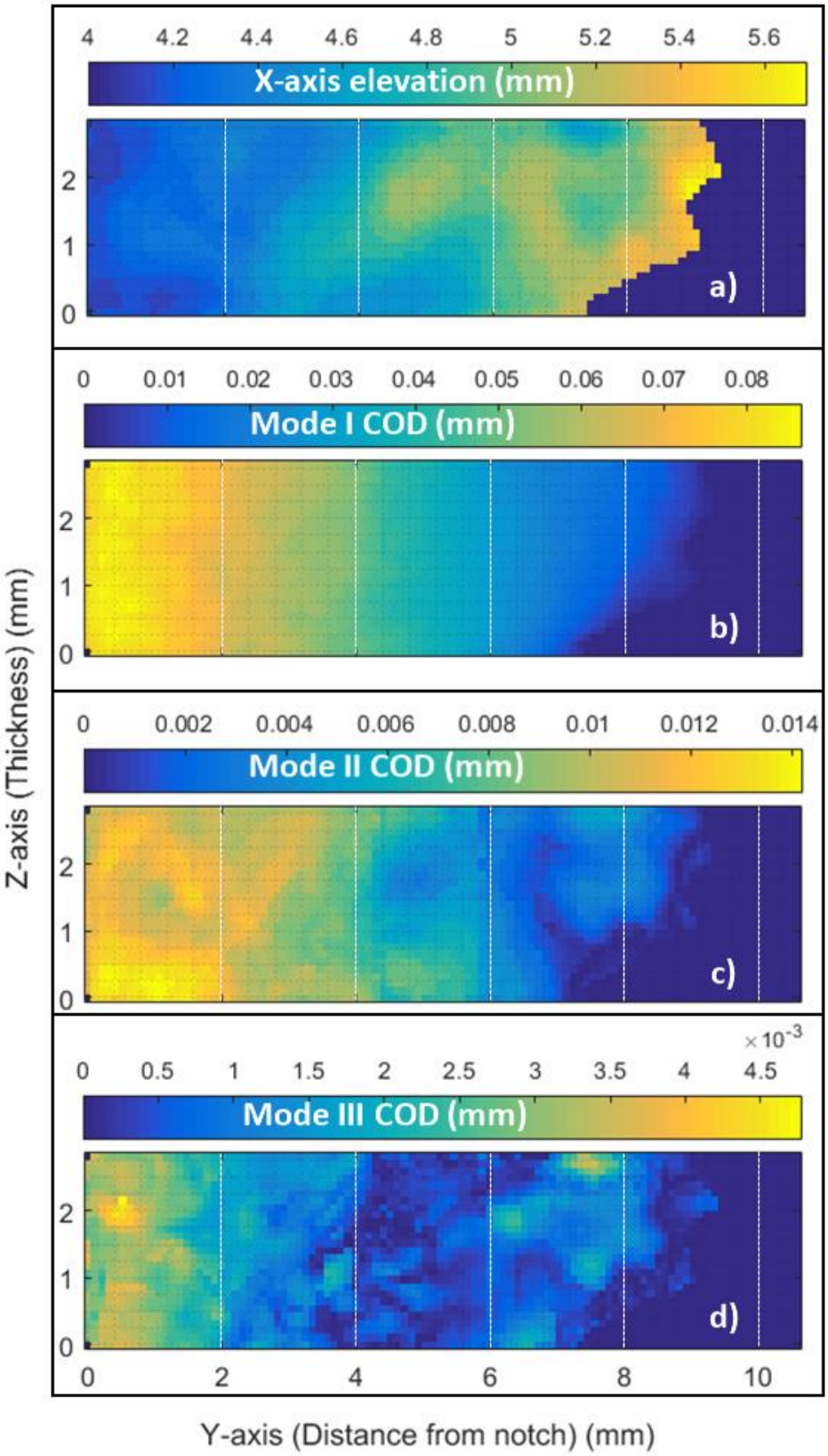

Figure 6.13 VPC-CD calculated crack parameters of Cycle 5 (loaded) a) Crack surface elevation, b) Mode I crack opening displacement through the thickness, c) Mode II crack opening displacement through the thickness, d) Mode III crack opening displacement through the thickness

The positional uncertainty of the crack surface depends on the interval between displacement vectors, which in this case was $100\ \mu m$. The crack length was also measured using the visual analysis of the tomographs (loaded) and compared to the VPC-CD analysis of the displacement field (loaded and unloaded). Visual measurements of the crack depth were made from the notch across the specimen thickness; the standard deviation of the observations provided the uncertainty in crack tip position, which was around $0.4\ mm$ for both types of analysis. A good agreement was observed between the two methods for the loaded crack, but the VPC-CD analysis of the unloaded displacements consistently showed a shorter crack length than the loaded data.

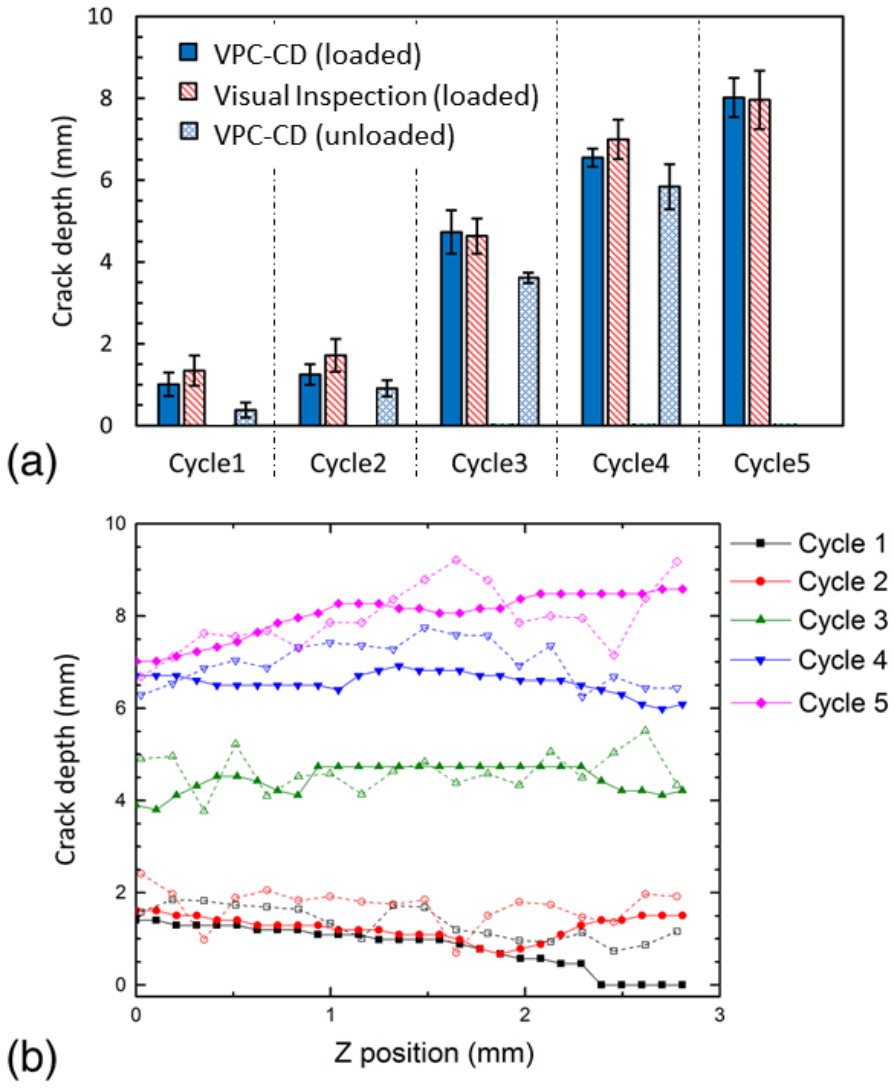

Figure 6.14 Measurement of the crack length: (a) Average crack depths (measured from notch tip at y=0 mm), obtained by assessment of the crack tip position by visual inspection of tomographs and VPC-CD analysis of the DVC displacement field.(b) Crack depth across the specimen thickness, measured under load – the full symbols show data obtained by VPC-CD (measurement error ~100 µm) of the DVC displacement field, open symbols show data obtained by visual inspection of tomographs (measurement error ~30 µm). [4]

The observations of the loaded crack define its shape based on how the crack opens (see Figure 6.14b). Crack initiation occurred in cycle 1, which is also indicated by the reduction in the load/displacement gradient observed above 40 N (see Figure 6.12) but the crack did not propagate fully across the specimen thickness; in this cycle the maximum deviation of the observed crack front from the average crack length (including the notch depth) was $\sim 8\%$, measured using VPC-CD. There was no significant propagation of the crack front in the second cycle. This is consistent with the linear load/displacement trace measured during loading in cycle 2, although in this cycle the crack developed fully across the specimen thickness to achieve a more uniform crack length. The load peak in cycle 4 and the load plateau in cycle 5 indicate further crack extension, which is confirmed by the tomographs, and although the load/displacement data in cycle 3 are sparse, there was a clear decrease in the load/displacement gradient above 40 N that is consistent with crack propagation. In cycles 2 to 5, the maximum deviation of the crack front from the average crack length, measured by VPC-CD, was $\sim 5\%$ (average 1.7%). The visual analysis of the tomographs shows that the crack was always within 0.4 mm of the central plane of the specimen, except for cycle 5 where the crack deviated by up to 1 mm at some positions with an agreement with VPC-CD crack surface (see Figure 6.13a). In all cycles, the maximum deviation of the crack plane was less than $17°$, measured over an arbitrary distance of 2 mm from the crack tip, thus in terms of the closest relevant standard (e.g. ASTM 647 [211]) the crack was essentially planar.

VPC-CD analysis of mode I crack opening displacement was compared (see Figure 6.15) to a method used previously here ([208]). The method (labelled DVC) applied in the previous study measures the difference between the Ux displacements on either side of the crack in a direction perpendicular to the notch plane. These were obtained at a fixed position of $Z = 1.5$ mm that is close to the specimen's central axis, along two 0.4 mm wide bands running in the X direction that are located approximately 0.4 mm on either side of the crack. The distance between each DVC data point is ~ 0.1 mm, so 4 points were average at each Y position. Data points where the standard deviation of the displacement vector magnitude of the averaged points was higher than their average value were censored. The censored points were less than 1% of the data and arise from poor DVC correlation and therefore affected regions where the tomographs overlapped (shown in light grey in Figure 6.15a and b). Censored points also arise from local effects of ring artefacts in the tomographs.

Ring artefacts are caused by defects in the optical imaging system, such as dust on the scintillator, the optics and/or the detector or faulty pixels on the sensor. This generates artefacts at a fixed position on the radiographs that become rings in the reconstructed image and influence the DVC measured strains [202].

The difference between VPC-CD to direct DVC analysis is that VPC-CD identifies the discontinuity of the crack and uses the displacement vectors closest to the discontinuity, so no data were extracted ahead of the crack tip. To make the observations comparable, a single data point slice (i.e. $Z = 1.5$ mm) from the VPC-CD COD was considered. Both crack opening profiles were quite similar, as shown by the examples in Figure 6.15a and b, and both showed the residual opening of the crack after unloading that is visualised in Figure 6.15b. The crack tip position was sharply defined by the VPC-CD method, but the DVC analysis showed a significant zone ahead of the loaded crack tip, several mm in length, with a measurable displacement difference across the crack plane. This was observed previously [206], and has been attributed to the effect of microcracking in the fracture process zone. The microcracking has not been found by the VPC-CD method, which is sensitive to steeper gradients in the displacement field.

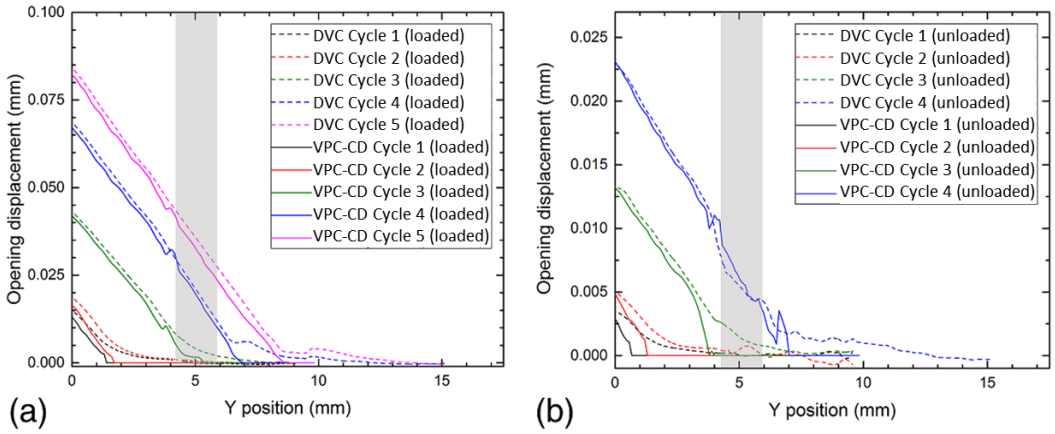

Figure 6.15: Measurements of the crack opening displacements. The mode I opening profile was obtained by both direct DVC analysis and VPC-CD analysis where the data is taken from the centreline position, (Z=1.5 mm) in the (a) loaded and (b) unloaded states (the region where tomographs overlap is indicated in light grey) [4]

6.4 Quasi–Brittle Material 2: Carbon fibre composite

Temperature driven fracture in a Carbon fibre composite is examined by coupling X-ray tomography, Digital Volume Correlation (DVC) and VPC-CD. The experiment was conducted at the Diamond Light Source on the I12 beamline. A small transverse crack between the weave layers, and parallel crack surface to the weave orientation was initiated at $-80°$ and observed in the tomography scan. The crack was too small to segment from the tomograph and microcracking was observed with its surrounding. DVC and VPC-CD was used to detect and obtain crack surface location and crack opening displacement through the thickness. The analysis was conducted with high spatial resolution (i.e. 32^3 pixels).) DVC analysis. The experimental application was designed and realised by Dr. James Meredith, University of Sheffield. The X-ray tomography data was made available to the author of this thesis for the purpose of detection and analysis of cracks. The author of this thesis takes no credit for the production of the experimental data but was responsible for the analysis of the tomographs.

6.4.1 Experimental details

The experimental dataset was obtained on Unidirectional (UD) prepreg carbon fibre reinforced polymers (CFRP). UD prepregs are inherently anisotropic, possessing fibre dominated longitudinal strengths of greater than $2000\ \mathrm{MPa}$ but comparatively poor resin dominated transverse strengths of approximately $30\ \mathrm{MPa}$ [212]. This, in combination with the widely differing longitudinal ($-0.3 \times 10^{-6}\ °\mathrm{C}^{-1}$) and transverse ($30 \times 10^{-6}\ °\mathrm{C}^{-1}$) linear coefficient of thermal expansion (CTE) [213] leads to residual stress within the laminate which can surpass the transverse strength of the ply leading to transverse crack formation [214-217].

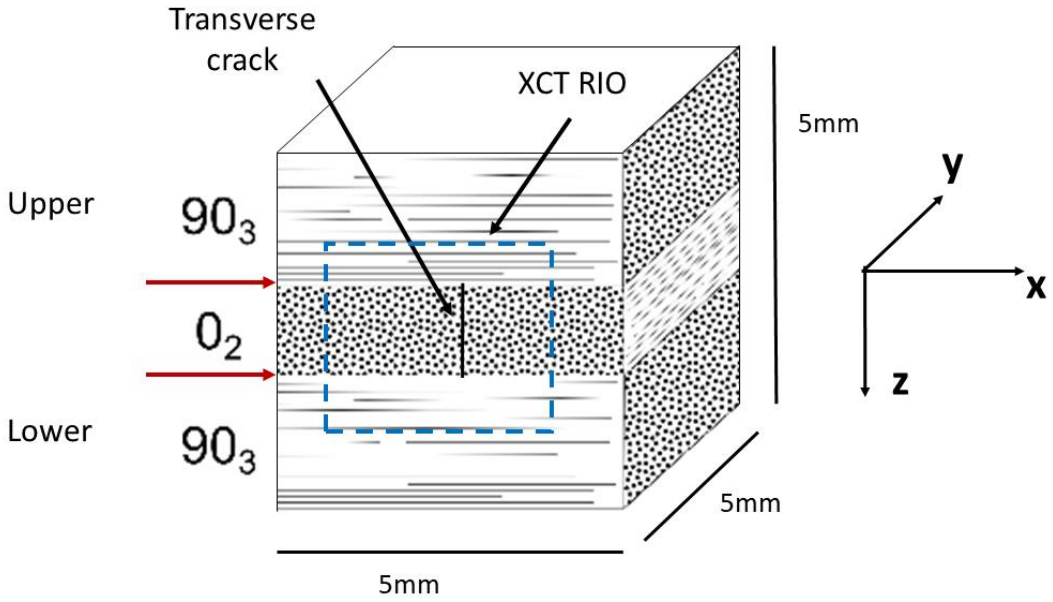

Figure 6.16 Specimen geometry, orientation of the layers and X-ray tomography region of interest.

Two layups were used for cryogenic fracture analysis, one composed solely of UD fibres and the other a typical aerospace layup designed to be robust against temperature driven fracture with a UD central core surrounded by woven material. A UD layup of [90_3, 0_2, 90_3] (see Figure 6.16) was chosen, as previous work has shown it to be particularly susceptible to temperature driven fracture [214]. The specimen for the cryogenic fracture experiment was cut in the shape of a cube with dimensions measuring $5 \times 5 \times 5$ mm^3. The fibre diameter was 6 µm which acted as the material pattern to be able to obtain displacement field through DVC analysis. The boundary of the layers is identified by the dark red arrows throughout this chapter.

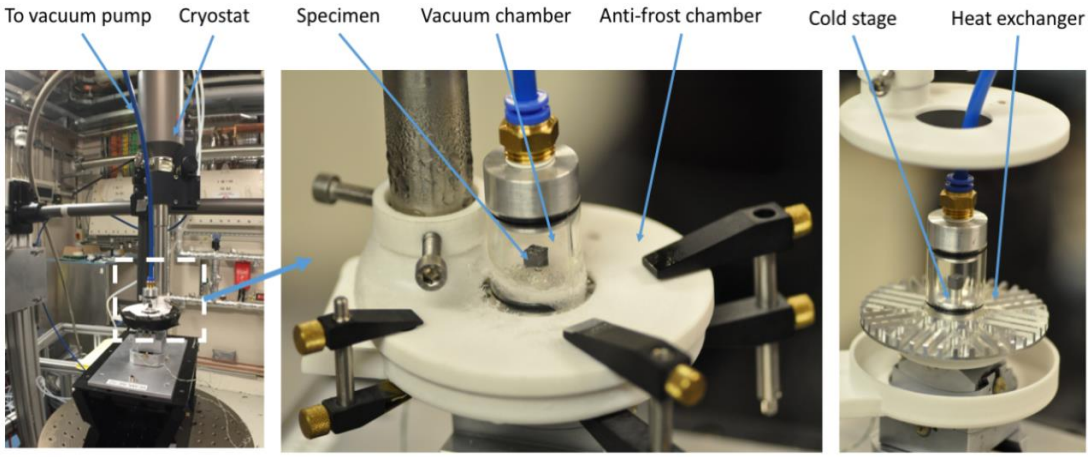

Figure 6.17 Experimental setup

The carbon fibre specimen was cooled down from $20°C$ (room temperature) to $-20°C$ then to $-80°C$ using I12's cryostat system. At each step, X-ray tomography scans were obtained. Figure 6.17 shows the setup of the experiment: the specimen was cooled on a cold stage, by blowing liquid nitrogen from the cryostat system onto an aluminium heat exchanger. The cold stage was placed within a vacuum chamber and the heat exchanger was encased within an anti-frost chamber. This setup minimised frost accumulation during the measurement taken for each temperature for a duration of up to 4 hours allowing for X-ray tomography scans to complete. Previous pre-experiment trials with samples equipped with thermocouples showed that a 5-minute wait was sufficient for the specimen's core temperature to reach steady state when the cryostat temperature was changed. This timing was followed in the experiment. Although the setup successfully prevented frost forming on the surface of the specimens, it restricted the movement of the stage and preventing collection of flat fields for each specimen. A number of flat fields were recorded at the end of this stage and was used for the reconstruction of the tomographs.

A monochromatic beam of energy $53.2\ \mathrm{keV}$ was used and radiographs were recorded using a PCO. 4000 CCD camera (2560×2160 pixels, 16-bit depth), with optics selected to image an area of $3.3\ \mathrm{mm} \times 2.8\ \mathrm{mm}$ (i.e. $1.3\ \mu\mathrm{m}$ per pixel). Tomography was performed with 3600 projections over $180°$ in each scan with a 0.7 seconds exposure.

Each data set was bi-cubically binned by 2×2 and down sampled from 16-bit and $1.3\ \mu\mathrm{m}$ per voxel dimension to 8-bit (i.e. 0 and 255) and $2.6\ \mu\mathrm{m}$ per voxel. The new dimensions of the tomographs are $1280 \times 1280 \times 1075$ pix. A 3D median filter with a radius of 3 pixels in all three dimensions was subsequently applied to the down-sampled and binned data. The 3D median filter was used for noise reduction while preserving the fibre features.

Figure 6.18 depicts the pre-processed tomographs, taking a slice at $Y = 0.78\ \mathrm{mm}$ on the XZ-plane. The deformed tomograms were examined manually for visible damage / cracks. A transverse crack was seen to be initiated and only appeared once the specimen was cooled down to $-80°C$ (Figure 6.18c and d) but did not appear in scan $-20°C$ (Figure 6.18b).

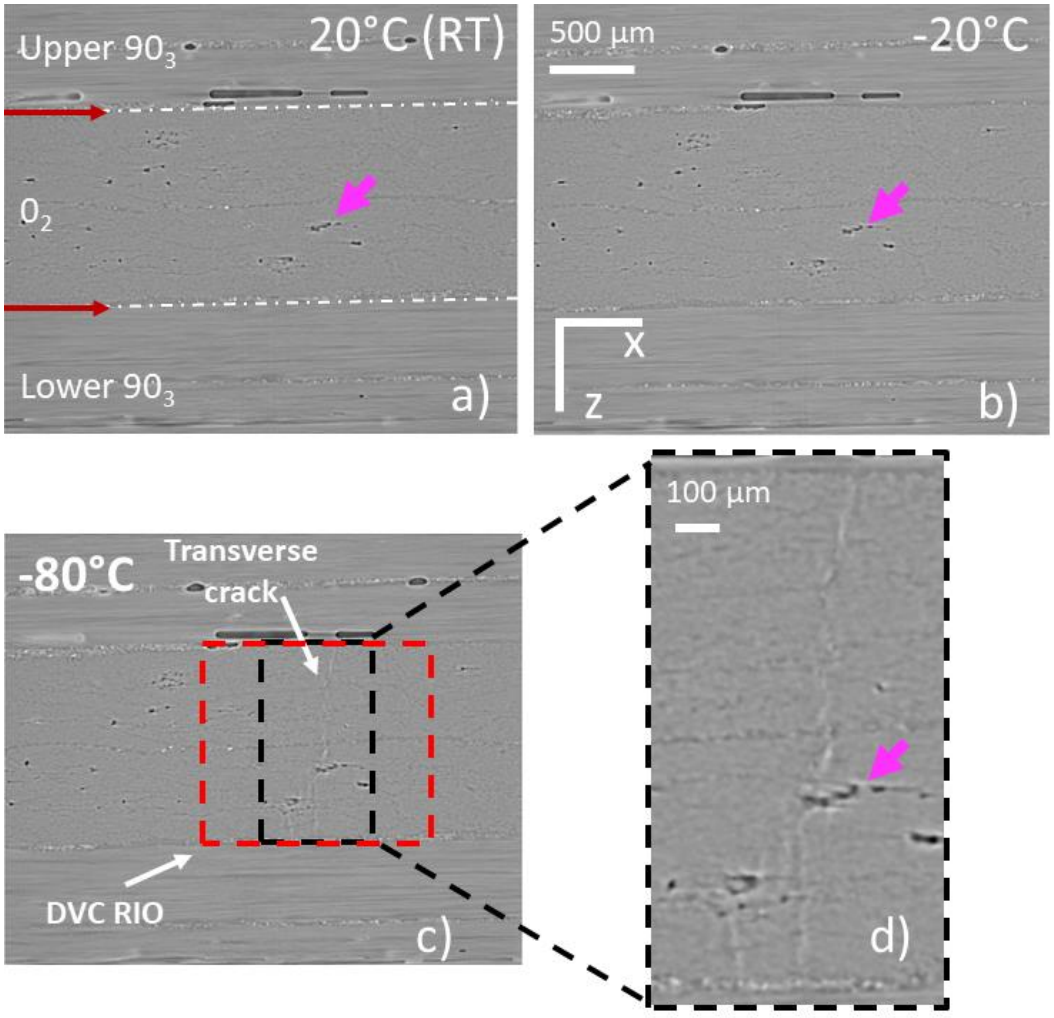

Figure 6.18 X-ray tomographs of the Carbon fibre composite of the XZ-plane at y=0.78mm, a) Reference tomograph at 20°C. The layer boundaries identified by the dark red arrows. , b) -20°C, no evidence of damage c) Deformed tomography at -80°C where is evidence of damage and DVC ROI defined. d) Magnification of c) at the region of the transverse crack

Later, the DVC analysis of scan $-20°C$ showed no evidence of a discontinuity which confirmed the observation. The damage was seen to be at the same orientation as the fibre orientation of the 0_2 weave (Figure 6.18c). Damage also completely cut through the full thickness of the 0_2 weave where the fracture stopped at the interface of the upper and lower 90_3 weave.

Region of interest for the DVC analysis is specified by the red dashed line, where only the 0_2 weave is considered measuring $1.48\ \text{mm} \times 3.3\ \text{mm} \times 1.14\ \text{mm}$ $(570 \times 1280 \times 440$ pixels). The region is specified so that different orientations of the weave are not analysed as a previous DVC analysis showed large discontinuity between the weave interfaces, hiding the localised damage.

6.4.2 Analysis and discussion

Digital Volume Correlation (DVC) analysis was applied to all tomographs to retrieve displacement field relative to the reference tomograph. The DVC analysis was performed using the LaVision DaVis (Version 8.3.0) software, employing a multipass FFT-based algorithm; the first pass used cubic subset size of 256^3 voxels with an overlap between subsets of 50%, second pass 64^3 voxels with an overlap of 75% and a third pass 32^3 voxels with an overlap of 75%. All points with a correlation coefficient below 0.8 were discarded (i.e. set to NaN values). The dataset was then corrected for rigid body displacements and rigid body rotations, measured relative to the reference, using the method described in [202]. The average uncertainty for the DVC analysis was 0.00029 mm (i.e. 0.11 voxels). The data point spacing was 9 voxels.

The VPC-CD algorithm was used to extract the crack parameters from the calculated displacement field. Displacement orientation Ux was selected for VPC algorithm using $XZ-$plane slices. An outlier deletion filter was applied to all displacement orientations, where optimum parameters were selected for window size and threshold of $9 \times 9 \times 9$ and 0.0001, respectively. Extrapolation method "*inpaintn.m*" was selected for this analysis. The volume Phase congruency was constructed with default PC parameters, $\lambda_{\min} = 4$ and $\mathrm{d}_{\mathrm{PC}} = 1.2$. A seed point at location $(0.6864, 0.832, 0.416)$ and default parameters were selected for the segmentation algorithm where the crack mask reached an optimum which ran for 155 iterations. Figure 6.19a depicts the segmentation of the transverse crack produced by the VPC-CD algorithm. The grey dotted area shows the slice location of Figure 6.18d. The algorithm used the segmentation to produce the crack elevation (see Figure 6.19b) and the crack opening displacement through the thickness (see Figure 6.19c). The VPC-CD algorithm took 259 seconds to compute. The crack opening in Uy and Uz displacement fields were minimal and within the noise threshold and therefore were not considered.

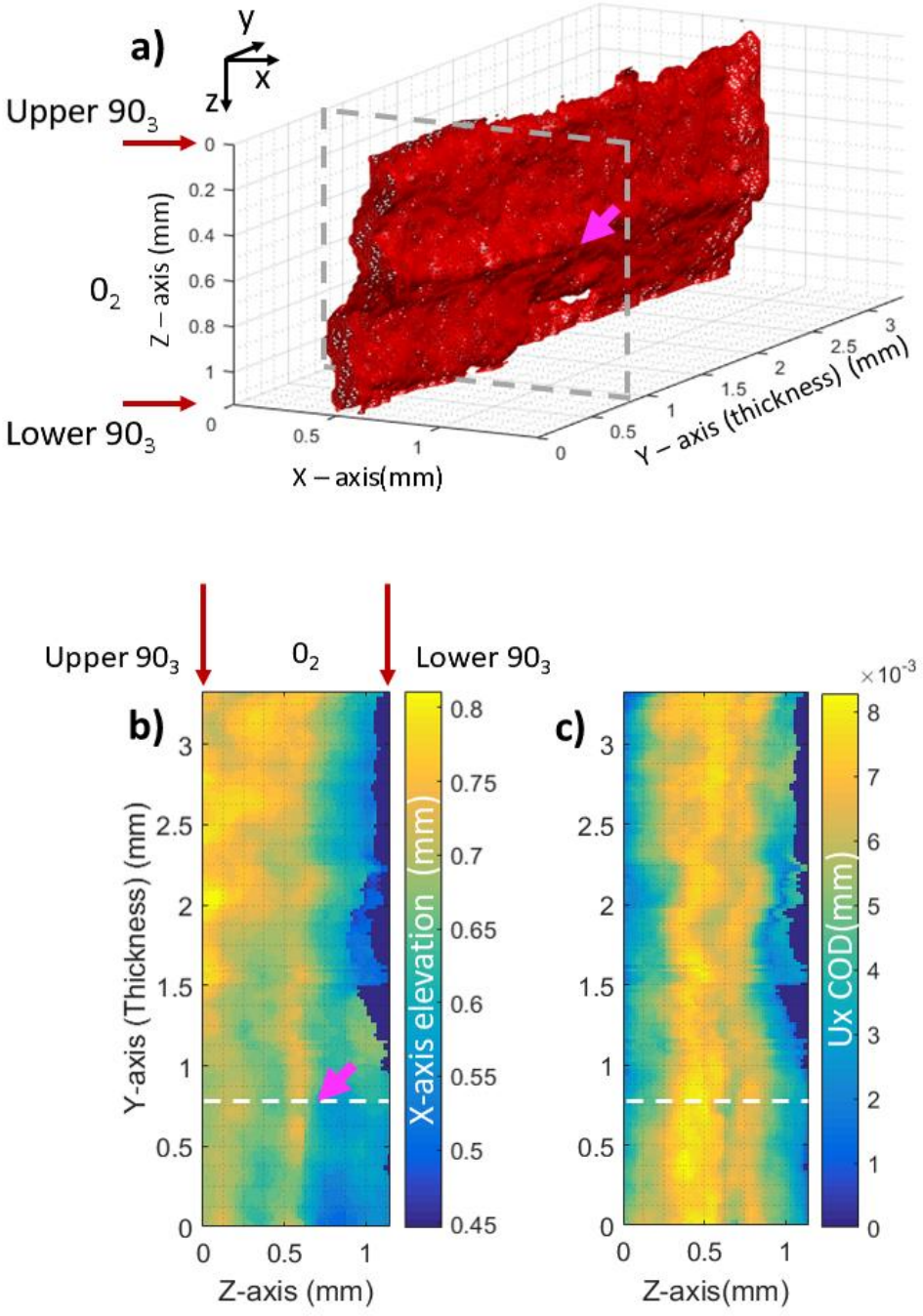

Figure 6.19 VPC-analysis of the transverse crack in the Carbon fibre composite a) VPC-CD segmentation , b) Crack surface / elevation c) Crack opening displacement through the thickness

Figure 6.19b shows the transverse crack elevation from the $YZ-$ plane origin ($X-$ axis location) where the tomography slice location ($Y = 0.78$ mm) from Figure 6.18 is marked as the white dashed line.

The crack surface is seen to be relatively planar, fluctuating by a maximum of $\sim 0.35\ \mathrm{mm}$ axis. At approximately $Z = 0.5 - 0.6\ \mathrm{mm}$, the crack elevation was observed to drastically change as the fibres as pointed by the purple arrow (see Figure 6.18(a, b and d)). The magnified tomography of the transverse crack (see Figure 6.18d) shows that the void appears to have affected the trajectory of the crack. The influence of the void on the crack propagation trajectory is seen throughout the thickness depicted clearly by the VPC-CD segmentation (see Figure 6.19a and b). Although the impact is seen, it is difficult to prove if the crack interacted with the void. The crack opening displacement (Figure 6.19c) shows that the crack opening appears to stay constant in amplitude, but maximal opening location varies between $Z = 0.4 - 0.6\ \mathrm{mm}$ through the thickness. The maximal crack opening is localised to the location of the void at $8\ \mu\mathrm{m}$. The void is a material imperfection during manufacturing and could be the cause of the transverse crack as the material is cooled.

6.5 Conclusion

The results presented in this chapter have shown the extraction of crack's geometrical volume information based on DVC processed displacement fields using the novel VPC-CD method. The application was seen to be highly versatile, easy to implement requiring minimal user judgement. The user is required to select a seeding point on the VPC-CD identified region, where the results from the VPC-CD method are invariant of the selected seeding point. The VPC-CD method was applied to three different material samples; one ductile and two quasi-brittle; where high depth crack information was successfully extracted with in the volume of the specimens. Crack parameters such as the crack surface, crack front and crack opening displacement in the thickness provided lucid understanding and the behaviour of the crack. The J-integral values were obtained in the thickness of the sample where 2D slice planes were chosen along the crack front.

7 CONCLUSION

The main objective of this research project was to study how image-based methods can be used to better understand fracture behaviour of a range of materials. The literature showed that image-based methods, once combined with displacement measurement techniques, are advantageous in fracture assessments. The combination allows for the full-field quantification of the mechanical properties. A strength of the method is that it can readily be applied to volume data which allows for an almost full quantification of mechanical behaviour within the material. This thesis identified the missing gap in the literature in the analysis of these measurements and addressed them. Indeed, the literature showed that the fracture analysis of the displacement fields lacked a methodology and required intensive user interaction. The bias and judgement driven analysis of fracture can give inconsistent results.

This thesis introduced a cutting-edge method called Phase Congruency based Crack Detection (PC-CD) which allowed the automatic extraction of crack parameters from measured displacement fields. The idea behind the novel PC-CD method is to identify which digital image correlation subsets interact with the crack and provides quantitative analysis of crack parameters such as opening displacement.

The identification of the discontinuous data points across the crack faces was determined by phase congruency, which is a mathematical image processing tool that is designed to identify features in all phase angles as opposed to gradient based methods which can only detect features in two orientations. Furthermore, phase congruency is said to represent the human visual cortex of what is perceived as an edge. Phase congruency is not only noise robust, but also its invariance to contrast, illumination and scale makes the automatic application to identify discontinuous displacement data points beneficial.

The quantitative identification of the crack faces was then used to build the crack model: displacement difference between the crack faces provide crack opening displacement; mid-point between the crack faces give an approximation of the crack path.

The PC-CD was shown to be more accurate and robust to noise than the widely used gradient based and Heaviside algorithms. Theoretical analysis also showed that while the uncertainty in the displacement field impacted the crack opening displacement measurement, the effects were minimal on the location of crack path location and crack length. The spatial resolution study based on the virtual experiments showed that selection of subset size, step size and subset positioning played a large role in the uncertainty of the crack path location and crack length.

Selection of the DIC parameters such as subset size, step size (i.e. data point spacing) and subset positioning play a critical part in the accuracy of PC-CD's crack extraction. Subset size selection is an optimization problem between, high spatial resolution, requiring small subsets, and high certainty requiring large subsets. Step size (i.e. data point spacing) and subset positioning determine the data point grid placement on the reference image and therefore, retrospectively define which subsets interact with the crack. It is key to note that if step size is 1, subset positioning becomes irrelevant as a data point is placed at each and every pixel location at the reference image.

To demonstrate the versatility, the method was applied to both quasi-brittle and ductile materials with different levels of deformation around the crack tip.

The crack parameters measured by the method were validated through high resolution optical microscopy, fractography and visual observation. The measurements by optical microscopy and fractography can be used as validation because of their higher resolution compared to the macro-image observation of the surface which was used to calculate the displacement measurements. However, what the higher resolution setups possess in accuracy, they lack in experimental easiness and versatility. For example, fractography data of a fractured sample can only be obtained at the end of the experiment where the specimen is split into two. High resolution image gives very valuable information regarding the failure behaviour where user judgement is required to characterise the data while carrying out the test. To obtain optical microscope data of a fractured surface, the sample requires to be placed on a steady stage while moving the sample along the crack path. The images are iteratively captured and stitched together to create a high resolution crack map, but at the cost of time. The optical microscope has a thin depth of field, so any small movements of the

sample, away or towards the microscope lens, will put the crack out of focus and unobservable limiting the experimental setup. Therefore the application of the optical microscope to observe the crack during mechanical loading can be inconvenient.

Digital Image Correlation is easy to implement, can capture thousands of images per second (i.e. high-speed imaging) and with the aid of PC-CD and with sufficient computer power, the method can characterise the captured images in real time. Unlike optical microscopy and fractography, crack opening displacement profiles can be obtained while under mechanical load.

Arguably, one drawback is that a reference image (i.e. uncracked surface or closed crack as demonstrated in section 5.4) is required, which may not be obtainable. However, typically in fracture assessment experiments, fracture is initiated in a controlled manner and therefore the reference image is obtainable.

A cracked ductile sample (i.e. Aluminium, section 5.3) surface was observed by both stereo-DIC and high resolution optical microscopy. The difference in crack path between high resolution optical microscopes combined with manual image segmentation vs. the faster automatic PC-CD was less than 3 pixels. A step size 1 with a subset size of 9 was used in the DIC calculation. Another cracked ductile sample (i.e. Bainitic steel, section 5.4) with crack closure and crack blunting was studied with stereo-DIC and fractography. The average crack length difference between the automatic PC-CD and fractography was approximately 6 pixels. Displacement field calculation was step size of 4 and subset size of 17.

Since the crack measurements are based on displacement fields, PC-CD method is not limited to a certain length scale and can be readily applied to any image-based discontinuous measurement. The limitation of the crack detection is the image resolution for displacement measurement and the discontinuity signal to noise ratio. While control of image resolution can be easy, it can prove more difficult and limited for the effect of noise (e.g. Image averaging, see section 5.4.2). Virtual experiment showed that with typical experimental noise (i.e. medium noise), PC-CD is able to accurately detect and quantify cracks that have a mouth opening of 0.1 pixel. The sub-pixel crack detection and characterisation were validated in the quasi-brittle sample (i.e. Rock, see section 5.2) where the crack opening was less than a pixel and the crack was only visually observed due to the impact of crack propagation on the microstructure.

The automatic extraction of a crack's parameters allow for the better understanding of its behaviour and interaction with the microstructure. While obtaining a crack geometry is important, quantifying crack parameters is also critical in fracture mechanics. This thesis presented a methodology (OUR-OMA) which can be used conjointly with PC-CD to obtain automatic Stress Intensity Factor (SIF) on traction for a given displacement field. The measured displacements on their own, lack the extra knowledge of the continuum mechanics as DIC is purely an image processing tool. OUR-OMA imports the displacement measurements in a Finite Element (FE) model, and applies smoothing based on the continuum mechanics. It also calculates the stress field using defined material properties. The J-integral values are then calculated from the stress on strain fields. The application of OUR-OMA and PC-CD is shown to be highly versatile and can be extended to elastic and elastic-plastic crack tip fields. The automatic SIF extraction means that the application can be effectively administered in real time to fracture assessment experiments.

The PC-CD method was expanded to the analysis of volumetric displacement measurements of cracked bodies. The VPC-CD method allowed the semi-automatic extraction of a crack's full volumetric geometrical parameters which gave more information and a better understanding of the failure mechanism. Crack opening displacement in the thickness of the crack can be calculated to paint valuable information as to the plane stress and plane strain conditions of a cracked body. A multi-phase ductile material (i.e. Al-Ti, section 6.2.2) was explored, semi-automatically, with the novel VPC-CD and OUR-OMA methodologies. The VPC-CD analysis showed complex and convoluted crack surface through the thickness of the sample, due to the microstructure. The crack surface, extracted by VPC-CD, was validated by superimposing it on the deformed tomograph, which showed strong agreement. The VPC-CD analysis also allowed for the study of opening displacement in the thickness which gave an insight into the complex mechanics of the crack. OUR-OMA methodology was applied to the displacement measurement and stress intensity factor through the thickness of the sample was extracted. The VPC-CD method was also applied to a further two quasi-brittle materials where the extraction of the crack's parameters gave in-depth information. The microstructure of graphite had pores, which were of the same grey-scale intensity as the crack, so it would have been difficult to segment the crack using image-based segmentation methods. Similar issues would have been experienced with carbon fibre due to the damage process zone impacting the grey-scale intensity of the microstructure. VPC-CD was shown to be powerful in the application of quasi-brittle materials.

8 FUTURE WORK

In this research, PC-CD and VPC-CD have both been proven to be powerful tools in the automatic extraction of crack parameters from measured displacement fields. However, like most algorithms, they are limited to the conditions initially instructed to achieve and hence have a few areas that can be improved which can increase the optimization and versatility.

To present an idealized proof of concept, this thesis successfully investigated cracked displacement fields of single, horizontal mode I fracture. Although, consciously, mixed mode fracture was not studied, two experiments showed evidence of mixed-mode loadings (i.e. Al-Ti, section 6.2.2 and Graphite, section 6.3) which validated PC-CD's approach. The displacement orientation that carries the highest discontinuity signal is selected for identification of discontinuous data points. However, the novel PC-CD method is required to be further verified with mixed-mode fracture experiments. The automatic selection of displacement would become necessary and can be achieved through statistical analysis, but was not considered in the research project due to the analysis of mode I fracture.

The automatic detection of multiple cracks from a single displacement field were very briefly investigated but not included in this research. The idea was to use Hough transform iteratively to obtain multiple initial crack masks.

Consider the following Figure 8.1: a) Phase congruency map of a cracked displacement field; b) Edge map; c) Hough transform is applied on the edge map to find the longest straight line, identified by the blue line. *SelectCC* is used to select all the connected components to end points of the blue line; d) The selected component is classified as initial mask for the first crack and the component is removed; e) A further iteration of the Hough transform is applied, but this time to d), to select the second initial mask, identified as the blue line; f) The two initial masks obtained from c) and e) are used to segment PC using automatic active contours.

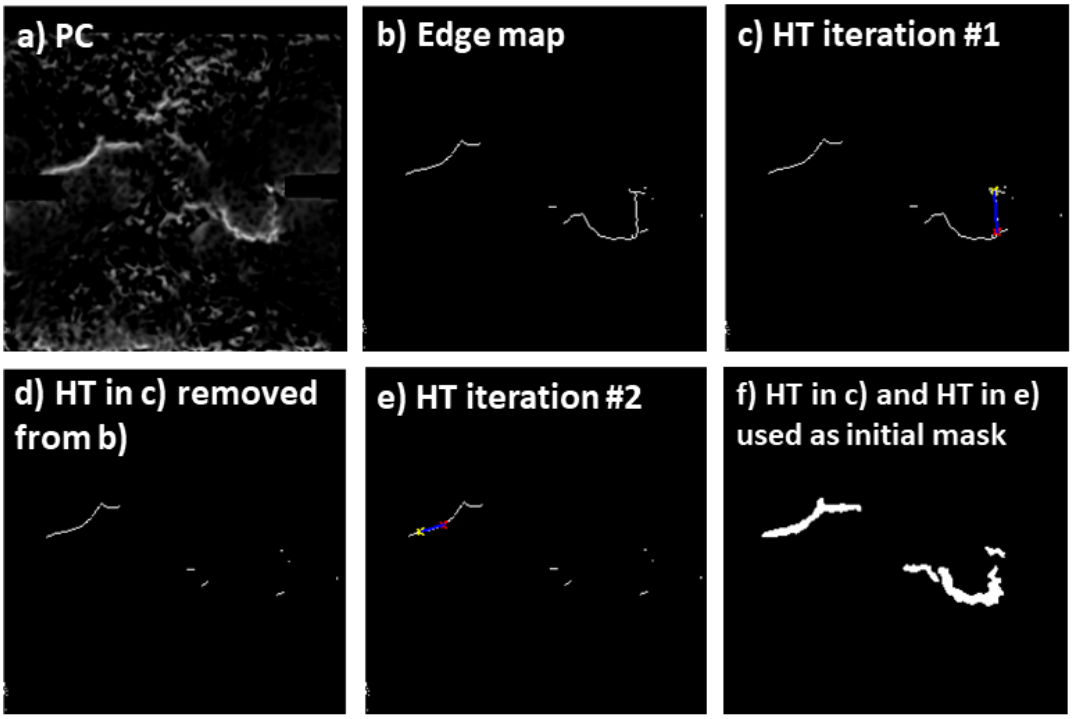

Figure 8.1 Automatic multiple crack detection a) Phase congruency map , b) Edge map c) Hough transform (HT) iteration #1 d) Detected initial mask removed from b), e) Hough transform iteration #2, f) Crack mask where detected lines from Hough transform from c) and e) are used as initial masks

This methodology is purely an idea to automatically detect multiple crack may make the PC-CD method more versatile.

The optimization of the two Phase congruency parameters, λ_{min} and d_{PC}, discussed in section 3.12, can better select the discontinuous data points. It was discussed that the DIC parameters, subset and step size, impact the sharpness of the discontinuity while the selection of λ_{min} and d_{PC} depend on the scale space of the feature. Hence, Phase congruency map can be optimized if the two variables, λ_{min} and d_{PC}, are informed on the selection of subset and step size.

Accurate classification of outliers in discontinuous displacement fields are important for the selection of spurious errors caused by the crack artefact or dust between the lens and the sample, as discussed in section 3.1. A literature review and study based on the different outlier tools can help PC-CD remove erroneous data points more effectively, and directly, improving the results. As mentioned in section 3.5, the wealth of PIV (Particle Imaging Velocimetry) literature can help with development of a better outlier deletion model.

Another process that can be optimized is the recovery of the missing displacement data points. Missing displacement data points are common in image correlation while accurate recovery can impact the extracted crack parameters (i.e. COD). An investigation based on the impact of different extrapolation or data recovery methods may lead to the improvement of PC-CD. One method to investigate would be to study Finite Element –based recovery, where the missing data points are approximated based on the known continuum mechanics, similar to the methodology used in OUR-OMA method.

The VPC-CD algorithm can be developed so that the crack initial mask is selected automatically. The automatic selection of the initial mask not only removes the user interaction, but also proposes better initial mask selection. Similar to the observation with PC-CD, better initial mask leads on to less iterations and faster convergence.

In theory, each step of the automatic crack detection procedure can be developed to three-dimensional space. The literature for volume application of 2D automatic crack detection steps can be found here:

- Step 6 - Volume Bilateral filter [218]
- Step 7 - Volume Sobel edge operator [219]
- Step 8 - Volume Hough Transform [220]
- Step 9 - Volume Select Connected Components [160].

Volume Hough transform is developed to detect the largest surface area rather than the longest line.

The Volume Phase congruency map can be improved so that instead of a slice by slice construction, as proposed by this research, the full volume is used to detect the discontinuous data points. This means that the development will solve the slice dependency problem (defined in section 3.3). Upon recent research, the author of this thesis found an algorithm which uses the full volume based on the monogenic filter. The 3DPC (Three dimensional Phase Congruency) was coded by Chris Bridge, Department of Engineering Science, University of Oxford. The ref to the code can be found here.[221]

The Graphite dataset(see section 6.3) for the last loading stage was used to show the difference between VPC (proposed by this research) and 3DPC [221]. Figure 8.2 shows the comparison between the two where $Y = 4.63$ mm slice is taken from both PC maps to show the difference.

The segmentation of VPC (Figure 8.2a) and 3DPC (Figure 8.2c) is seen to be almost identical. It was seen that the difference in crack opening displacement was much below the noise threshold. The slice maps of VPC and 3DPC shows an identical feature of the crack, however it seems that 3DPC is much sharper and better localised. The investigation of VPC and 3DPC is interesting and is added to future work.

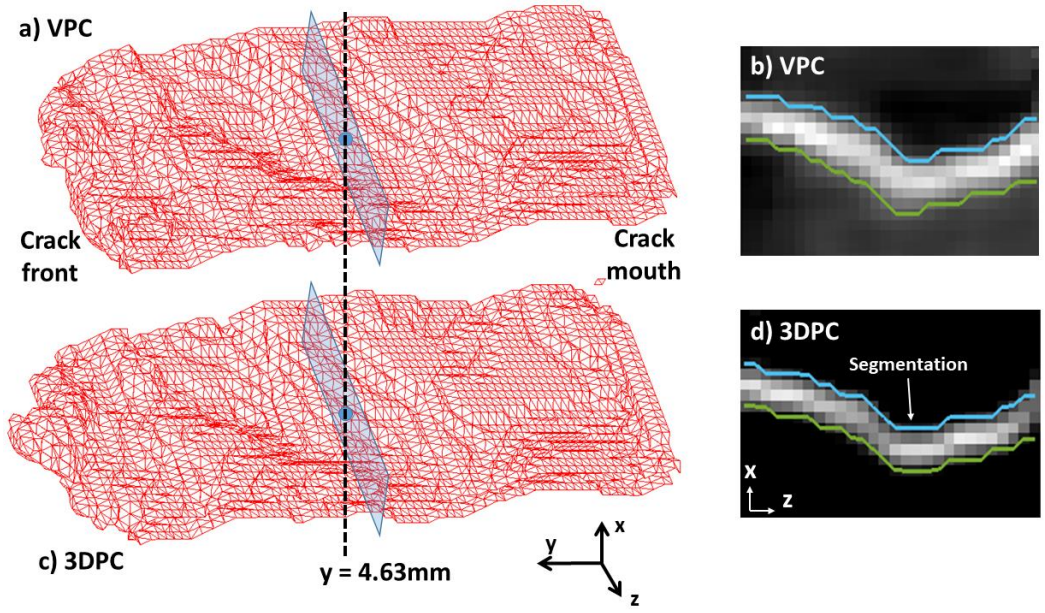

Figure 8.2 Segmentation comparison VPC vs 3DPC a) Segmentation of VPC , b) Slice of VPC at y=4.63mm c) Segmentation of 3DPC d) Slice of 3DPC at y=4.63

Appendix A

```
%% Automatic Crack detection tool by Ahmet Cinar, Department of Mechanical
Engineering, University of Sheffield, UK

% Selim Barhli, Department of Materials, University of Oxford, UK

% Dave Hollis, LaVision, UK

% Rachel Tomlinson, Department of Mechanical Engineering, University of
Sheffield, UK

% James Marrow, Department of Materials, University of Oxford, UK

% Mahmoud Mostafavi, Department of Mechanical Engineering, University of
Bristol, UK

 %For enquiries email :

% afcinar1@sheffield.ac.uk

% ahmetron@gmail.com

 %Paper for citation: https://doi.org/10.1016/j.optlaseng.2017.04.010

%% Manual

% 1) Change directory of "FolderName" to select path for "CrackDetection"
folder

% 2) Set paths for "Add_on"

% 3) Edit fine tuning parameters if nessesary

% 4) Run code "Main_Example.m"

% 5) Select region of interest (RIO) then double click inside the ROI

% 6) Select orientation of the crack (Default for example - Verticle (Press

% V and hit enter"

% 7) Option to apply Outlier filter (Deletion and fil) (Default for example
- Y (Press Y and hit enter)

 %% Output:

% CrackPath_X - Estimated Crack path location in X-axis

% CrackPath_Y - Estimated Crack path location in Y-axis

% COD_Ux - Crack opening dispalcement Ux

% COD_Uy - Crack opening dispalcement Uy

%% (Optional)

%SubP_CrackPath_X - Estimated sub-point Crack Path location in X-axis using

%Weighted mean

%SubP_CrackPath_Y - Estimated sub-point Crack Path location in Y-axis using

%Weighted mean

%COD_Ux_3P - 3 point average, Crack Opening displacement Ux

%COD_Uy_3P - 3 point average, Crack Opening displacement Uy

%% Main Code starts here
```

```
close all

clear all

clc

 %%%% Fine tuning parameters

% % Outlier deletion

% ODw = 5;  % Outlier deletion window (ODw) - Deletion search window (Default
- 5, Range: 3-20)

% ODt = 0.01; % Outlier deletion threshold (ODt) - Deletion treshold (Default
- 0.0 , Range: 0.1 - 0.00001)

% % Phase congruency

% PC_1 = 4 % Feature size in scale space (Phase congruency parameter 1) -
(Default - 4 , Range: 2-20)

% PC_2 = 1.2 %Feature frequency cut-off point (Phase congruency parameter 2)
- (Default - 1.2, Range: 0.8-1.6)

% %Active contour

% ittern = 100; %Maximum number of itterations - (Default - 100, Range:100-
1000)

% SEG_1 = 0.8; %Segmentation alpha - active contour smoothness (Default -
0.8, Range: 0.001-1)

FolderName = 'C:\Users\Ahmet\Dropbox\'; % Change Directory that contains
displacement file, "CrackDetecion" in this example

FileName = 'DisplacementData.txt'; %Displacement data file name

%% Step 1

temp=importdata([FolderName FileName]);

DLast = temp.data;

j=-1;

k=1;

while j<0

    if DLast(k,2)==DLast(k+1,2)

        k=k+1;

    else

        lx=k;

        j=1;

    end

end

ly=size(DLast,1)/lx;

X=reshape(DLast(:,1),lx,ly);

Y=reshape(DLast(:,2),lx,ly);

Ux=reshape(DLast(:,3),lx,ly);

Uy=reshape(DLast(:,4),lx,ly);

Ux(Ux==0)=nan;
```

```
Uy(Uy==0)=nan;


V = sqrt((Ux.^2)+(Uy.^2));
[~, rec] = imcrop(V);
close all
rec =[round(rec(1))  round(rec(2))  round(rec(3))  round(rec(4))];




C_X = imcrop(X,rec);
C_Y = imcrop(Y,rec);
C_Uy = imcrop(Uy,rec);
C_Ux=imcrop(Ux,rec);

%% Step 2
prompt = 'Select orientation of crack! Vertical (Y-axis) or  Horizontal (X-
axis) - crack? [V/H]: ';
Orientation = input(prompt,'s');

%% Step 3

FC_Ux = inpaint_nans(C_Ux,1);
FC_Uy = inpaint_nans(C_Uy,1);

figure
if Orientation == 'V'
    imagesc(FC_Uy')
else
    imagesc(FC_Ux')
end

%% Step 4
prompt1 = 'Would you like to apply Outlier deletion? [Y/N] ';
str1 = input(prompt1,'s');
if str1=='Y'
    ODw = 5;
    ODt = 0.01;
```

```
    OFC_Ux = OutDel(FC_Ux,ODw,ODt);
    OFC_Uy = OutDel(FC_Uy,ODw,ODt);
    figure
    if Orientation == 'V'
        imagesc(OFC_Uy')
    else
        imagesc(OFC_Ux')
    end

    %% Step 5

    FOFC_Ux = inpaint_nans(OFC_Ux,1);
    FOFC_Uy = inpaint_nans(OFC_Uy,1);
    if Orientation == 'V'
        imagesc(FOFC_Uy')
    else
        imagesc(FOFC_Ux')
    end

elseif str1=='N'
    display('No Outlier applied')
end
%% Automatic Crack Detection

if Orientation == 'V'
    if exist('FOFC_Uy')==1
        CrackDetection = FOFC_Uy;
    else
        CrackDetection = FC_Uy;
    end
elseif  Orientation == 'H'
    if exist('FOFC_Ux')==1
        CrackDetection = FOFC_Ux;
    else
        CrackDetection = FC_Ux;
    end
else
    return
```

```
end


%% Step 6
B_CrackDetection = bfilter2(NormalizeMatrix(CrackDetection),2,[20 0.1]);
B_CrackDetection(B_CrackDetection==1) = nan;
B_CrackDetection =inpaint_nans(B_CrackDetection,1);


%% Step 7
Edge_B_CrackDetection = edge(B_CrackDetection,'sobel');


%% Step 8
H_Theta_Min = -90;
H_Theta_Max = 89;
H_minlength = 10;
H_fillgap = 5;



[Hough_H,Hough_T,Hough_R] = hough(Edge_B_CrackDetection,'Theta',H_Theta_Min:1:H_Theta_Max);
Hough_P  = houghpeaks(Hough_H,10,'threshold',ceil(0.5*max(Hough_H(:))));
lines = houghlines(Edge_B_CrackDetection,Hough_T,Hough_R,Hough_P,'FillGap',H_fillgap,'MinLength',H_minlength);


max_len = 0;


% Determine the endpoints of the longest line segment
for k = 1:length(lines)
    xy = [lines(k).point1; lines(k).point2];


    len = norm(lines(k).point1 - lines(k).point2);
    if ( len > max_len)
        max_len = len;
        xy_long = xy;
    end
end
% "xy_long" is the longest line
% highlight the longest line segment
figure, imshow(Edge_B_CrackDetection), hold on
```

```
plot(xy_long(:,1),xy_long(:,2),'LineWidth',2,'Color','blue')


line_theta         =         (atan((xy_long(1,2)-xy_long(2,2))/(xy_long(1,1)-
xy_long(2,1))))*57.2957795;




%% Step 9


Initial_mask = selectCc(Edge_B_CrackDetection,[],xy_long(2,2),xy_long(2,1));



%% Step 10

PC_1 = 4;

PC_2 = 1.2;


PC = phasecongmono(CrackDetection, 6,PC_1, 2, 0.55, 1.0,0.25,10,PC_2,-1);


%% Step 11


ittern = 100;

SEG_1 = 0.8; %Seg_Alpha


CrackSeg = region_seg(PC, Initial_mask, ittern,SEG_1);

 %% Crack Parameter Extraction

if exist('FOFC_Uy')==1

    Seg_Ux = FOFC_Ux;

    Seg_Ux(CrackSeg==1)=nan;

    Seg_Uy = FOFC_Uy;

    Seg_Uy(CrackSeg==1)=nan;

else

    Seg_Ux = FC_Ux;

    Seg_Ux(CrackSeg==1)=nan;

    Seg_Uy = FC_Uy;

    Seg_Uy(CrackSeg==1)=nan;

end


[COD_Ux,    COD_Uy,    COD_Ux_3P,    COD_Uy_3P,    CrackPath_X,    CrackPath_Y,
SubP_CrackPath_X,    SubP_CrackPath_Y]    =    CrackParameterExtraction(Seg_Ux,
Seg_Uy, C_X, C_Y,PC,CrackSeg,Orientation);
```

```
if Orientation == 'V'

    figure
    title('Crack Path co-ordinate location')
    plot(CrackPath_X,CrackPath_Y)
    hold on
    plot(SubP_CrackPath_X,SubP_CrackPath_Y)
    legend('Mid-point', 'PC Weighted-Mean')

    figure
    title('Crack Opening displacement (Ux)')
    plot(CrackPath_X, COD_Ux)
    hold on
    plot(CrackPath_X, COD_Ux_3P)
    legend('Ux COD', 'Ux 3 point average COD')


    figure
    title('Crack Opening displacement (Uy)')
    plot(CrackPath_X, COD_Uy)
    hold on
    plot(CrackPath_X, COD_Uy_3P)
    legend('Uy COD', 'Uy 3 point average COD')


else
    title('Crack Path co-ordinate location')
    figure
    plot(CrackPath_Y,CrackPath_X)
    hold on
    plot(SubP_CrackPath_Y,SubP_CrackPath_X)
    legend('Mid-point', 'PC Weighted-Mean')

    figure
    title('Crack Opening displacement (Ux)')
```

```
    plot(CrackPath_Y, COD_Ux)
    hold on
    plot(CrackPath_Y, COD_Ux_3P)
    legend('Ux COD', 'Ux 3 point average COD')


    figure
    title('Crack Opening displacement (Uy)')
    plot(CrackPath_Y, COD_Uy)
    hold on
    plot(CrackPath_Y, COD_Uy_3P)
    legend('Uy COD', 'Uy 3 point average COD')
end
```

Appendix B

```
function [COD_Ux, COD_Uy, COD_Ux_3P, COD_Uy_3P, CrackPath_X,
CrackPath_Y, SubP_CrackPath_X, SubP_CrackPath_Y] =
CrackParameterExtraction(Seg_Ux, Seg_Uy, C_X, C_Y,PC,CrackSeg,
Orientation);


%% Find Crack Boundaries and Faces

[m_size, n_size] = size(Seg_Ux);

Seg_X = C_X;

Seg_X(CrackSeg==1)=nan;

Seg_Y = C_Y;

Seg_Y(CrackSeg==1)=nan;

if Orientation=='V'


    for i=1:m_size

        if sum(isnan(Seg_Ux(i,:)))>1

            NaNLoc = find(isnan(Seg_Ux(i,:))==1);

            UpperB(i) = max(NaNLoc);

            LowerB(i) = min(NaNLoc);

            UpperFace(i) = UpperB(i) + 1;

            LowerFace(i) = LowerB(i) - 1;


            UpperFace3P = [UpperFace(i) UpperFace(i)+1
UpperFace(i)+2];

            LowerFace3P = [LowerFace(i) LowerFace(i)-1 LowerFace(i)-
2];


            %% Step 12


            COD_Ux(i) = abs(Seg_Ux(i,UpperFace(i))-
Seg_Ux(i,LowerFace(i)));

            COD_Uy(i) = abs(Seg_Uy(i,UpperFace(i))-
Seg_Uy(i,LowerFace(i)));

            COD_Ux_3P(i) = abs(mean(Seg_Ux(i,UpperFace3P))-
mean(Seg_Ux(i,LowerFace3P)));

            COD_Uy_3P(i) = abs(mean(Seg_Uy(i,UpperFace3P))-
mean(Seg_Uy(i,LowerFace3P)));
```

```
            CartSpaceUpperX(i) = Seg_X(i,UpperFace(i));
            CartSpaceLowerX(i) = Seg_X(i,LowerFace(i));
            CartSpaceUpperY(i) = Seg_Y(i,UpperFace(i));
            CartSpaceLowerY(i) = Seg_Y(i,LowerFace(i));




        end
    end
    %% Step 13
    % Crack Path (Mid-point)

    CrackPath_X = CartSpaceUpperX;
    CrackPath_Y = (CartSpaceUpperY + CartSpaceLowerY)/2;

    % PC-weighted mean (Sub-point CrackPath)
    ii = 0;
    for i=1:size(CrackSeg,1)
        if sum(CrackSeg(i,:)==1)>1
            ii = ii + 1;
            CP_Y = [];
            CP_Y = find(CrackSeg(i,:)==1);
            SubP_CrackPath_Y(ii) =
(sum(PC(i,CP_Y).*C_Y(i,CP_Y)))./sum(PC(i,CP_Y));
        else continue
        end
    end
    SubP_CrackPath_X = CrackPath_X;
    %%

elseif Orientation=='H'
    for i=1:n_size
        if sum(isnan(Seg_Ux(:,i)))>1
```

```
            NaNLoc = find(isnan(Seg_Ux(:,i))==1);
            UpperB(i) = max(NaNLoc);
            LowerB(i) = min(NaNLoc);
            UpperFace(i) = UpperB(i) + 1;
            LowerFace(i) = LowerB(i) - 1;

            UpperFace3P(i) = [UpperFace(i) UpperFace(i)+1
UpperFace(i)+2];
            LowerFace3P(i) = [LowerFace(i) LowerFace(i)-1
LowerFace(i)-2];

            %% Step 12
            COD_Ux(i) = abs(Seg_Ux(UpperFace(i),i)-
Seg_Ux(LowerFace(i),i));
            COD_Uy(i) = abs(Seg_Uy(UpperFace(i),i)-
Seg_Uy(LowerFace(i),i));
            COD_Ux_3P(i) = abs(mean(Seg_Ux(UpperFace3P,i))-
mean(Seg_Ux(LowerFace3P,i)));
            COD_Uy_3P(i) = abs(mean(Seg_Uy(UpperFace3P,i))-
mean(Seg_Uy(LowerFace3P,i)));

            CartSpaceUpperX(i) = Seg_X(UpperFace(i),i);
            CartSpaceLowerX(i) = Seg_X(LowerFace(i),i);
            CartSpaceUpperY(i) = Seg_y(UpperFace(i),i);
            CartSpaceLowerY(i) = Seg_Y(LowerFace(i),i);

        end
    end
    %% Step 13
    % Crack Path (Mid-point)

    CrackPath_X = (CartSpaceUpperX + CartSpaceLowerX)/2;
    CrackPath_Y = CartSpaceUpperY;

    % PC-weighted mean (Sub-point CrackPath)
    ii = 0;
```

```
    for i=1:size(CrackSeg,1)
        if sum(CrackSeg(:,i)==1)>1
            ii = ii + 1;
            CP_X = [];
            CP_X = find(CrackSeg(:,i)==1);
            SubP_CrackPath_X(ii) =
(sum(PC(CP_X,i).*C_X(CP_X,i))./sum(PC(CP_X,i));
        else continue
        end
    end

    SubP_CrackPath_Y = CrackPath_Y;

end

COD_Ux(COD_Ux==0) = [];
COD_Uy(COD_Uy==0) = [];
COD_Ux_3P(COD_Ux_3P==0) = [];
COD_Uy_3P(COD_Uy_3P==0) = [];
CrackPath_X(CrackPath_X==0) = [];
CrackPath_Y(CrackPath_Y==0) = [];
SubP_CrackPath_X(SubP_CrackPath_X==0) = [];
SubP_CrackPath_Y(SubP_CrackPath_Y==0) = [];

end
```

Appendix C

Phase congruence intensity at each data point is used to find the peak and sub-point approximation of the crack location by using the weighted mean function.

The weighted mean is given by:

$$\mathrm{WM\_CPX_j} = \frac{\sum_i \mathrm{C\_X_{i,j}} * \mathrm{PC_{i,j}}}{\sum_i \mathrm{PC_{i,j}}} \quad (58)$$

Weighted mean crack path co-ordinate = $(\mathrm{WM\_CPX_j}, \mathrm{C\_Y_{1,j}})$

$$\mathrm{WM\_CPY_i} = \frac{\sum_j \mathrm{C\_Y_{i,j}} * \mathrm{PC_{i,j}}}{\sum_i \mathrm{PC_{i,j}}} \quad (59)$$

Weighted mean crack path co-ordinate $= (\mathrm{C\_X_{i,1}}, \mathrm{WM\_CPY_i})$

Depending on the selected orientation of the crack from Step 2, Eq. (58) is used for vertical or Eq. (59) is used for horizontal discontinuity.

$\mathrm{WM\_CPX}$ and $\mathrm{WM\_CPY}$ are the calculated weighted mean for X and $Y-$ axis component of crack path location. $\mathrm{C\_X}$ and $\mathrm{C\_Y}$ is the data point coordinate location in X and $Y-$ axis (pixels / mm) and *PC* is the phase congruence intensity.

i and j are the index locations for the data points that only exist within the boundaries of the crack mask ($\mathrm{CrackMask}$) (i.e. green points in Figure 3.15b)

A line profile of Phase congruency is taken across the crack at each data point along the crack. The weighted mean is calculated for each line profile to approximate the point of discontinuity location. This enables the algorithm to approximate the crack path location between data points and achieve a sub-point estimate.

Data points and their Phase congruence intensity has been used to find the Weighted-mean crack path location in Figure 3.15b where the red cross shows the calculated approximation. No obvious difference is seen for crack path between Mid-point method and PC weighted

mean method by comparing Figure 3.15(a and b). Figure 3.14b shows a magnified y-coordinate approximation of the location of both calculations; the blue line shows the Mid-point method, the orange line shows the PC-weighted mean and the yellow line shows the prescribed crack path location.

It can be observed from Figure 3.14b, the crack path location for mid-point method can only exist exactly on data points or half way between two data points. Data point spacing (step size) for the following dataset is 4 pixels – giving the mid-point method a precision of 2 pix. The prescribed crack path is at Y coordinate of 1023, while due to the data point spacing and positioning, the crack path for the mid-point method can only exist in multiples of two (i.e. $Y = 1020, 1022, 1024, 1026$). This observation validates the crack path dependence on grid placement and data point spacing.

PC-weighted mean method allows for the crack path to be approximated between the data point grid spacing and is not limited like the mid-point method. If the discontinuity is accurately captured, the PC-weighted mean method can give the calculation more flexibility and a better precision as seen in the Figure 3.14b. RSME (Root Square Mean Error using Eq. (53)) of mid-point is given to be 3.39 pixels while RSME for PC-weighted mean is slightly more accurate at 3.32 pixels compared to the prescribed crack path.

Bibliography

[1] A. Cinar, S. Barhli, D. Hollis, M. Flansbjer, R. Tomlinson, T. Marrow*, et al.*, "An autonomous surface discontinuity detection and quantification method by digital image correlation and phase congruency," *Optics and Lasers in Engineering,* vol. 96, pp. 94-106, 2017.

[2] M. M. Selim Matthias Barhli, Ahmet F Cinar, David Hollis, Thomas James Marrow, "J-integral calculation by finite element processing of measured full-field surface displacements," *Experimental mechanics,* vol. 57.6, pp. 997-1009, 2017.

[3] S. M. B. M. M. A. F. C. D. H. T. J. Marrow, "J-integral calculation by finite element processing of measured full-field surface displacements," *Experimental mechanics,* vol. 57.6, pp. 997-1009, 2017.

[4] S. Barhli, L. Saucedo-Mora, M. Jordan, A. Cinar, C. Reinhard, M. Mostafavi*, et al.*, "Synchrotron X-ray characterisation of crack strain fields in polygranular graphite," *Carbon,* vol. 124, pp. 357-371, 2017.

[5] P. Wilson, A. Cinar, M. Mostafavi, and J. Meredith, "Temperature driven failure of carbon epoxy composites–A quantitative full-field study," *Composites Science and Technology,* vol. 155, pp. 33-40, 2017.

[6] A. F. Cinar, S. M. Barhli, D. Hollis, R. A. Tomlinson, T. J. Marrow, and M. Mostafavi, "Autonomous surface discontinuity detection method with Digital Image Correlation," presented at the 10th BSSM International Conference on Advances in Experimental Mechanics, Heriot-Watt University, Edinburgh, UK, 2015.

[7] A. F. Cinar, S. M. Barhli, D. Hollis, R. A. Tomlinson, T. J. Marrow, and M. Mostafavi, "Application of 3D phase congruency in crack identification within materials," presented at the 11th BSSM International Conference on Advances in Experimental Mechanics, University of Exeter, Exeter, UK, 2016.

[8] A. F. C. C. Simpson, P. Lopez-Crespo, M. Mostafavi, T. Connolley, P.J. Withers, "The evolution of crack tip stress fields as a function of R-ratio and overload during fatigue crack growth in a bainitic steel," in *12th International Conference on Fatigue Damage of Structural Materials*, 2016.

[9] C. W. T. Connolley, F. Wang, M. Mostafavi, A.F. Cinar, D. Eskin and J. Mi, "In-Situ X-Ray Observations of the Effect of Ultrasound on Liquid and Semi-Solid Metal Alloys," in *THERMEC 2016 International Conference on Processing & Manufacturing Of Advanced Materials*, 2016.

[10] D. H. A.F.Cinar, R.A. Tomlinson, C. Reinhard, T. Connolley, T.J. Marrow, M.Mostafavi, "Crack characterization in a Metal Matrix Composite with 3D Phase Congruency and Digital Volume Correlation," in *12th*

International Conference on Advances in Experimental Mechanics (BSSM), Sheffield, University of Sheffield, 2017.

[11] E. Astm, "399-90:" Standard test method for plane-strain fracture toughness of metallic materials," *Annual book of ASTM standards,* vol. 3, pp. 506-536, 1991.

[12] J. R. Rice, "A path independent integral and the approximate analysis of strain concentration by notches and cracks," *Journal of applied mechanics,* vol. 35, pp. 379-386, 1968.

[13] A. A. Griffith and M. Eng, "VI. The phenomena of rupture and flow in solids," *Phil. Trans. R. Soc. Lond. A,* vol. 221, pp. 163-198, 1921.

[14] G. R. Irwin, "Analysis of Stresses and Strains Near the End of a Crack Traversing a Plate," *J. Appl. Mech., //* 1957.

[15] E. Orowan, "Fracture and strength of solids," *Reports on Progress in Physics,* vol. 12, pp. 185-232, 1949/01/01 1949.

[16] N. I. Muskhelishvili, *Some basic problems of the mathematical theory of elasticity*: Springer Science & Business Media, 2013.

[17] H. M. Westergaard, "Bearing pressures and cracks," *Trans AIME, J. Appl. Mech.,* vol. 6, pp. 49-53, 1939 1939.

[18] M. Williams, "The bending stress distribution at the base of a stationary crack," *Trans. ASME,* vol. 79, pp. 109-114, 1957.

[19] A. A. Wells, "Unstable crack propagation in metals: cleavage and fast fracture," in *Proceedings of the crack propagation symposium*, 1961.

[20] A. Kobayashi, S. Chiu, and R. Beeuwkes, "A numerical and experimental investigation on the use of J-integral," *Engineering Fracture Mechanics,* vol. 5, pp. 293-305, 1973.

[21] C. Shih, "Relationships between the J-integral and the crack opening displacement for stationary and extending cracks," *Journal of the Mechanics and Physics of Solids,* vol. 29, pp. 305-326, 1981.

[22] Y. Yao and B. Glisic, "Detection of steel fatigue cracks with strain sensing sheets based on large area electronics," *Sensors,* vol. 15, pp. 8088-8108, 2015.

[23] Y. Yao, S. T. E. Tung, and B. Glisic, "Crack detection and characterization techniques—An overview," *Structural Control and Health Monitoring,* vol. 21, pp. 1387-1413, 2014.

[24] J. Otegui, U. Mohaupt, and D. Burns, "A strain gauge technique for monitoring small fatigue cracks in welds," *Engineering fracture mechanics,* vol. 40, pp. 549-569, 1991.

[25] Y. Okabe, S. Yashiro, T. Kosaka, and N. Takeda, "Detection of transverse cracks in CFRP composites using embedded fiber Bragg grating sensors," *Smart Materials and Structures,* vol. 9, p. 832, 2000.

[26] J. Tikka, R. Hedman, and A. Silijander, "Strain gauge capabilities in crack detection," in *4th International Workshop on Structural Health Monitoring*, 2003, pp. 15-17.

[27] I. Kang, M. J. Schulz, J. H. Kim, V. Shanov, and D. Shi, "A carbon nanotube strain sensor for structural health monitoring," *Smart materials and structures,* vol. 15, p. 737, 2006.
[28] Y. Zhang, "In situ fatigue crack detection using piezoelectric paint sensor," *Journal of Intelligent Material Systems and Structures,* vol. 17, pp. 843-852, 2006.
[29] G. Schajer, "Application of finite element calculations to residual stress measurements," *Journal of engineering materials and technology,* vol. 103, pp. 157-163, 1981.
[30] M. Lengsfeld, J. Schmitt, P. Alter, J. Kaminsky, and R. Leppek, "Comparison of geometry-based and CT voxel-based finite element modelling and experimental validation," *Medical engineering & physics,* vol. 20, pp. 515-522, 1998.
[31] K. Akça, M. C. Çehreli, and H. İplikçioğlu, "A comparison of three-dimensional finite element stress analysis with in vitro strain gauge measurements on dental implants," *International Journal of Prosthodontics,* vol. 15, 2002.
[32] S. Natarajan, P. M. Baiz, S. Bordas, T. Rabczuk, and P. Kerfriden, "Natural frequencies of cracked functionally graded material plates by the extended finite element method," *Composite structures,* vol. 93, pp. 3082-3092, 2011.
[33] Y. Narkis, "Identification of crack location in vibrating simply supported beams," *Journal of sound and vibration,* vol. 172, pp. 549-558, 1994.
[34] P. Cawley and R. Adams, "The location of defects in structures from measurements of natural frequencies," *The Journal of Strain Analysis for Engineering Design,* vol. 14, pp. 49-57, 1979.
[35] M. Hicks and A. Pickard, "A comparison of theoretical and experimental methods of calibrating the electrical potential drop technique for crack length determination," *International Journal of Fracture,* vol. 20, pp. 91-101, 1982.
[36] L. Gandossi, S. Summers, N. Taylor, R. Hurst, B. Hulm, and J. Parker, "The potential drop method for monitoring crack growth in real components subjected to combined fatigue and creep conditions: application of FE techniques for deriving calibration curves," *International journal of pressure vessels and piping,* vol. 78, pp. 881-891, 2001.
[37] I. Hwang, "A multi-frequency AC potential drop technique for the detection of small cracks," *Measurement Science and Technology,* vol. 3, p. 62, 1992.
[38] J. D. Butterfield, V. Meruane, R. P. Collins, G. Meyers, and S. B. Beck, "Prediction of leak flow rate in plastic water distribution pipes using vibro-acoustic measurements," *Structural Health Monitoring,* p. 1475921717723881, 2017.

[39] D. Post and W. Baracat, "High-sensitivity moiré interferometry—a simplified approach," *Experimental Mechanics,* vol. 21, pp. 100-104, 1981.
[40] G. Nicoletto, "Moiré interferometry determination of residual stresses in the presence of gradients," *Experimental Mechanics,* vol. 31, pp. 252-256, 1991.
[41] B. C. Stockley and C. H. Buckberry, "Photoelastic stress analysis," ed: Google Patents, 1995.
[42] J. Dulieu-Barton and P. Stanley, "Development and applications of thermoelastic stress analysis," *The Journal of Strain Analysis for Engineering Design,* vol. 33, pp. 93-104, 1998.
[43] G. Pitarresi and E. Patterson, "A review of the general theory of thermoelastic stress analysis," *The Journal of Strain Analysis for Engineering Design,* vol. 38, pp. 405-417, 2003.
[44] T. Chu, W. Ranson, and M. A. Sutton, "Applications of digital-image-correlation techniques to experimental mechanics," *Experimental mechanics,* vol. 25, pp. 232-244, 1985.
[45] M. Sutton, S. McNeill, J. Helm, and Y. Chao, "Advances in two-dimensional and three-dimensional computer vision," *Photomechanics,* pp. 323-372, 2000.
[46] B. Han, D. Post, and P. Ifju, "Moiré interferometry for engineering mechanics: current practices and future developments," *The Journal of Strain Analysis for Engineering Design,* vol. 36, pp. 101-117, 2001.
[47] S. Horowitz, T. Chen, V. Chandrasekaran, K. Tedjojuwono, T. Nishida, L. Cattafesta*, et al.*, "A micromachined geometric moire interferometric floating-element shear stress sensor," in *42nd AIAA Aerospace Sciences Meeting and Exhibit*, 2004.
[48] M. Françon, "Optical interferometry," in *Neutron interferometry*, ed, 1979.
[49] K. Ramesh, "Digital photoelasticity," ed: IOP Publishing, 2000.
[50] W. Bradley and A. Kobayashi, "An investigation of propagating cracks by dynamic photoelasticity," *Experimental Mechanics,* vol. 10, pp. 106-113, 1970.
[51] M. Schroedl, J. McGowan, and C. Smith, "An assessment of factors influencing data obtained by the photoelastic stress freezing technique for stress fields near crack tips," *Engineering Fracture Mechanics,* vol. 4, pp. 801-809, 1972.
[52] M. Schroedl, J. McGowan, and C. Smith, "Use of a Taylor series correction method in photoelastic stress intensity determination," VIRGINIA POLYTECHNIC INST AND STATE UNIV BLACKSBURG DEPT OF ENGINEERING SCIENCE AND MECHANICS1973.
[53] J. Kalthoff, J. Beinert, and S. Winkler, "Measurements of dynamic stress intensity factors for fast running and arresting cracks in double-

cantilever-beam specimens," in *Fast Fracture and Crack Arrest*, ed: ASTM International, 1977.
[54] B. R. Boyce, "Steps to modern thermoelastic stress analysis," in *ATEM Conference, Ube, Japan*, 1999.
[55] P. Broberg, "Surface crack detection in welds using thermography," *NDT & E International,* vol. 57, pp. 69-73, 2013.
[56] D. Marr and E. Hildreth, "Theory of edge detection," *Proceedings of the Royal Society of London. Series B. Biological Sciences,* vol. 207, pp. 187-217, 1980.
[57] P. Dare, H. Hanley, C. Fraser, B. Riedel, and W. Niemeier, "An operational application of automatic feature extraction: the measurement of cracks in concrete structures," *The Photogrammetric Record,* vol. 17, pp. 453-464, 2002.
[58] I. Abdel-Qader, O. Abudayyeh, and M. E. Kelly, "Analysis of edge-detection techniques for crack identification in bridges," *Journal of Computing in Civil Engineering,* vol. 17, pp. 255-263, 2003.
[59] T. Yamaguchi and S. Hashimoto, "Fast crack detection method for large-size concrete surface images using percolation-based image processing," *Machine Vision and Applications,* vol. 21, pp. 797-809, 2010.
[60] S. Roux, J. Réthoré, and F. Hild, "Digital image correlation and fracture: an advanced technique for estimating stress intensity factors of 2D and 3D cracks," *Journal of Physics D: Applied Physics,* vol. 42, p. 214004, 2009.
[61] S. Avril, A. Vautrin, and Y. Surrel, "Grid method: application to the characterization of cracks," *Experimental mechanics,* vol. 44, pp. 37-43, 2004.
[62] F. Sur and M. Grediac, "Towards deconvolution to enhance the grid method for in-plane strain measurement," *Inverse Problems and Imaging,* vol. 8, pp. 259-291, 2014.
[63] W. Peters and W. Ranson, "Digital imaging techniques in experimental stress analysis," *Optical Engineering,* vol. 21, pp. 213427-213427-, 1982.
[64] M. Sutton, W. Wolters, W. Peters, W. Ranson, and S. McNeill, "Determination of displacements using an improved digital correlation method," *Image and vision computing,* vol. 1, pp. 133-139, 1983.
[65] T. Chu, W. Ranson, and M. Sutton, "Applications of digital-image-correlation techniques to experimental mechanics," *Experimental mechanics,* vol. 25, pp. 232-244, 1985.
[66] H. W. Schreier and M. A. Sutton, "Systematic errors in digital image correlation due to undermatched subset shape functions," *Experimental Mechanics,* vol. 42, pp. 303-310, 2002.

[67] B. Pan, K. Qian, H. Xie, and A. Asundi, "Two-dimensional digital image correlation for in-plane displacement and strain measurement: a review," *Measurement science and technology,* vol. 20, p. 062001, 2009.
[68] B. Pan, A. Asundi, H. Xie, and J. Gao, "Digital image correlation using iterative least squares and pointwise least squares for displacement field and strain field measurements," *Optics and Lasers in Engineering,* vol. 47, pp. 865-874, 2009.
[69] D. Lecompte, A. Smits, S. Bossuyt, H. Sol, J. Vantomme, D. Van Hemelrijck*, et al.*, "Quality assessment of speckle patterns for digital image correlation," *Optics and lasers in Engineering,* vol. 44, pp. 1132-1145, 2006.
[70] S. Yaofeng and J. H. Pang, "Study of optimal subset size in digital image correlation of speckle pattern images," *Optics and lasers in engineering,* vol. 45, pp. 967-974, 2007.
[71] B. Pan, H. Xie, Z. Wang, K. Qian, and Z. Wang, "Study on subset size selection in digital image correlation for speckle patterns," *Optics express,* vol. 16, pp. 7037-7048, 2008.
[72] M. Sutton, J. Yan, V. Tiwari, H. Schreier, and J. Orteu, "The effect of out-of-plane motion on 2D and 3D digital image correlation measurements," *Optics and Lasers in Engineering,* vol. 46, pp. 746-757, 2008.
[73] P. Luo, Y. Chao, M. Sutton, and W.-H. Peters, "Accurate measurement of three-dimensional deformations in deformable and rigid bodies using computer vision," *Experimental Mechanics,* vol. 33, pp. 123-132, 1993.
[74] S. Mallon, B. Koohbor, A. Kidane, and M. Sutton, "Fracture behavior of prestressed composites subjected to shock loading: a DIC-based study," *Experimental Mechanics,* vol. 55, pp. 211-225, 2015.
[75] J.-H. Yan, M. A. Sutton, X. Deng, Z. Wei, and P. Zavattieri, "Mixed-mode crack growth in ductile thin-sheet materials under combined in-plane and out-of-plane loading," *International journal of fracture,* vol. 160, pp. 169-188, 2009.
[76] M. A. Sutton, J. Yan, X. Deng, C.-S. Cheng, and P. Zavattieri, "Three-dimensional digital image correlation to quantify deformation and crack-opening displacement in ductile aluminum under mixed-mode I/III loading," *Optical Engineering,* vol. 46, pp. 051003-051003-17, 2007.
[77] P.-F. Luo, Y. J. Chao, and M. A. Sutton, "Application of stereo vision to three-dimensional deformation analyses in fracture experiments," *OPTICAL ENGINEERING-BELLINGHAM-INTERNATIONAL SOCIETY FOR OPTICAL ENGINEERING-,* vol. 33, pp. 981-981, 1994.
[78] A. Thompson, J. Llacer, L. C. Finman, E. Hughes, J. Otis, S. Wilson*, et al.*, "Computed tomography using synchrotron radiation," *Nuclear Instruments and Methods in Physics Research,* vol. 222, pp. 319-323, 1984.

[79] M. E. Phelps, J. Mazziotta, and H. Schelbert, *Positron emission tomography*: Los Alamos National Laboratory, 1988.
[80] X. Liu and C. Bathias, "Defects in squeeze-cast Al 2 O 3/Al alloy composites and their effects on mechanical properties," *Composites science and technology,* vol. 46, pp. 245-252, 1993.
[81] J. Kinney, T. Breunig, T. Starr, D. Haupt, M. Nichols, S. Stock*, et al.*, "X-ray tomographic study of chemical vapor infiltration processing of ceramic composites," *Science,* vol. 260, pp. 789-792, 1993.
[82] J.-Y. Buffiere, E. Maire, J. Adrien, J.-P. Masse, and E. Boller, "In situ experiments with X ray tomography: an attractive tool for experimental mechanics," *Experimental mechanics,* vol. 50, pp. 289-305, 2010.
[83] L. A. Feldkamp, L. Davis, and J. W. Kress, "Practical cone-beam algorithm," *Josa a,* vol. 1, pp. 612-619, 1984.
[84] L. Landweber, "An iteration formula for Fredholm integral equations of the first kind," *American journal of mathematics,* vol. 73, pp. 615-624, 1951.
[85] J. D. O'Sullivan, J. Behnsen, T. Starborg, A. S. MacDonald, A. T. Phythian-Adams, K. J. Else*, et al.*, "X-ray micro-computed tomography (μCT): an emerging opportunity in parasite imaging," *Parasitology,* vol. 145, pp. 848-854, 2018.
[86] T. Marrow, J.-Y. Buffiere, P. Withers, G. Johnson, and D. Engelberg, "High resolution X-ray tomography of short fatigue crack nucleation in austempered ductile cast iron," *International journal of fatigue,* vol. 26, pp. 717-725, 2004.
[87] A. Hodgkins, T. Marrow, P. Mummery, B. Marsden, and A. Fok, "X-ray tomography observation of crack propagation in nuclear graphite," *Materials Science and Technology,* vol. 22, pp. 1045-1051, 2006.
[88] H. Toda, I. Sinclair, J.-Y. Buffière, E. Maire, T. Connolley, M. Joyce*, et al.*, "Assessment of the fatigue crack closure phenomenon in damage-tolerant aluminium alloy by in-situ high-resolution synchrotron X-ray microtomography," *Philosophical Magazine,* vol. 83, pp. 2429-2448, 2003.
[89] B. K. Bay, T. S. Smith, D. P. Fyhrie, and M. Saad, "Digital volume correlation: three-dimensional strain mapping using X-ray tomography," *Experimental mechanics,* vol. 39, pp. 217-226, 1999.
[90] T. S. Smith, B. K. Bay, and M. M. Rashid, "Digital volume correlation including rotational degrees of freedom during minimization," *Experimental Mechanics,* vol. 42, pp. 272-278, 2002.
[91] M. Gates, J. Lambros, and M. Heath, "Towards high performance digital volume correlation," *Experimental Mechanics,* vol. 51, pp. 491-507, 2011.
[92] K. Madi, G. Tozzi, Q. Zhang, J. Tong, A. Cossey, A. Au*, et al.*, "Computation of full-field displacements in a scaffold implant using digital volume

correlation and finite element analysis," *Medical engineering & physics,* vol. 35, pp. 1298-1312, 2013.

[93] A. Benoit, S. Guérard, B. Gillet, G. Guillot, F. Hild, D. Mitton*, et al.*, "3D analysis from micro-MRI during in situ compression on cancellous bone," *Journal of biomechanics,* vol. 42, pp. 2381-2386, 2009.

[94] A. Germaneau, P. Doumalin, and J.-C. Dupré, "Comparison between X-ray micro-computed tomography and optical scanning tomography for full 3D strain measurement by digital volume correlation," *NDT & E International,* vol. 41, pp. 407-415, 2008.

[95] M. A. Sutton, M. L. Boone, F. Ma, and J. D. Helm, "A combined modeling–experimental study of the crack opening displacement fracture criterion for characterization of stable crack growth under mixed mode I/II loading in thin sheet materials," *Engineering Fracture Mechanics,* vol. 66, pp. 171-185, 2000.

[96] W. Mekky and P. S. Nicholson, "The fracture toughness of Ni/Al 2 O 3 laminates by digital image correlation I: experimental crack opening displacement and R-curves," *Engineering fracture mechanics,* vol. 73, pp. 571-582, 2006.

[97] J. Rethore, A. Gravouil, F. Morestin, and A. Combescure, "Estimation of mixed-mode stress intensity factors using digital image correlation and an interaction integral," *International Journal of Fracture,* vol. 132, pp. 65-79, 2005.

[98] S. McNeill, W. Peters, and M. Sutton, "Estimation of stress intensity factor by digital image correlation," *Engineering fracture mechanics,* vol. 28, pp. 101-112, 1987.

[99] T. Becker, M. Mostafavi, R. Tait, and T. Marrow, "An approach to calculate the J-integral by digital image correlation displacement field measurement," *Fatigue & Fracture of Engineering Materials & Structures,* vol. 35, pp. 971-984, 2012.

[100] R. Hamam, F. Hild, and S. Roux, "Stress intensity factor gauging by digital image correlation: Application in cyclic fatigue," *Strain,* vol. 43, pp. 181-192, 2007.

[101] J. Yates, M. Zanganeh, and Y. Tai, "Quantifying crack tip displacement fields with DIC," *Engineering Fracture Mechanics,* vol. 77, pp. 2063-2076, 2010.

[102] S. Roux and F. Hild, "Stress intensity factor measurements from digital image correlation: post-processing and integrated approaches," *International Journal of Fracture,* vol. 140, pp. 141-157, 2006.

[103] M. Gosz, J. Dolbow, and B. Moran, "Domain integral formulation for stress intensity factor computation along curved three-dimensional interface cracks," *International Journal of Solids and Structures,* vol. 35, pp. 1763-1783, 1998.

[104] J. Réthoré, F. Hild, and S. Roux, "Extended digital image correlation with crack shape optimization," *International Journal for Numerical Methods in Engineering,* vol. 73, pp. 248-272, 2008.
[105] J. Chen, X. Zhang, N. Zhan, and X. Hu, "Deformation measurement across crack using two-step extended digital image correlation method," *Optics and Lasers in Engineering,* vol. 48, pp. 1126-1131, 2010.
[106] E. Fagerholt, T. Børvik, and O. Hopperstad, "Measuring discontinuous displacement fields in cracked specimens using digital image correlation with mesh adaptation and crack-path optimization," *Optics and Lasers in Engineering,* vol. 51, pp. 299-310, 2013.
[107] J. D. Helm, "Digital image correlation for specimens with multiple growing cracks," *Experimental mechanics,* vol. 48, pp. 753-762, 2008.
[108] J. Réthoré, N. Limodin, J.-Y. Buffiere, F. Hild, W. Ludwig, and S. Roux, "Digital volume correlation analyses of synchrotron tomographic images," *The Journal of Strain Analysis for Engineering Design,* vol. 46, pp. 683-695, 2011.
[109] J. Réthoré, N. Limodin, J.-Y. Buffière, S. Roux, and F. Hild, "Three-dimensional analysis of fatigue crack propagation using X-Ray tomography, digital volume correlation and extended finite element simulations," *Procedia IUTAM,* vol. 4, pp. 151-158, 2012.
[110] N. Limodin, J. Réthoré, J.-Y. Buffiere, F. Hild, S. Roux, W. Ludwig*, et al.*, "Influence of closure on the 3D propagation of fatigue cracks in a nodular cast iron investigated by X-ray tomography and 3D volume correlation," *Acta Materialia,* vol. 58, pp. 2957-2967, 2010.
[111] D. Christen, A. Levchuk, S. Schori, P. Schneider, S. K. Boyd, and R. Müller, "Deformable image registration and 3D strain mapping for the quantitative assessment of cortical bone microdamage," *Journal of the mechanical behavior of biomedical materials,* vol. 8, pp. 184-193, 2012.
[112] J. Lachambre, J. Réthoré, A. Weck, and J.-Y. Buffiere, "Extraction of stress intensity factors for 3D small fatigue cracks using digital volume correlation and X-ray tomography," *International Journal of Fatigue,* vol. 71, pp. 3-10, 2015.
[113] M. Mostafavi, S. McDonald, P. Mummery, and T. Marrow, "Observation and quantification of three-dimensional crack propagation in poly-granular graphite," *Engineering Fracture Mechanics,* vol. 110, pp. 410-420, 2013.
[114] M. Mostafavi, N. Baimpas, E. Tarleton, R. Atwood, S. McDonald, A. Korsunsky*, et al.*, "Three-dimensional crack observation, quantification and simulation in a quasi-brittle material," *Acta Materialia,* vol. 61, pp. 6276-6289, 2013.
[115] D. Steglich and T. F. Morgeneyer, "Failure of Magnesium Sheets Under Monotonic Loading: 3D Examination of Fracture Mode and

Mechanisms," *International Journal of Fracture,* vol. 183, pp. 105-112, September 01 2013.
[116] F. Z. Li, C. F. Shih, and A. Needleman, "A comparison of methods for calculating energy release rates," *Engineering Fracture Mechanics,* vol. 21, pp. 405-421, 1985/01/01/ 1985.
[117] S. M. Barhli, "Advanced quantitative analysis of crack fields, observed by 2D and 3D image correlation, volume correlation and diffraction mapping," University of Oxford, 2017.
[118] M. Williams, "The bending stress distribution at the base of a stationary crack," *J Appl Mech,* vol. 24, pp. 109-14, 1957.
[119] J. Poissant and F. Barthelat, "A novel “subset splitting” procedure for digital image correlation on discontinuous displacement fields," *Experimental mechanics,* vol. 50, pp. 353-364, 2010.
[120] A. M. R. Sousa, J. Xavier, J. J. L. Morais, V. M. J. Filipe, and M. Vaz, "Processing discontinuous displacement fields by a spatio-temporal derivative technique," *Optics and Lasers in Engineering,* vol. 49, pp. 1402-1412, 12// 2011.
[121] E. Fagerholt, T. Børvik, and O. S. Hopperstad, "Measuring discontinuous displacement fields in cracked specimens using digital image correlation with mesh adaptation and crack-path optimization," *Optics and Lasers in Engineering,* vol. 51, pp. 299-310, 2013/03/01/ 2013.
[122] E. Fagerholt, E. Østby, T. Børvik, and O. S. Hopperstad, "Investigation of fracture in small-scale SENT tests of a welded X80 pipeline steel using Digital Image Correlation with node splitting," *Engineering Fracture Mechanics,* vol. 96, pp. 276-293, 2012/12/01/ 2012.
[123] S. Yoneyama, J. Koyanagi, and S. Arikawa, "Measurement of discontinuous displacement/strain using mesh-based digital image correlation," *Advanced Composite Materials,* vol. 25, pp. 329-343, 2016/07/03 2016.
[124] B. Pan, "Reliability-guided digital image correlation for image deformation measurement," *Applied optics,* vol. 48, pp. 1535-1542, 2009.
[125] P. Lopez-Crespo, A. Shterenlikht, E. Patterson, J. Yates, and P. Withers, "The stress intensity of mixed mode cracks determined by digital image correlation," *The Journal of Strain Analysis for Engineering Design,* vol. 43, pp. 769-780, 2008.
[126] S. Vanlanduit, J. Vanherzeele, R. Longo, and P. Guillaume, "A digital image correlation method for fatigue test experiments," *Optics and Lasers in Engineering,* vol. 47, pp. 371-378, 2009.
[127] T. L. Nguyen, S. A. Hall, P. Vacher, and G. Viggiani, "Fracture mechanisms in soft rock: Identification and quantification of evolving displacement discontinuities by extended digital image correlation," *Tectonophysics,* vol. 503, pp. 117-128, 4/25/ 2011.

[128] Z. Yang, W. Ren, M. Mostafavi, S. A. Mcdonald, and T. J. Marrow, "Characterisation of 3D fracture evolution in concrete using in-situ X-ray computed tomography testing and digital volume correlation," in *VIII International Conference on Fracture Mechanics of Concrete and Concrete Structures*, 2013, pp. 1-7.

[129] M. Mostafavi, S. A. McDonald, H. Çetinel, P. M. Mummery, and T. J. Marrow, "Flexural strength and defect behaviour of polygranular graphite under different states of stress," *Carbon,* vol. 59, pp. 325-336, 2013/08/01/ 2013.

[130] P. Leplay, J. Réthoré, S. Meille, M.-C. Baietto, J. Adrien, J. Chevalier*, et al.*, "Three-dimensional Analysis of an In Situ Double-torsion Test by X-ray Computed Tomography and Digital Volume Correlation," *Experimental Mechanics,* vol. 53, pp. 1265-1275, September 01 2013.

[131] J. Adam, M. Klinkmüller, G. Schreurs, and B. Wieneke, "Quantitative 3D strain analysis in analogue experiments simulating tectonic deformation: Integration of X-ray computed tomography and digital volume correlation techniques," *Journal of Structural Geology,* vol. 55, pp. 127-149, 2013/10/01/ 2013.

[132] P. Kovesi, "Phase congruency: A low-level image invariant," *Psychological research,* vol. 64, pp. 136-148, 2000.

[133] P. Kovesi, "Phase congruency detects corners and edges," in *The australian pattern recognition society conference: DICTA 2003*, 2003.

[134] M. C. Morrone and D. Burr, "Feature detection in human vision: A phase-dependent energy model," *Proceedings of the Royal Society of London B: Biological Sciences,* vol. 235, pp. 221-245, 1988.

[135] M. C. Morrone, J. Ross, D. C. Burr, and R. Owens, "Mach bands are phase dependent," *Nature,* vol. 324, pp. 250-253, 1986.

[136] M. C. Morrone and R. A. Owens, "Feature detection from local energy," *Pattern recognition letters,* vol. 6, pp. 303-313, 1987.

[137] M. C. Morrone and D. Burr, "Feature detection in human vision: A phase-dependent energy model," *Proceedings of the Royal Society of London. Series B, biological sciences,* pp. 221-245, 1988.

[138] S. Venkatesh and R. Owens, "On the classification of image features," *Pattern Recognition Letters,* vol. 11, pp. 339-349, 1990.

[139] P. Kovesi, "Image features from phase congruency," *Videre: Journal of computer vision research,* vol. 1, pp. 1-26, 1999.

[140] M. Felsberg and G. Sommer, "The monogenic signal," *IEEE Transactions on Signal Processing,* vol. 49, pp. 3136-3144, 2001.

[141] P. D. Kovesi, "MATLAB and Octave functions for computer vision and image processing," *Centre for Exploration Targeting, School of Earth and Environment, The University of Western Australia,* 2000.

[142] A. M. Shinneeb, J. D. Bugg, and R. Balachandar, "Variable threshold outlier identification in PIV data," *Measurement Science and Technology,* vol. 15, pp. 1722-1732, 2004/07/24 2004.
[143] J. Westerweel and F. Scarano, "Universal outlier detection for PIV data," *Experiments in Fluids,* vol. 39, pp. 1096-1100, December 01 2005.
[144] J. Duncan, D. Dabiri, J. Hove, and M. Gharib, "Universal outlier detection for particle image velocimetry (PIV) and particle tracking velocimetry (PTV) data," *Measurement Science and Technology,* vol. 21, p. 057002, 2010.
[145] G. Besnard, F. Hild, and S. Roux, ""Finite-Element" Displacement Fields Analysis from Digital Images: Application to Portevin–Le Châtelier Bands," *Experimental Mechanics,* vol. 46, pp. 789-803, December 01 2006.
[146] D. Garcia, "A fast all-in-one method for automated post-processing of PIV data," *Experiments in Fluids,* vol. 50, pp. 1247-1259, May 01 2011.
[147] P. Wang, F. Pierron, and O. T. Thomsen, "Identification of Material Parameters of PVC Foams using Digital Image Correlation and the Virtual Fields Method," *Experimental Mechanics,* vol. 53, pp. 1001-1015, July 01 2013.
[148] J. D'Errico, "Inpaint nans," *MATLAB Central File Exchange,* 2004.
[149] W. Thielicke and E. Stamhuis, "PIVlab–towards user-friendly, affordable and accurate digital particle image velocimetry in MATLAB," *Journal of Open Research Software,* vol. 2, 2014.
[150] D. Garcia, "Robust smoothing of gridded data in one and higher dimensions with missing values," *Computational statistics & data analysis,* vol. 54, pp. 1167-1178, 2010.
[151] M. Molteno and T. Becker, "Mode I–III Decomposition of the J-integral from DIC Displacement Data," *Strain,* vol. 51, pp. 492-503, 2015.
[152] P. Lopez-Crespo, A. Shterenlikht, E. A. Patterson, J. R. Yates, and P. J. Withers, "The stress intensity of mixed mode cracks determined by digital image correlation," *The Journal of Strain Analysis for Engineering Design,* vol. 43, pp. 769-780, 2008.
[153] S. Bhattacharjee and D. Deb, "Automatic detection and classification of damage zone(s) for incorporating in digital image correlation technique," *Optics and Lasers in Engineering,* vol. 82, pp. 14-21, 2016/07/01/ 2016.
[154] S. Paris and F. Durand, "A Fast Approximation of the Bilateral Filter Using a Signal Processing Approach," in *Computer Vision – ECCV 2006: 9th European Conference on Computer Vision, Graz, Austria, May 7-13, 2006, Proceedings, Part IV*, A. Leonardis, H. Bischof, and A. Pinz, Eds., ed Berlin, Heidelberg: Springer Berlin Heidelberg, 2006, pp. 568-580.

[155] C. Tomasi and R. Manduchi, "Bilateral filtering for gray and color images," in *Computer Vision, 1998. Sixth International Conference on*, 1998, pp. 839-846.
[156] D. Lenman, "Bilateral Filtering," 06 September 2006.
[157] N. Otsu, "A Threshold Selection Method from Gray-Level Histograms," *IEEE Transactions on Systems, Man, and Cybernetics,* vol. 9, pp. 62-66, 1979.
[158] H. P. VC, "Method and means for recognizing complex patterns," ed: Google Patents, 1962.
[159] D. H. Ballard, "Generalizing the Hough transform to detect arbitrary shapes," *Pattern recognition,* vol. 13, pp. 111-122, 1981.
[160] R. Shadmi, "Select Connected Components in N-D Array," 27 November 2012.
[161] M. Kass, A. Witkin, and D. Terzopoulos, "Snakes: Active contour models," *International journal of computer vision,* vol. 1, pp. 321-331, 1988.
[162] H. Fang, J. Kim, and J.-W. Jang, "A Fast Snake Algorithm for Tracking Multiple Objects," *JIPS,* vol. 7, pp. 519-530, 2011.
[163] D. Mumford and J. Shah, "Optimal approximations by piecewise smooth functions and associated variational problems," *Communications on pure and applied mathematics,* vol. 42, pp. 577-685, 1989.
[164] T. F. Chan and L. A. Vese, "Active contours without edges," *IEEE Transactions on image processing,* vol. 10, pp. 266-277, 2001.
[165] S. Lankton, "Active Contour Segmentation," 31 March 2016.
[166] Y. Zhang, "2D/3D image segmentation toolbox," 28 January 2013.
[167] V. Caselles, R. Kimmel, and G. Sapiro, "Geodesic active contours," *International journal of computer vision,* vol. 22, pp. 61-79, 1997.
[168] Y. Zhang, B. J. Matuszewski, L.-K. Shark, and C. J. Moore, "Medical image segmentation using new hybrid level-set method," in *BioMedical Visualization, 2008. MEDIVIS'08. Fifth International Conference*, 2008, pp. 71-76.
[169] J. Weickert and G. Kühne, "Fast methods for implicit active contour models," *Geometric level set methods in imaging, vision, and graphics,* pp. 43-57, 2003.
[170] M. Bornert, F. Brémand, P. Doumalin, J.-C. Dupré, M. Fazzini, M. Grédiac*, et al.*, "Assessment of digital image correlation measurement errors: methodology and results," *Experimental mechanics,* vol. 49, pp. 353-370, 2009.
[171] H. W. Schreier, J. R. Braasch, and M. A. Sutton, "Systematic errors in digital image correlation caused by intensity interpolation," 2000, p. 7.
[172] H. W. Schreier, J. R. Braasch, and M. A. Sutton, "Systematic errors in digital image correlation caused by intensity interpolation," *Optical engineering,* vol. 39, pp. 2915-2921, 2000.

[173] S. Choi and S. P. Shah, "Measurement of deformations on concrete subjected to compression using image correlation," *Experimental Mechanics,* vol. 37, pp. 307-313, September 01 1997.
[174] R. Zhang and L. He, "Measurement of mixed-mode stress intensity factors using digital image correlation method," *Optics and Lasers in Engineering,* vol. 50, pp. 1001-1007, 2012.
[175] S. Yoneyama, Y. Morimoto, and M. Takashi, "Automatic evaluation of mixed-mode stress intensity factors utilizing digital image correlation," *Strain,* vol. 42, pp. 21-29, 2006.
[176] M. D. Abràmoff, P. J. Magalhães, and S. J. Ram, "Image processing with ImageJ," *Biophotonics international,* vol. 11, pp. 36-42, 2004.
[177] MATLAB, "imnoise."
[178] L. Liu and E. F. Morgan, "Accuracy and precision of digital volume correlation in quantifying displacements and strains in trabecular bone," *Journal of Biomechanics,* vol. 40, pp. 3516-3520, 2007/01/01/ 2007.
[179] H. Leclerc, J.-N. Périé, S. Roux, and F. Hild, "Voxel-Scale Digital Volume Correlation," *Experimental Mechanics,* vol. 51, pp. 479-490, April 01 2011.
[180] H. Leclerc, J.-N. Périé, F. Hild, and S. Roux, "Digital volume correlation: what are the limits to the spatial resolution?," *Mechanics & Industry,* vol. 13, pp. 361-371, 2012.
[181] B. C. Roberts, E. Perilli, and K. J. Reynolds, "Application of the digital volume correlation technique for the measurement of displacement and strain fields in bone: A literature review," *Journal of Biomechanics,* vol. 47, pp. 923-934, 2014/03/21/ 2014.
[182] N. Limodin, J. Réthoré, J. Adrien, J.-Y. Buffière, F. Hild, and S. Roux, "Analysis and Artifact Correction for Volume Correlation Measurements Using Tomographic Images from a Laboratory X-ray Source," *Experimental Mechanics,* vol. 51, pp. 959-970, July 01 2011.
[183] L. Yu and B. Pan, "The errors in digital image correlation due to overmatched shape functions," *Measurement Science and Technology,* vol. 26, p. 045202, 2015.
[184] C. Franck, S. Hong, S. A. Maskarinec, D. A. Tirrell, and G. Ravichandran, "Three-dimensional Full-field Measurements of Large Deformations in Soft Materials Using Confocal Microscopy and Digital Volume Correlation," *Experimental Mechanics,* vol. 47, pp. 427-438, June 01 2007.
[185] S. Barhli, M. Mostafavi, A. Cinar, D. Hollis, and T. Marrow, "J-integral calculation by finite element processing of measured full-field surface displacements," *Experimental mechanics,* pp. 1-13, 2017.
[186] M. Williams, "The bending stress distribution at the base of a stationary crack," *Journal of applied mechanics,* vol. 28, pp. 78-82, 1961.

[187] J.-S. Lee, "Digital image smoothing and the sigma filter," *Computer Vision, Graphics, and Image Processing,* vol. 24, pp. 255-269, 1983.
[188] P. J. G. Schreurs, "Fracture Mechanics " *Eindhoven University of Technology,* 2012.
[189] D. Smith, M. Ayatollahi, and M. Pavier, "The role of T-stress in brittle fracture for linear elastic materials under mixed-mode loading," *Fatigue & Fracture of Engineering Materials & Structures,* vol. 24, pp. 137-150, 2001.
[190] S. Barhli, D. Hollis, B. Wieneke, M. Mostafavi, and T. Marrow, "Advanced 2D and 3D Digital Image Correlation of the Full-Field Displacements of Cracks and Defects," in *Evaluation of Existing and New Sensor Technologies for Fatigue, Fracture and Mechanical Testing*, ed: ASTM International, 2015.
[191] J. C. Mullikin, L. J. van Vliet, H. Netten, F. R. Boddeke, G. van der Feltz, and I. T. Young, "Methods for CCD camera characterization," 1994, pp. 73-84.
[192] S. A. Stanier, J. Blaber, W. A. Take, and D. White, "Improved image-based deformation measurement for geotechnical applications," *Canadian Geotechnical Journal,* vol. 53, pp. 727-739, 2015.
[193] A. Baldi and F. Bertolino, "Experimental Analysis of the Errors due to Polynomial Interpolation in Digital Image Correlation," *Strain,* vol. 51, pp. 248-263, 2015.
[194] W. Tong, "Subpixel image registration with reduced bias," *Optics letters,* vol. 36, pp. 763-765, 2011.
[195] A. Sousa, J. Xavier, M. Vaz, J. Morais, and V. Filipe, "Cross-Correlation and Differential Technique Combination to Determine Displacement Fields," *Strain,* vol. 47, pp. 87-98, 2011.
[196] J. Franklin, S. ZONGQI, B. Atkinson, P. Meredith, F. Rummel, W. Mueller*, et al.*, "Suggested methods for determining the fracture toughness of rock," *INTERNATIONAL JOURNAL OF ROCK MECHANICS AND MINING & GEOMECHANICS ABSTRACTS,* vol. 25, 1988.
[197] T. L. Anderson, *Fracture mechanics: fundamentals and applications*: CRC press, 2017.
[198] P. Wang, F. Pierron, M. Rossi, P. Lava, and O. Thomsen, "Optimised experimental characterisation of polymeric foam material using DIC and the virtual fields method," *Strain,* vol. 52, pp. 59-79, 2016.
[199] H. Sehitoglu and W. Sun, "Modeling of plane strain fatigue crack closure," *ASME, Transactions, Journal of Engineering Materials and Technology,* vol. 113, pp. 31-40, 1991.
[200] J. Lankford and D. L. Davidson, "The effect of overloads upon fatigue crack tip opening displacement and crack tip opening closing loads in aluminium alloys," in *ICF5, Cannes (France) 1981*, 1981.

[201] E. ASTM, "8M. Standard test methods of tension testing of metallic materials [metric]," *Annual book of ASTM standards,* vol. 3, 2003.
[202] J. Marrow, C. Reinhard, Y. Vertyagina, L. Saucedo-Mora, D. Collins, and M. Mostafavi, "3D studies of damage by combined X-ray tomography and digital volume correlation," *Procedia Materials Science,* vol. 3, pp. 1554-1559, 2014.
[203] M. Drakopoulos, T. Connolley, C. Reinhard, R. Atwood, O. Magdysyuk, N. Vo*, et al.*, "I12: the Joint Engineering, Environment and Processing (JEEP) beamline at Diamond Light Source," *J Synchrotron Radiat,* vol. 22, pp. 828-38, May 2015.
[204] S. Preston and B. Marsden, "Changes in the coefficient of thermal expansion in stressed Gilsocarbon graphite," *Carbon,* vol. 44, pp. 1250-1257, 2006.
[205] T. J. Marrow, D. Liu, S. M. Barhli, L. Saucedo Mora, Y. Vertyagina, D. M. Collins*, et al.*, "In situ measurement of the strains within a mechanically loaded polygranular graphite," *Carbon,* vol. 96, pp. 285-302, 2016/01/01/ 2016.
[206] M. Mostafavi, S. A. McDonald, P. M. Mummery, and T. J. Marrow, "Observation and quantification of three-dimensional crack propagation in poly-granular graphite," *Engineering Fracture Mechanics,* vol. 110, pp. 410-420, 2013/09/01/ 2013.
[207] M. Mostafavi and T. J. Marrow, "Quantitative in situ study of short crack propagation in polygranular graphite by digital image correlation," *Fatigue & Fracture of Engineering Materials & Structures,* vol. 35, pp. 695-707, 2012.
[208] M. Mostafavi, N. Baimpas, E. Tarleton, R. C. Atwood, S. A. McDonald, A. M. Korsunsky*, et al.*, "Three-dimensional crack observation, quantification and simulation in a quasi-brittle material," *Acta Materialia,* vol. 61, pp. 6276-6289, 2013/09/01/ 2013.
[209] S. Titarenko, P. J. Withers, and A. Yagola, "An analytical formula for ring artefact suppression in X-ray tomography," *Applied Mathematics Letters,* vol. 23, pp. 1489-1495, 2010/12/01/ 2010.
[210] C. A. Schneider, W. S. Rasband, and K. W. Eliceiri, "NIH Image to ImageJ: 25 years of image analysis," *Nat Meth,* vol. 9, pp. 671-675, 07//print 2012.
[211] A. International, *Standard test method for measurement of fatigue crack growth rates*: ASTM International, 2011.
[212] A. c. group. (2005, MTM46 intermediate service temperature vacuum processable prepreg.
[213] N. L. Hancox, "Thermal effects on polymer matrix composites: Part 1. Thermal cycling," *Materials & Design,* vol. 19, pp. 85-91, 6/1/ 1998.

[214] D. S. Adams, D. E. Bowles, and C. T. Herakovich, "Thermally induced transverse cracking in graphite-epoxy cross-ply laminates," *Journal of reinforced Plastics and composites,* vol. 5, pp. 152-169, 1986.

[215] J. Varna, L. A. Berglund, R. Talreja, and A. Jakovics, "A Study of the Opening Displacement of Transverse Cracks in Cross-Ply Laminates," *International Journal of Damage Mechanics,* vol. 2, pp. 272-289, 1993.

[216] J. E. Bailey, P. T. Curtis, and A. Parvizi, "On the Transverse Cracking and Longitudinal Splitting Behaviour of Glass and Carbon Fibre Reinforced Epoxy Cross Ply Laminates and the Effect of Poisson and Thermally Generated Strain," *Proceedings of the Royal Society of London. A. Mathematical and Physical Sciences,* vol. 366, pp. 599-623, 1979.

[217] J. F. Timmerman, B. S. Hayes, and J. C. Seferis, "Cure temperature effects on cryogenic microcracking of polymeric composite materials," *Polymer Composites,* vol. 24, pp. 132-139, 2003.

[218] G. Fernandez, H. Bischof, and R. Beichel, "Nonlinear filters on 3D CT imaging-bilateral filter and mean shift filter," *Proc. CVWW,* vol. 3, pp. 21-26, 2003.

[219] N. Kazakova, M. Margala, and N. G. Durdle, "Sobel edge detection processor for a real-time volume rendering system," in *Circuits and Systems, 2004. ISCAS'04. Proceedings of the 2004 International Symposium on*, 2004, pp. II-913.

[220] D. Borrmann, J. Elseberg, K. Lingemann, and A. Nüchter, "The 3D Hough Transform for plane detection in point clouds: A review and a new accumulator design," *3D Research,* vol. 2, p. 3, November 03 2011.

[221] K. Rajpoot, V. Grau, and J. A. Noble, "Local-phase based 3d boundary detection using monogenic signal and its application to real-time 3-d echocardiography images," in *Biomedical Imaging: From Nano to Macro, 2009. ISBI'09. IEEE International Symposium on*, 2009, pp. 783-786.